LEABHARLANN CHOLÁISTE NA TRÍONÓIDE, BAILE ÁTHA CLIATH | TRINITY COLLEGE LIBRARY DUBLIN
Ollscoil Átha Cliath | The University of Dublin

Terms and Conditions of Use of Digitised Theses from Trinity College Library Dublin

Copyright statement

All material supplied by Trinity College Library is protected by copyright (under the Copyright and Related Rights Act, 2000 as amended) and other relevant Intellectual Property Rights. By accessing and using a Digitised Thesis from Trinity College Library you acknowledge that all Intellectual Property Rights in any Works supplied are the sole and exclusive property of the copyright and/or other IPR holder. Specific copyright holders may not be explicitly identified. Use of materials from other sources within a thesis should not be construed as a claim over them.

A non-exclusive, non-transferable licence is hereby granted to those using or reproducing, in whole or in part, the material for valid purposes, providing the copyright owners are acknowledged using the normal conventions. Where specific permission to use material is required, this is identified and such permission must be sought from the copyright holder or agency cited.

Liability statement

By using a Digitised Thesis, I accept that Trinity College Dublin bears no legal responsibility for the accuracy, legality or comprehensiveness of materials contained within the thesis, and that Trinity College Dublin accepts no liability for indirect, consequential, or incidental, damages or losses arising from use of the thesis for whatever reason. Information located in a thesis may be subject to specific use constraints, details of which may not be explicitly described. It is the responsibility of potential and actual users to be aware of such constraints and to abide by them. By making use of material from a digitised thesis, you accept these copyright and disclaimer provisions. Where it is brought to the attention of Trinity College Library that there may be a breach of copyright or other restraint, it is the policy to withdraw or take down access to a thesis while the issue is being resolved.

Access Agreement

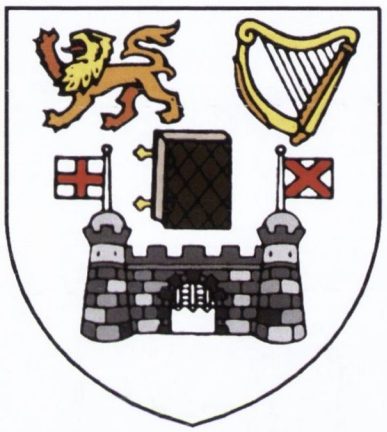
By using a Digitised Thesis from Trinity College Library you are bound by the following Terms & Conditions. Please read them carefully.

I have read and I understand the following statement: All material supplied via a Digitised Thesis from Trinity College Library is protected by copyright and other intellectual property rights, and duplication or sale of all or part of any of a thesis is not permitted, except that material may be duplicated by you for your research use or for educational purposes in electronic or print form providing the copyright owners are acknowledged using the normal conventions. You must obtain permission for any other use. Electronic or print copies may not be offered, whether for sale or otherwise to anyone. This copy has been supplied on the understanding that it is copyright material and that no quotation from the thesis may be published without proper acknowledgement.

Synthesis and structural characterisation of metal-organic frameworks composed of transition or lanthanide metal cations linked *via* tritopic ligands

Gerard Martin Tobin

B.A. (Mod)



A thesis submitted to the University of Dublin for the degree of Doctor of Philosophy

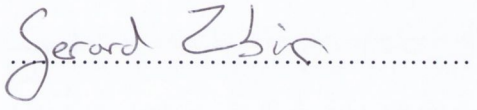
Department of Chemistry
University of Dublin
2014

TRINITY COLLEGE
0 9 JUN 2014
LIBRARY DUBLIN
Thesis 10405

Declaration

I declare that this thesis has not been submitted as an exercise for a degree at this or any other university and it is entirely my own work, except where otherwise cited, referenced, acknowledged or accredited.

I agree to deposit this thesis in the University's open access institutional repository or allow the library to do so on my behalf, subject to Irish Copyright Legislation and Trinity College Library conditions of use and acknowledgement. I agree that the Library may at their discretion lend or copy this thesis upon request.



Gerard Martin Tobin B.A. (Mod.)

Summary

The work presented in this thesis is concerned with the design and synthesis of metal-organic frameworks (MOFs). MOFs are a class of hybrid inorganic-organic material composed of metal-ions or clusters of metal-ions linked *via* organic linkers into high dimensional frameworks. Interest in MOFs arises from their advantageous physicochemical properties such as porosity and ease of functionalisation, which facilitate their use in a diverse range of potential applications such as energy storage, drug delivery and catalysis. The research outlined in this thesis focuses on the synthesis and characterisation of novel MOFs composed of tritopic ligands and both transition and rare-earth metal cations. The first chapter introduces the reader to the subject area of MOFs and in the second chapter the specific objectives of this research are outlined.

Chapter three, details the synthesis of two tritopic ligands 3,5-di(1H-tetrazol-1-yl)benzoic acid, **L1** and 5-(1H-tetrazol-1-yl)isophthalic acid, **L2**, which contain N-donor tetrazole and O-donor carboxylate functionalities. Complexation of **L1** with Co^{II} and Mn^{II} ions produced the respective MOFs $[Co(\mathbf{L2})_2]$, (**1**) and $[Mn(\mathbf{L1})_2]$, (**2**). Bidentate carboxylate groups bridge neighbouring metal centres in **1** and **2** into infinite 1D polymeric chains and the differing arrangement of **L1** in both compounds led to 2D and 3D MOFs, respectively. The modification of **L1**, through the substitution of a tetrazole group with a carboxylic acid moiety, led to the synthesis of **L2** and initially yielded $[Cd(\mathbf{L2})_2(MeOH)]$, (**3**). **3** contains mononuclear Cd^{II} secondary building units (SBUs) connected by **L2** into 2D sheets and hydrogen bonding and π-π stacking interactions facilitate the 3D supramolecular structure of **3**. $[Zn(\mathbf{L2})(H_2O)_2]$, (**4**), is comprised of mononuclear trigonal bipyramidal SBUs, joined by **L2** into a 3D MOF. [Cu(**L2**)], (**5**), is the final compound in this chapter and is composed of dinuclear $\{Cu_2(COO)_4\}$ paddlewheel SBUs, linked *via* **L2** into a 3D porous framework, with a solvent accessible void volume of 52% of the unit cell volume and a BET surface area of *ca.* 935 $m^2\ g^{-1}$. Furthermore, **5** demonstrates a high CO_2 storage capacity of 29 wt% at 1 atm and 290 K.

In chapter four, the synthesis and characterisation of four MOFs, composed of rigid multinuclear SBUs linked *via* the tritopic ligand 1,3,5-benzene-trisethynyl benzoic acid (**L3**) are discussed. The reaction of **L3** and Zn^{II} yielded the compound $[Zn_3(\mathbf{L3})_2(DMF)_2]$, (**6**), which contains trinuclear zinc SBUs and through **L3** a 3D open-framework is generated with a solvent accessible void volume of 68% of the cell volume. Modification of the reaction

conditions produced pentanuclear zinc SBUs and the formation of the porous MOF $(Me_2NH_2)[Zn_5(\mathbf{L3})_3(\mu_3\text{-}OH)_2(DMF)_2]$, (**7**), with a BET surface area of 1338 $m^2\ g^{-1}$. The use of a comparable synthetic methodology resulted in the generation of $(Me_2NH_2)[Co_5(\mathbf{L3})_3(\mu_3\text{-}OH)_2(DMF)_2]$, (**8**). Finally, the **pto**-type framework $[Cu_3(\mathbf{L3})_2(H_2O)_3]$, (**9**) is discussed, which has a large solvent accessible void volume of 77% of the cell volume and is formed by the combination of the tritopic ligand **L3** and a four-connecting copper paddlewheel SBU.

Chapter five describes two series of structurally related lanthanide MOFs (LnMOFs). The rigid and augmented nature of **L3** facilitated the formation of a rare example of a porous LnMOF, namely $[Ho(\mathbf{L3})(H_2O)_2]$, (**10**). **10** contains infinite $[Ho(CO_2)_3]_n$ SBUs that are linked *via* **L3** into an open-framework, with 1D open-channels that give rise to a void volume of *ca.* 60% of the cell volume. Thermal treatment of **10** results in a permanently porous framework, with a corresponding BET surface area of *ca.* 760 $m^2\ g^{-1}$. The temperature dependent magnetic susceptibility of **10** was also measured and revealed antiferromagnetic interactions between the Ho^{III} ions. Lanthanide (Dy^{III}, Er^{III}, Eu^{III}, Tb^{III} and Yb^{III}) compounds structurally related to **10** were synthesised using analogous synthetic conditions and characterised through a combination of FT-IR spectroscopy, PXRD measurements, and elemental and thermogravimetric analyses. Within this chapter the photoluminescent properties of **10(Eu)** and the related compounds **Nd(L3)** and **Sm(L3)** are also discussed. $[Ho_2(\mathbf{L2})_4(H_2O)_4]$, (**11**), in a comparable manner to **10**, contains Ho^{III} ions linked by bridging carboxylate groups into infinite 1D Ho-Ho chains, which are further connected to each other through **L2** to form 2D sheets. Hydrogen bonding interactions facilitate the supramolecular layered lamellar structure found in **11**. Finally, the isostructural LnMOFs **11(Dy)** and **11(Yb)** are also detailed.

Chapter six provides concluding remarks and chapter seven discusses the experimental details of the synthesis and characterisation of the compounds described in this study.

Acknowledgements

First and foremost I would like to extend my extreme gratitude towards my supervisor Dr. Wolfgang Schmitt, for his support over the previous four years and for providing me with the opportunity to study under his tutelage. I would also like to thank Science Foundation Ireland for providing the finances that funded this work.

Although research can sometimes appear to be a solitary pursuit, it is very much a team effort and as such I would like to thank those who helped me reach this point. A special thank you is extended to Dr. Nianyong Zhu, Dr. Thomas McCabe and Dr. Lei Zhang for conducting the single crystal X-ray diffractometry measurements discussed in this work. I would also like to thank Prof. Rodolphe Clérac for conducting the magnetic measurements presented in the report and Dr. Steve Comby for his help with the photoluminescence studies that were conducted.

I would like to thank the academic, administrative, technical and administrative staff within the School of Chemistry. Especially Drs. John O'Brien, Manual Ruther and Martin Feeney for their help with NMR and mass spectrometry. My sincerest apologies if I have left anybody out.

Past and present members of the Schmitt group have been a joy to work with and always willing to provide help and assistance, I hope I have given back as much as I have received. I would like to personally thank Dr. Camelia Onet and Adam Patterson for proof reading this thesis.

I would like to thank my friends who although not involved in this work, provided me with constant support.

Last but definitely not least I would like to thank my family, my parents Seán and Mary, my sister Anne, my brother Paul and brother in-law Billy, for all the support you have shown me over the last four years and beyond, even when it looked like I would be a student forever.

Table of Contents

Declaration i

Summary ii

Acknowledgements iv

Table of Contents v

Abbreviations x

List of ligands and compounds xiii

1 Introduction 1

1.1 Supramolecular chemistry 2

1.2 Metal-organic frameworks 4

1.2.1 Introduction to metal-organic frameworks 4

1.2.2 Classifying metal-organic frameworks 5

1.2.3 Reticular Synthesis 8

1.2.4 Nitrogen and N-O type ligands 13

1.2.5 Synthesis of metal-organic frameworks 14

1.2.6 Applications of MOFs 16

1.3 Gas storage in porous materials 20

1.3.1 Measuring gas uptake and surface areas in MOFs 20

1.3.2 Introduction to hydrogen storage 21

1.3.3 Gas storage in MOFs 23

1.4 Lanthanides 24

1.4.1 Introduction to lanthanides 24

1.4.2 Lanthanide luminescence 26

1.4.3 Lanthanide metal-organic frameworks 29

1.5 References 32

2 Objectives of this project 40

2.1 Project objectives 41

2.2 Specific aims of this study 42
2.3 References 43

3 Metal-organic frameworks synthesised using tetrazole and carboxylate functionalised aromatic ligands 44
3.1 Introduction 45
3.2 Ligand synthesis 46
3.2.1 Synthesis of 3,5-di(1H-tetrazol-1-yl)benzoic acid, **L1** 46
3.2.2 Synthesis of 5-(1H-tetrazol-1-yl)isophthalic acid, **L2** 47
3.3 [Co(**L1**)$_2$], (**1**). 48
3.3.1 Synthesis and structural characterisation of compound **1** 48
3.3.2 Further characterisation of **1** 53
3.4 [Mn(**L1**)], (**2**) 54
3.4.1 Synthesis and structural characterisation of compound **2** 54
3.4.2 Further characterisation of **2** 60
3.5 [Cd(**L2**)$_2$(MeOH)], (**3**) 62
3.5.1 Synthesis and structural characterisation of compound **3** 62
3.5.2 Further characterisation of **3** 67
3.6 [Zn(**L2**)(H$_2$O)$_2$], (**4**) 69
3.6.1 Synthesis and structural characterisation of compound **4** 69
3.6.2 Further characterisation of **4** 75
3.7 [Cu(**L2**)], **5** 77
3.7.1 Synthesis and structural characterisation of compound **5** 77
3.7.2 Further characterisation of **5** 83
3.7.3 Surface area determination of compound **5** 85
3.8 Conclusion 87
3.9 References 89

4 The exploitation of carboxylate stabilised SBUs for the generation of porous MOFs 91
4.1 Introduction 92
4.2 Ligand Synthesis 92
4.3 [Zn$_3$(**L3**)$_2$(DMF)$_2$], (**6**) 95
4.3.1 Synthesis and structural characterisation of compound **6** 95
4.3.2 Further characterisation of **6** 101
4.4 (Me$_2$NH$_2$)[Zn$_5$(**L3**)$_3$(μ_3-OH)$_2$(DMF)$_2$], (**7**) 102

4.4.1 Synthesis and structural characterisation of compound **7** 102
4.4.2 Further characterisation of **7** 109
4.4.3 BET surface area determination of compound **7** 111
4.5 $(Me_2NH_2)[Co_5(\mathbf{L3})_3(\mu_3\text{-}OH)_2(DMF)_2]$, (**8**) 112
4.5.1 Synthesis and structural characterisation of compound **8** 112
4.5.2 Further characterisation of **8** 117
4.5.3 Surface area determination of compound **8** 118
4.6 $[Cu_3(\mathbf{L3})_2(H_2O)_3]$, (**9**) 119
4.6.1 Synthesis and structural characterisation of compound **9** 119
4.6.2 Further characterisation of **9** 126
4.7 Conclusion 127
4.8 References 129

5 Lanthanide-organic frameworks 131
5.1 Introduction 132
5.2 $[Ho(\mathbf{L3})(H_2O)_2]$, (**10**) 132
5.2.1 Synthesis and structural characterisation of compound **10** 132
5.2.2 Further characterisation of **10** 139
5.2.3 BET Surface area determination of **10** 141
5.2.4 Magnetic properties of **10** 144
5.3 Lanthanide compounds structurally related to **10** 145
5.3.1 PXRD studies of the Ln^{III} compounds structurally related to **10** 145
5.3.2 FT-IR spectra of Ln compounds structurally related to **10** 147
5.3.3 TGA of Ln^{III} compounds structurally related to **10** 149
5.3.4 Magnetic studies of **10(Dy)** 150
5.4 Photoluminescent studies 151
5.4.1 L3 emission and excitation spectra 151
5.4.2 Photoluminescent studies of **10(Eu)** 152
5.4.3 Luminescent studies of **10(Eu)** doped with 2-naphthoyltrifluoroacetone (NTA) 155
5.4.4 Luminescent studies of a **Nd(L3)** compound 157
5.4.5 Luminescent studies of a **Sm(L3)** compound 160
5.5 $[Ho_2(\mathbf{L2})_4(H_2O)_4]$, (**11**) 162
5.5.1 Synthesis and structural characterisation of compound **11** 162
5.5.2 Further characterisation of **11** 169
5.6 Lanthanide compounds structurally related to **11** 171

5.6.1 PXRD studies of the Ln^{III} compounds structurally related to **11** 171
5.6.2 FT-IR of Ln(**L2**) compounds isostructural to **11** 172
5.6.3 TGA of Ln^{III} compounds isostructural to **11** 174
5.7 Conclusion 175
5.8 References 177

6 Conclusions 180

7 Experimental 182
7.1 Materials and methods 183
7.1.1 Reagents 183
7.1.2 Nuclear magnetic resonance spectroscopy 183
7.1.3 Infrared spectroscopy 183
7.1.4 Mass spectrometry 183
7.1.5 Elemental analysis 183
7.1.6 Single crystal X-ray diffraction 184
7.1.7 X-ray powder diffraction 184
7.1.8 Solvothermal synthesis 184
7.1.9 Thermogravimetric Analysis 185
7.1.10 Magnetic measurements 185
7.1.11 Photoluminescence spectroscopy 185
7.1.12 Gas sorption measurements 185
7.2 Ligand Synthesis 187
7.2.1 Synthesis of 3,5-di(1H-tetrazol-1-yl)benzoic acid, (**L1**) 187
7.2.2 Synthesis of 5-(1H-tetrazol-1-yl)isophthalic acid, (**L2**) 187
7.2.3 Synthesis of 1,3,5-tris(2-methyl-2-hydroxy-3-butnyl)-benzene 188
7.2.4 Synthesis of 1,3,5-triethynylbenzene 189
7.2.5 Synthesis of trimethyl-4,4',4"-(benzene-1,3,5–triyltris(ethyne-2,1-diyl))tribenzoate 189
7.2.6 Synthesis of 1,3,5-Benzene-trisethynyl benzoic acid, (**L3**) 190
7.3 Synthesis of Coordination Compounds 190
7.3.1 Synthesis of $[Co(\mathbf{L1})_2]$, (**1**) 190
7.3.2 Synthesis of $[Mn(\mathbf{L1})_2]$, (**2**) 191
7.3.3 Synthesis of $[Cd(\mathbf{L2})_2MeOH]$, (**3**) 191
7.3.4 Synthesis of $[Zn(\mathbf{L2})(H_2O)_2]$, (**4**) 192
7.3.5 Synthesis of [Cu(**L2**)], (**5**) 192

7.3.6 Synthesis of $[Zn_3(\mathbf{L3})_2(DMF)_2]$, (**6**) 193
7.3.7 Synthesis of $(Me_2NH_2)[Zn_5(\mathbf{L3})_3(\mu_3\text{-}OH)_2(DMF)_2]$, (**7**) 193
7.3.8 Synthesis of $(Me_2NH_2)[Co_5(\mathbf{L3})_3(\mu_3\text{-}OH)_2(DMF)_2]$, (**8**) 193
7.3.9 $[Cu_3(\mathbf{L3})_2(H_2O)_3]$, (**9**) 194
7.3.10 Synthesis of $[Ho(\mathbf{L3})(H_2O)_2]$, (**10**) 194
7.3.11 Compounds structurally related to $[Ho(\mathbf{L3})(H_2O)_2]$, (**10**) 195
7.3.12 Synthesis of $[Ho_2(\mathbf{L2})_4(H_2O)_4]$, (**11**) 196
7.3.13 Compounds structurally related to **11** 197
7.4 References: 197

Abbreviations

1D:	One dimensional
^{1}H-NMR:	Proton nuclear magnetic resonance
2D:	Two dimensional
3D:	Three dimensional
ac:	Alternating current
atm:	Atmosphere
AU:	Arbitrary units
BDC:	1,4-benzenedicarboxylic acid
BET:	Brunauer-Emmett-Teller
BPDC:	Biphenyl-4,4'-dicarboxylate
BTC:	1,3,5-benzene tricarboxylic acid
CHN:	Carbon hydrogen nitrogen elemental analysis
CNT:	Carbon nanotubes
CPD:	Critical point drying
CPS:	Counts per second
dc:	Direct current
DCM:	Dichloromethane
DMF:	*N*,*N*-Dimethylformamide
DMSO:	Dimethyl sulphoxide
DNA:	Deoxyribonucleic acid
DOBC:	Dioxybenzenedicarboxylate
DOE:	United States Department of Energy
DTPA:	Diethylenetriaminepentacetate

ESMS:	Electon spray mass spectrometry
FT-IR:	Fourier transform infrared spectroscopy
g:	Landé g-factor
HBDT:	1,4-benzeneditetrazol-5-yl
HKUST:	Hong Kong University of Science and Technology
IRMOF:	Isoreticular metal-organic framework
J:	Coupling constant
Ln:	Lanthanide metal
LnMOF:	Lanthanide metal-organic frameworks
M:	Magnetisation
MIL:	Materials of Institut Lavoisier
min:	Minute
MMOF:	Microporous metal-organic frameworks
MOF:	Metal-organic frameworks
MRI:	Magnetic resonance imaging
NIR:	Near-infrared
NMR:	Nuclear magnetic resonance
NU:	Northwestern University
P:	Pressure
P_0:	Saturation pressure
PCN:	Porous coordination network
PVDC:	4, 4'-[(2, 5-dimethoxy-1, 4-phenylene)di-2, 1-ethenediyl]bis-benzoic acid
PXRD:	Powder X-ray diffraction
R1:	Magnetic resonance imaging longitudinal relaxation
S:	Spin quantum number

SBU:	Secondary building units
SCO:	Spin-crossover
SCOF:	Spin-crossover frameworks
SNU:	Seoul National University
SQUID:	Superconducting quantum interface device
T:	Temperature
TATB:	4,4',4''-s-triazine-2,4,6-triyltribenzoate
TCM:	Trinity College material
TGA:	Thermogravimetric analysis
TMA:	1,3,5-benzene tricarboxylic acid
UV:	Ultraviolet
W:	Weight of adsorbed gas
wt%:	Weight percent
wt:	Weight
XRD:	X-ray diffraction
δ:	Chemical shift
λ:	Wavelength
λ_{an}:	Analysis wavelength
λ_{ex}:	Excitation wavelength
ν_a:	Asymmetric stretch
ν_s:	Symmetric stretch
χ:	Magnetic susceptibility

List of Ligands and Compounds

Ligands:

L1: 3,5-di(1H-tetrazol-1-yl)benzoic acid

L2: 5-(1H-tetrazol-1-yl)isophthalic acid

L3: 1,3,5-Benzene-trisethynyl benzoic acid

Compounds:

1: [Co(**L1**)$_2$]

2: [Mn(**L1**)$_2$]

3: [Cd(**L2**)$_2$MeOH]

4: [Zn(**L2**)(H$_2$O)$_2$]

5: [Cu(**L2**)]

6: [Zn$_3$(**L3**)$_2$(DMF)$_2$]

7: (Me$_2$NH$_2$)[Zn$_5$(**L3**)$_3$(μ_3-OH)$_2$(DMF)$_2$]

8: (Me$_2$NH$_2$)[Co$_5$(**L3**)$_3$(μ_3-OH)$_2$(DMF)$_2$]

9: [Cu$_3$(**L3**)$_2$(H$_2$O)$_3$]

10: [Ho(**L3**)(H$_2$O)$_2$]

10(Dy): [Dy(**L3**)(H$_2$O)$_2$]

10(Er): [Er(**L3**)(H$_2$O)$_2$]

10(Eu): [Eu(**L3**)(H$_2$O)$_2$]

10(Tb): [Tb(**L3**)(H$_2$O)$_2$]

10(Yb): [Yb(**L3**)(H$_2$O)$_2$]

11: [Ho$_2$(**L2**)$_4$(H$_2$O)$_4$]

11(Dy): [Dy$_2$(**L2**)$_4$(H$_2$O)$_4$]

11(Yb): [Yb$_2$(**L2**)$_4$(H$_2$O)$_4$]

Chapter 1

Introduction

1 Introduction

1.1 Supramolecular chemistry

The ultimate aim of crystal engineering is to provide protocols for the synthesis of novel materials whose structure and properties are predetermined by the designer and was first proposed by Schmidt in 1971.[1] He recognised the crucial role that intermolecular interactions play in the stability of crystal lattices and hypothesised that a greater understanding of these intermolecular forces could lead to the "control of molecular packing" and eventually to the engineering of crystal structures for a particular purpose.

Shortly after Schmidt's seminal paper, J. M. Lehn defined the concept of supramolecular chemistry as *'the chemistry of molecular assemblies and of the intermolecular bond'* or more simply *'chemistry beyond the molecule'*.[2,3] Supramolecular chemistry is concerned with how weaker non-covalent interactions, such as van der Waals forces,[4,5] hydrogen bonding[6,7] and π-π stacking interactions,[8,9] can influence the reversible self-assembly of molecules into predetermined structures. It is when such supramolecular interactions are combined in numbers, that they can instigate the self-assembly process into multicomponent aggregates through molecular recognition.

Molecular recognition encompasses the concept of complementarity that is necessary for intermolecular interactions between molecules. Hydrogen bonding is one such example of this complementarity and occurs between a hydrogen atom, covalently linked to a more electronegative atom and second electronegative atom *e.g.* fluorine, oxygen or nitrogen. The energy of a hydrogen bond can vary between 4 kJ mol^{-1} for two uncharged pairs and 17 kJ mol^{-1} for a charged donor-acceptor pair.[10] The directional nature of a hydrogen bond, where the O-O bond distance between two hydrogen bonding pairs typically range between 2.5 and 3.2 Å, and the ease with which hydrogen bonding functionalities can be added to organic molecules, makes them very appealing to chemists when designing supramolecular assemblies.[11]

Arguably the most important example of the complementarity of hydrogen bonding is that of deoxyribonucleic acid (DNA), which is assembled *via* complimentary base pairing.[12] DNA strands self-assemble into a double helix *via* hydrogen bonding interactions between complimentary base pairs, with Adenine (A) binding to thymine (T) through two hydrogen bonding base pairs and guanine (G) binding *via* three base pairs to cytosine (C)

(**Figure 1.1**). The precise ordering of these base pairs facilitates the encoding of genetic information and it is the reversible nature of these bonds that facilitates DNA replication, as it allows the helices to break up and reassemble under certain conditions, such as high or low temperature or a change in pH.[13]

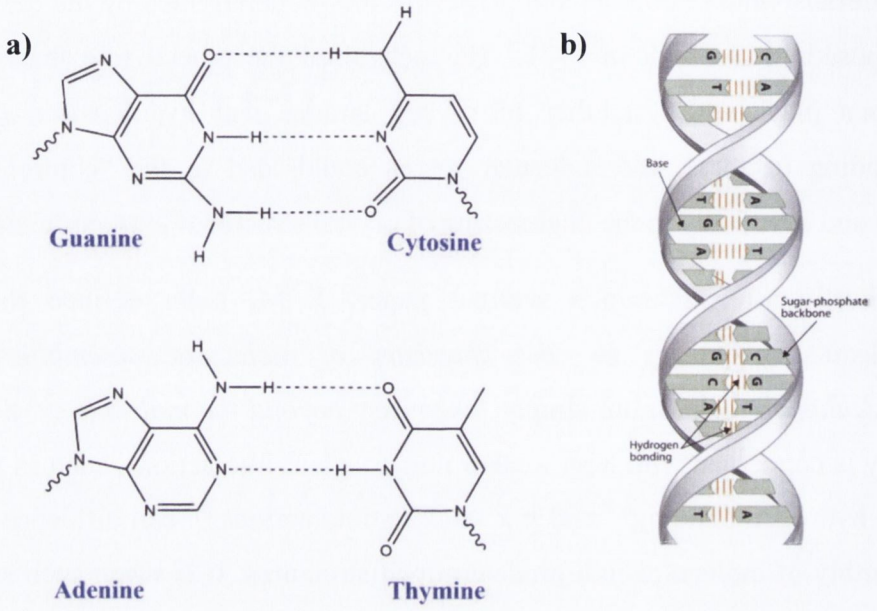


Figure 1.1: a) Complimentary base pairs, with the dotted lines representing hydrogen bonding, **b)** simplified diagram of the DNA double helix, (G: guanine, C: cytosine, A: adenine, T: thymine).[14]

F. M. Menger attributed the importance of research into supramolecular systems to a number of factors, chiefly the vast number of industrial applications *e.g.* the encapsulation of an active drug molecule in a self-assembling vesicle that ensures that the drug is only released in certain environments, such as a cancerous cell, and how the ever increasing knowledge of supramolecular interactions can help us understand how certain biological components self-assemble through supramolecular interactions.[15]

1.2 Metal-organic frameworks

1.2.1 Introduction to metal-organic frameworks

Porous materials have proven to be invaluable to many industrial applications, where they are commonly used in gas-separation,[16] drug storage and delivery systems,[17] catalysis,[18] and are increasingly being investigated for their gas-storage properties (see 1.3: Gas storage in porous materials).

However, up until relatively recent times, porous materials were either purely organic (*e.g.* activated charcoal[19] and more recently carbon nanotubes[20]) or inorganic systems (*e.g.* zeolites[21]). But this changed with the development of metal-organic frameworks (MOFs). MOFs are a class of crystalline solid composed of metal ions or clusters of metal ions, linked *via* organic ligands into high dimensional frameworks. This combination of organic and inorganic components confers certain advantages to MOFs over purely inorganic porous materials. One such advantage being the extremely wide variety of metal cations (*e.g.* main group metals,[22,23] transition metals[24,25] or rare earth elements[26,27] (see section 1.4.3)) that can be used to synthesise MOFs. This feature contrasts with zeolites and other porous aluminosilicates, which are typically composed of tetrahedrally coordinated silicon and aluminium centres. The differing geometries associated with each metal cation leads to a vast potential of possible framework architectures and when combined with the near infinite possibilities for the organic linker, means the number of unique MOFs with different topologies is almost limitless. This flexibility enables the fine tuning of MOFs for a particular application, some of which will be outlined in section 1.2.6. Finally, the value placed on MOFs is evident by the huge growth in research papers focusing on MOFs and their applications over the last decade (**Figure 1.2**).[28]

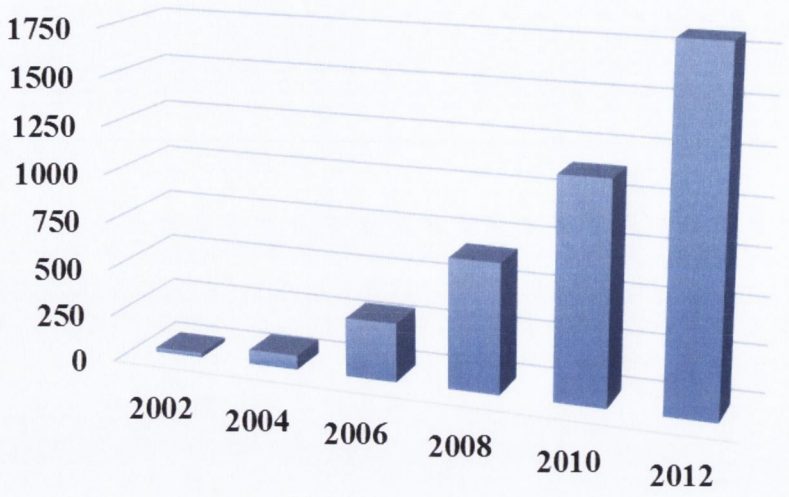


Figure 1.2: Number of publications containing the term metal-organic framework in the topic *versus* year.[28]

1.2.2 Classifying metal-organic frameworks

The complicated topologies of MOFs can be simplified through the use of 'net-descriptors'. This approach envisages nets as infinite arrays of connecting nodes and was first proposed by Wells over twenty years ago.[29] These nodes may be metal ions, metal clusters or ligands. To qualify as node it must be connected to three or more other nodes *via* two-way connecting linkers, therefore if a ligand, is connected to three or more nodes, it too must be considered as a node.

Wells' codes adopt the concept of shortest circuits when describing the topology of a net according to the notation (n, p), where n is the number of nodes in the smallest closed circuit of a net and the connectivity of each node is represented as p. A shortest circuit is the minimum number of nodes encountered when making a loop between two linkers from a given node. Thus, the shortest circuit in the square shaped net depicted in **Figure 1.3**, is four and in the hexagonal net it is a six membered ring.[30] Consequently the square net has a Well's code of (*4*, *4*) and the hexagonal net has a (*6*, *3*) code (**Figure 1.3**).

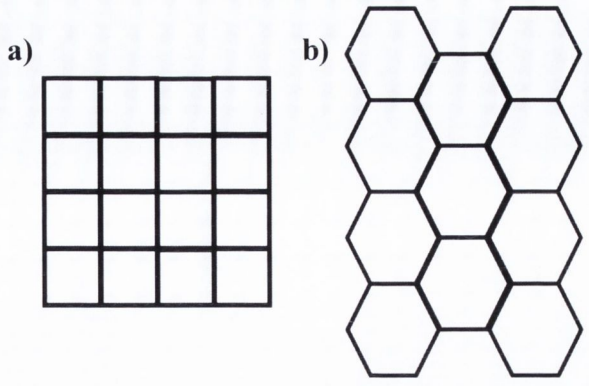


Figure 1.3: Schematic representation of **a)** (4, 4) or a $4^4.6^2$ net and **b)** (6, 3) or 6^3 net.[30]

The shortest circuit concept is again utilised in Schläfli notation. However, the notation differs from Wells' codes, whereby the amount of nodes in each short circuit is listed and a number in superscript represents the number of occurrences of identically sized rings. Therefore, the hexagonal net has a Schläfli symbol of 6^3 and the square shaped net a corresponding $4^4.6^2$ symbol (**Figure 1.3**). The $4^4.6^2$ symbol arises as the shortest circuit between the *trans* linkers is six. A useful equation for calculating the unique pairs of links is $p(p\text{-}1)/2$, *i.e.* for the square shaped net each node has a connectivity of 4, therefore 4(4-1)/2, gives six unique pairs of links. Thus, Schläfli symbols follow the notation $n^{p(p-1)/2}$. If a network contains multiple types of shortest circuits, the notation $A^a.B^b.C^c$ *etc.* is used, where A<B<C (**Figure 1.3**).[31]

In addition to Well's codes and Schläfli notation, the topology of a 3D network may also be described by naming it after a well-known material with a relevant topology, *e.g.* NbO, PtS or CaB_6 (**Figure 1.4**).[32] The Reticular Chemistry Structure Resource (RCSR) database can be used to assign three letter codes to nets, thus a network with a topology similar to that of a Pt_3O_4 can be described as a **pto**-type net or if $ThSi_2$ a **ths** net *etc.*[33,34] These RCSR symbols are modelled on the Atlas of Zeolite Frameworks Types, used to describe the topology of zeolites, *e.g.* a zeolite with a topology similar to the mineral sodalite has a zeolite code of **SOD** and a corresponding MOF would have a RCSR code of **sod**.[34]

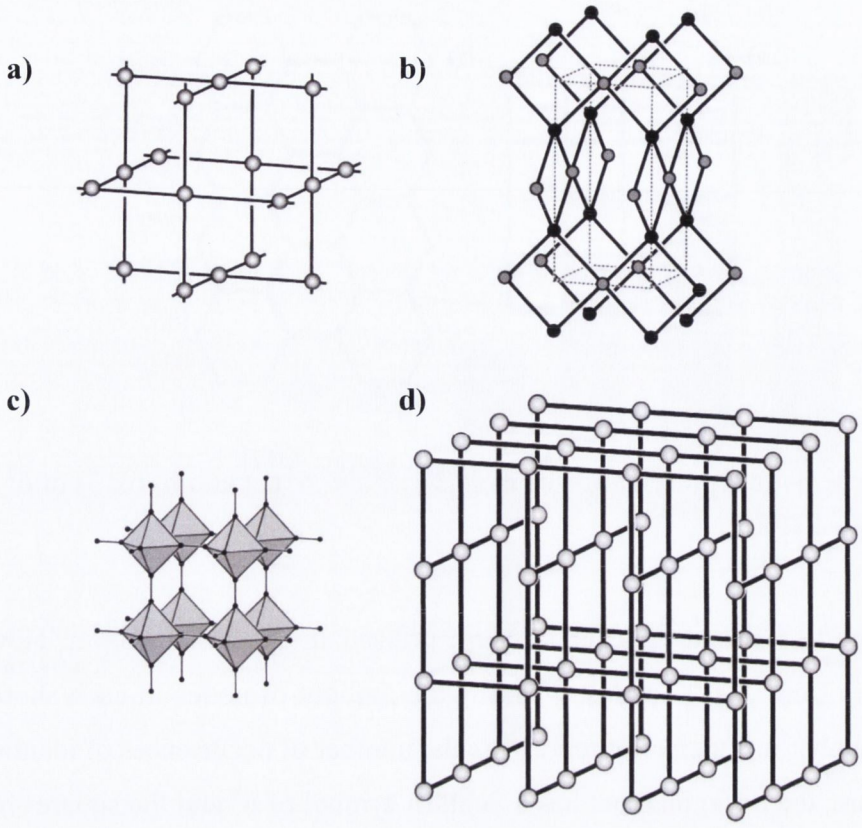


Figure 1.4: Network topology of **a)** NbO, **b)** PtS, platinum grey, sulphur black, **c)** CaB_6, with the calcium ions in the large cavities and the boron represented as the grey octahedron, **d)** $CdSO_4$.[32]

As with many new rapidly developing disciplines in science, overlapping or often contradictory terminologies can enter the scientific community through large numbers of publications. Unfortunately, this has proven to be the case for MOFs as they are also referred to as coordination networks and coordination polymers. Coordination polymer is in fact an IUPAC approved term, used to describe 1D straight chained polymers composed of metal ions linked in one direction by organic ligands through coordination bonds.[35] Coordination networks and MOFs are however, interchangeable and are used to describe 2D and 3D network structures composed of inorganic and organic moieties. It has confusingly led to both terms being used in literature.

There are also disagreements over which type of compound can be classified as a MOF, with contentious issues including whether or not they need to be porous and indeed if this has been proven experimentally. IUPAC has recognised the need for more exact terminology and has set up a task force specifically to address this confusing nomenclature, under the project name *'Coordination polymers and metal–organic frameworks: terminology and nomenclature guidelines'*.[36] For the purpose of simplicity the term MOF

shall be used henceforth in this thesis and will be used to describe both 2D and 3D porous and non-porous frameworks (**Figure 1.5**).

The dimensionality of a network structure can be established by observing how the SBUs and the organic linkers expand in space. A 1D structure is formed when the SBUs and linkers expand along one distinct direction, conversely 2D and 3D structures are formed when the SBUs and linkers expand along two and three distinct directions in space, respectively.

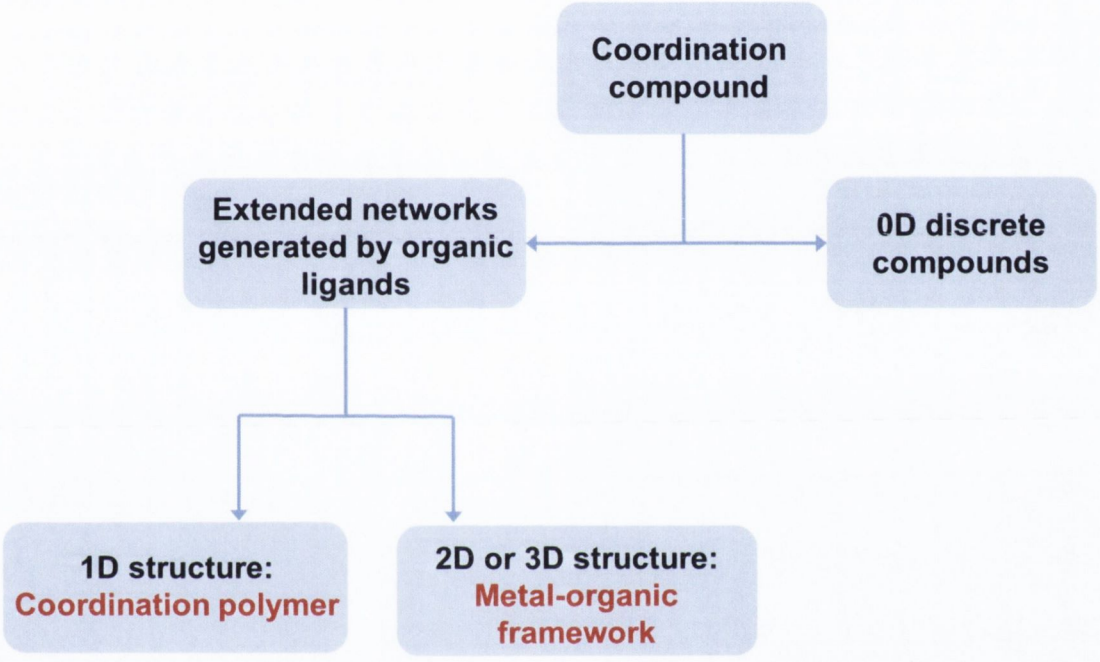


Figure 1.5: Classification of coordination compounds

1.2.3 Reticular Synthesis

The almost infinite possibilities for MOFs can appear daunting at first, but the concept of reticular synthesis can aid the design of new frameworks by reducing the number of possible topologies through the rational design and choice of the ligand and metal cation used. Thus, enabling the optimisation of a framework for a precise purpose.

Reticular synthesis was first proposed by Yaghi *et al.*, and uses net topologies as a template for the design of MOFs, with the term reticular inferring that it resembles a net in form.[37] It proposes the use of building blocks to direct the assembly of ordered frameworks

with default topologies similar to those of zeolites and other minerals *e.g.* sodalite and NbO.[38,39] These rigid molecular building blocks or secondary building units (SBUs) can be defined as "*molecular complexes and cluster entities in which ligand coordination modes and metal coordination environments can be utilized in the transformation of these fragments into extended porous networks using polytopic linkers*".[40] SBUs stabilised by carboxylate groups are inherently rigid, as the metal atoms are locked into place by the carboxylate functionalities to give large rigid vertices, from which a MOF can be assembled. Rigid frameworks can be synthesised by linking these SBUs together *via* polycarboxylate organic ligands. MOFs differ from supramolecular assemblies, as the frameworks are composed of strong bonds throughout.

The multiple coordination modes demonstrated by carboxylate groups, *e.g.* monodentate, chelating and bidentate bridging modes, makes them ideal for the generation of rigid SBUs (**Figure 1.6**).[41] Furthermore, the anionic nature of deprotonated carboxylic acid groups may also result in the formation of neutral networks, as the negative charge can counter the positive charge of the metal cations of SBUs. This is important as charged networks require counterions, which will lower the available void volume in porous structures.[42]

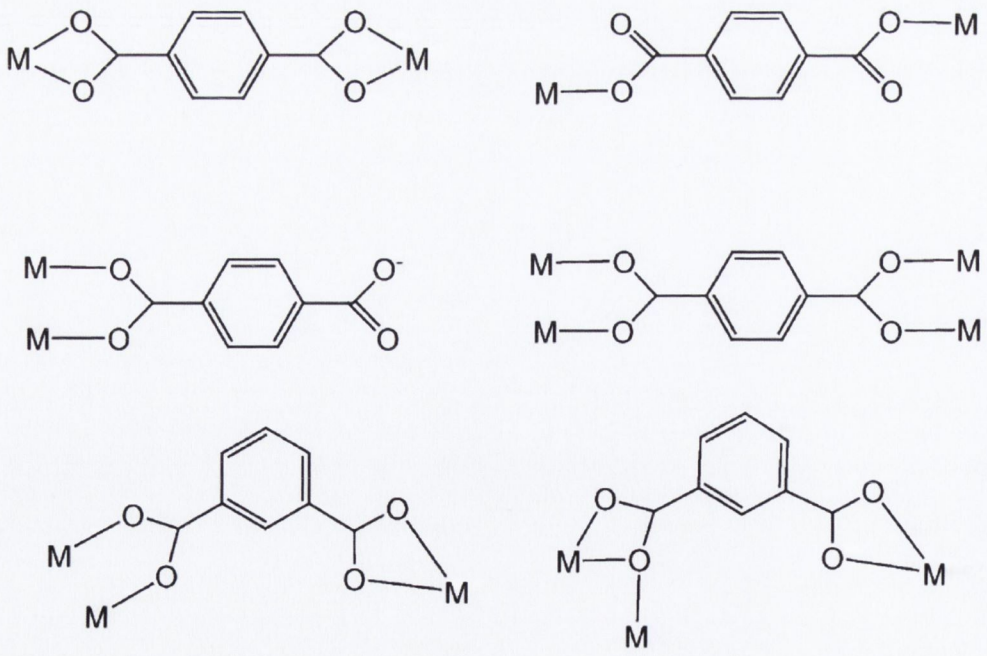


Figure 1.6: Possible coordination modes of 1,4-dicarboxylic acid (terephthalic acid) and 1,3-dicarboxylic acid (isophthalic acid).[41]

As was discussed in section 1.2.2, it is possible to rationalise the topology of MOFs by visualising their SBUs as the nodes of a net linked *via* covalent bonds. A SBU based on a transition-metal carboxylate cluster can be simplified to a polyhedron by envisaging the carboxylate carbon atoms as the points of extension of the vertices. Using this approach it is possible to generate a vast number of possible nodes, which vary between three and 66 points of extension, of which a small number are depicted in **Figure 1.7**.[43]

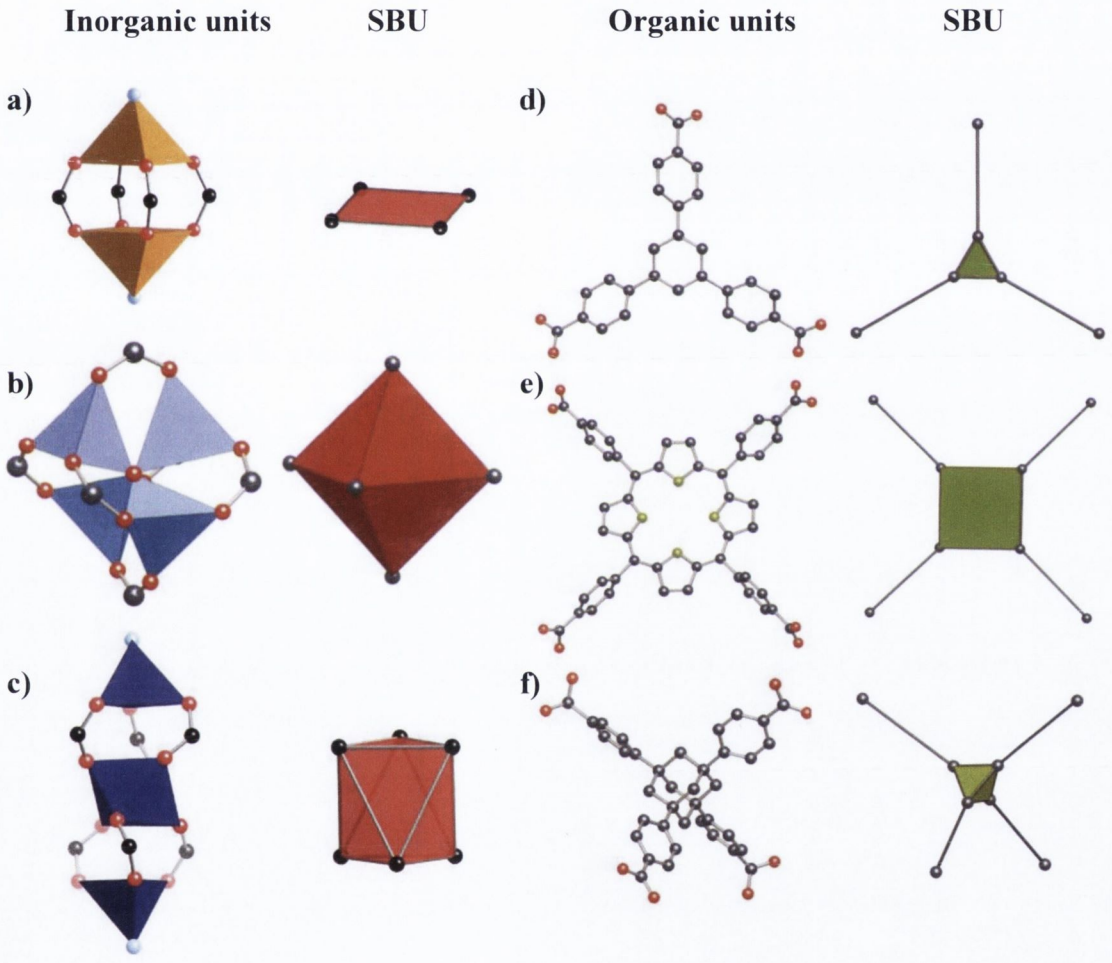


Figure 1.7: a) $\{M_2(CO_2)_4(DMF)_2\}$ paddlewheel SBU and as a four connecting node, **b)** Octahedral $\{M_4O(CO_2)_6\}$ SBU and as a six connecting node, **c)** octahedral $\{M_3CO_2)_3(DMF)_2\}$ hourglass SBU and as a six connecting node, **d) - f)** polytopic organic ligands and their corresponding simplified polyhedra. Colour scheme: Cu orange, Zn blue, C black, O red, N light blue. [37,43]

Through the careful choice of ligand and the necessary conditions to generate a given SBU, it is possible to predetermine the topology of the resulting MOF, a partial list of possible topologies is summarised in **Table 1.1**.

Table 1.1: Examples of net topologies with one or more kinds of node.[40]

Coordination	SBU geometry	SBU geometry	Network
3	Triangle	Triangle	$SrSi_2$
3	Triangle	Triangle	$ThSi_2$
3	Triangle	Triangle	6^3 honeycomb
3,4	Triangle	Square	Pt_3O_4
4	Square	Square	NbO
4	Tetrahedron	Tetrahedron	Diamond (C)
4,4	Square	Tetrahedron	Cooperite (PtS)
4	Square	Square	4^4 square lattice
6	Octahedron	Octahedron	Primitive cubic
8	Cube	Cube	Body-centred cubic

Yaghi *et al.* demonstrated the reticular synthesis concept through the use of the $\{Zn_4O(CO_2)_6\}$ octahedral subunit (**Figure 1.7**).[44] The widely used $\{M_4O(CO_2)_6\}$ octahedron contains four metal ions linked to a central oxygen atom and are capped by six carboxylate groups, resulting in six points of extension (**Figure 1.7**).[45,46] In MOF-5, $Zn_4O(BDC)_3$, the octahedral subunits are linked *via* the linear ligand 1,4-benzenedicarboxylate (BDC), resulting in a 3D framework with a primitive cubic topology. The topology of MOF-5 resembles that of the boron net found in CaB_6, whereby the zinc subunits replace the boron atoms (**Figure 1.4**). By substituting BDC with elongated analogues, Yaghi *et al.* were able to synthesise a series of isoreticular (based on the same net) MOFs, with ever increasing pore volumes and crucially based on the same default CaB_6 topology, with the void volume increasing from 56 to 91% as the ligand was expanded from BDC to triphenyl dicarboxylic acid (**Figure 1.8**). The process of using longer ligands whilst maintaining the default topology is known as expansion.

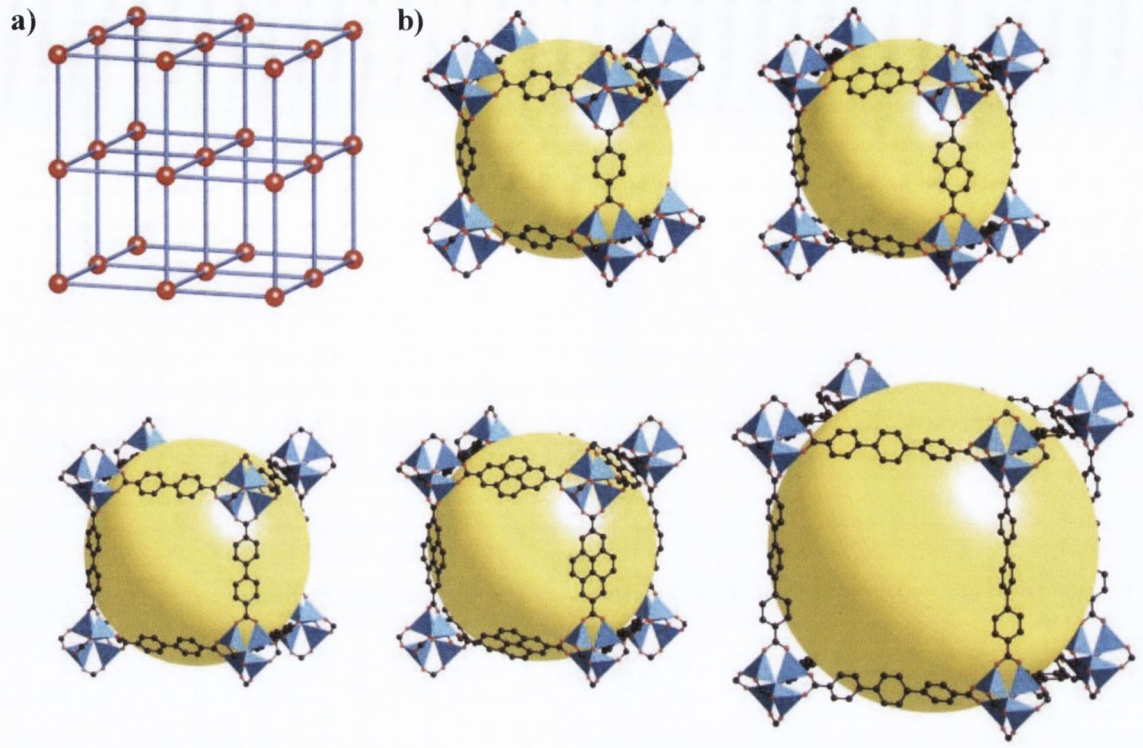


Figure 1.8: a) Simplified depiction of a primitive cubic network, **b)** MOF-5 and related isostructural compounds, whereby the $\{Zn_4O(CO_2)_6\}$ octahedral subunits are linked by organic linkers of ever increasing length. The yellow spheres represent the available void volume. Colour code: Zn blue, O red, C black.[44,47]

As was previously mentioned in this section, there are a wide array of possible SBUs, with varying points of extension, *e.g.* the paddlewheel motif, whereby two metal centres are bridged by four carboxylate groups and is a common four connecting node (**Figure 1.7**).[48,49,50] In many cases one is not limited to a single SBU for a given connectivity. One such example being the hourglass SBU, which like $\{Zn_4O(CO_2)_6\}$ also has six points of extension and is composed of a central zinc ion in an octahedral coordination environment, bridged *via* six carboxylate groups to two zinc ions which both adopt tetrahedral coordination geometries (**Figure 1.7**).[51,52] A comprehensive list of SBUs and their points of extension was published by Yaghi *et al.* in 2009.[43]

It is also possible for polytopic organic molecules to be considered as pre-synthesised SBUs (**Figure 1.7**). This is an important aspect, as it enables the synthesis of certain topologies, *e.g.* that of Pt_3O_4 which is generated *via* the linking of square and triangular SBUs, *e.g.* a paddlewheel motif and a tritopic ligand.[53]

1.2.4 Nitrogen and N-O type ligands

Although reticular synthesis is focussed on the use of carboxylate functionalised ligands, the synthesis of MOFs is not solely limited to carboxylate based ligands. In fact some of the earliest frameworks were composed of N-donor ligands, with Robson *et al.* in 1989 reporting the first example of a 3D MOF, namely $[Cu^{I}$(4,4',4",4"'-tetracyanotetraphenylmethane)$_4][BF_4]$, with an adamantane like topology and a void volume of *ca.* 66% (**Figure 1.9**).[54, 55,56] Long *et al.* built on this earlier research by utilising the ligand 1,4-benzeneditetrazol-5-yl (HBDT), to generate the 3D porous network $\{Zn_3(BDT)_3(DMF)_4(H_2O)_2\}$ (**Figure 1.9**).[57] Their MOF contains trinuclear Zn^{II} SBUs, similar to the hourglass SBU depicted in **Figure 1.7**, thus demonstrating the ability of N-donors to generate rigid SBUs. These SBUs are linked *via* the ditopic ligand into a 3D porous framework with 1D channels, with a surface area of 640 m^2 g^{-1} and a hydrogen storage capacity of 1.46 wt%.

The combination of nitrogen and oxygen based donor groups has led to the synthesis of neutral porous MOFs, with research focussing on combinations of pyridyl and carboxylate functionalities.[58] Su *et al.* exploited the ligand 5-(pyridin-4-yl)isophthalic acid to synthesise the 3D MOF $\{Cu(5\text{-(pyridin-4-yl)isophthalate})_3 \cdot 2H_2O \cdot 1.5DMF\}_\infty$, composed of copper paddlewheel subunits, generated by bridging carboxylate groups, with the pyridine N-donors coordinating in the apical positions of the copper ion's square pyramidal coordination environment (**Figure 1.9**).[59] The resulting framework contains 1D channels 6.2 Å in width and has a void volume of 54%. Tetrazole functionalities have also been effectively employed as the N-donor in mixed N-O donor ligands. Bu *et al.* effectively utilised 4-(1H-tetrazol-5-yl)benzoic acid to link tetrahedral zinc and cobalt ions into a 3D MOF with a diamond like topology and a formula of $\{Co_{0.04}Zn_{0.96}$(4-(1H-tetrazol-5-yl)benzoate)$_2\}$ (**Figure 1.9**).[60]

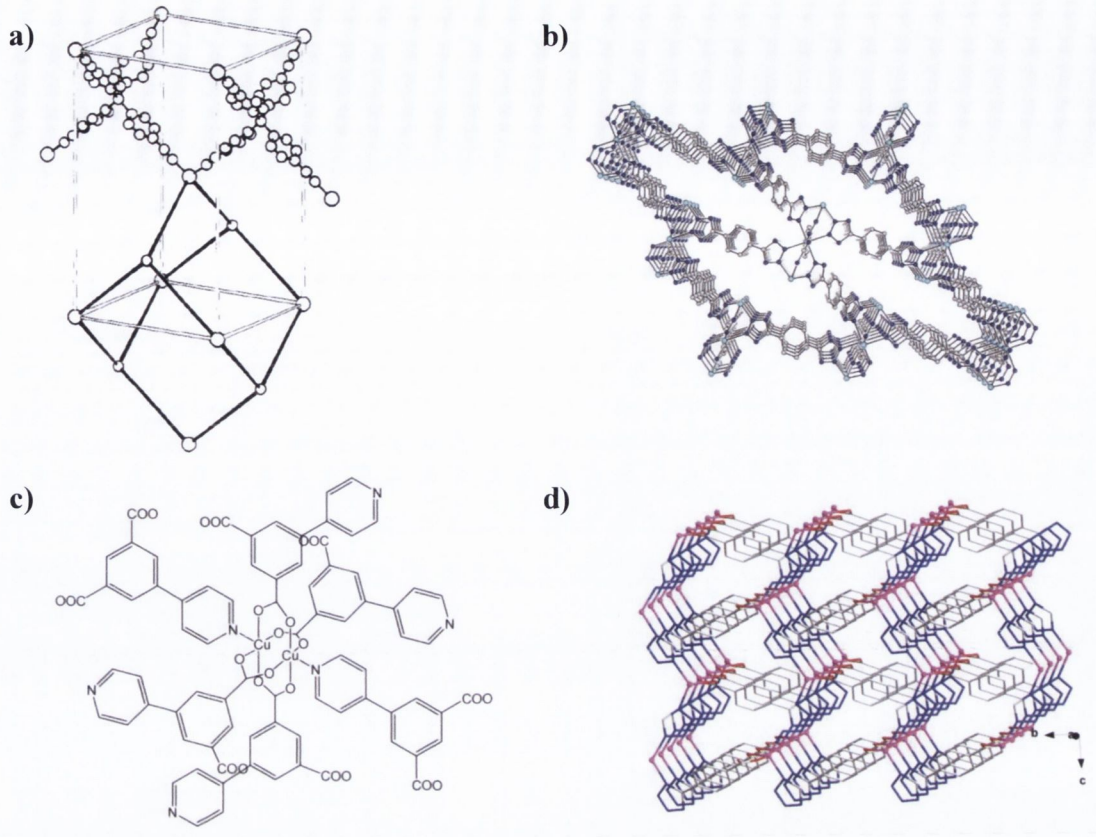


Figure 1.9: a) Adamantane topology found in [Cu^{I}(4,4',4",4"'-tetracyanotetraphenylmethane)$_4$][BF_4], **b)** {$Zn_3(BDT)_3(DMF)_4(H_2O)_2$}, **c)** coordination environment found in {Cu(5-(pyridin-4-yl)isophthalate)$_3$·$2H_2O$·1.5DMF}$_\infty$, **d)** {$Co_{0.04}Zn_{0.96}$(4-(1H-tetrazol-5-yl)benzoate)$_2$}. Colour code: C grey, Zn/Co pink, N blue, Zn teal.[54,57,59,60]

1.2.5 Synthesis of metal-organic frameworks

MOFs are typically synthesised under solvothermal conditions using superheated solvents, *i.e.* at temperatures above the boiling point of the solvent and consequently at elevated vapour pressures. Although this may not always be the case with temperatures below the boiling point of the solvent also being used. Teflon™ lined reaction vessels which are placed in steel lined autoclaves to ensure a safe controlled environment, are primarily used and heated using conventional ovens (**Figure 1.10**).[61]

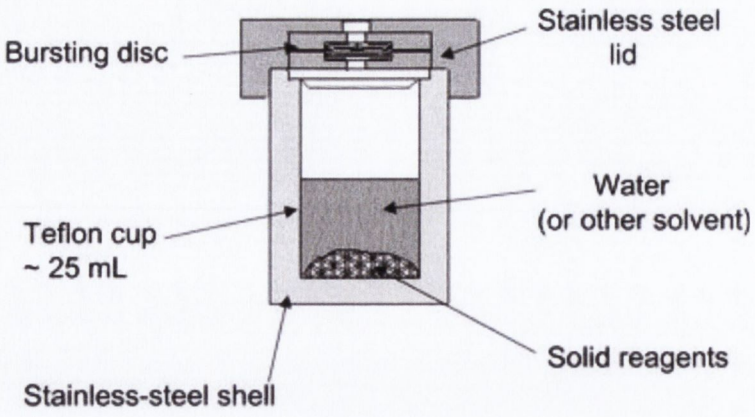


Figure 1.10: Simplified diagram of a Teflon™ lined autoclave used in solvothermal synthesis.[61]

The benefit of superheated solvents is that they have reduced dielectric constants, resulting in reactants which were previously insoluble becoming soluble at elevated temperatures.[62] This is particularly important due to the low solubility of many of the extended aromatic ligands used in the synthesis of MOFs. The insolubility of the synthesised MOFs ensures that they can be easily separated from the reaction solution at the end of the synthetic process. The disadvantage to such methods is the inability to monitor the reaction *in situ*, meaning one has to allow the reaction to take place for the allotted time before it can be investigated if it was successful or not, making it sometimes a time consuming process.

The main difficulty in synthesising MOFs is finding the correct balance of variable parameters to facilitate the growth of the crystalline material. The principle variables are the reaction temperature, metal to ligand ratio, concentration of reactants, pH values, length of reaction time, the solvent and indeed which metal salt to use.[63] Water, dialkyl formamides, alcohols and acetonitrile are the most commonly used solvents. As the precursors to MOFs are often ionic, polar solvents tend to be used.[64]

The effect of temperature on the resulting compounds was elegantly demonstrated by Cheetham *et al.* through a series of experiments conducted using equal quantities of cobalt hydroxide, succinic acid and water in each experiment, with the only variable being the temperature.[65] By using this approach they were able to synthesise five unique cobalt succinate, phase pure compounds: 1D chains of $Co(H_2O)_4(C_4H_4O_4)_2$ formed at 60 °C, 1D chains of $Co(H_2O)_2(C_4H_4O_4)_2$ at 100 °C, 2D sheets of $Co_4(H_2O)_2(OH)_2(C_4H_4O_4)_3 \cdot 2H_2O$ formed at 150 °C and the 3D MOFs $Co_6(OH)_2(C_4H_4O_4)_5 \cdot 2H_2O$ and $Co_5(OH)_2(C_4H_4O_4)_4$ formed at 190 and 250 °C, respectively (**Figure 1.11**). Although this is just one isolated

example, it helps to highlight the synthetic difficulties that one faces when synthesising MOFs.

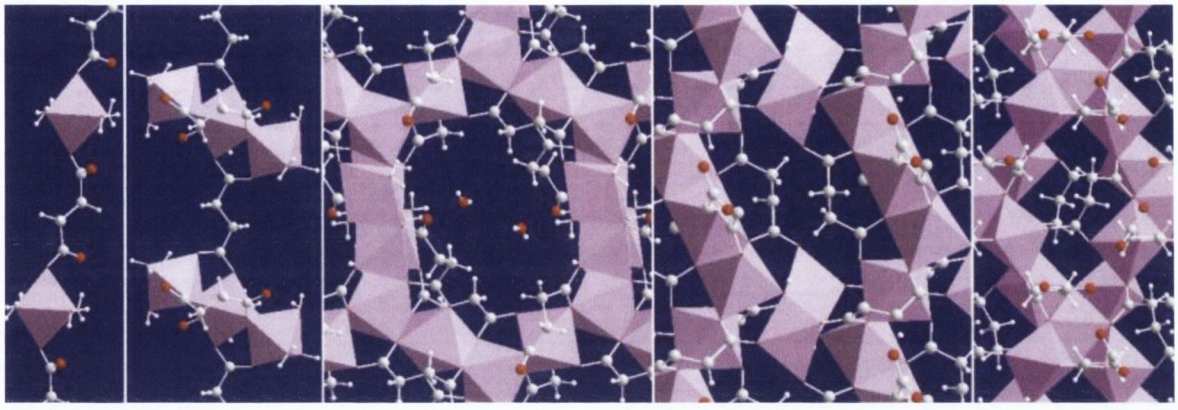


Figure 1.11: Phase changes in a cobalt hydroxide, succinic acid system, as temperature is varied. From left to right: 1D chains of $Co(H_2O)_4(C_4H_4O_4)_2$ at 60 °C, 1D chains of $Co(H_2O)_2(C_4H_4O_4)_2$ at 100 °C, 2D sheets of $Co_4(H_2O)_2(OH)_2(C_4H_4O_4)_3 \cdot 2H_2O$ formed at 150 °C, 3D MOF $Co_6(OH)_2(C_4H_4O_4)_5 \cdot 2H_2O$ at 190 °C, $Co_5(OH)_2(C_4H_4O_4)_4$ formed at 250 °C.[65]

Microwave synthesis has also been adopted for the production of MOFs, often resulting in MOF nanoparticles.[66,67] As is the case for the microwave synthesis of more traditional purely organic or inorganic compounds, shorter time periods are involved.[68,69]

1.2.6 Applications of MOFs

The growth in publications linked to MOFs (**Figure 1.2**) is largely due to their unique properties which facilitate their use in a diverse range of potential applications. Their use as gas-storage media and as sensors for small molecules and ions will be discussed in more detail in sections 1.3 and 1.4.

The tuneable pore and cavity size of MOFs combined with their ease of functionalisation has led to MOFs being investigated as possible drug delivery systems, either through the encapsulation of bioactive molecules in their pores or by incorporating the drug along with biocompatible metals into the framework itself.[70,71] Férey *et al.* were the first to recognise the potential for MOFs to control drug delivery rates by incorporating ibuprofen in the large cavities of the Cr^{III} based MOFs MIL-100 ($Cr_3F(H_2O)O(BTC)$) and MIL-101 ($Cr_3F(H_2O)O(BDC)$).[72] MIL-100 and MIL-101 are 3D MOFs composed of

trimeric Cr^{III} octahedral clusters linked *via* 1,3,5-benzene tricarboxylic acid (BTC) or 1,4-benzene dicarboxylic acid (BDC) respectively, to give zeotype frameworks with large cavities. The delivery rates and capacities compared very favourably with other porous solids, with MIL-101 having a storage capacity nine times that of the mesoporous silicate MCM-41, which possesses cavities comparable in size to MIL-100 and MIL-101 (**Figure 1.12**). Furthermore, Férey *et al.* studied the release of ibuprofen in simulated body fluids at 37 °C and found that there was a slow release of the drug, requiring a period of three weeks for the dissociation of all the stored ibuprofen into the fluid. They did, however, note the toxicity of chromium compounds and merely emphasised their system as a proof of concept. Progress from these initial studies has shown that a diverse range of bioactive compounds including anti-arrhythmic, anti-viral and anti-tumoral drugs can be stored in MOFs.[73,74] But a comparative lack of *in vivo* studies has thus far hampered wider research into their use.

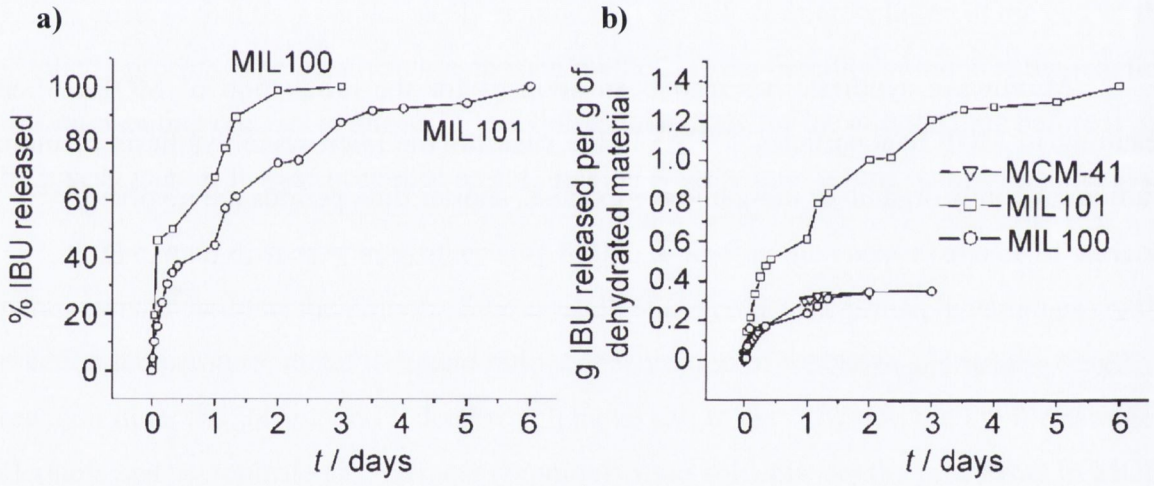


Figure 1.12: a) Release of ibuprofen into simulated bodily fluids at 37 °C (%) *versus* time (days), **b)** release of ibuprofen (g/g of dehydrated material) *versus* time (days).[72]

Kim *et al.* in a recent review outlined the progress to date in the use of homochiral MOFs for heterogeneous catalysis.[75] In the review, they summarise seventeen different reactions catalysed by homochiral MOFs, ranging from the cyanosilylation of aldehydes[76] and the hydrogenation of aromatic ketones[77] to Diels-Alder reactions,[78] often with conversion rates >99% and in high enantiomeric excess. The catalytic activity of MOFs may stem from metal centres, a functionalised linker or indeed from cavities within the frameworks, this bestows a great deal of flexibility onto the design of frameworks for

catalysis (**Figure 1.13**).[79] Furthermore, the inherent long range order of crystalline MOFs ensures that the material is uniform throughout.

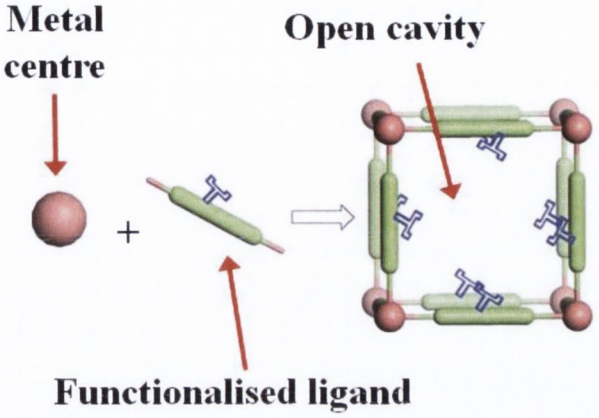


Figure 1.13: Schematic representation of the sources of catalytic activity in a MOF.[79]

An example of one such catalytic framework is the microporous MOF $Zn_2(bpdc)_2(salen(Mn))\cdot 10DMF\cdot 8H_2O$, synthesised by Albrecht-Schmitt *et al.*, where bpdc is biphenyldicarboxylate and salen(Mn) is depicted in **Figure 1.14**.[80] They successfully utilised the resulting framework as an asymmetric catalyst for olefin epoxidation. Salen(Mn) catalysts often lose their catalytic activity after a short period of time. This is due to the salen ligand becoming oxidised through reactive encounters with other catalytic units. Interestingly, the framework-immobilised salen(Mn) catalyst was far more robust than free salen(Mn), with the activity of the free catalyst diminishing completely after a few hours, whereas, when the catalyst was locked in the framework it maintained its activity almost indefinitely (**Figure 1.14**). They reasoned that this was due to salen(Mn) units not coming into close contact with each other and consequently avoiding oxidation and no subsequent loss of catalytic activity.

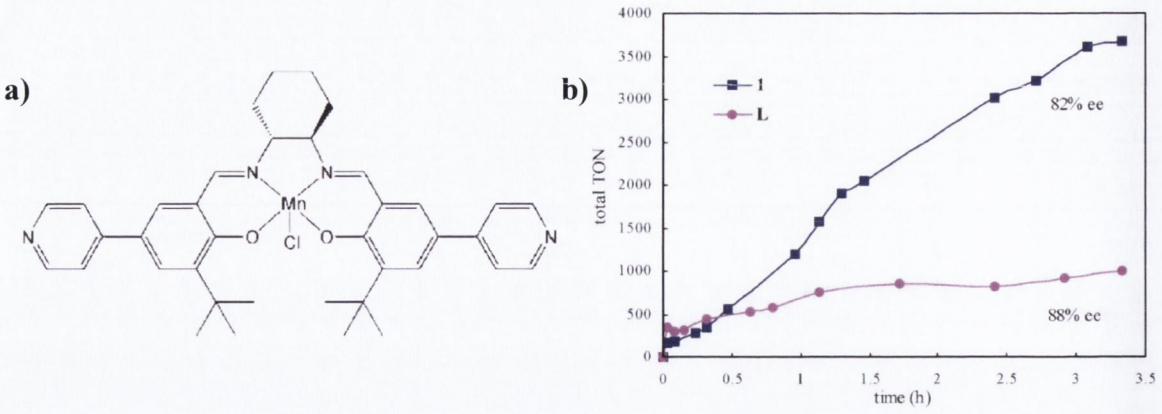


Figure 1.14: a) Salen(Mn)Cl, **b)** the total turnover number versus time (hours) for the epoxidation of 2,2-dimethyl-2H-chromene, where 1 is the framework and L is free Mn(salen).[80]

MOFs may also possess interesting magnetic properties for potential device applications *e.g.* memory storage.[81] By combining first row transition metals and ligands of an intermediate field strength, the energy gap between the HS and LS states ($\Delta E°_{HL}$) may be sufficiently small, so that an external perturbation such as light irradiation, a temperature change or a change in pressure can initiate a spin transition, leading to a change in the magnetic, optical and structural properties of the compound. This phenomenon is known as spin-crossover (SCO). The incorporation of SCO centres into MOFs is highly desirable, as they may result in bistable domains and therefore hysteresis at higher temperatures, as the organic linkers can enable cooperativity between the metal centres.[82] This new class of materials is often referred to as spin-crossover frameworks (SCOFs). Zarembowitch *et al.* in 1990, were the first to synthesise a 2D framework exhibiting SCO behaviour. Their compound, $[Fe(4,4'\text{-bis-}1,2,4\text{-triazole})_2(NCS)_2]\cdot H_2O$, showed a very abrupt spin transition curve and a 21 K wide hysteresis loop, as a result of the high level of cooperativity between the SCO centres.[83] The alteration of the triazole ligand resulted in wider hysteresis loops which were achieved at temperatures above room temperature (313 K).[84] However, despite their interesting properties, the number of SCOFs reported remains low, with particular emphasis on compounds that contain Fe^{II} centres bridged by pyridyl[82] or cyanometallate groups.[85]

Together with the potential applications highlighted in this section and the gas storage and luminescent sensors outlined in sections 1.3.3 and 1.4.3, MOFs have also shown promise in other diverse areas such as non-linear optics[86,87] and conductivity.[88,89] It is this diversity that has led to the phenomenal growth in publications linked to MOFs and will ensure that this trend continues.

1.3 Gas storage in porous materials

1.3.1 Measuring gas uptake and surface areas in MOFs

The two principle methods for measuring the uptake of gases in MOFs are gravimetry and volumetry. The gravimetric method calculates the increase in mass caused by the adsorbed hydrogen in a MOF using a highly accurate balance. Volumetry on the other hand calculates the pressure change in a sample chamber of a fixed volume in order to derive the amount of gas adsorbed or desorbed.[90]

There are of course advantages and disadvantages to each method. Gravimetry can lead to significant errors due to the adsorption of H_2O molecules present in the gas stream, as each H_2O molecule adsorbed has the same mass as *ca.* nine H_2 molecules. This is less of an issue for heavier gas molecules *e.g.* CO_2. To counteract this effect, hydrogen gas of a very high purity is used, but samples are typically exposed to a stream of hydrogen for an extended period of time to ensure the total uptake of hydrogen and as such significant amounts of H_2O can be adsorbed, often leading to inaccurate results. In addition, difficult to calculate buoyancy corrections need to be made to gravimetric measurements. The adsorption of water molecules is less of an issue for the volumetric method as it is the pressure change of a gas that is observed and not a change in mass. The major drawback to volumetry is the fact that the adsorption is measured by the indirect determination of the adsorbed gas, leading to inherent errors, which can arise from leaks or the inaccurate measurement of the temperature, pressure or indeed the mass of the sample itself. Taking these considerations into account and the ease of operation has led to volumetry becoming the most widespread method for calculating gas uptake.[91]

Excess adsorption is the figure most often quoted when evaluating the uptake of a gas in a MOF. Simply speaking, it is a measurement of the total quantity of gas that it is adsorbed onto the surface of a MOF. However, absolute absorption is a more accurate representation of the amount of gas adsorbed, as it includes the gas molecules stored in the pores of a MOF in addition to taking into account the amount of a gas adsorbed onto the surface. Although absolute absorption is a more accurate value for the total amount of stored gas molecules, the difficulty in obtaining the amount of gas stored in pores, which is estimated theoretically, means that excess adsorption is the most commonly quoted value.[92]

From the measured adsorption values it is possible to calculate the surface area of a material. The Brunauer-Emmett-Teller (BET) theory takes multilayer adsorption into account when calculating surface areas. This is important as multilayers of adsorbed gases can often form in MOFs, particularly in microporous MOFs. For this reason BET isotherms are thought to give more accurate results than Langmuir isotherms, which fail to take multilayers into account. Langmuir derived surface areas are often considerably higher than the corresponding BET values, with the Langmuir and BET derived surface areas of MOF-210 being 10,400 and 6,240 m^2g^{-1}, respectively.[24] It is typically the N_2 adsorption isotherm, measured at 77 K, that is used when calculating the surface areas of MOFs.

1.3.2 Introduction to hydrogen storage

Hydrocarbons being a finite resource, means a new fuel source will eventually be required in order to maintain our current energy and transportation needs.[93] Renewable and nuclear energy sources have the ability to replace fossil fuels in the industrial generation of electricity in power plants and this can be used to power electric vehicles. But the limited range and long recharging times of battery powered vehicles will continue to hamper their widespread adoption.

There is clearly a need for an alternative energy source which can be obtained ideally from renewable sources and that offers the travelling range of a conventional thermal-combustion engine. Technologies using H_2 can meet these prerequisites. Typically liquid hydrocarbons have a gravimetric heat of combustion of *ca.* 47 MJ kg^{-1}, whereas hydrogen can produce 142 MJ kg^{-1}, making it an ideal fuel source. This converts to a car using an internal combustion engine requiring approximately 24 kg of petrol to cover 400 km with only 4 kg of hydrogen needed if a hydrogen fuel cell is used.[94] It also possesses other desirable traits: it is highly abundant and the only product of its oxidation (by combustion or when used in fuel cells) is water. There is, however one major caveat with regards to using hydrogen in automobiles, namely its safe storage. Recognising this, the US Department of Energy (DOE) has set targets for the storage of H_2 of 4.5 wt% (weight of the stored hydrogen as a percentage of the systems total weight) by 2010 and 5.5 wt% by 2015 at conditions of -40 to 80 °C and up to 100 atm.[95]

The three principle methods of storing gases are liquefaction, storing under high pressure and finally in a solid material through either chemisorption or physisorption. It is possible to store hydrogen gas at high pressures using steel cylinders, but these are limited to 300 bar for safety reasons, which equates to a fuel tank 230 L in size to store 4 kg of hydrogen.[94] Aside from the unwieldy size of the fuel tank, there are also significant safety fears associated with highly pressurised gas cylinders in automobiles, particularly when these canisters contain explosive gases such as hydrogen. Liquefaction offers one notable advantage over storage under high pressure, namely its ability to store a greater mass of hydrogen per unit volume. However, the liquefaction process requires large amounts of energy and expensive storage tanks. This combined with the constant boiling off of hydrogen gas to prevent a critical build-up of pressure, limits large-scale adoption of H_2 as a mobile fuel source in automobiles. It should be noted that both liquefaction and high-pressure hydrogen have both been used as prototype fuel storage methods in vehicles.[96, 97]

Another method for storing hydrogen is storage in a solid material either through chemisorption or physisorption of molecular hydrogen onto the surface of a material. Metal hydrides have been the subject of intensive research evaluating their potential as hydrogen storage medium.[98] The high hydrogen storage capacity of hydrides make them a possible solution, but their use is hampered by the large amount of energy needed to break the chemical bonds to release hydrogen, thus requiring heating cycles which are above the DOE temperature targets. In addition, the complete charging of the materials may take several hours, thus reducing their effectiveness in real-world scenarios.[99]

The alternative method of physisorption of hydrogen onto the surface of a solid material makes use of weak interactions, *e.g.* van der Waals forces and dipole interactions, between the solid material and molecular hydrogen. Possible candidates for physisorption are zeolites, carbon nanotubes (CNTs) and MOFs.[100] Zeolites are hindered by their relatively high weight and low surface areas which limits their hydrogen uptake to between 1-1.9 wt% at 1 bar.[101] Initial reports suggested that CNTs had a very high propensity for the uptake of hydrogen. However, this was later disproven as it was shown that metal impurities in the CNTs or the applied measuring techniques (which resulted in H_2O impurities) led to false results.[102] The tuneable pore geometries, high surface areas and the relative ease of changing the functionality of the organic linker, has led to MOFs receiving significant attention with regards to gas storage and will be the main focus of section 1.3.3.

1.3.3 Gas storage in MOFs

Kitagawa *et al.* were the first to recognise the possibility of storing gases in MOFs.[103] Using a series of MOFs of a general formula $M_2(4,4'\text{-bipyridine})_3(NO_3)_4(H_2O)$, where M is either Co^{II}, Ni^{II} or Zn^{II}, they studied their ability to adsorb CH_4, N_2 and O_2. Following on from this Yaghi *et al.* demonstrated the potential to store hydrogen in MOFs using MOF-5 ($Zn_4O(BDC)_3$), described in section 1.2.3 (**Figure 1.8**), which demonstrated a storage capacity of 4.5 wt% at 77 K.[47] Since then there has been a general trend towards MOFs with higher surface areas, as a linear relationship between the surface area of a MOF and their hydrogen storage capacity at 77 K has been calculated (**Figure 1.15**).[104] The high surface area of 6240 $m^2\ g^{-1}$ demonstrated by MOF-210 has a corresponding H_2 uptake of 8.6 wt% at 56 bar and 77 K (**Figure 1.15**).[24] MOF-210 is a metal organic framework composed of $\{Zn_4O(CO_2)_6\}$ subunits, which were previously mentioned in section 1.2.3, linked *via* the tritopic carboxylate ligand 4,4',4''-(benzene-1,3,5-triyl-tris(ethyne-2,1-diyl))tribenzoate and the co-ligand biphenyl-4,4'-dicarboxylate, to give a 3D framework containing large cavities and a void volume of 89 %.

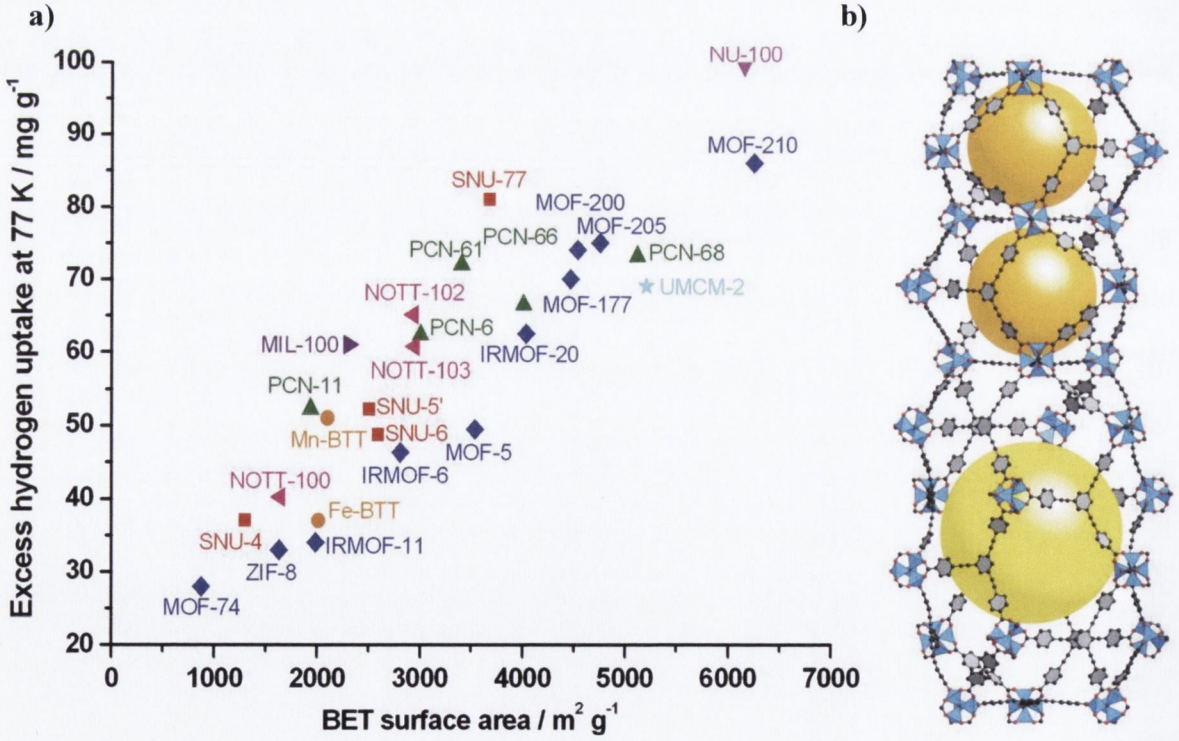


Figure 1.15: a) Excess high pressure H_2 uptake capacities versus BET surface areas for some highly porous MOFs at 77 K and 56 bar, **b)** MOF-210, with the yellow spheres depicting the void volume of the cavities. Colour code: Zn blue, C black, O red. [24,104]

Although MOF-210 has shown a remarkable storage capacity for hydrogen, it does so at temperatures which are far lower than those demanded by the DOE targets. There is an inverse relationship between the amount of gas adsorbed and temperature, as thermal vibrations increase with temperature and become similar in magnitude to the gases heat of adsorption.[105] One solution is to use MOFs with smaller pore sizes, as the gas molecules can interact with several walls of a pore, this increases the expected surface area that is in contact with any one molecule of a gas, thereby increasing the interactions between the two. This was demonstrated using the 3D framework HKUST-1, $Cu_3(TMA)_2$, which is composed of copper paddlewheel subunits linked *via* the tritopic ligand TMA (1,3,5-benzene tricarboxylic acid).[106] Neutron powder diffraction and inelastic scattering studies showed that H_2 was initially adsorbed onto the surface of the smaller pores before being adsorbed onto the surface of the larger pores.[107,108] This correlates with data produced for the adsorption of hydrogen on purely carbon materials where the lowest hydrogen binding energies were found to be in flat carbon structures, *e.g.* graphite and activated carbon and the highest values were found in confined spaces and the interstitial sites in carbon nanotubes, where multiple surfaces were in contact with hydrogen molecules.[109] The interpenetration of two frameworks, which results in diminished void volumes when compared to their non-interpenetrated equivalents, has also been shown to increase the adsorption of gases.[110]

Alternative methods to increase gas uptakes in MOFs include the removal of coordinated solvent molecules from SBUs to induce a $M^{\delta+}$-$O^{\delta-}$ dipole, leading to a greater interaction with gas molecules and the post-synthetic introduction of additional metal ions, which have a high heat of adsorption for H_2 *e.g.* Li^{I}, into a MOF through chemical doping.[111,112]

1.4 Lanthanides

1.4.1 Introduction to lanthanides

Lanthanide chemistry is dominated by the +III oxidation state, as ionisation of a lanthanide metal, Ln, is generally unfeasible beyond that of Ln^{III}. A few notable exceptions are europium and ytterbium which can both adopt +II oxidation states. This is attributable to Eu^{II} and Yb^{II} having half-filled and fully occupied 4*f* orbitals respectively, *i.e.* [Xe] $4f^7$ and

[Xe] $4f^{14}$. Due to the large size of the lanthanide ions, they typically form complexes with high coordination numbers of six or greater. As a direct result of the small crystal field splitting of the degenerate 4*f* orbitals and the minor role of crystal field stabilisation energy in lanthanide chemistry, the resulting coordination number and geometry of lanthanide complexes tend to be moderated by steric effects. Furthermore, lanthanide ions are characterised as hard Lewis acids according to the Pearson classification[113] and consequently have a propensity to form complexes with hard donor atoms such as ligands containing oxygen and nitrogen based functionalities.[114]

The importance of the lanthanide series of elements is reflected in their widespread use in many of today's cutting edge technologies and this is as a result of their unique physicochemical properties, which will be discussed in greater detail in sections 1.4.2 and 1.4.3. Their luminescent properties has led to their adoption in many different industries. They play a crucial role as luminescent phosphors in the high-definition screens which have become commonplace in our everyday lives and enable the delivery of much of the content we view on these screens through their use as optical amplifiers in high speed fibre-optic broadband networks.[115,116] In the health sciences, they are widely used as luminescent labels in fluoro-immunoassays, leading to the highly accurate testing of biologically significant bodies at nano- to pico-molar concentrations and as MRI contrast agents.[117,118]

Neodymium and samarium have become irreplaceable to many of the technologies which we rely on today. A few examples highlighting their uses and showcasing their diverse range of applications are consumer electronics, *e.g.* hard drives and magnets in headphones, the renewable energy sector where they are routinely found in wind turbine generators and indeed in the electric motors which drive many of today's more environmentally friendly hybrid and electric cars.[119] Cerium is also used in the catalytic converters of petrol and diesel powered vehicles. Cerium oxide is used to moderate oxygen levels in the converter. In 'lean' times it is able to store oxygen and during 'rich' periods it is able to release oxygen, ensuring the proper reduction of NO_x and the oxidation of CO and hydrocarbons that are present in the exhaust fumes.[120]

1.4.2 Lanthanide luminescence

Luminescence can be defined as the emission of light which occurs after the absorption of energy and photons are the source of energy in photoluminescence. Photoluminescence can itself be subdivided into two distinct classifications: fluorescence which is spin allowed and has lifetimes on the order of nanoseconds and phosphorescence which is spin-forbidden and consequently has longer lifetimes which may be up to several seconds long.

Lanthanide ions tend to be weakly coloured, displaying narrower more defined emission bands with longer lifetimes than those associated with transition metal ions. Their emissions cover the entire spectrum from UV (Gd^{III}), to the visible spectrum (red Sm^{III}, red Eu^{III}, green Tb^{III} and blue Tm^{III}) and to the NIR (Pr^{III}, Nd^{III}, Ho^{III}, Er^{III} and Yb^{III}), with the exceptions being lanthanum (La^{III}) and lutetium (Lu^{III}) which show no luminescence due to their empty (f^0) and full (f^{14}) respective orbitals.[121] The narrow nature of the bands is due to the small radial extension of the 4*f* orbitals, which are completely shielded by filled 5*s* and 5*p* orbitals, meaning they are relatively insensitive to the nature of the coordinated ligand. Thus, the promotion of an electron into a 4*f* orbital of higher energy does not alter the chemical bond lengths, keeping the inter-nuclear distances the same and consequently resulting in narrow emission bands. Contrasting with these narrow bands are the broad emission bands associated with organic molecules and *d-d* transitions, where the excitation of an electron can lead to the lengthening of chemical bonds and therefore a widening of the bands.

The 4*f* orbitals, however, are not degenerate, giving rise to complicated spectra (**Figure 1.16**).[117] There are three principle reasons for this lack of degeneracy. The foremost being electronic repulsion between orbiting electrons, which is responsible for splitting the energy levels by an order of 10^4 cm^{-1}. Spin-orbit coupling is responsible for a further splitting of the terms by an order of magnitude of 10^3 cm^{-1} into J-levels. Finally, weak interactions with the ligand results in a further very slight removal of the J-level degeneracy of around 10^2 cm^{-1} (**Figure 1.17**). The term symbols for the J-levels are derived from the Russel-Saunders coupling scheme and are written as $^{2S+1}L_J$, where S is the total spin quantum number, L is the orbital angular momentum and J is the total angular momentum quantum number, (J= L+S, L+S-1, … |L-S|). The value of L is represented by the historical key: S (L=0), P (L=1), D (L=2), F (L=3), G (L=4), H (L=5), *etc.*

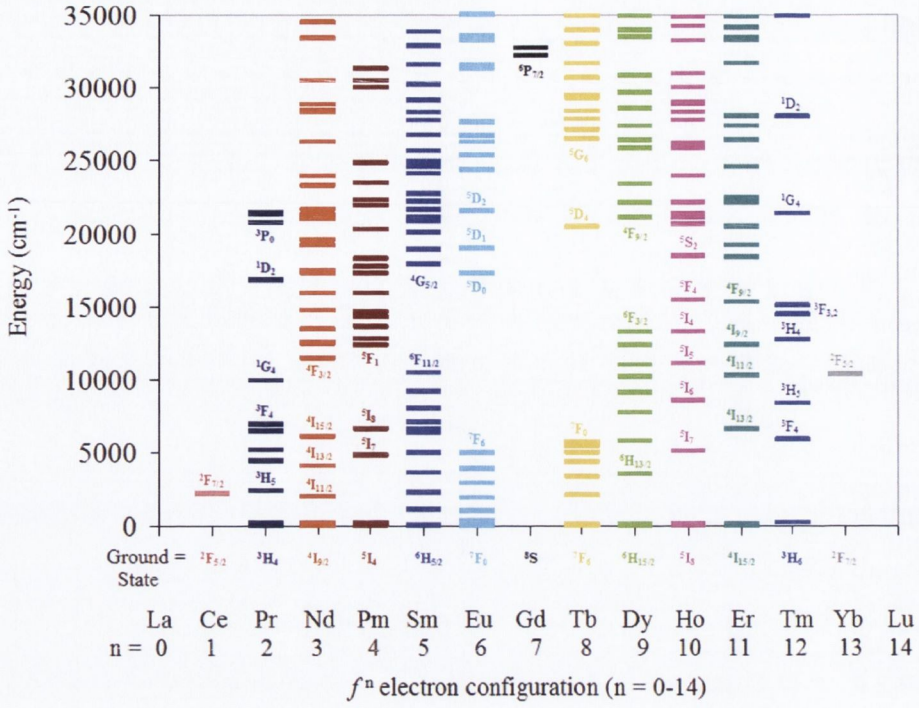


Figure 1.16: Electronic excited states for the Ln^{III} series.[117]

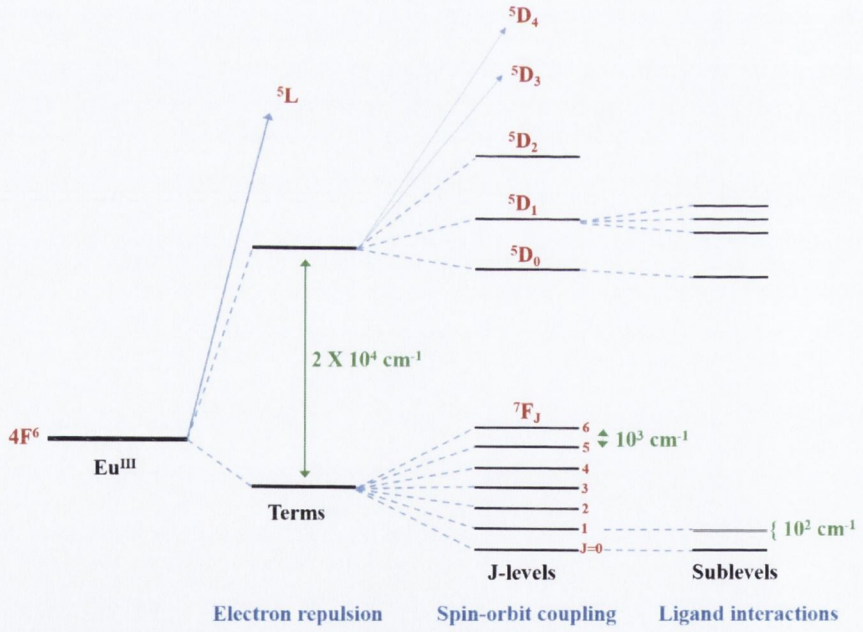


Figure 1.17: Splitting of the Eu^{III} 4*f* energy levels.

The Laporte forbidden nature of *f-f* transitions in lanthanide ions results in very low absorption coefficients of around 10 M^{-1} cm^{-1}, with no relaxation of the Laporte rules possible due to their weak interactions with ligand orbitals. This at first would appear to be

a major drawback to the use of lanthanides for luminescent purposes, but it can be effectively overcome by making use of organic antennae chromophores. These ligands typically have much higher absorption coefficients of *ca.* 10^3 - 10^6 M^{-1} cm^{-1} and through the sensitisation pathway can effectively facilitate lanthanide luminescence.

The sensitisation pathway occurs over four steps (**Figure 1.18**): (1) the excitation of an organic ligand from its singlet ground state S_0 into the singlet S_1 excited state; (2) non-radiative intersystem crossing results in a change in electron spin state from S_1 to the ligands excited triplet state T_1, indeed the chances of intersystem crossing from S_1 to the ligands excited triplet state T_1 is greatly enhanced by the external heavy atom effect;[122] (3) intramolecular energy transfer from the ligand T_1 state to an excited 4*f* state of a Ln^{III} ion; (4) finally intra 4*f* transitions within the lanthanide ion possibly resulting in luminescence.[123]

The amount of absorbed energy transferred from the ligand to the Ln^{III} ion is limited by non-radiative processes and radiative processes, namely fluorescence and phosphorescence of the ligand. The heavy atom effect results in some mixing of the singlet and triplet wave functions of the antennae, consequently the triplet state gains some singlet state characteristics and *vice versa*, allowing previously spin-forbidden transitions to take place. In order for an organic ligand to be an effective antenna chromophore it must possess and excited triplet state similar in energy to that of the Ln^{III} triplet state, but needs to be at least 1850 cm^{-1} greater in energy in order to prevent thermal repopulation of the ligand triplet state.[124]

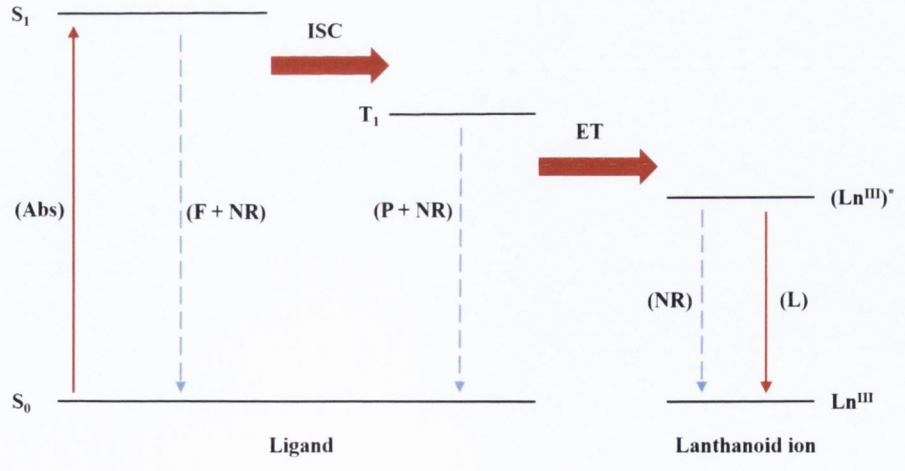


Figure 1.18: Schematic representation of the sensitisation pathway. Abbreviations: Abs= absorption; F= Fluorescence; NR= non-radiative processes, ISC= intersystem crossing; P= phosphorescence; ET= energy transfer; L= lanthanide luminescence. Blue broken arrows indicate processes competing with lanthanide luminescence.

1.4.3 Lanthanide metal-organic frameworks

The incorporation of lanthanides into MOFs has led to an exciting new class of frameworks known as lanthanide metal-organic frameworks (LnMOFs). They combine many of the fundamental attributes of main group and transition metal MOFs, which were discussed in section 1.2, with the luminescent properties of lanthanide complexes. Preliminary investigations have shown them to be ideal candidates for the sensing of ions[125] and small molecules,[126] luminescent labels[127] and as MRI contrast agents.[128]

The first LnMOF capable of detecting cations was reported by Wang *et al.* in 2004.[129] Their 3D LnMOF Na[Eu(1,4,8,11-tetraazacyclotetradecane-1,4,8,11-tetrapropionate)$(H_2O)_4]_3 \cdot 2H_2O$, was successfully able to detect a series of metal cations, namely: Cu^{II}, Ag^{I}, Zn^{II}, Cd^{II}, and Hg^{II} (**Figure 1.19**). In each case, there was a measurable decrease in the fluorescence spectrum of the LnMOF upon coordination of a metal cation to one of the ligand's vacant azacyle coordination sites. The coordination of one equivalent of Ag^{I} resulted in a marked difference in the overall Eu^{III} emission spectrum, with a reduction in the intensity of the bands associated with the $^5D_0 \rightarrow {}^7F_1$ and $^5D_0 \rightarrow {}^7F_4$ transitions and an increase in intensity of the hypersensitive $^5D_0 \rightarrow {}^7F_2$ transition, whose emission intensity increased almost by a factor of five (**Figure 1.19**). This was attributed to the enhanced rigidity and the change in paramagnetic spin state of the LnMOF due to the coordinated Ag^{I}.

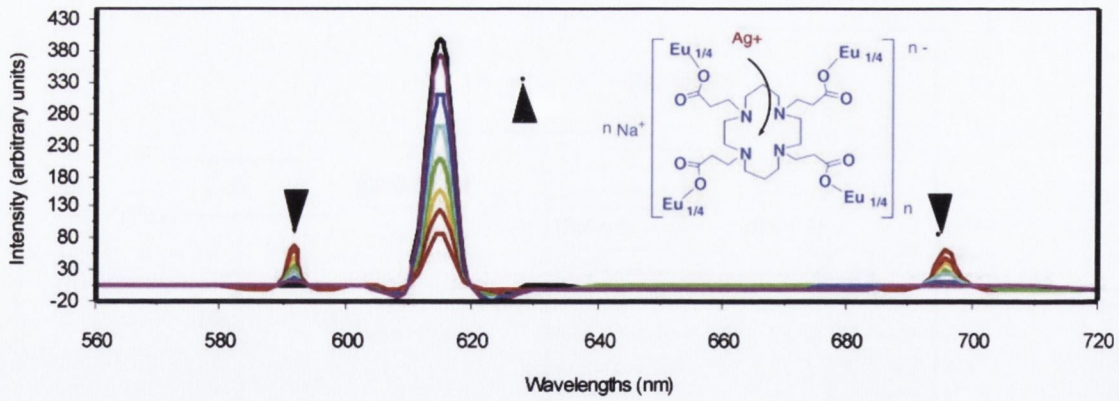


Figure 1.19: Increase in luminescence upon addition of Ag^{I} to a 1.0 x 10^{-4} M solution of $Na[EuL(H_2O)_4]_3 \cdot 2H_2O$. Inset: the ligand L (1,4,8,11-tetraazacyclotetradecane-1,4,8,11-tetrapropionic acid) coordinating to Ag^{I}.[129]

Hydrogen bonding has proven to be a useful tool when designing anion sensors.[130,131] Lanthanide frameworks containing N-H and O-H functional groups in either the ligand or in

coordinated solvent molecules may interact with anions through hydrogen bonding, possibly leading to an observable change in luminescence. Lanthanide luminescence can be effectively quenched by the high frequency vibrations of certain coordinated molecules, in particular –OH and –NH groups. This is caused by vibronic coupling between the excited lanthanide ion and the coordinated high frequency oscillators, *e.g.* H_2O, which results in a non-radiative deactivation pathway to the lanthanide ground state.[132] Lobkovsky *et al.* used this principle for the detection of F^- anions using the 3D LnMOF MOF-76b, Tb(BTC)·MeOH, which contains accessible 1D channels, where BTC is benzene-1,3,5-tricarboxylate.[133] In this case, a sample of MOF-76b was evacuated of all guest solvent molecules which were residing in the channels and added to a methanol solution containing NaF. Upon incorporation of F^- anions into the pores of the LnMOF it was found that there was a considerable enhancement in the luminescent bands associated with Tb^{III}. It was reasoned that this was due to hydrogen bonding interactions between the F^- anions and the methanol -OH moieties, which restrict the bond stretching of the O-H functionality, thus reducing its quenching ability. They repeated the experiment with a series of different anions, Br^-, Cl^-, SO_4^{2-} and CO_3^{2-} in methanol, but the most profound increase in luminescence was found for F^-, which was expected to arise from its strong hydrogen bonding ability.

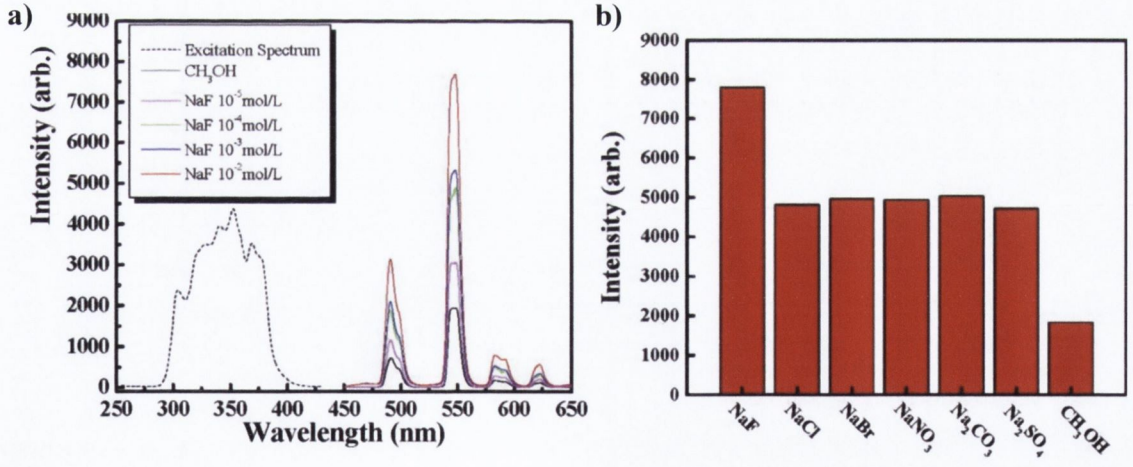


Figure 1.20: a) Luminescence spectrum of an activated sample of MOF-76b in varying concentrations of NaF/methanol solutions, **b)** $^5D_4 \rightarrow {}^7F_5$ transition intensities of activated MOF-76b in various 10^{-2} M NaX and Na_2X methanol solutions (excited and monitored at 353 and 548 nm, respectively).[133]

As was previously mentioned, NIR emitting lanthanide complexes have many possible applications, particularly in the telecommunication industry, yet the number of

reported NIR emitting LnMOFs remains low, with research mainly focussing on LnMOFs which emit in the visible spectrum. Yb-PVDC reported by Rosi *et al.* in 2009, was the first example of a sensitised NIR emitting LnMOF, where PVDC is 4,4'-[(2,5-dimethoxy-1,4-phenylene)di-2,1-ethenediyl]bis-benzoic acid.[134] Yb-PVDC contains infinite 1D Yb^{III}-carboxylate chains, linked *via* PVDC ligands into a 3D framework with 1D channels (**Figure 1.21**).

Following on from this work Rosi *et al.* proposed one of the more novel uses for luminescent LnMOFs, utilising a series of LnMOFs based on Er_xYb_{1-x}-PVDC-1 to generate NIR barcodes (**Figure 1.21**).[127] With the Er^{III}-LnMOF showing a sharp signal at 1,530 nm and the Yb^{III} equivalent emitting at 980 nm, they were able to tune the luminescent properties of the mixed metal LnMOF by altering the metal ratios, as the NIR emission intensities vary linearly with their relative concentrations. Furthermore, by adding additional lanthanides to the LnMOF they were able to increase the number of unique code combinations, enabling the materials to possibly be used in specialist areas such as bioanalytical assays.

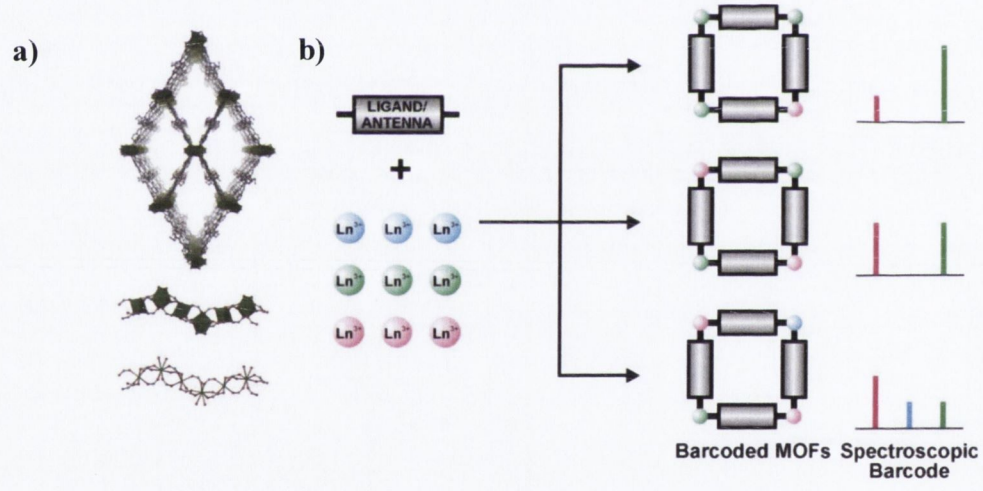


Figure 1.21: a) Yb-PVDC, **b)** preparation of LnMOF barcodes.[134,127]

The attributes that the organic ligand, metal centre and resulting porosity can impart onto LnMOFs results in compounds with properties that are not possible with any other type of material. But as research into LnMOFs is very much in its infancy it will be necessary to conduct further research if we are to fully understand how to combine their component parts in such a way that best utilises their synergistic properties and to ultimately see their use in sensors and photonic applications become a viable reality.

1.5 References

1. G. M. J. Schmidt, *Pure and Applied Chemistry*, 1971, **27**, 647-678.
2. J. M. Lehn, *Pure and Applied Chemistry*, 1978, **50**, 871-892.
3. J. M. Lehn, *Supramolecular chemistry : concepts and perspectives*, VCH, Weinheim ; Cambridge, 1995.
4. K. J. M. Bishop, C. E. Wilmer, S. Soh and B. A. Grzybowski, *Small*, 2009, **5**, 1600-1630.
5. J. G. Angyan, *Journal of Chemical Physics*, 2007, **127**, 24108-24101.
6. T. Steiner, *Angewandte Chemie-International Edition*, 2002, **41**, 48-76.
7. P. A. Kollman and L. C. Allen, *Chemical Reviews*, 1972, **72**, 283-303.
8. C. Janiak, *Journal of the Chemical Society-Dalton Transactions*, 2000, 3885-3896.
9. S. Grimme, *Angewandte Chemie-International Edition*, 2008, **47**, 3430-3434.
10. C. L. Perrin and J. B. Nielson, *Annual Review of Physical Chemistry*, 1997, **48**, 511-544.
11. G. A. Jeffrey, *An introduction to hydrogen bonding*, Oxford University Press, New York ; Oxford, 1997.
12. J. D. Watson and F. H. C. Crick, *Nature*, 1953, **171**, 737-738.
13. L. E. Kay, *Who wrote the book of life? : a history of the genetic code*, Stanford University Press ; Cambridge University Press, Stanford, California, Cambridge, 2000.
14. FWK, *Nucleic acid structure*, http://catalog.flatworldknowledge.com/bookhub/reader/2547?e=gob-ch19_s02, Accessed 09/04/2013, 2013.
15. F. M. Menger, *Proceedings of the National Academy of Sciences of the United States of America*, 2002, **99**, 4818-4822.
16. J. R. Li, R. J. Kuppler and H. C. Zhou, *Chemistry Society Reviews*, 2009, **38**, 1477-1504.
17. M. Dierendonck, S. De Koker, C. Cuvelier, J. Grooten, C. Vervaet, J. P. Remon and B. G. De Geest, *Angewandte Chemie-International Edition*, 2010, **49**, 8620-8624.
18. Z. Wang, G. Chen and K. L. Ding, *Chemical Reviews*, 2009, **109**, 322-359.
19. E. Matisova and S. Skrabakova, *Journal of Chromatography A*, 1995, **707**, 145-179.
20. S. L. Candelaria, Y. Y. Shao, W. Zhou, X. L. Li, J. Xiao, J. G. Zhang, Y. Wang, J. Liu, J. H. Li and G. Z. Cao, *Nano Energy*, 2012, **1**, 195-220.
21. Z. P. Wang, J. H. Yu and R. R. Xu, *Chem. Soc. Rev.*, 2012, **41**, 1729-1741.

22. K. M. Fromm, *Coordination Chemistry Reviews*, 2008, **252**, 856-885.

23. X. T. Wang, L. K. San, H. Nguyen, N. M. Shafer, M. T. Hernandez and Z. X. Chen, *Journal of Coordination Chemistry*, 2013, **66**, 826-835.

24. H. Furukawa, N. Ko, Y. B. Go, N. Aratani, S. B. Choi, E. Choi, A. O. Yazaydin, R. Q. Snurr, M. O'Keeffe, J. Kim and O. M. Yaghi, *Science*, 2010, **329**, 424-428.

25. O. K. Farha, A. O. Yazaydin, I. Eryazici, C. D. Malliakas, B. G. Hauser, M. G. Kanatzidis, S. T. Nguyen, R. Q. Snurr and J. T. Hupp, *Nature Chemistry*, 2010, **2**, 944-948.

26. B. A. Xu, H. L. Guo, S. Wang, Y. Y. Li, H. J. Zhang and C. G. Liu, *Crystengcomm*, 2012, **14**, 2914-2919.

27. R. F. D'Vries, M. Iglesias, N. Snejko, E. Gutierrez-Puebla and M. A. Monge, *Inorganic Chemistry*, 2012, **51**, 11349-11355.

28. I. W. o. Science, http://goo.gl/TLUI1, Accessed 21/03/2013, 2013.

29. A. Wells, *Three dimensional nets and polyhedra*, Wiley, New York, 1977.

30. L. R. MacGillivray, *Metal-Organic Frameworks: Design and Application*, John Wiley & Sons, Inc., Hoboken, NJ, USA, 2010.

31. O. Delgado-Friedrichs and M. O'Keeffe, *Journal of Solid State Chemistry*, 2005, **178**, 2480-2485.

32. M. O'Keeffe, M. Eddaoudi, H. L. Li, T. Reineke and O. M. Yaghi, *Journal of Solid State Chemistry*, 2000, **152**, 3-20.

33. M. O'Keeffe, M. A. Peskov, S. J. Ramsden and O. M. Yaghi, *Accounts of Chemical Research*, 2008, **41**, 1782-1789.

34. C. Baerlocher and L. McCusker, *Database of Zeolite Structures*, http://www.iza-structure.org/databases/, Accessed 05/08/2013, 2013.

35. L. G. Donaruma, B. P. Block, K. L. Loening, N. Plate, T. Tsuruta, K. C. Buschbeck, W. H. Powell and J. Reedijk, *Pure and Applied Chemistry*, 1985, **57**, 149-168.

36. IUPAC, *Coordination polymers and metal organic frameworks: terminology and nomenclature guidelines*, http://www.iupac.org/nc/home/projects/project-db/project-details.html?tx_wfqbe_pi1%5bproject_nr%5d=2009-012-2-200, Accessed 10/04/2013, 2013.

37. O. M. Yaghi, M. O'Keeffe, N. W. Ockwig, H. K. Chae, M. Eddaoudi and J. Kim, *Nature*, 2003, **423**, 705-714.

38. P. Cui, Y. G. Ma, H. H. Li, B. Zhao, J. R. Li, P. Cheng, P. B. Balbuena and H. C. Zhou, *Journal of the American Chemical Society*, 2012, **134**, 18892-18895.

39. S. Kitagawa and S. Noro, *Comprehensive Coordination Chemistry*, 2004, **7**, 231-261.

40. M. Eddaoudi, D. B. Moler, H. L. Li, B. L. Chen, T. M. Reineke, M. O'Keeffe and O. M. Yaghi, *Accounts of Chemical Research*, 2001, **34**, 319-330.

41. B. H. Ye, M. L. Tong and X. M. Chen, *Coordination Chemistry Reviews*, 2005, **249**, 545-565.

42. T. R. Cook, Y. R. Zheng and P. J. Stang, *Chemical Reviews*, 2013, **113**, 734-777.

43. D. J. Tranchemontagne, J. L. Mendoza-Cortes, M. O'Keeffe and O. M. Yaghi, *Chemistry Society Reviews*, 2009, **38**, 1257-1283.

44. M. Eddaoudi, J. Kim, N. Rosi, D. Vodak, J. Wachter, M. O'Keeffe and O. M. Yaghi, *Science*, 2002, **295**, 469-472.

45. P. Jaitner, C. Rieker and K. Wurst, *Chemical Communications*, 1997, 1245-1246.

46. A. Tulinsky, C. R. Worthington and E. Pignataro, *Acta Crystallographica*, 1959, **12**, 623-626.

47. N. L. Rosi, J. Eckert, M. Eddaoudi, D. T. Vodak, J. Kim, M. O'Keeffe and O. M. Yaghi, *Science*, 2003, **300**, 1127-1129.

48. X. L. Wang, C. Qin, E. B. Wang, Y. G. Li, Z. M. Su, L. Xu and L. Carlucci, *Angewandte Chemie-International Edition*, 2005, **44**, 5824-5827.

49. E. V. Dikarev, B. Li, V. V. Chernyshev, R. V. Shpanchenko and M. A. Petrukhina, *Chemical Communications*, 2005, 3274-3276.

50. M. Kramer, S. B. Ulrich and S. Kaskel, *Journal of Materials Chemistry*, 2006, **16**, 2245-2248.

51. C. J. Milios, T. C. Stamatatos, P. Kyritsis, A. Terzis, C. P. Raptopoulou, R. Vicente, A. Escuer and S. P. Perlepes, *European Journal of Inorganic Chemistry*, 2004, 2885-2901.

52. E. N. Coker, T. J. Boyle, M. A. Rodriguez and T. M. Alam, *Polyhedron*, 2004, **23**, 1739-1747.

53. H. Furukawa, Y. B. Go, N. Ko, Y. K. Park, F. J. Uribe-Romo, J. Kim, M. O'Keeffe and O. M. Yaghi, *Inorganic Chemistry*, 2011, **50**, 9147-9152.

54. B. F. Hoskins and R. Robson, *Journal of the American Chemical Society*, 1989, **111**, 5962-5964.

55. B. F. Hoskins and R. Robson, *Journal of the American Chemical Society*, 1990, **112**, 1546-1554.

56. B. F. Abrahams, B. F. Hoskins, J. P. Liu and R. Robson, *Journal of the American Chemical Society*, 1991, **113**, 3045-3051.

57. M. Dinca, A. F. Yu and J. R. Long, *Journal of the American Chemical Society*, 2006, **128**, 8904-8913.

58. P. Teo and T. S. A. Hor, *Coordination Chemistry Reviews*, 2011, **255**, 273-289.

59. S. Xiang, J. Huang, L. Li, J. Zhang, L. Jiang, X. Kuang and C.-Y. Su, *Inorganic Chemistry*, 2011, **50**, 1743-1748.

60. W. C. Song, J. R. Li, P. C. Song, Y. Tao, Q. Yu, X. L. Tong and X. H. Bu, *Inorganic Chemistry*, 2009, **48**, 3792-3799.

61. R. I. Walton, *Chemistry Society Reviews*, 2002, **31**, 230-238.

62. R. H. Laye and E. J. L. McInnes, *European Journal of Inorganic Chemistry*, 2004, 2811-2818.

63. P. M. Forster, N. Stock and A. K. Cheetham, *Angewandte Chemie-International Edition*, 2005, **44**, 7608-7611.

64. E. R. Parnham and R. E. Morris, *Accounts of Chemical Research*, 2007, **40**, 1005-1013.

65. P. M. Forster, A. R. Burbank, C. Livage, G. Férey and A. K. Cheetham, *Chemical Communications*, 2004, 368-369.

66. A. G. Marquez, A. Demessence, A. E. Platero-Prats, D. Heurtaux, P. Horcajada, C. Serre, J. S. Chang, G. Férey, V. A. de la Pena-O'Shea, C. Boissiere, D. Grosso and C. Sanchez, *European Journal of Inorganic Chemistry*, 2012, 5165-5174.

67. T. Chalati, P. Horcajada, R. Gref, P. Couvreur and C. Serre, *Journal of Materials Chemistry*, 2011, **21**, 2220-2227.

68. E. Haque, N. A. Khan, J. H. Park and S. H. Jhung, *Chemistry-A European Journal*, 2010, **16**, 1046-1052.

69. W. B. Liang and D. M. D'Alessandro, *Chemical Communications*, 2013, **49**, 3706-3708.

70. P. Horcajada, C. Serre, G. Maurin, N. A. Ramsahye, F. Balas, M. Vallet-Regi, M. Sebban, F. Taulelle and G. Férey, *Journal of the American Chemical Society*, 2008, **130**, 6774-6780.

71. W. J. Rieter, K. M. Pott, K. M. Taylor and W. Lin, *Journal of the American Chemical Society*, 2008, **130**, 11584-11585.

72. P. Horcajada, C. Serre, M. Vallet-Regi, M. Sebban, F. Taulelle and G. Férey, *Angewandte Chemie-International Edition*, 2006, **45**, 5974-5978.

73. J. Y. An, S. J. Geib and N. L. Rosi, *Journal of the American Chemical Society*, 2009, **131**, 8376-8377.

74. P. Horcajada, T. Chalati, C. Serre, B. Gillet, C. Sebrie, T. Baati, J. F. Eubank, D. Heurtaux, P. Clayette, C. Kreuz, J. S. Chang, Y. K. Hwang, V. Marsaud, P. N. Bories, L. Cynober, S. Gil, G. Férey, P. Couvreur and R. Gref, *Nature Materials*, 2010, **9**, 172-178.

75. M. Yoon, R. Srirambalaji and K. Kim, *Chem. Rev.*, 2012, **112**, 1196-1231.

76. O. R. Evans, H. L. Ngo and W. B. Lin, *Journal of the American Chemical Society*, 2001, **123**, 10395-10396.

77. A. G. Hu, H. L. Ngo and W. B. Lin, *Journal of the American Chemical Society*, 2003, **125**, 11490-11491.

78. K. S. Jeong, Y. B. Go, S. M. Shin, S. J. Lee, J. Kim, O. M. Yaghi and N. Jeong, *Chemical Science*, 2011, **2**, 877-882.

79. L. Q. Ma, J. M. Falkowski, C. Abney and W. B. Lin, *Nature Chemistry*, 2010, **2**, 838-846.

80. S. H. Cho, B. Q. Ma, S. T. Nguyen, J. T. Hupp and T. E. Albrecht-Schmitt, *Chemical Communications*, 2006, 2563-2565.

81. M. Kurmoo, *Chemistry Society Reviews*, 2009, **38**, 1353-1379.

82. G. J. Halder, C. J. Kepert, B. Moubaraki, K. S. Murray and J. D. Cashion, *Science*, 2002, **298**, 1762-1765.

83. W. Vreugdenhil, J. H. Vandiemen, R. A. G. Degraaff, J. G. Haasnoot, J. Reedijk, A. M. Vanderkraan, O. Kahn and J. Zarembowitch, *Polyhedron*, 1990, **9**, 2971-2979.

84. J. Krober, J. P. Audiere, R. Claude, E. Codjovi, O. Kahn, J. G. Haasnoot, F. Groliere, C. Jay, A. Bousseksou, J. Linares, F. Varret and A. Gonthiervassal, *Chemistry of Materials*, 1994, **6**, 1404-1412.

85. G. Agusti, S. Cobo, A. B. Gaspar, G. Molnar, N. O. Moussa, P. A. Szilagyi, V. Palfi, C. Vieu, M. C. Munoz, J. A. Real and A. Bousseksou, *Chemistry of Materials*, 2008, **20**, 6721-6732.

86. O. R. Evans and W. B. Lin, *Accounts of Chemical Research*, 2002, **35**, 511-522.

87. W. W. Zhou, J. T. Chen, G. Xu, M. S. Wang, J. P. Zou, X. F. Long, G. J. Wang, G. C. Guo and J. S. Huang, *Chemical Communications*, 2008, 2762-2764.

88. D. F. Sun, R. Cao, J. B. Weng, M. C. Hong and Y. C. Liang, *Journal of the Chemical Society-Dalton Transactions*, 2002, 291-292.

89. C. N. R. Rao, A. Ranganathan, V. R. Pedireddi and A. R. Raju, *Chemical Communications*, 2000, 39-40.

90. D. P. Broom, *International Journal of Hydrogen Energy*, 2007, **32**, 4871-4888.

91. Y. H. Hu and L. Zhang, *Advanced Materials*, 2010, **22**, E117-E130.

92. H. Furukawa, M. A. Miller and O. M. Yaghi, *Journal of Materials Chemistry*, 2007, **17**, 3197-3204.

93. IEA, *World Energy Outlook 2010*, http://www.worldenergyoutlook.org/media/weo2010.pdf, Accessed 25/03/2013, 2013.

94. L. Schlapbach and A. Zuttel, *Nature*, 2001, **414**, 353-358.

95. U.S.D.O.E., *Targets for onboard hydrogen storage systems for light-duty vehicles*, http://www1.eere.energy.gov/hydrogenandfuelcells/storage/pdfs/targets_onboard_hydro_storage_explanation.pdf, Accessed 25/03/2013, 2013.

96. BMW, *BMW Clean Energy*, http://www.bmw.com/com/en/insights/technology/cleanenergy/phase_2/cleanenergy.html, Accessed 05/08/2013, 2013.

97. Honda, *Honda FC-X Clarity*, http://world.honda.com/FCXClarity/package/index.html, Accessed 25/03/2013, 2013.

98. S. I. Orimo, Y. Nakamori, J. R. Eliseo, A. Zuttel and C. M. Jensen, *Chemical Reviews*, 2007, **107**, 4111-4132.

99. W. Grochala and P. P. Edwards, *Chem. Rev.*, 2004, **104**, 1283-1315.

100. R. E. Morris and P. S. Wheatley, *Angewandte Chemie-International Edition*, 2008, **47**, 4966-4981.

101. A. Zecchina, S. Bordiga, J. G. Vitillo, G. Ricchiardi, C. Lamberti, G. Spoto, M. Bjorgen and K. P. Lillerud, *Journal of the American Chemical Society*, 2005, **127**, 6361-6366.

102. H. W. Langmi and G. S. McGrady, *Coordination Chemistry Reviews*, 2007, **251**, 925-935.

103. M. Kondo, T. Yoshitomi, K. Seki, H. Matsuzaka and S. Kitagawa, *Angewandte Chemie-International Edition*, 1997, **36**, 1725-1727.

104. M. P. Suh, H. J. Park, T. K. Prasad and D. W. Lim, *Chemical Reviews*, 2012, **112**, 782-835.

105. D. Zhao, D. Q. Yuan and H. C. Zhou, *Energy & Environmental Science*, 2008, **1**, 222-235.

106. S. S. Y. Chui, S. M. F. Lo, J. P. H. Charmant, A. G. Orpen and I. D. Williams, *Science*, 1999, **283**, 1148-1150.

107. V. K. Peterson, Y. Liu, C. M. Brown and C. J. Kepert, *Journal of the American Chemical Society*, 2006, **128**, 15578-15579.

108. Y. Liu, C. M. Brown, D. A. Neumann, V. K. Peterson and C. J. Kepert, *Journal of Alloys and Compounds*, 2007, **446**, 385-388.

109. P. Benard and R. Chahine, *Scripta Materialia*, 2007, **56**, 803-808.

110. S. Q. Ma, J. Eckert, P. M. Forster, J. W. Yoon, Y. K. Hwang, J. S. Chang, C. D. Collier, J. B. Parise and H. C. Zhou, *Journal of the American Chemical Society*, 2008, **130**, 15896-15902.

111. Y. G. Lee, H. R. Moon, Y. E. Cheon and M. P. Suh, *Angewandte Chemie-International Edition*, 2008, **47**, 7741-7745.

112. K. L. Mulfort and J. T. Hupp, *Journal of the American Chemical Society*, 2007, **129**, 9604-9605.

113. R. G. Pearson and J. Songstad, *Journal of the American Chemical Society*, 1967, **89**, 1827-1836.

114. D. Parker and J. A. G. Williams, *Journal of the Chemical Society-Dalton Transactions*, 1996, **18**, 3613-3628.

115. W. S. Song, K. H. Lee, Y. S. Kim and H. Yang, *Materials Chemistry and Physics*, 2012, **135**, 51-57.

116. K. Kuriki, Y. Koike and Y. Okamoto, *Chemical Reviews*, 2002, **102**, 2347-2356.

117. E. G. Moore, A. P. S. Samuel and K. N. Raymond, *Accounts of Chemical Research*, 2009, **42**, 542-552.

118. B. Imaging, *Magnevist*, http://bayerimaging.com/products/magnevist/, Accessed 06/03, 2013.

119. X. Y. Du and T. E. Graedel, *Journal of Industrial Ecolology*, 2011, **15**, 836-843.

120. M. Shelef and R. W. McCabe, *Catalysis Today*, 2000, **62**, 35-50.

121. J. C. G. Bunzli, S. Comby, A. S. Chauvin and C. D. B. Vandevyver, *Journal of Rare Earths*, 2007, **25**, 257-274.

122. J. C. G. Bunzli and C. Piguet, *Chemical Society Reviews*, 2005, **34**, 1048-1077.

123. S. I. Klink, G. A. Hebbink, L. Grave, F. Van Veggel, D. N. Reinhoudt, L. H. Slooff, A. Polman and J. W. Hofstraat, *Journal of Applied Physics*, 1999, **86**, 1181-1185.

124. M. Latva, H. Takalo, V. M. Mukkala, C. Matachescu, J. C. RodriguezUbis and J. Kankare, *Journal of Luminescence*, 1997, **75**, 149-169.

125. K. L. Wong, G. L. Law, Y. Y. Yang and W. T. Wong, *Advanced Materials*, 2006, **18**, 1051-+.

126. Z. Y. Guo, H. Xu, S. Q. Su, J. F. Cai, S. Dang, S. C. Xiang, G. D. Qian, H. J. Zhang, M. O'Keeffe and B. L. Chen, *Chemical Communications*, 2011, **47**, 5551-5553.

127. K. A. White, D. A. Chengelis, K. A. Gogick, J. Stehman, N. L. Rosi and S. Petoud, *Journal of the American Chemical Society*, 2009, **131**, 18069-18071.

128. G. A. Pereira, J. A. Peters, F. A. A. Paz, J. Rocha and C. Geraldes, *Inorganic Chemistry*, 2010, **49**, 2969-2974.

129. W. S. Liu, T. Q. Jiao, Y. Z. Li, Q. Z. Liu, M. Y. Tan, H. Wang and L. F. Wang, *Journal of the American Chemical Society*, 2004, **126**, 2280-2281.

130. R. Custelcean, P. Remy, P. V. Bonnesen, D.-E. Jiang and B. A. Moyer, *Angewandte Chemie-International Edition*, 2008, **47**, 1866-1870.

131. Q. M. Wang and H. Tamiaki, *Journal of Photochemistry and Photobiology a-Chemistry*, 2009, **206**, 124-128.

132. Y. Haas and G. Stein, *Journal of Physical Chemistry*, 1971, **75**, 3677-3681.

133. B. L. Chen, L. B. Wang, F. Zapata, G. D. Qian and E. B. Lobkovsky, *Journal of the American Chemical Society*, 2008, **130**, 6718-6719.

134. K. A. White, D. A. Chengelis, M. Zeller, S. J. Geib, J. Szakos, S. Petoud and N. L. Rosi, *Chemical Communications*, 2009, 4506-4508.

Chapter 2

Objectives of this project

2 Objectives of this project

2.1 Project objectives

The aim of this research project was to synthesise and characterise novel MOFs, composed of both mononuclear and polynuclear SBUs, linked *via* tritopic organic linkers. The initial part of this study focused on the use of ligands that incorporate both N- and O-donor functionalities to generate MOFs (**Figure 2.1**). As was outlined in Chapter 1, the combination of N-donor heterocycles and carboxylate groups has led to the formation of neutral MOFs, with research primarily focussing on mixtures of pyridine and carboxylate functionalities.[1,2,3] Our research group has extensive experience in synthesising coordination compounds based on ligands containing both N- and O-donor moieties.[4,5,6] We believed that the incorporation of the lesser utilised combination of tetrazole and carboxylate moieties into rigid ligands, would enable us to apply our knowledge of such systems in the synthesis and characterisation of novel transition metal based MOFs, specifically Cd^{II}, Co^{II}, Cu^{II}, Mn^{II}, and Zn^{II}, with new and interesting topologies. With this objective in mind we synthesised the rigid tritopic ligands 3,5-di(1H-tetrazol-1-yl)benzoic acid, **L1** and 5-(1H-tetrazol-1-yl)isophthalic acid, **L2** (**Figure 2.1**).

In the second section of this study we explored the highly extended tritopic ligand 1,3,5-benzene-trisethynyl benzoic acid (**L3**), with the intention of forming MOFs with open-topologies and high surface areas (**Figure 2.1**). The bridging capabilities of the carboxylate groups present on **L3**, make them ideal functionalities for the generation of rigid polynuclear SBUs, which facilitated the formation of the open-frameworks we desired.[7]

The final aspect of this work is concerned with the development of LnMOFs. It was our ambition to expand on the number of reported lanthanide based frameworks by using the tritopic ligands **L1-L3**, to synthesise multifunctional LnMOFs with desirable properties, such as porosity and photoluminescence. LnMOFs with open-framework topologies are comparatively rare when compared to transition metal based MOFs, owing to the high coordination number and diminished ligand field stabilisation effects of coordinated lanthanide ions, which often results in densely packed frameworks.[8,9] It was our opinion that the extended nature of **L3** would counteract these points and produce 3D MOFs with open-topologies and large void volumes. By developing the synthetic strategy it facilitated the

generation of multiple series of isostructural LnMOFs and through the characterisation of these systems it enabled the better understanding of their interesting properties and how best to implement them in future applications.

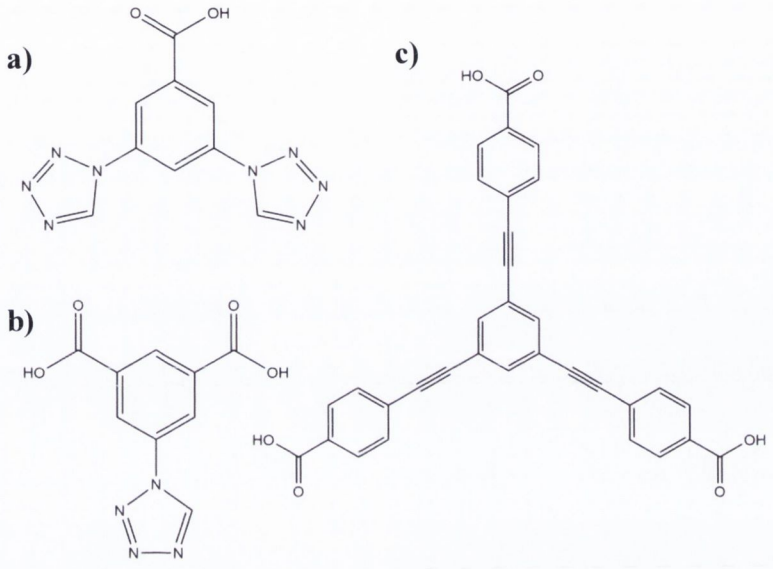


Figure 2.1: Structure of the ligands utilised in this research project, **a)** 3,5-di(1H-tetrazol-1-yl)benzoic acid, **L1**, **b)** 5-(1H-tetrazol-1-yl)isophthalic acid, **L2**, **c)** 1,3,5-benzene-trisethynyl benzoic acid, **L3**.

2.2 Specific aims of this study

To achieve the objectives of this project, we set out to attain the following:

a) To synthesise and fully characterise the rigid polydentate ligands **L1-L3**, which incorporate carboxylate and N-donor tetrazole functionalities.

b) Utilise these rigid ligands in the formation of novel MOFs, through the exploitation of transition and lanthanide metal ions.

c) Apply single crystal X-ray diffraction to structurally characterise the resulting metal complexes.

d) Characterise the physicochemical properties (*e.g.* thermal stability, phase purity, *etc.*) of these compounds.

e) Investigate the BET surface areas of relevant materials.

2.3 References

1. P. Teo and T. S. A. Hor, *Coordination Chemistry Reviews*, 2011, **255**, 273-289.
2. S. Xiang, J. Huang, L. Li, J. Zhang, L. Jiang, X. Kuang and C.-Y. Su, *Inorganic Chemistry*, 2011, **50**, 1743-1748.
3. H. Chun and J. Seo, *Inorganic Chemistry*, 2009, **48**, 9980-9982.
4. I. McKeogh, J. P. Hill, E. S. Collins, T. McCabe, A. K. Powell and W. Schmitt, *New Journal of Chemistry*, 2007, **31**, 1882-1886.
5. D. P. Walsh, R. Clerac, N. G. R. Hearns, P. E. Kruger and W. Schmitt, *Crystengcomm*, 2009, **11**, 1666-1673.
6. G. La Spina, R. Clerac, E. S. Collins, T. McCabe, M. Venkatesan, I. Ichinose and W. Schmitt, *Dalton Transactions*, 2007, 5248-5252.
7. D. J. Tranchemontagne, J. L. Mendoza-Cortes, M. O'Keeffe and O. M. Yaghi, *Chemistry Society Reviews*, 2009, **38**, 1257-1283.
8. J. Rocha, L. D. Carlos, F. A. A. Paz and D. Ananias, *Chemistry Society Reviews*, 2011, **40**, 926-940.
9. T. Devic, V. Wagner, N. Guillou, A. Vimont, M. Haouas, M. Pascolini, C. Serre, J. Marrot, M. Daturi, F. Taulelle and G. Férey, *Microporous and Mesoporous Materials*, 2011, **140**, 25-33.

Chapter 3

Metal-organic frameworks synthesised using tetrazole and carboxylate functionalised aromatic ligands

3 Metal-organic frameworks synthesised using tetrazole and carboxylate functionalised aromatic ligands

3.1 Introduction

This chapter primarily focusses on the synthesis and structural characterisation of a series of transition metal based MOFs, with a diverse range of topologies that range between layered lamellar structures to 3D open-frameworks. Multi-functional ligands containing both oxygen and nitrogen based donor groups have proven to be excellent ligands for producing porous frameworks with unique topologies, with research focusing on ligands containing combinations of pyridyl and carboxylate groups.[1,2,3] However, the numbers of reported frameworks synthesised using a combination of carboxylate and 5-membered N-heterocycles remains low. Therefore, we set out to develop a series of MOFs using ligands which incorporate these dual functionalities, specifically carboxylate and tetrazole groups, as the limited reported examples of these ligands identified them to be capable of producing 3D networks with interesting topologies.[4,5]

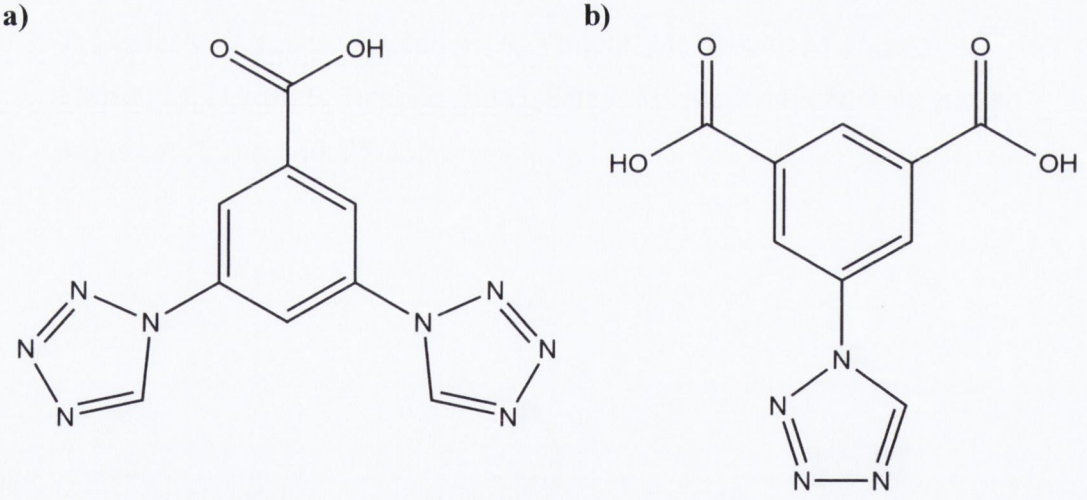


Figure 3.1: a) 3,5-di(1H-tetrazol-1-yl)benzoic acid, **L1**, **b)** 5-(1H-tetrazol-1-yl)isophthalic acid, **L2**.

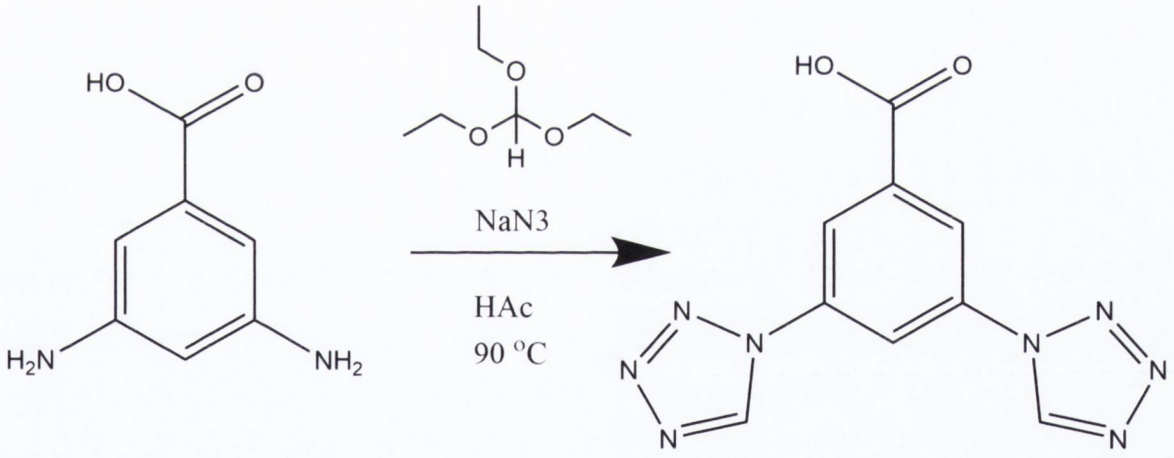
The ligands outlined in this chapter, 3,5-di(1H-tetrazol-1-yl)benzoic acid, **L1**, and 5-(1H-tetrazol-1-yl)isophthalic acid, **L2**, were considered to be ideal candidates for our initial studies in the synthesis of MOFs (**Figure 3.1**). They possess the dual functionality which we desired to study, in addition their multi-dentate nature would enable the formation of

network structures and the inherent rigidity of these ligands could facilitate the generation of open-frameworks. Furthermore, the carboxylic acid functionalities generate anionic ligands upon deprotonation, balancing the positive charge of the metal cations, removing the need for counterions. This is important as a network with an overall charge must contain guest species which act as counter ions, thus decreasing the overall surface area of the obtained framework.

3.2 Ligand synthesis

3.2.1 Synthesis of 3,5-di(1H-tetrazol-1-yl)benzoic acid, L1

The ligand 3,5-di(1H-tetrazol-1-yl)benzoic acid, **L1**, was synthesised *via* a known literature procedure, which involves a cyclisation reaction of a primary amine with an *ortho*-carboxylic acid ester and sodium azide, in glacial acetic acid, which acts as both the solvent and as the acid catalyst (**Scheme 3.1**).[6]



Scheme 3.1: Reaction scheme for the synthesis of **L1**.

To synthesise **L1**, 3,5-diaminobenzoic acid was reacted with 2.2 mole equivalents of sodium azide (*i.e.* 1.1 equivalents of sodium azide per primary amine) and six equivalents of triethyl *ortho*-formate (three equivalents per amine functionality) in glacial acetic acid. The ligand forms in a moderate yield of 53% and elemental analysis (CHN) is in accordance with the proposed structure. ^{1}H-NMR of **L1** in deuterated DMSO shows the presence of three singlets at 10.36 (2H, tetrazole), 8.83 (1H, aromatic) and 8.61 (2H, aromatic) ppm (**Figure 3.2**). The FT-IR spectrum of **L1** indicates the presence of a protonated carboxylic

acid group, with a strong signal at 1713 cm^{-1} arising from the C=O bond stretch. Mass spectrometry provided additional evidence for the formation of **L1**.

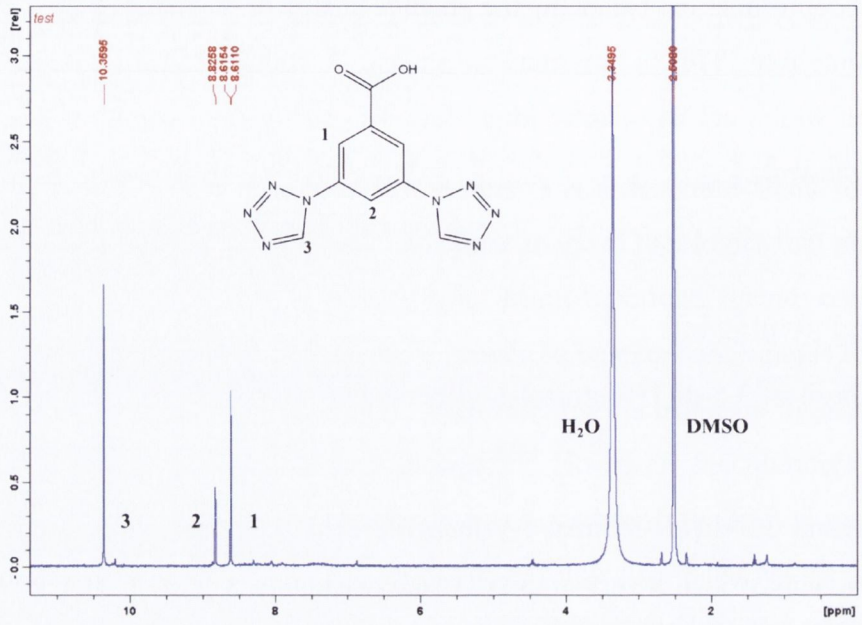


Figure 3.2: ^{1}H-NMR (DMSO-D_6) spectrum of **L1**.

3.2.2 Synthesis of 5-(1H-tetrazol-1-yl)isophthalic acid, L2

The same cyclisation reaction employed in the formation of **L1** was used for the synthesis of 5-(1H-tetrazol-1-yl)isophthalic acid, **L2**. However, 5-aminoisophthalic acid was used as the primary amine, along with 1.1 mole equivalents of sodium azide and three equivalents of triethyl *ortho*-formate. As for **L1**, **L2** formed in a moderate yield of 50%. The ^{1}H-NMR spectrum of **L2** in deuterated DMSO has three singlets at 10.35 (1H, tetrazole), 8.66 (1H, aromatic) and 8.57 ppm (1H, aromatic) (**Figure 3.3**). FT-IR analysis of **L2** reveals a signal at 1714 cm^{-1}, resulting from the C=O stretching vibration of the protonated carboxylic acid groups found in **L2**. Elemental analysis and mass spectrometry further confirmed the synthesis of **L2**.

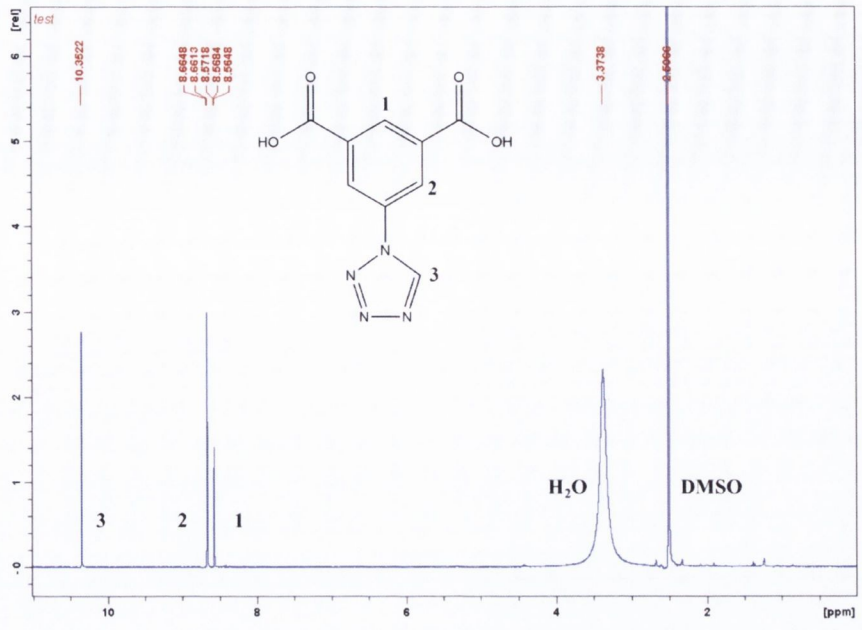


Figure 3.3: ^{1}H-NMR (DMSO-D_6) spectrum of **L2**.

3.3 [Co(**L1**)$_2$], (**1**).

3.3.1 Synthesis and structural characterisation of compound **1**

Small orange crystals of the novel framework [Co(**L1**)$_2$], **1**, form *via* the reaction of $Co(NO_3)\cdot 4H_2O$ and the ligand **L1** in a MeOH/H_2O (7:1, v:v) solution at 120 °C. Single crystal X-ray diffraction (XRD) reveals that compound **1** crystallises in the monoclinic space group $P2_1/c$. The small size of the crystals made characterisation by single-crystal XRD difficult, resulting in a relatively high R1 value of 0.1331.

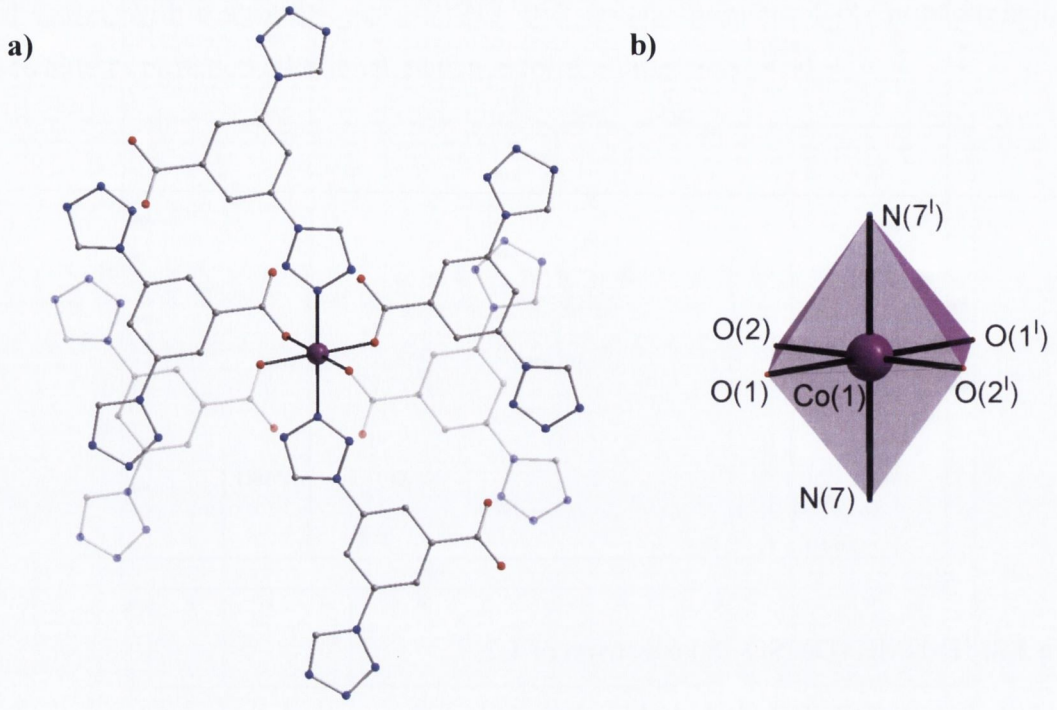


Figure 3.4: a), b) Co^{II} coordination environment in **1**. Symmetry code: (I) -x, -y, 1-z. Colour code: Co violet, C grey, O red, N blue. H atoms omitted for clarity.

The asymmetric unit of **1** contains one symmetry independent Co^{II} ion and one ligand molecule. The Co^{II} metal centres are coordinated to six donor atoms, from six separate **L1** ligands, resulting in each metal centre having a slightly distorted octahedral coordination geometry (**Figure 3.4**). The equatorial positions of the octahedral coordination spheres are provided by four oxygen atoms (O(1), O(2), O(1^{I}), O(2^{I})), from four deprotonated **L1** carboxylate groups. The remaining axial positions of the octahedral coordination environment are occupied by two nitrogen atoms, derived from two separate symmetry related **L1** tetrazole groups (N(7), N(7^{I})). The slight distortion in the coordination geometry is demonstrated by evaluating the bond angles O(1)-Co(1)-O(2) (88.8(2)°), O(1)-Co(1)-N(7) (90.5(2)°) and O(2)-Co(1)-N(7) (86.4(3)°), which closely resemble the ideal angle of 90°. Coordination bond lengths are summarised in **Table 3.1** and are consistent with previously reported Co-O and Co-N bond lengths.[7,8]

Table 3.1: Selected bond distances and angles for **1**. Symmetry code: (I) -x, -y, 1-z.

Atoms	Distance (Å)	Atoms	Angle(°)
Co(1)-O(1)	**2.068(6)**	O(1)-Co(1)-O(2)	**88.8(2)**
Co(1)-O(2)	**2.043(6)**	O(1)-Co(1)-O(2^{I})	**91.2(2)**
Co(1)-N(7)	**2.162(7)**	O(1)-Co(1)-N(7)	**90.5(2)**
		O(1)-Co(1)-N(7^{I})	**89.5(2)**
		O(2)-Co(1)-N(7)	**86.4(3)**
		O(2)-Co(1)-N(7^{I})	**93.6(3)**

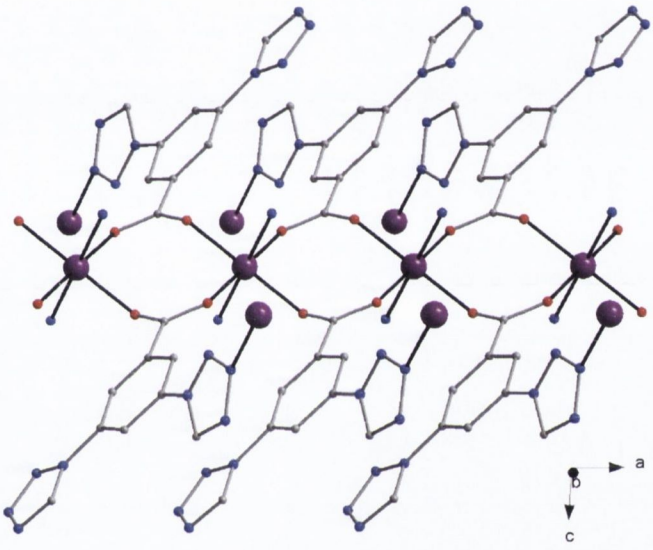


Figure 3.5: 1D polymeric chain formed through bridging carboxylate groups as seen in the direction of the crystallographic *b*-axis. Colour code: Co violet, C grey, O red, N blue. H atoms omitted for clarity.

The carboxylate groups act in a bidentate *syn-syn* μ_2 mode, bridging neighbouring Co^{II} ions. This has the effect of generating 1D Co-Co chains, with an interatomic Co···Co distance of *ca.* 4.5Å, which extend parallel to the crystallographic *a*-axis (**Figure 3.5**). These 1D chains are linked to neighbouring chains through a tetrazole nitrogen atom from each bridging ligand, resulting in 2D sheets which extend in the crystallographic *ab* plane. The 2D sheets are generated through symmetry operations, with each Co^{II} ion being located on an inversion centre, with a 2_1 screw axis running parallel to the crystallographic *b*-axis. These neutral layers have a cross sectional width of *ca.* 15.4 Å and pack in the direction of the *c*-axis to form a layered lamellar packing structure, linked *via* weak dispersion forces

(**Figure 3.6**). The neutral layers can be further simplified to that of a 2D net with a Schläfli symbol of ($3^6.4^6.5^3$), by visualising each Co^{II} ion as a six-connecting node (**Figure 3.7**).

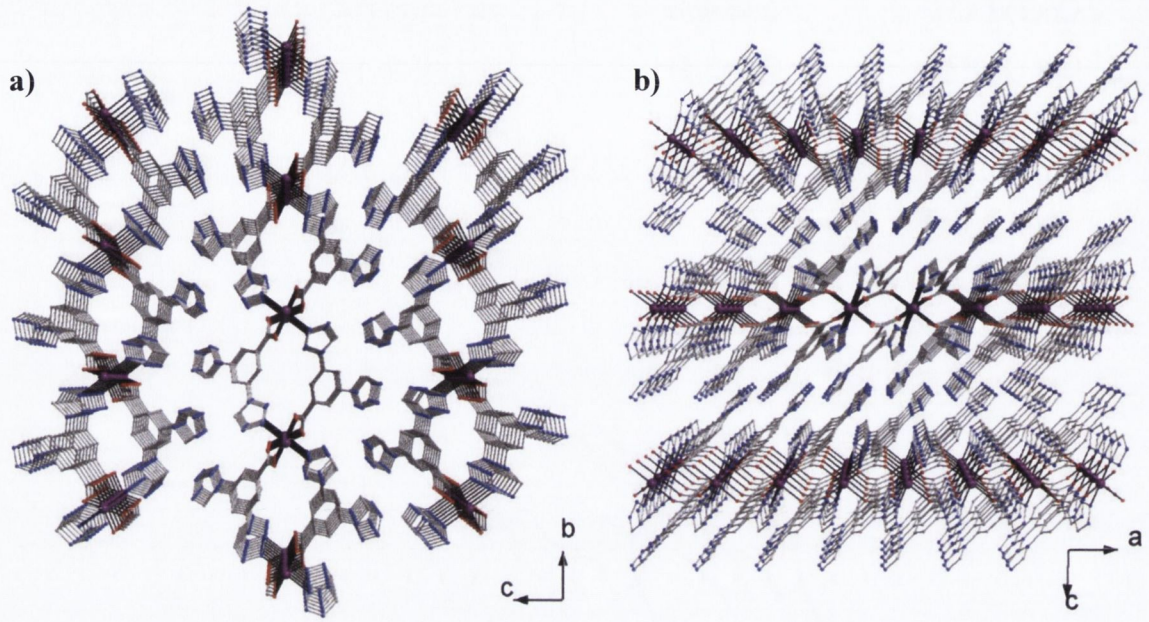


Figure 3.6: The 2D network structure of compound **2** as seen along the crystallographic **a)** *a*-axis, **b)** *b*-axis. Colour code: Co violet, C grey, O red, N blue. H atoms omitted for clarity.

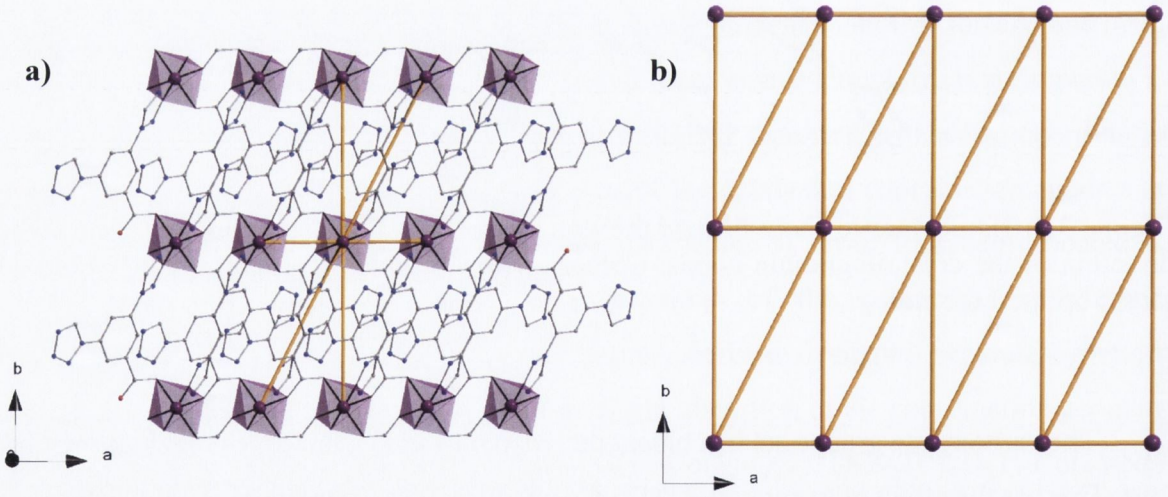


Figure 3.7: a) Simplification model used to generate the, **b)** ($3^6.4^6.5^3$) net topology found in **1**. Colour code: Co violet, C grey, O red, N blue. H atoms omitted for clarity.

Table 3.2: Crystal data and details of the structure determination for **1**.

Identification code	**1**	
Empirical formula	$C_{18}H_{10}N_{16}O_4Co$	
Formula weight	573.32 g mol^{-1}	
Temperature	153(2) K	
Wavelength	0.71075 Å	
Crystal system	Monoclinic	
Space group	$P2_1/c$	
Unit cell dimensions	a = 4.55019(9) Å	α= 90°.
	b = 8.9995(2) Å	β= 92.74(3)°.
	c = 25.014(5) Å	γ= 90°.
Volume	1023.1(4) $Å^3$	
Z	2	
Density (calculated)	1.861 Mg/m^3	
Absorption coefficient	0.912 mm^{-1}	
F(000)	578	
Crystal size	0.3 x 0.2 x 0.2 mm^3	
Theta range for data collection	1.63 to 31.38°.	
Index ranges	$-4\leq h\leq 6$, $-12\leq k\leq 12$, $-35\leq l\leq 36$	
Reflections collected	12235	
Independent reflections	3134 [R(int) = 0.0966]	
Completeness to theta = 31.38°	92.8 %	
Refinement method	Full-matrix least-squares on F^2	
Data / restraints / parameters	3134 / 6 / 178	
Goodness-of-fit on F^2	1.408	
Final R indices [I>2sigma(I)]	R1 = 0.1331, wR2 = 0.3877	
R indices (all data)	R1 = 0.1784, wR2 = 0.4215	
Largest diff. peak and hole	2.303 and -1.390 e.$Å^{-3}$	

3.3.2 Further characterisation of **1**

A freshly filtered sample of **1** was subjected to a PXRD measurement. The resulting powder pattern closely matches that of a simulated pattern calculated from the single crystal diffraction data using the computer programme Mercury, thus confirming the accuracy of the refined crystallography model and the phase-purity of the bulk sample (**Figure 3.8**).[9]

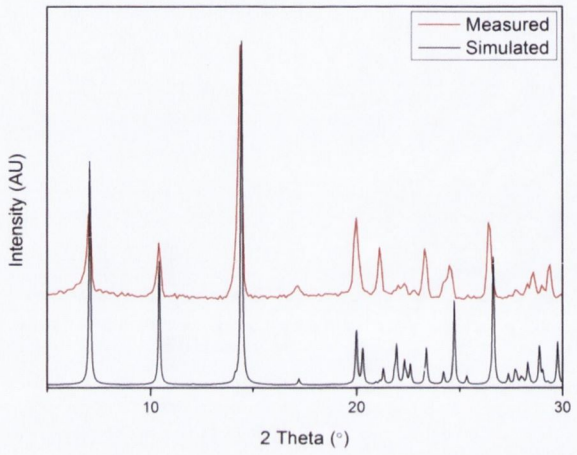


Figure 3.8: PXRD analysis of compound **1**, with the simulated pattern in black and the measured pattern in red.

The IR spectrum of **1** displays a signal at 3115 cm^{-1} arising from aromatic C-H vibrations. Adjacent to this is a band at 1615 cm^{-1} assignable to the C=N stretch of the tetrazole unit. The characteristic asymmetric stretch of a carboxylate group (ν_a(COO)) is present at 1580 cm^{-1}. The overlapping signals at 1415 and 1390 cm^{-1} arise from symmetric (ν_a(COO)) and C-N stretching vibrations, respectively (**Figure 3.9**). The difference between the asymmetric and symmetric stretches, *i.e.* $\Delta\nu = \nu_a - \nu_s$, is 165 cm^{-1}, is indicative of the bidentate bridging carboxylate functionalities found in **1**.[10]

The thermogravimetric analysis (TGA) of compound **1** in an air atmosphere is characterised by two distinct decomposition events (**Figure 3.10**). The layered structure is stable up to 200 °C, upon which there is an initial weight loss of 20% between *ca.* 200 and 300 °C. This is followed by a further weight loss of 55% between approximately 310 and 540 °C due to the oxidative decomposition of the remaining organic material, most likely resulting in inorganic oxides.

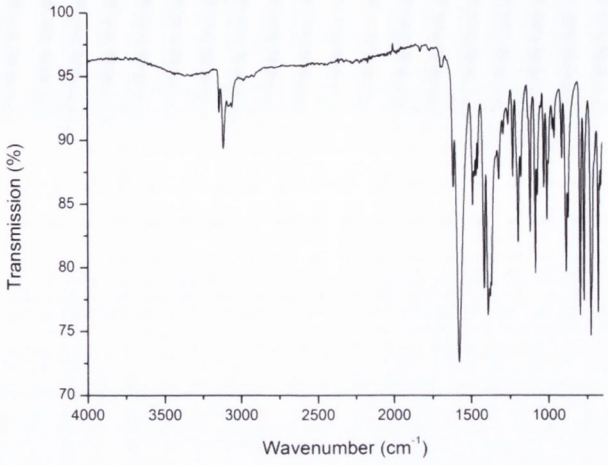


Figure 3.9: IR spectrum of **1**.

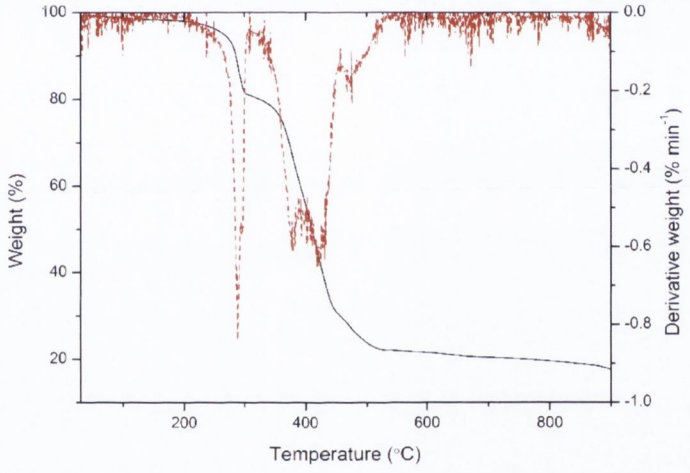


Figure 3.10: TGA of compound **1**, showing the percentage weight loss as a black line and the derivative of the percentage weight loss as the broken red line.

3.4 [Mn(**L1**)], (**2**)

3.4.1 Synthesis and structural characterisation of compound **2**

The manganese coordination compound [Mn(**L1**)$_2$], **2**, forms *via* the solvothermal treatment of $Mn(CH_3COO)_2{\cdot}4H_2O$ and **L1** in a $MeOH/H_2O$ (9:1 ratio, v:v) solution at 115°C. The light brown crystals which form in moderate yield, crystallise in the monoclinic crystal system, in the space group $P2_1/c$.

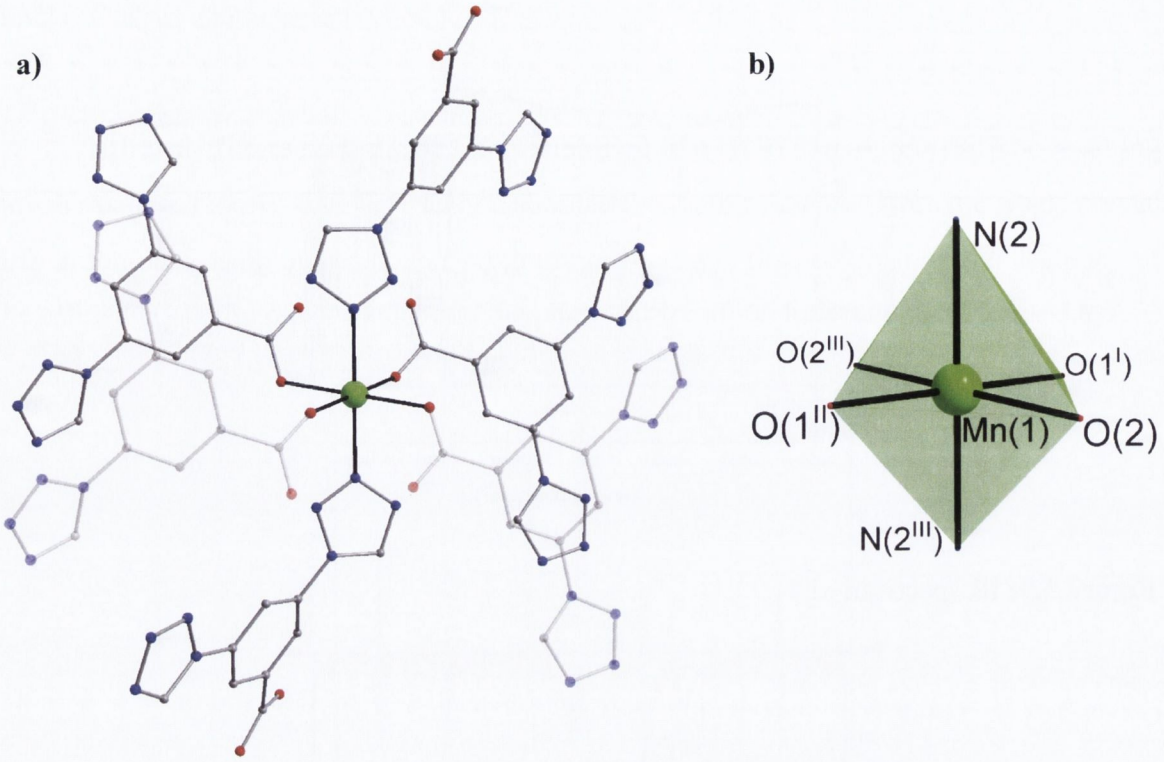


Figure 3.11: a), b) Mn^{II} coordination environment in **2**. Symmetry codes: (I) -1 + x, y, z, (II) 3-x, 2- y, z, (III) 2- x, 2- y,- z. Colour code: Mn green, C grey, O red, N blue. H atoms omitted for clarity.

The structure of **2** contains one symmetry independent Mn^{II} ion and one organic ligand. The coordination environment of the Mn^{II} ions in compound **2** are comparable to that of the Co^{II} ions found in **1**. Each individual Mn^{II} centre adopts an octahedral coordination geometry, whereby each metal ion is coordinated to six donor atoms that are derived from six distinct deprotonated **L1** ligands (**Figure 3.11**). Further similarities to **1** arise as the four equatorial positions of the octahedral coordination sphere are provided by carboxylate O-donors, but with longer bond lengths than those found in **1** (Mn(1)-O(1) = 2.113(3) Å and Mn(1)-O(2) = 2.174(3) Å). As observed in **1**, the axial positions are provided by tetrazole N-donors, (Mn(1)-N(2) = 2.282(3) Å), which correspond to previously reported Mn-N bond lengths.[11] The bond angle $O(1^I)$-Mn(1)-O(2) of 87.07(1)° closely resembles the ideal bond angle of 90°, likewise the $O(1^I)$-Mn(1)-N(2) angle of 87.31(1) is close to the ideal value of 90°. A more detailed list of bond angles and lengths can be found in **Table 3.3**.

Table 3.3: Selected bond distances and angles for **2**. Symmetry codes: (I) -1 + x, y, z, (II) 3-x, 2- y, z, (III) 2- x, 2- y,- z.

Atoms	Distance (Å)	Atoms	Angle(°)
Mn(1)-O(1)	**2.113(3)**	$O(1^{I})$-Mn(1)-O(2)	**87.07(1)**
Mn(1)-O(2)	**2.174(3)**	$O(1^{I})$-Mn(1)-$O(2^{III})$	**92.93(1)**
Mn(1)-N(2)	**2.282(3)**	$O(1^{I})$-Mn(1)-N(2)	**92.69 (1)**
		O(1)-Mn(1)-$N(2^{III})$	**87.31(1)**
		O(2)-Mn(1)-N(2)	**91.02(1)**
		O(2)-Mn(1)-$N(2^{III})$	**88.98(1)**

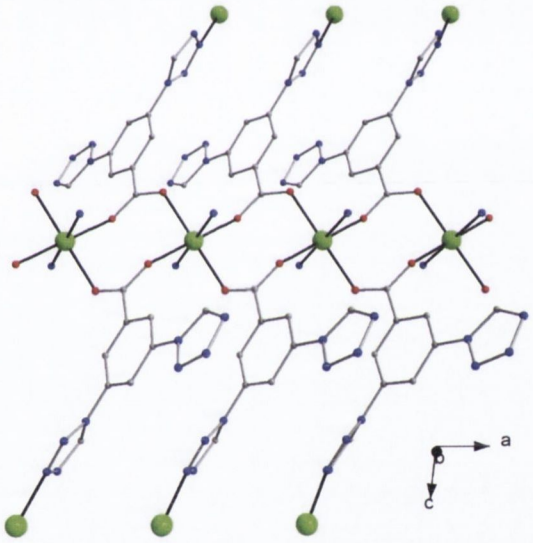


Figure 3.12: 1D polymeric Mn-Mn chain formed through carboxylate groups acting in a bidentate syn-syn μ_2 bridging mode. Colour code: Mn green, C grey, O red, N blue. H atoms omitted for clarity.

Additional similarities with **1** arises as the carboxylate functionalities of **L1** act in a bidentate *syn-syn* μ_2 mode, bridging neighbouring Mn^{II} ions to generate infinite 1D Mn-Mn chains which extend in the direction of the crystallographic *a*-axis and display interatomic Mn···Mn distances of 4.63 Å (**Figure 3.12**). However, unlike for compound **1** where the tetrazole moieties link neighbouring chains into 2D sheets, the tetrazole moieties in **2** link the polymeric Mn-Mn chains in approximately the *b* and *c* directions, to produce a densely packed 3D coordination network (**Figure 3.13** and **Figure 3.14**). The overall network structure is generated through symmetry operations, with each Mn^{II} ion being situated on an

inversion centre. The symmetry of the structure is characterised by a 2_1 screw axis running parallel to the [010] direction. By envisaging each Mn^{II} ion as a ten connecting node it is possible to simplify the network topology with the Schläfli symbol ($3^{12}.4^{28}.5^5$) (**Figure 3.15**).

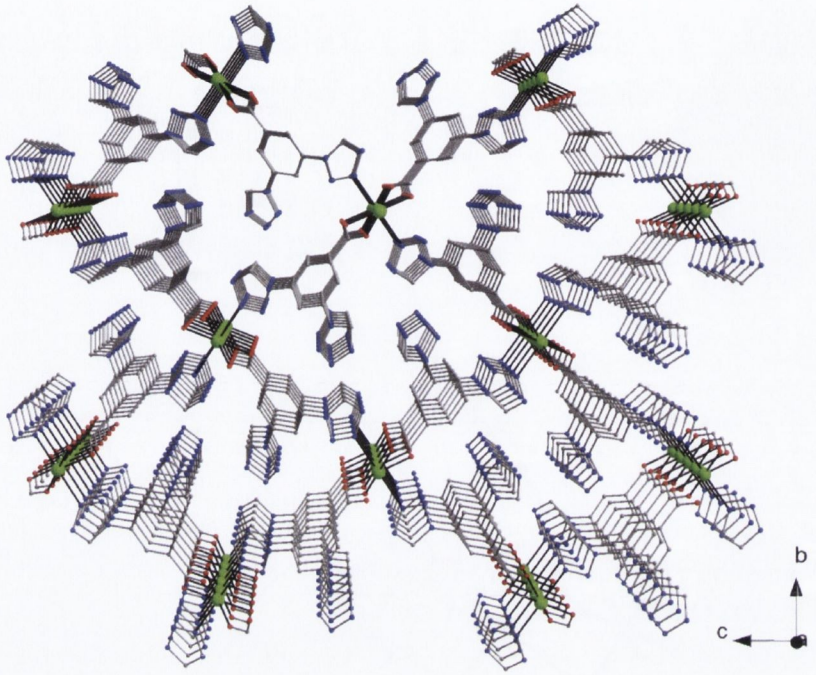


Figure 3.13: The network structure of compound **2** as seen along the crystallographic *a*-axis. Colour code: Mn green, C grey, O red, N blue. H atoms omitted for clarity.

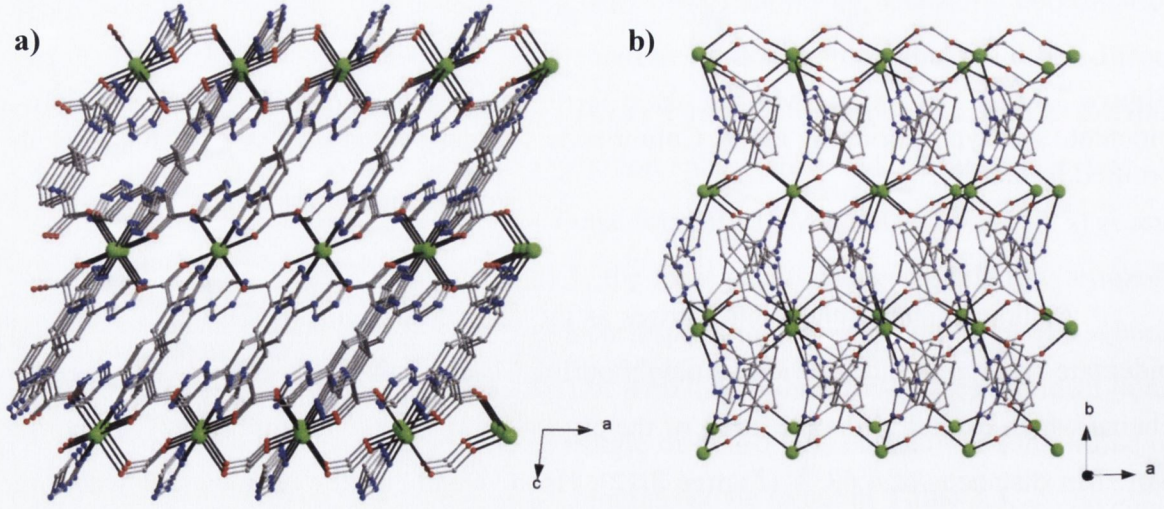


Figure 3.14: The network structure of **2** as viewed along the crystallographic **a)** *b*-axis, **b)** *c*-axis. H atoms omitted for clarity. Colour code: Mn green, C grey, O red, N blue. H atoms omitted for clarity.

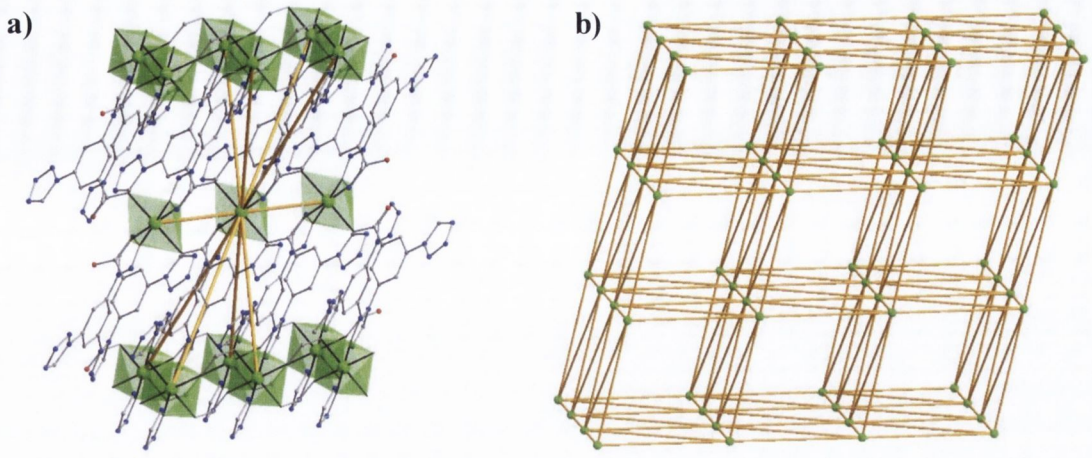


Figure 3.15: a) Simplification model used to generate the net topology found in **2**, whereby each Co^{II} ion is visualised as a ten connecting node, **b)** ($3^{12}.4^{28}.5^5$) net topology found in **2**. Colour code: Mn green, C grey, O red, N blue. H atoms omitted for clarity.

Table 3.4: Crystal data and details of the structure determination for **2**.

Identification code	**2**	
Empirical formula	$C_{18}H_{10}N_{16}O_4Mn$	
Formula weight	569.32 g mol^{-1}	
Temperature	153 (2) K	
Wavelength	0.71073 Å	
Crystal system	Monoclinic	
Space group	$P2_1/c$	
Unit cell dimensions	a = 4.6286(9) Å	α= 90°.
	b = 13.441(3) Å	β= 96.08(3)°.
	c = 16.632(3) Å	γ= 90°.
Volume	1028.9(4) $Å^3$	
Z	2	
Density (calculated)	1.838 Mg/m^3	
Absorption coefficient	0.715 mm^{-1}	
F(000)	574	
Crystal size	0.5x 0.4 x 0.2 mm^3	
Theta range for data collection	1.95 to 31.33°.	
Index ranges	$-4\leq h\leq 6$, $-18\leq k\leq 17$, $-24\leq l\leq 23$	
Reflections collected	11609	
Independent reflections	3106 [R(int) = 0.0468]	
Completeness to theta = 31.33°	91.8 %	
Refinement method	Full-matrix least-squares on F^2	
Data / restraints / parameters	3106 / 0 / 178	
Goodness-of-fit on F^2	1.205	
Final R indices [I>2sigma(I)]	R1 = 0.0652, wR2 = 0.1893	
R indices (all data)	R1 = 0.0919, wR2 = 0.2462	
Largest diff. peak and hole	0.979 and -1.412 e.$Å^{-3}$	

3.4.2 Further characterisation of **2**

The phase purity of the bulk sample was confirmed by comparing the measured PXRD pattern of a freshly filtered sample of compound **2** and the powder pattern simulated from the single crystal XRD data (**Figure 3.16**). The closely matching patterns indicate that it is a phase-pure sample and endorses the accuracy of the refined crystallographic model.

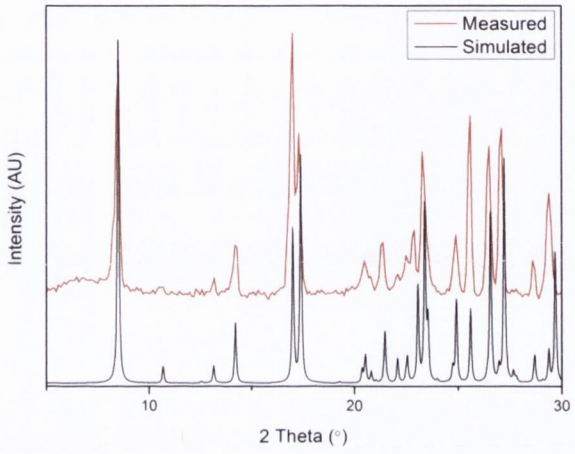


Figure 3.16: PXRD analysis of compound **2**, with the simulated pattern in black and the measured pattern in red.

Analysis of the IR spectrum of **2** reveals an initial band at 3125 cm^{-1} resulting from the aromatic C-H stretching vibrations. Adjacent to this is the signal characteristic of the C=N tetrazole stretch at 1615 cm^{-1}. The asymmetric stretching frequency of the deprotonated carboxylate group, ν_a(COO), is found at 1575 cm^{-1}, with the symmetric stretch ,ν_s(COO), at 1413 cm^{-1} (**Figure 3.17**). The difference between the asymmetric and symmetric stretches was found to be 162 cm^{-1} and is in the range expected for bridging carboxylate functionalities.[10] A C-N stretching vibration is present at 1380 cm^{-1}.

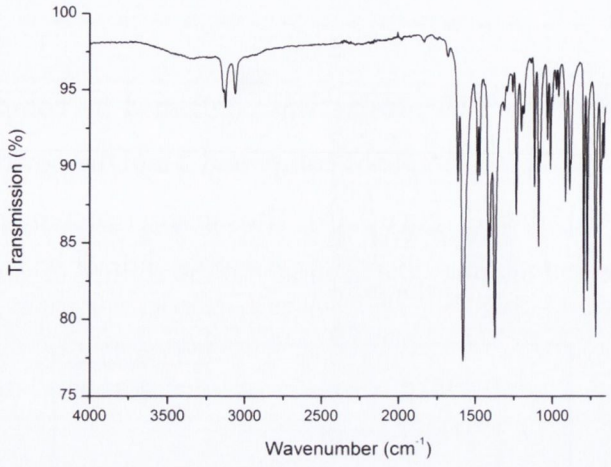


Figure 3.17: IR spectrum of compound **2**.

TGA of **2** was performed in an air atmosphere and shows the framework decomposing at approximately 240 °C, with a weight loss of 71% (**Figure 3.18**). The degradation of the framework above 270 °C is characterised by a further weight loss of 20% between 300 °C and 490 °C due to the oxidation of the remaining organic material, with the end product most likely being manganese oxide. The combined decomposition values of *ca.* 93% corresponds to the combustion of the organic ligand (theoretical 91%).

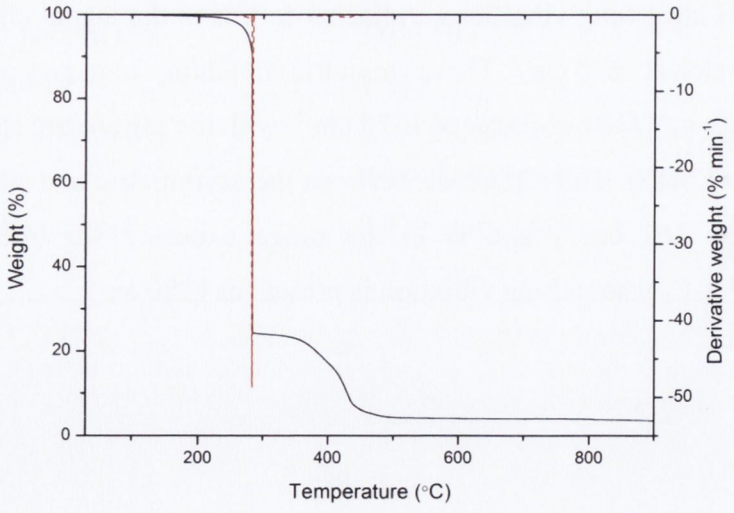


Figure 3.18: TGA of compound **2**, showing the percentage weight loss as a black line and the derivative of the percentage weight loss as the broken red line.

3.5 [Cd(**L2**)$_2$(MeOH)], (**3**)

Having noticed in the previously described structures that only one of the two tetrazole groups on each ligand was involved in coordination bonding, we decided to modify the ligand by substituting one of the tetrazole groups with a carboxylic acid group to create **L2**. The first compound which we synthesised with **L2** was [Cd(**L2**)$_2$(MeOH)], **3**.

3.5.1 Synthesis and structural characterisation of compound **3**

The solvothermal treatment of $Cd(NO_3)_2 \cdot 4H_2O$ and **L2** in a MeOH/H_2O (in a 8:3 ratio, v:v) solution at 100 °C afforded small pale yellow rectangular crystals. Upon single crystal XRD analysis it was revealed that **3** crystallises in the monoclinic crystal system in the space group $P2_1/c$.

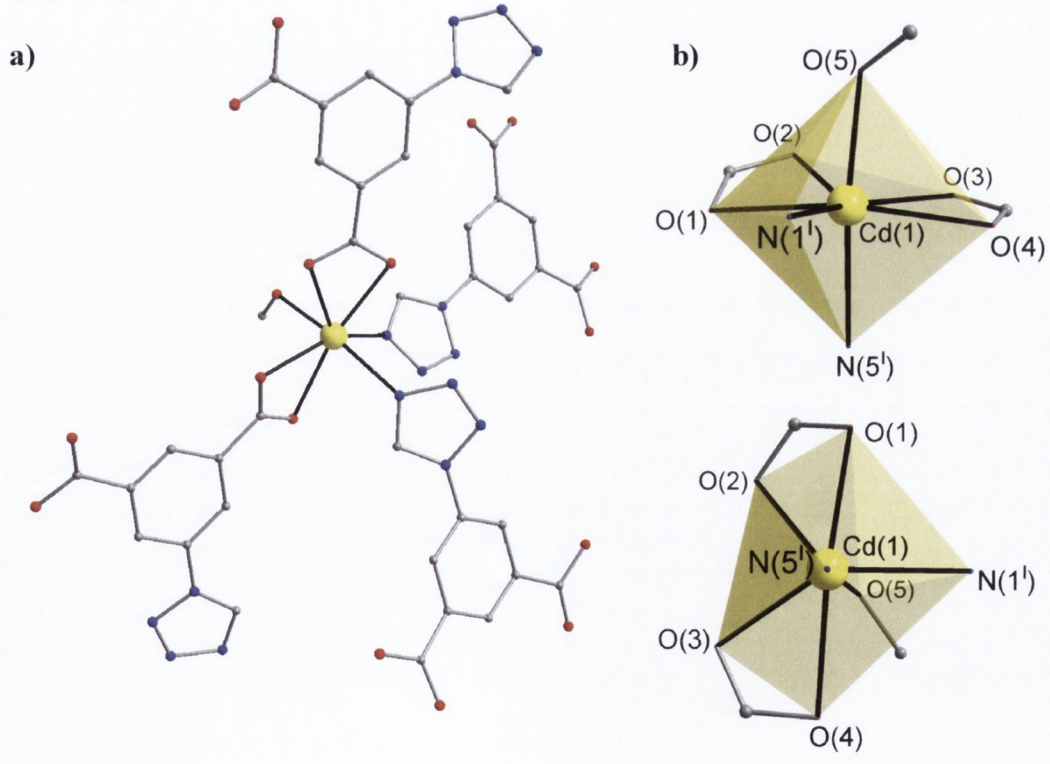


Figure 3.19: a) The Cd^{II} centre coordinated to four **L2** ligands and one MeOH molecule, **b)** the Cd^{II} coordination environment in **3** as seen from two separate viewpoints. Symmetry codes: (I) 1- x, -0.5 + y, 1.5 –z, (II) –x, 0.5 + y, 1.5 – z. Colour code: Cd yellow, C grey, O red, N blue. H atoms omitted for clarity.

The asymmetric unit of **3** contains one Cd^{II} ion, two partially deprotonated organic ligands and a single MeOH ligand. Through symmetry operations a 2D coordination network is formed which is composed of mononuclear secondary building units. The coordination environment of each individual Cd^{II} centre can best be described as being that of a highly distorted hepta-coordinated geometry (**Figure 3.19**). The distorted nature of the coordination environment can be explained by the lack of ligand field stabilisation energy of the d^{10} metal centre and its coordination behaviour resembles that of group 2 structures. Each metal centre is coordinated by four **L2** ligands and one MeOH ligand. The carboxylate functionalities of two **L2** ligands chelate the Cd^{II} centre. A further two **L2** ligands bind through the N-donors of their tetrazole functionalities to Cd(1). The coordination environment is completed by a MeOH ligand. Each **L2** ligand in turn binds to two separate Cd^{II} centres, through a chelating carboxylate group to one metal centre and *via* a tetrazole N-donor to a second Cd^{II} ion. The remaining carboxylate group is not involved in bonding and remains protonated.

This distortion leads to significantly different bond lengths for the chelating O donors of the carboxylate groups. The carboxylate O donors O(3) and O(4) reveal Cd-O bond lengths of 2.336(2) Å and 2.484(1) Å, respectively, with the remaining carboxylate O-donors O(1) and O(2) displaying respective Cd-O bond lengths of 2.322(1) Å and 2.413(4) Å. The MeOH O-donor has a shorter Cd-O bond length of 2.303(3) Å. Finally, the tetrazole N donors $N(1^{I})$ and $N(5^{I})$ display Cd-N bond lengths of 2.397(2) and 2.352(3) Å. These bond lengths are similar to previously reported structures that compromise of Cd^{II} ions with distorted hepta-coordinated geometries and similar N- and O- donor ligands.[2,12] A more detailed list of bond lengths and angles can be found in **Table 3.5**.

Table 3.5: Selected bond distances and angles for **3**. Symmetry codes: (I) 1- x, -0.5 + y, 1.5 –z, (II) –x, 0.5 + y, 1.5 – z.

Atoms	Distance (Å)/ Angle (°)	Atoms	Angle(°)
Cd(1)-O(1)	**2.413(3)**	O(2)-Cd(1)-O(3)	**82.99(9)**
Cd(1)-O(2)	**2.322(3)**	O(2)-Cd(1)-O(4)	**135.74(9)**
Cd(1)-O(3)	**2.336(3)**	O(2)-Cd(1)-O(5)	**80.63(1)**
Cd(1)-O(4)	**2.484(3)**	O(2)-Cd(1)-$N(1^{I})$	**128.58(1)**
Cd(1)-O(5)	**2.302(3)**	O(2)-Cd(1)-$N(5^{I})$	**118.46(1)**
Cd(1)-$N(1^{I})$	**2.397(3)**	O(3)-Cd(1)-O(5)	**89.27(1)**

Cd(1)-N(5^{I})	**2.352(3)**	O(3)-Cd(1)-N(1^{I})	**145.01(1)**
		O(3)-Cd(1)-N(5^{I})	**96.68(1)**
O(1)-Cd(1)-O(3)	**133.62(9)**	O(4)-Cd(1)-O(5)	**88.31(1)**
O(1)-Cd(1)-O(4)	**168.13(9)**	O(4)-Cd(1)-N(1^{I})	**91.65(1)**
O(1)-Cd(1)-O(5)	**100.23(1)**	O(4)-Cd(1)-N(5^{I})	**80.39(1)**
O(1)-Cd(1)-N(1^{I})	**81.37(2)**	O(5)-Cd(1)-N(5^{I})	**160.5(1)**
O(1)-Cd(1)-N(5^{I})	**89.07(1)**		

As in the previously described compounds, the symmetry of the structure is defined by 2_1 screw axes which extends parallel to the [010] direction, to generate 2D sheets that extend in the *ab* plane (**Figure 3.20**).

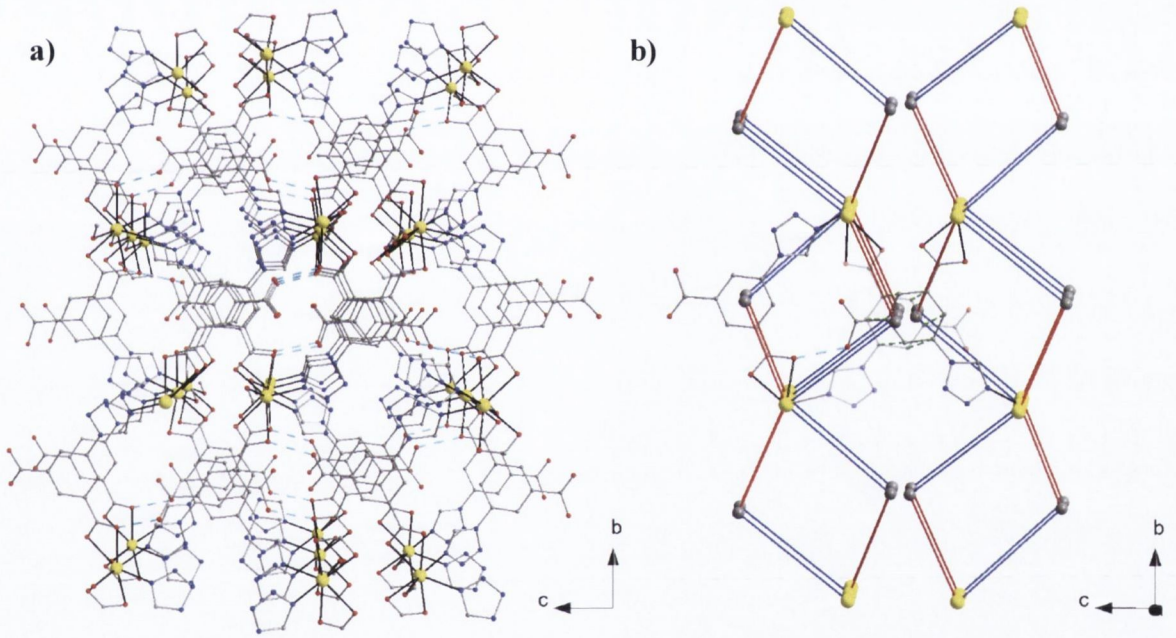


Figure 3.20: a) Packing structure of **3** as seen along the crystallographic *a*-axis, **b)** Simplified representation of the packing structure in **3**, with the bonds generated through carboxylate groups represented as red lines and the bonds generated *via* tetrazole groups represented by blue lines. Colour code: Cd yellow, C grey, O red, N blue. H atoms omitted for clarity.

The 3D supramolecular structure is assembled through hydrogen bonding interactions present between the protonated acid functionalities that point in the *c*-direction and the oxygen atoms of the coordinated carboxylate moieties on neighbouring sheets (**Figure 3.20** and **Figure 3.21**). These H-bonding interactions are characterised by a O(1)···O(6') distance of 2.619(2) Å. Furthermore, there are intermolecular π-π stacking

interactions between adjacent sheets, with an average distance of *ca.* 3.48 Å between the adjoining aromatic rings of neighbouring layers (**Figure 3.19** and **Figure 3.21**). The network structure can be simplified as an infinite 2D net with a $(4^4.6^2)$ Schläfli symbol, whereby each Cd^{II} ion is considered as a four-connecting node (**Figure 3.22**).

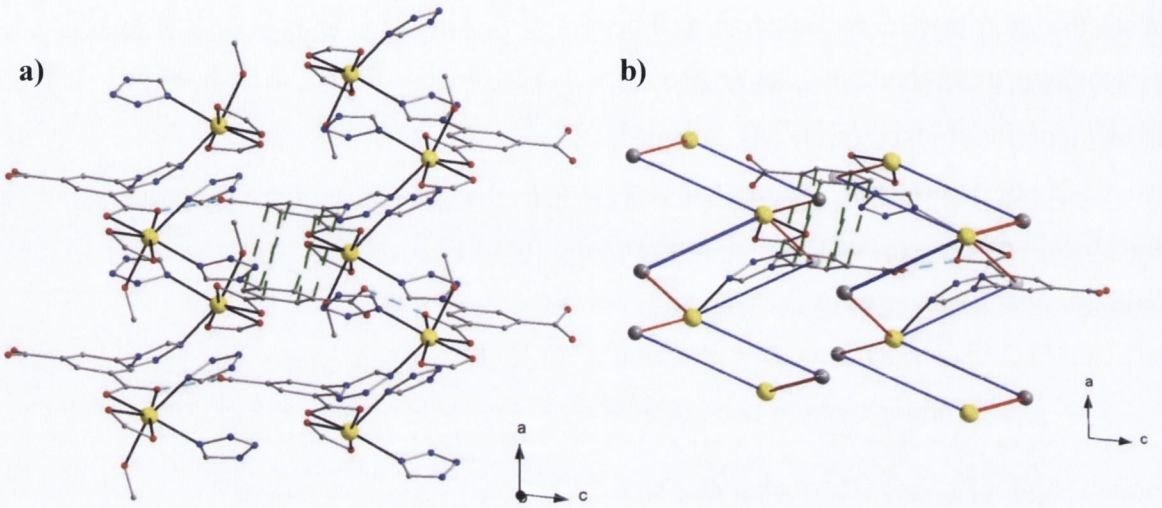


Figure 3.21: a) Packing structure of **3** viewed in the direction of the crystallographic *b*-axis, **b)** Simplified representation of the packing structure in **3**, with the bonds generated through carboxylate groups represented as red lines and the bonds generated *via* tetrazole groups represented by blue lines. Colour code: Cd yellow, C grey, O red, N blue. π-π stacking interactions are represented as dashed green lines and hydrogen bonding is denoted as dashed cyan lines. H atoms omitted for clarity.

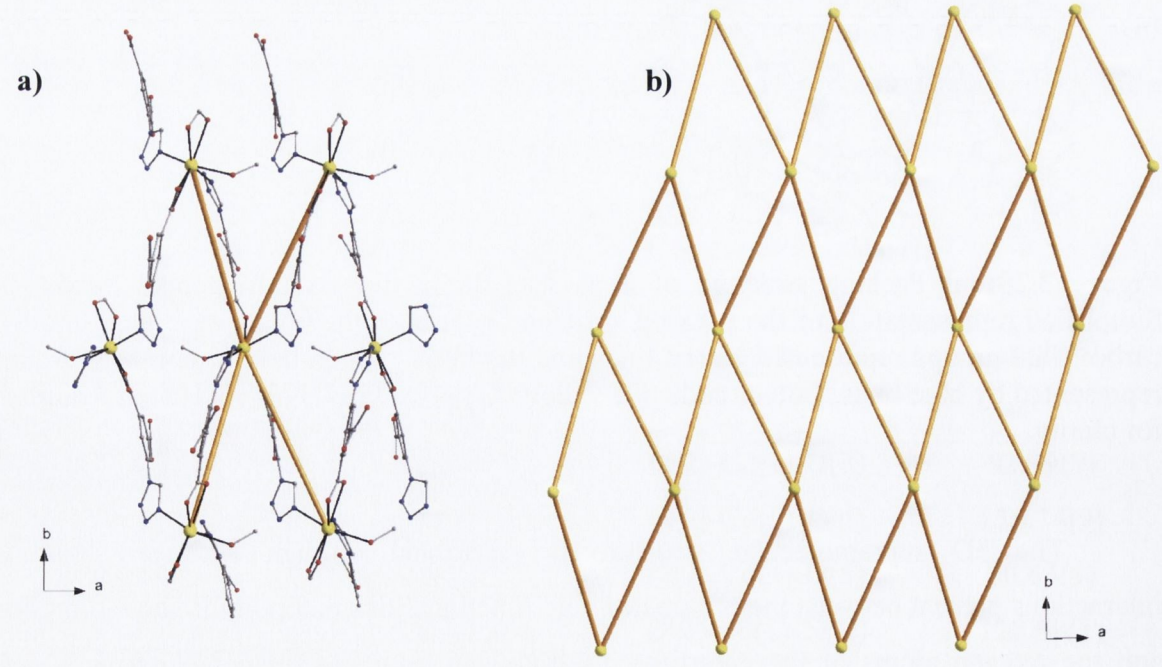


Figure 3.22: a) Simplification model where each Cd^{II} ion is considered as a four-connecting node, **b)** $(4^4.6^2)$ network found in **3**.

Table 3.6: Crystal data and details of the structure determination for **3**.

Identification code	**3**	
Empirical formula	$C_{19}H_{11}N_8O_9Cd$	
Formula weight	607.77 g mol^{-1}	
Temperature	150(2) K	
Wavelength	0.71073 Å	
Crystal system	Monoclinic	
Space group	$P2_1/c$	
Unit cell dimensions	a = 7.0515(1) Å	α= 90°.
	b = 18.422(4) Å	β= 96.66(3)°.
	c = 16.355(3) Å	γ= 90°.
Volume	2110.2(7) $Å^3$	
Z	4	
Density (calculated)	1.913 Mg/m^3	
Absorption coefficient	1.110 mm^{-1}	
F(000)	1204	
Crystal size	0.6x 0.3 x 0.2 mm^3	
Theta range for data collection	1.67 to 25.14°.	
Index ranges	$-8\leq h\leq 8$, $-21\leq k\leq 21$, $-13\leq l\leq 19$	
Reflections collected	11967	
Independent reflections	3759 [R(int) = 0.0400]	
Completeness to theta = 25.14°	99.4 %	
Refinement method	Full-matrix least-squares on F^2	
Data / restraints / parameters	3759 / 0 / 329	
Goodness-of-fit on F^2	1.047	
Final R indices [I>2sigma(I)]	R1 = 0.0366, wR2 = 0.0867	
R indices (all data)	R1 = 0.0433, wR2 = 0.0893	
Largest diff. peak and hole	0.741 and -0.521 $e.Å^{-3}$	

3.5.2 Further characterisation of **3**

The synthesis of compound **3** produces large yellow block shaped crystals, together with a microcrystalline material. As a result of this it was necessary to manually separate the block crystals from the microcrystalline material prior to PXRD measurements. The measured PXRD pattern of **3** correlates generally very well with a simulated pattern, with a small reflection present at 9.1° indicating a slight impurity in the crystalline sample most likely resulting from the presence of small quantities of the microcrystalline material (**Figure 3.23**). However, it is worth mentioning that elemental analysis and TGA (which is discussed below) of the bulk sample fit very well for this compound indicating a high level of purity, which can be obtained reproducibly in a good yield. This suggests that the block crystals and the microcrystalline material are composed of the same compound, with slight differences in their respective crystalline phases.

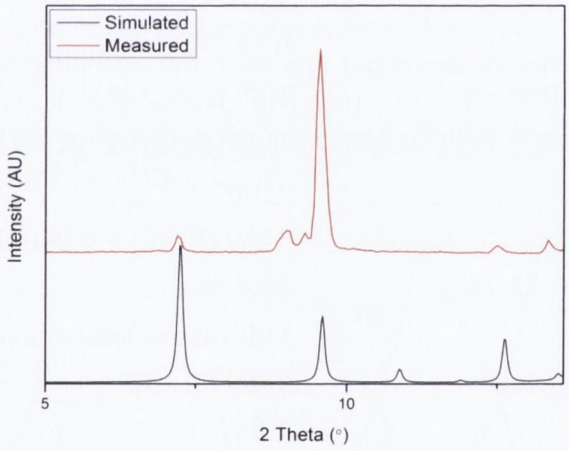


Figure 3.23: PXRD analysis of compound **3**, with the simulated pattern in black and the measured pattern in red.

The IR spectrum of compound **3** reveals further evidence of hydrogen bonding with a broad band centred at 3150 cm^{-1} (**Figure 3.24**). The presence of a signal at 1704 cm^{-1} is indicative of the protonated carboxylic acid group found in **3**. In addition the bands at 1550 and 1427 cm^{-1}, are typical of the asymmetric and symmetric stretches of the chelating carboxylate groups present in **3**.[10] The characteristic vibrations of the tetrazole C=N and C-N stretches are found at 1615 and 1377 cm^{-1}, respectively.

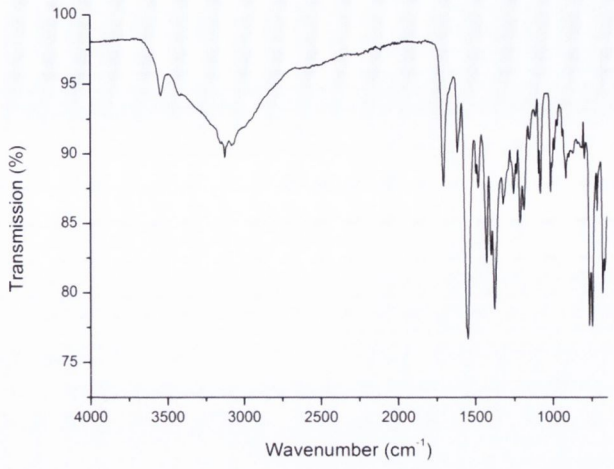


Figure 3.24: IR spectrum of **3**.

Compound **3** remains stable under thermal treatment until 180 °C. A thermogravimetric step between 180 and 220 °C results in a weight loss of 6% which can be attributed to the loss of the coordinated MeOH molecules (theoretical 5%) (**Figure 3.25**). This process is followed by the two-step decomposition of the ligand **L2**, between 220 and 550 °C (actual 74%, theoretical 76%), with the most likely end product being cadmium oxide.

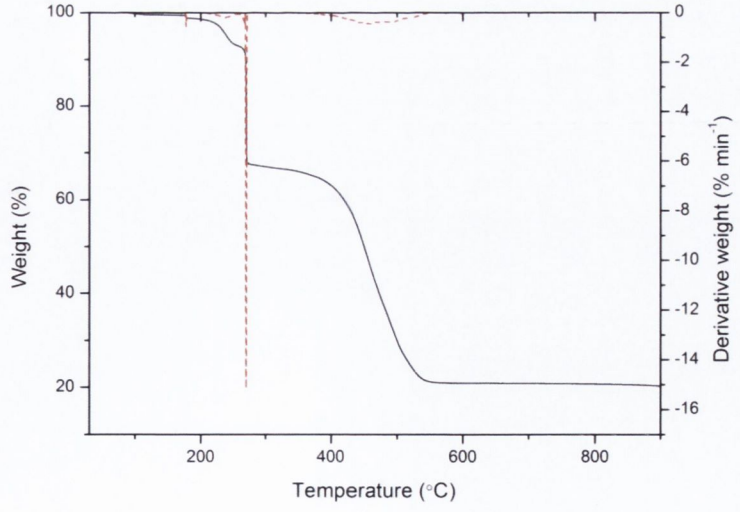


Figure 3.25: TGA of compound **3**, showing the percentage weight loss as a black line and the derivative of the percentage weight loss as the broken red line.

3.6 [Zn(**L2**)(H_2O)$_2$], (**4**)

Following on from compound **3**, it was decided to explore Zn^{II} ions to potentially generate SBUs. However, the necessary reaction conditions to synthesise $[Zn(\mathbf{L2})(H_2O)_2]$, **(4)**, were significantly different to those found in **3**.

3.6.1 Synthesis and structural characterisation of compound 4

The reaction of $Zn(NO_3)_2 \cdot 6H_2O$ and **L2** in a H_2O/KOH solution at 85 °C, yielded colourless crystals of the novel MOF $[Zn(\mathbf{L2})(H_2O)_2]$, **4**, which crystallises in the orthorhombic space group *P*nma. The network is composed of two symmetry independent Zn^{II} metal ions, four water molecules and two ligand molecules, with the resulting 3D MOF generated through symmetry operations.

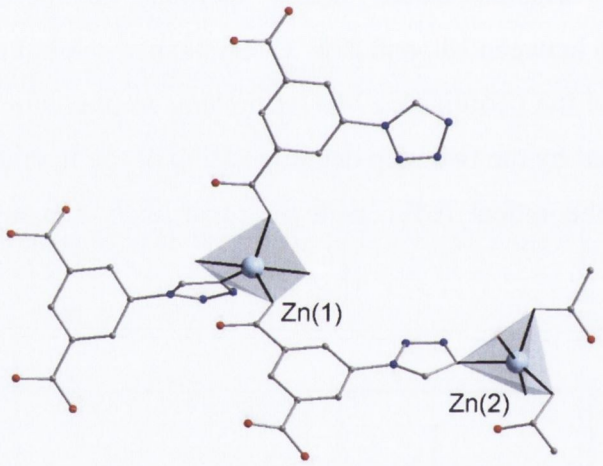


Figure 3.26: The two crystallographically unique trigonal bipyramidal Zn^{II} centres (Zn(1) and Zn(2)). Colour code: Zn pale blue, C grey, O red, N blue.

The overall coordination environment of each Zn(1) metal centre is that of a distorted trigonal bipyramid, with each individual Zn(1) ion being coordinated to three separate **L2** ligands and two water molecules to generate a mononuclear Zn^{II} SBU (**Figure 3.26**). The three equatorial positions of Zn(1) are provided by two carboxylate oxygen atoms (O(3) and O(3^{I})) and one tetrazole N-donor (N(1)), with two water molecules (O(1) and O(2)) furnishing the two axial positions. The distortion from the ideal trigonal bipyramidal geometry is most clearly demonstrated by examining the coordination bond angles, with the

angles of O(3)-Zn(1)-N(1) (125.56°) and O(3)-Zn(1)-O(3^{I}) (108.8°) differing from the ideal angle between equatorial donors of 120°. However, the angle between the two axial water molecules positions (O(1)-Zn(1)-O(2)) of 178.94° closely resembles the ideal angle of 180°. Likewise, the angles O(1)-Zn(1)-N(1) and O(1)-Zn(1)-O(3), 94.16(1) and 86.39(1)° respectively, are close to the angle expected between axial and equatorial positions of 90°. The Zn(1) bond lengths found in **4** are in the range of other previously published trigonal bipyramidal Zn^{II} coordination compounds.[13,14]

Zn(2) exhibits a distorted coordination environment between that of a trigonal bipyramid and a square based pyramid. Like Zn(1), Zn(2) is coordinated to two unidentate carboxylate functionalities (O(5) and O(6)), a tetrazole N-donor (N(5)) and to two water molecules (O(7) and O(8)). The angles of O(5)-Zn(2)-N(5) (103.62(1)) and O(6)-Zn(2)-N(5) (135.47(1)) differ noticeably from the ideal angle of 120°. The distortion results in a relatively high Zn-O(7) bond length of 2.240(3) Å, and a more detailed list of bond lengths and angles can be found in **Table 3.7**.

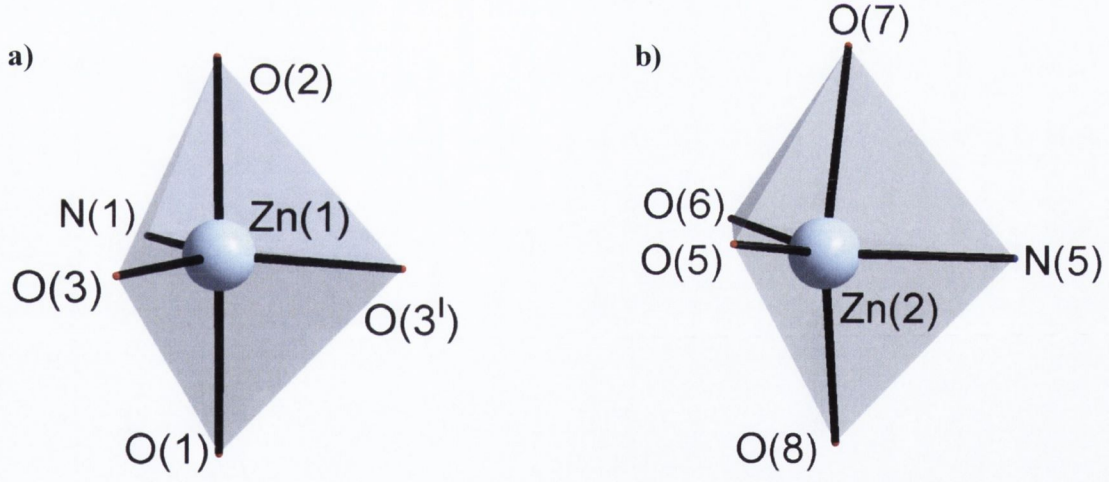


Figure 3.27: The coordination environment of **a)** Zn(1) and **b)** Zn(2). Symmetry code: (I) x, 1.5-y, z. Colour code: Zn pale blue, C grey, O red, N blue.

Table 3.7: Selected bond distances and angles for **4**. Symmetry code: (I) x, 1.5-y, z.

Atoms	Distance (Å)/ Angle (°)	Atoms	Angle(°)
Zn(1)-O(1)	**2.146(4)**	O(1)-Zn(1)-O(3)	**86.39(1)**
Zn(1)-O(2)	**2.145(4)**	O(1)-Zn(1)-N(1)	**94.16(1)**
Zn(1)-O(3)	**1.990(3)**	O(2)-Zn(1)-O(3)	**94.27(2)**
Zn(1)-N(1)	**2.018(5)**	O(2)-Zn(1)-N(1)	**85.66(2)**
		O(3)-Zn(1)-N(1)	**125.56(1)**
O(1)-Zn(1)-O(2)	**178.86(2)**	O(3)-Zn(1)-O(3^{I})	**108.8(3)**
Zn(2)-O(5)	**1.990(3)**	O(5)-Zn(2)-O(8)	**101.33(1)**
Zn(2)-O(6)	**2.005(3)**	O(5)-Zn(2)-N(5)	**103.62(1)**
Zn(2)-O(7)	**2.240(3)**	O(6)-Zn(2)-O(7)	**83.47(1)**
Zn(2)-O(8)	**2.037(3)**	O(6)-Zn(2)-O(8)	**95.32(1)**
Zn(2)-N(5)	**2.088(3)**	O(6)-Zn(2)-N(5)	**135.47(1)**
		N(5)-Zn(2)-O(7)	**84.94(1)**
O(5)-Zn(2)-O(6)	**119.67(1)**	N(5)-Zn(2)-O(8)	**87.57(1)**
O(5)-Zn(2)-O(7)	**89.64(1)**	O(7)-Zn(2)-O(8)	**167.89(1)**

As was previously stated, each Zn^{II} metal centre is coordinated to three deprotonated **L2** ligands and each ligand in turn is coordinated to three separate Zn^{II} ions, with the tetrazole functionality and the two carboxylate groups all coordinating in a monodentate mode, to generate a 3D MOF (**Figure 3.28**). The network topology of **4** contains two different nodes, with each individual Zn^{II} ion and the phenyl units of **L2** acting as three connecting nodes, giving a $(6.10^2)(6.12^2)$ Schläfli symbol (**Figure 3.30** and **Figure 3.31**).

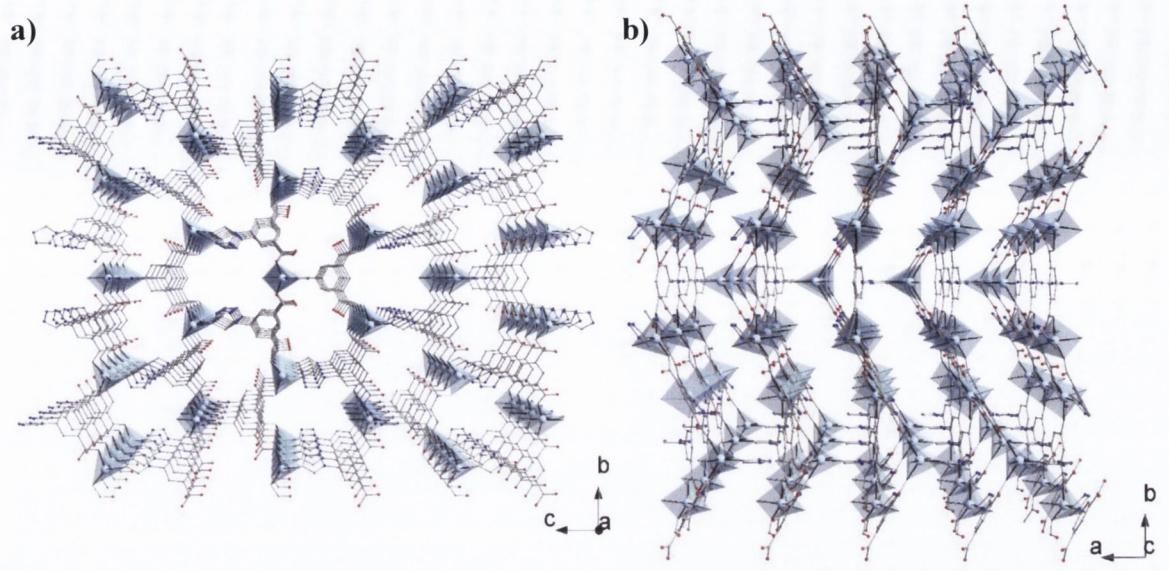


Figure 3.28: Network structure of **4** as seen along the crystallographic **a)** *a*-axis and **b)** *c*-axis. Colour code: Zn pale blue, C grey, O red, N blue. H atoms omitted for clarity.

The structure however, is composed of dual interpenetrating frameworks, resulting in an overall densely packed structure. (**Figure 3.29**). The catenation is facilitated by hydrogen bonding interactions between coordinated water molecules and carboxylate oxygen atoms from an adjacent framework, with O-O distances of 2.84 and 3.03 Å (**Figure 3.29**). Furthermore, there are weak π-π stacking interactions between the phenyl moieties of the ligands on adjacent frameworks that are characterised by a distance of 3.97 Å between the centres of the aromatic rings (**Figure 3.29** and **Figure 3.30**).

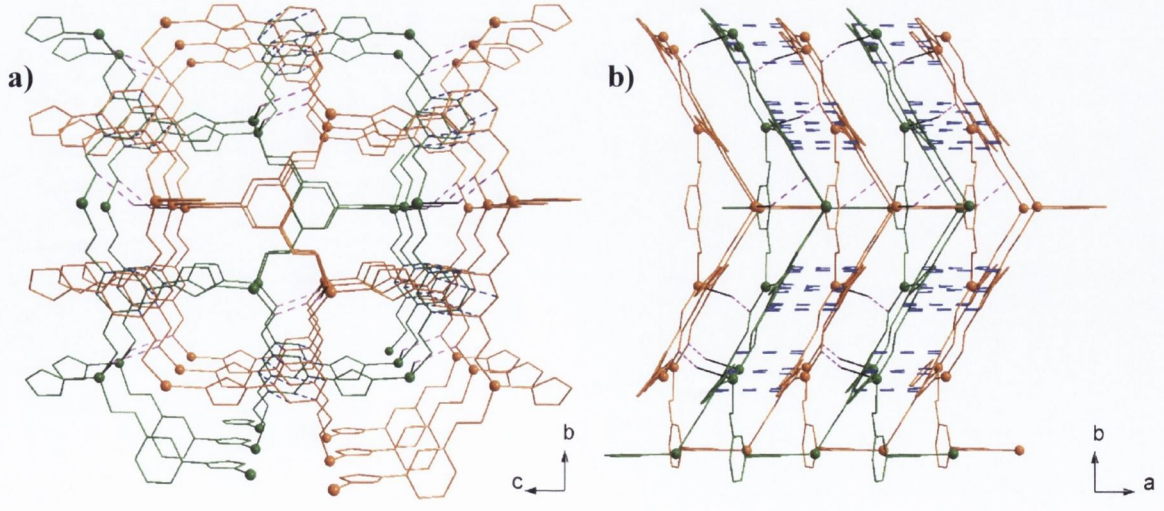


Figure 3.29: Interpenetrated structure in **4**, with the separate networks coloured differently for clarity, as seen along the **a)** *a*-axis, **b)** *b*-axis. The larger green and orange atoms denote

the Zn^{II} centres. Dashed blue lines represent π-π stacking interactions and the dashed pink lines represent hydrogen bonding interactions between adjacent networks.

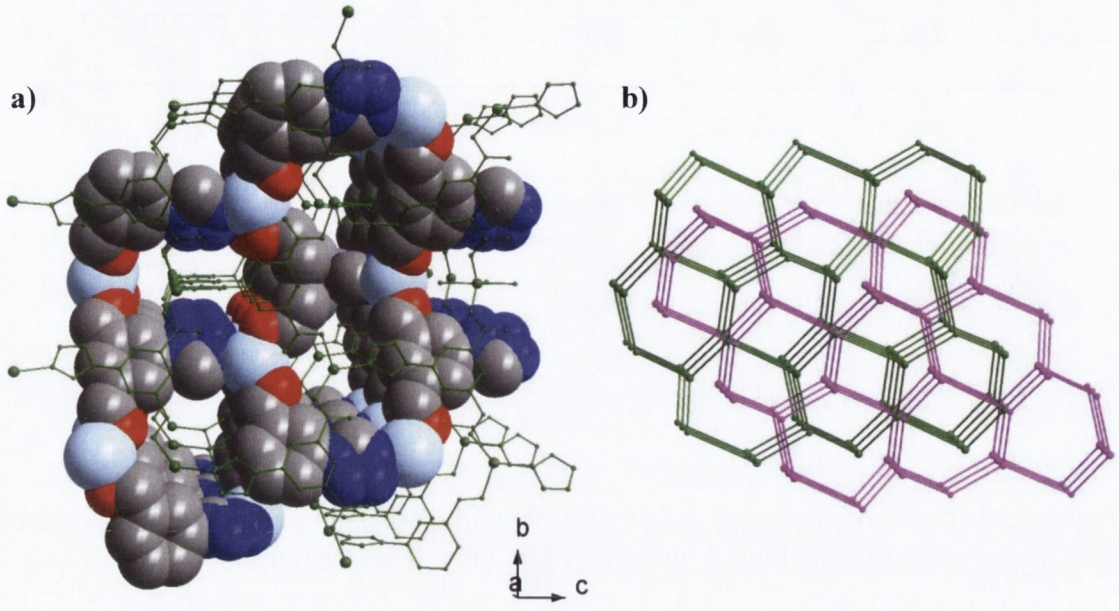


Figure 3.30: a) Catenated structure, with one framework depicted as a space-filled model and the second framework depicted as a green ball and stick model, as seen slightly offset along the *a*-axis. Colour code: Zn pale blue, C grey, O red, N blue. H atoms omitted for clarity, **b)** Two-fold interpenetrated $(6.10^2)(6.12^2)$ nets found in **4**.

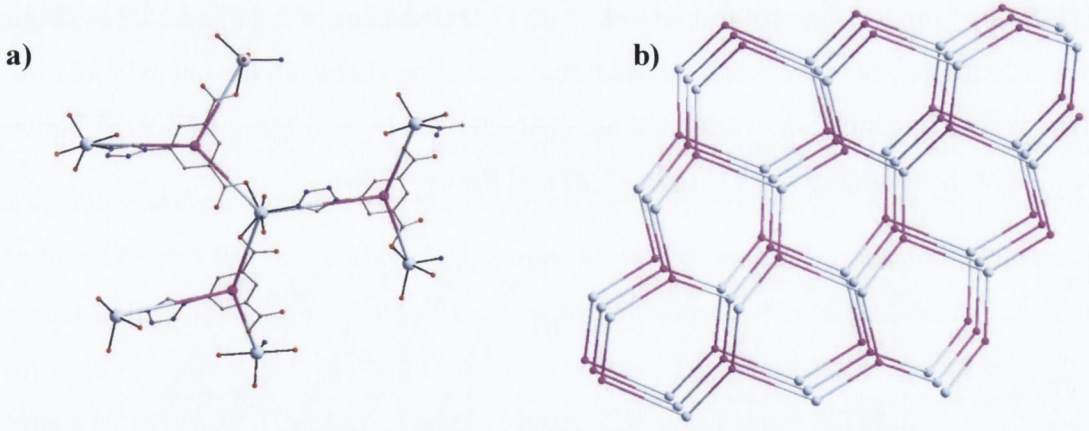


Figure 3.31: a) Zn^{II} ions and **L2** ligands envisaged as three-connecting nodes, **b)** $(6.10^2)(6.12^2)$ network found in **4**.

Table 3.8: Crystal data and details of the structure determination for **4**.

Identification code	**4**	
Empirical formula	$C_{18}H_{16}N_8O_{12}Zn_2$	
Formula weight	667.13 g mol^{-1}	
Temperature	150(2) K	
Wavelength	0.71073 Å	
Crystal system	Orthorhombic	
Space group	*P*nma	
Unit cell dimensions	a = 7.7360(2) Å	α= 90°.
	b = 27.507(6) Å	β= 90°.
	c = 16.915(3) Å	γ= 90°.
Volume	3599.5(12) $Å^3$	
Z	6	
Density (calculated)	1.841 Mg/m^3	
Absorption coefficient	2.087 mm^{-1}	
F(000)	2008	
Crystal size	0.4x 0.3 x 0.6 mm^3	
Theta range for data collection	1.41 to 28.33°.	
Index ranges	$-10\leq h\leq 9$, $-36\leq k\leq 35$, $-22\leq l\leq 18$	
Reflections collected	15600	
Independent reflections	4569[R(int) = 0.0609]	
Completeness to theta = 28.33°	99.7 %	
Refinement method	Full-matrix least-squares on F^2	
Data / restraints / parameters	4569/0/315	
Goodness-of-fit on F^2	1.134	
Final R indices [I>2sigma(I)]	R1 = 0.0586, wR2 = 0.1151	
R indices (all data)	R1 = 0.0784, wR2 = 0.1224	
Largest diff. peak and hole	0.709 and -1.248 e.$Å^{-3}$	

3.6.2 Further characterisation of **4**

The synthetic procedure used to synthesise **4**, produces the large block shaped crystals characteristic of **4**, together with smaller quantities of a colourless microcrystalline material. Consequently, crystals of **4** had to be separated manually under an optical microscope prior to further analysis. This process proved to be problematic, with samples appearing to lose their crystallinity during the time consuming separation procedure. This is reflected in the PXRD analysis of **4**, which reveals a broadening of the measured signals (**Figure 3.32**).

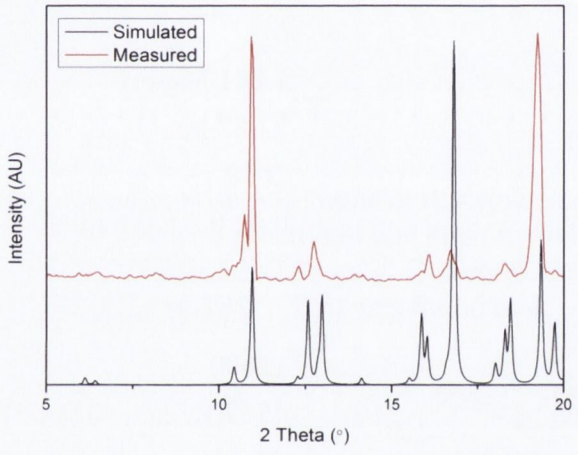


Figure 3.32: PXRD pattern of compound **4**, showing the simulated pattern as a black line and the measured pattern in red.

Analysis of the IR spectrum of **4** reveals a broad band centred at 3300 cm^{-1}, typical of the hydrogen bonding interactions that prevail between the catenated frameworks. The band present at 1615 cm^{-1} results from the characteristic tetrazole C=N stretch. The signal corresponding to the coordinated carboxylate group's asymmetric stretch is at 1569 cm^{-1}. The overlapping signals at 1377 and 1365 cm^{-1} result from C-N and symmetric C=O bond stretches (**Figure 3.33**).

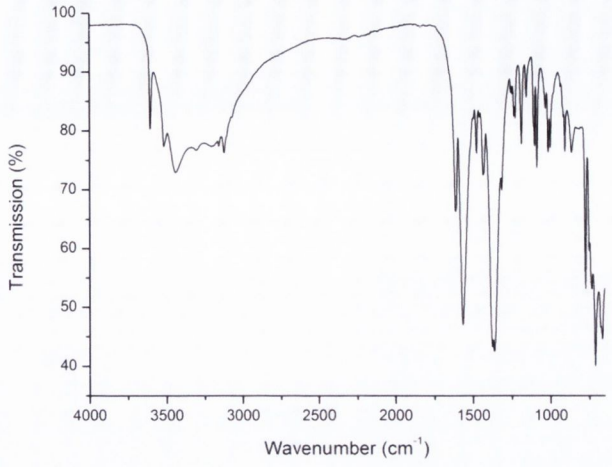


Figure 3.33: IR spectrum of **4**.

TGA of **4** reveals an initial weight loss of 12% between 90 and 130 °C attributable to the loss of the coordinated water molecules, (theoretical 11%) (**Figure 3.34**). This thermogravimetric step is followed by two subsequent decomposition events in the temperature range between 280 and 480 °C due to the oxidation of the organic material.

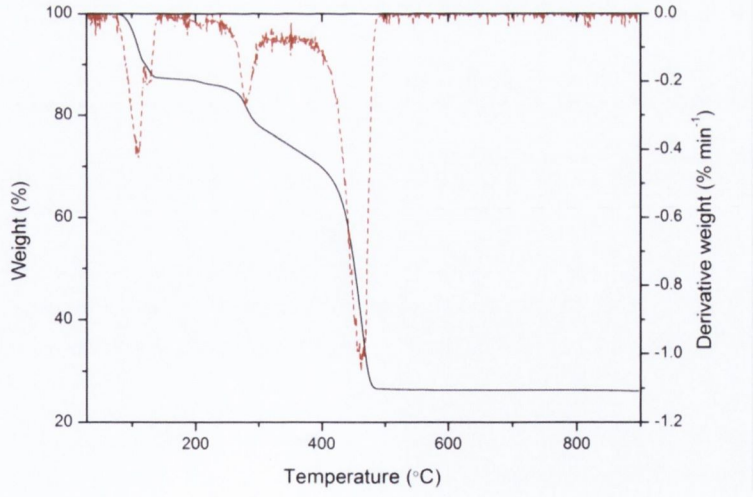


Figure 3.34: TGA of compound **4**.

3.7 [Cu(**L2**)], **5**

The 3D framework found in **4** encouraged us to try additional transition metal ions, with the motivation of producing similar, however, non-interpenetrated open-framework structures.

3.7.1 Synthesis and structural characterisation of compound **5**

The reaction of **L2** and $Cu(NO_3)_2 \cdot 4H_2O$ in a DMF/MeOH solution under solvothermal conditions at 85 °C, yields small green rectangular crystals of [Cu(**L2**)], **5**, which crystallise in the monoclinic space group $P2_1/c$. The small size of the crystals and high void volume of the structure contributed to the high R1 value.

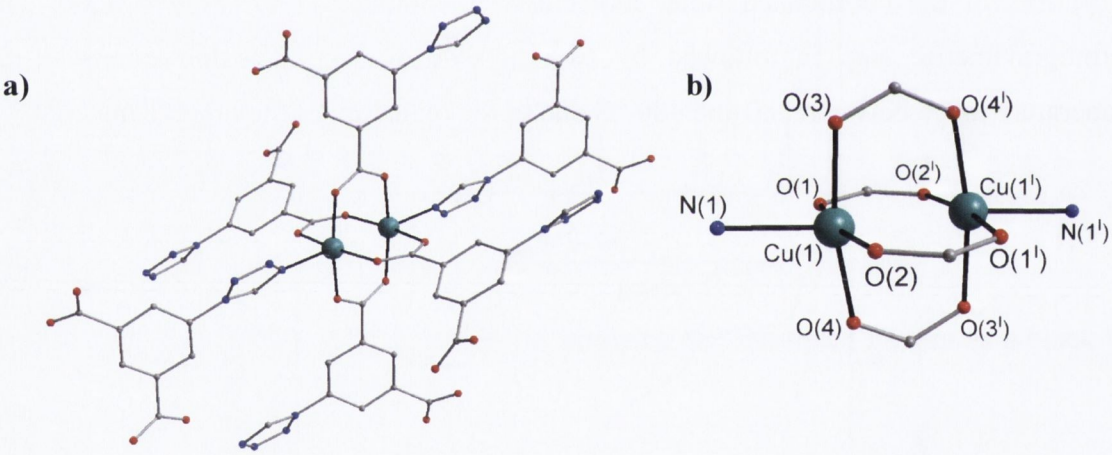


Figure 3.35: a), b) Coordination environment of the $\{Cu_2(COO)_4\}$ paddlewheel SBU in **5**. Symmetry code: (I) -1 -x, 1-y, -z. Colour code: Cu teal, C grey, O red, N blue. H atoms omitted for clarity.

Each fully deprotonated ligand is coordinated to five metal centres, with the individual carboxylate groups being linked to two separate Cu^{II} ions in a bis-monodentate *syn-syn* μ_2 bridging mode (**Figure 3.35**). These bridging carboxylate functionalities generate the $\{Cu_2(COO)_4\}$ paddlewheel SBUs found in **5**. The individual dinuclear paddlewheel units are stabilised by four bidentate carboxylate moieties, derived from four separate **L2** ligands, which are arranged at *ca.* 90° angles with respect to each other. The tetrazole group of **L2**

binds in a monodentate fashion to a single Cu^{II} ion of the dinuclear Cu^{II} unit, with the tetrazole N-donors being situated in the apical 'tip' positions of the paddlewheel. There is an inversion centre situated in the centre of the dinuclear complex, with both Cu^{II} ions in the dinuclear paddlewheel being crystallographically equivalent.

The individual Cu^{II} ions, which make up the $\{Cu_2(COO)_4\}$ paddlewheel SBUs, adopt a distorted square pyramidal geometry (**Figure 3.35**). This distortion is most clearly demonstrated by the angles of O(1)-Cu(1)-O(2) and O(3)-Cu(1)-O(4), which differ somewhat from the ideal value of 180°, at 167.74(2)° and 167.18(2)° respectively. The Cu-O and Cu-N bond lengths found in **5** correlate to previously reported copper paddlewheel structures and are summarised in **Table 3.9**.[15]

Table 3.9: Selected bond distances and angles for **5**. Symmetry code: (I) -1 -x, 1-y, -z.

Atoms	**Distance (Å)/ Angle (°)**	**Atoms**	**Angle(°)**
Cu(1)-O(1)	**1.968(5)**	O(1)-Cu(1)-O(4)	**86.7(2)**
Cu (1)-O(2)	**1.972(5)**	O(2)-Cu(1)-O(3)	**90.2(2)**
Cu (1)-O(3)	**1.984(5)**	O(2)-Cu(1)-O(4)	**90.2(2)**
Cu (1)-O(4)	**1.963(5)**	O(3)-Cu(1)-O(4)	**167.18(2)**
Cu (1)-N(1)	**2.188(4)**	O(1)-Cu(1)-N(1)	**88.72(2)**
		O(2)-Cu(1)-N(1)	**103.15(2)**
O(1)-Cu(1)-O(2)	**167.74(2)**	O(3)-Cu(1)-N(1)	**89.96(2)**
O(1)-Cu(1)-O(3)	**90.3(2)**	O(4)-Cu(1)-N(1)	**102.43(2)**

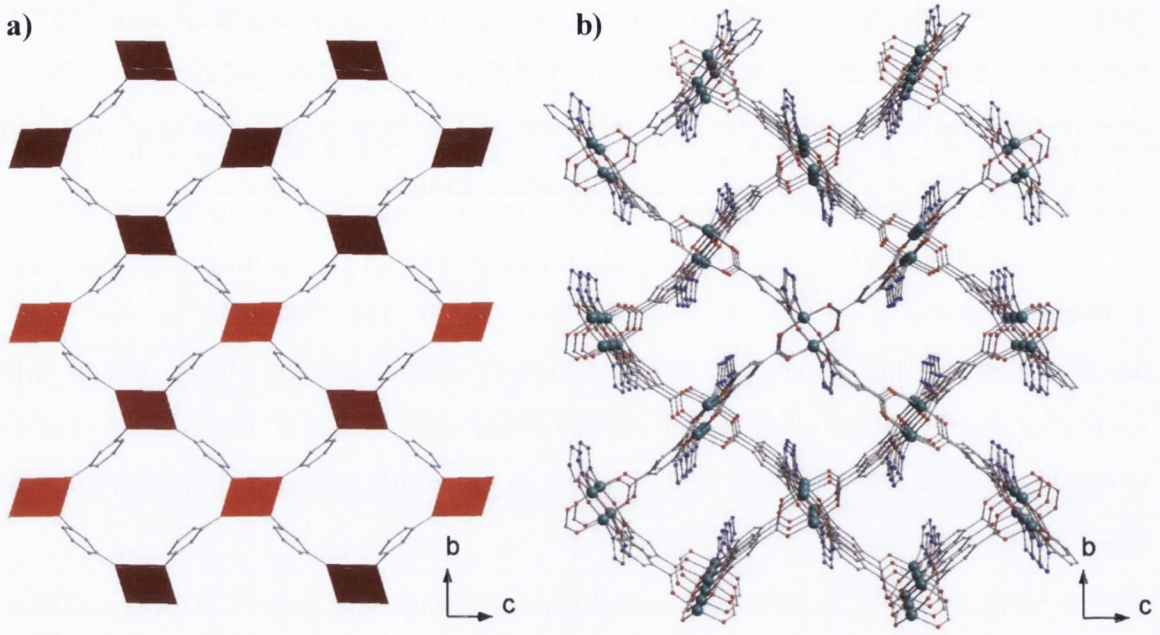


Figure 3.36: a) Schematic representation of the topological net along the *a*-axis, **b)** The network structure of **5** as seen along the *a*-axis. Colour code: Cu teal, C grey, O red, N blue. H atoms omitted for clarity.

By solely considering the carboxylate functionalities, it is possible to envisage the paddlewheel units as plane rectangular SBUs. These units are connected *via* the isophthalic acid moiety of **L2**, into 2D nets which extends in the *bc* plane (**Figure 3.36**). Through the tetrazole N-donors these individual sheets are connected to each other along the *a*-axis to form a porous 3D MOF with a Schläfli symbol of $(4.6^2)_2(4^2.6^8.8^5)$ (**Figure 3.37** and **Figure 3.39**). The network contains channels extending along the crystallographic *a*-axis with a cross-sectional diameter of *ca.* 10Å, which contain DMF and MeOH solvent molecules (**Figure 3.38**). Upon removal of the guest molecules the void volume was calculated by Platon to be 52% of the cell volume (897 out of 1725 Å).[16] A similar copper based structure has recently been reported.[17]

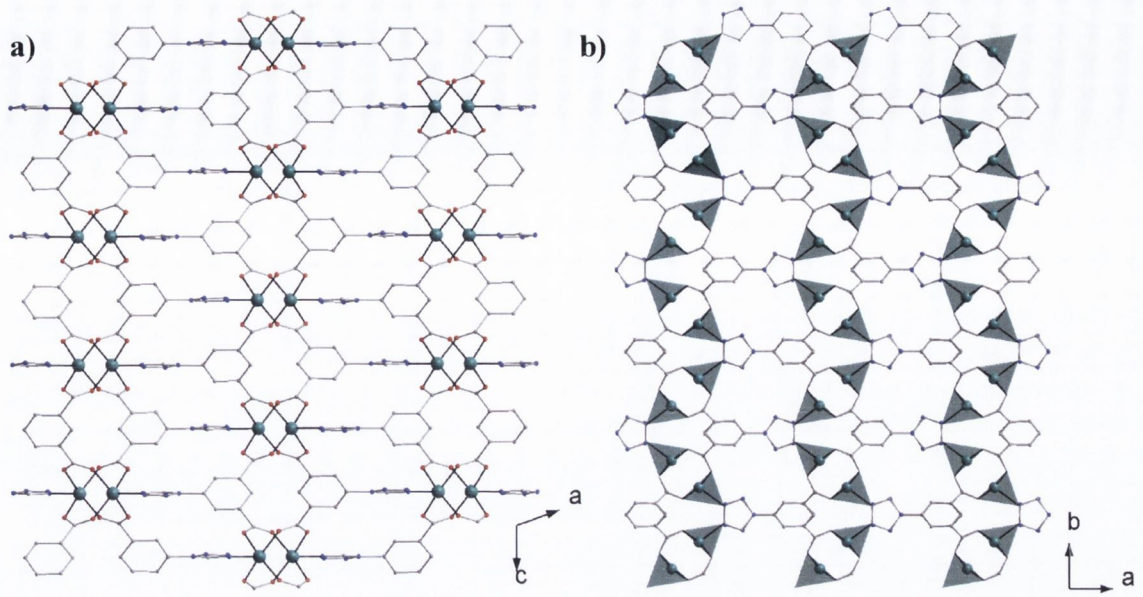


Figure 3.37: The network structure of **5** viewed in the **a)** *b*-axis, **b)** *c*-axis. Colour code: Cu teal, C grey, O red, N blue. H atoms omitted for clarity.

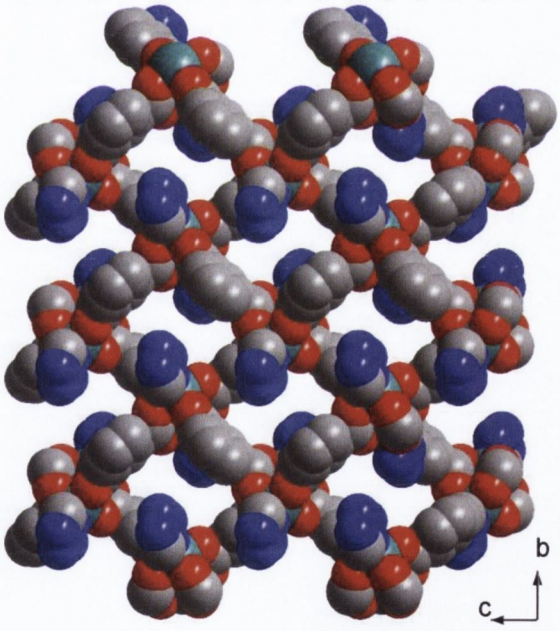


Figure 3.38: Space filled model of **5** viewed in the *a*-axis. Colour code: Cu teal, C grey, O red, N blue. H atoms omitted for clarity.

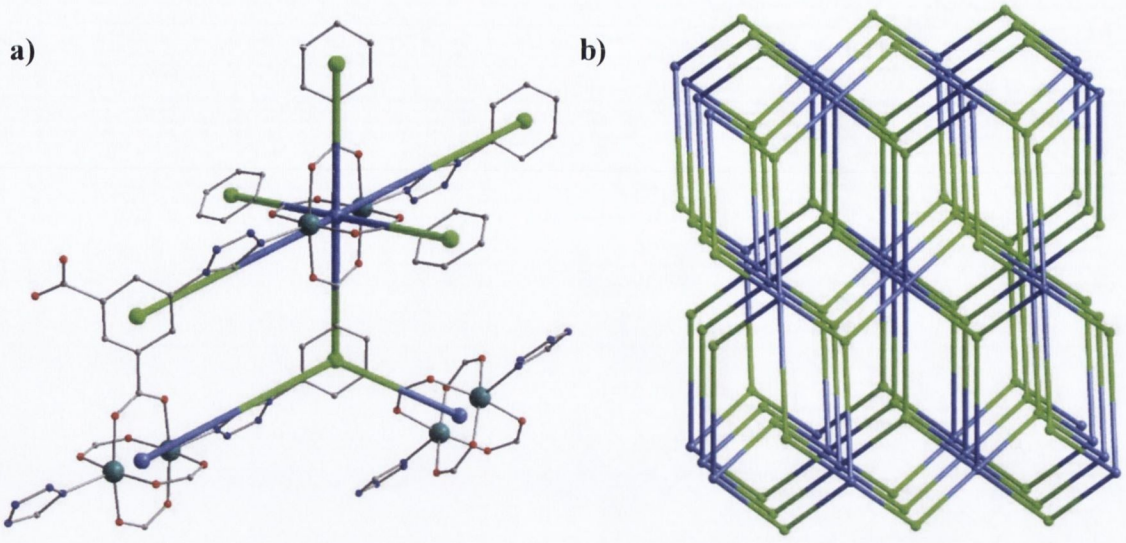


Figure 3.39: a) Cu^{II} paddlewheel units envisaged as six-connecting nodes and **L2** ligands as three-connecting nodes, **b)** $(4.6^2)_2(4^2.6^8.8^5)$ net found in **5**.

Table 3.10: Crystal data and details of the structure determination for **5**.

Identification code	**5**	
Empirical formula	$C_9H_4N_4O_4Cu$	
Formula weight	295.75 g mol^{-1}	
Temperature	153 (2) K	
Wavelength	0.71073 Å	
Crystal system	Monoclinic	
Space group	$P2_1/c$	
Unit cell dimensions	a = 10.943(2) Å	α= 90°.
	b = 11.383(2) Å	β= 109.55(3)°.
	c = 14.692(3) Å	γ = 90°.
Volume	1724.7(6) $Å^3$	
Z	4	
Density (calculated)	1.139 Mg/m^3	
Absorption coefficient	1.274 mm^{-1}	
F(000)	588	
Crystal size	0.2 x 0.2 x 0.1 mm^3	
Theta range for data collection	1.97 to 31.32°.	
Index ranges	$-15\leq h\leq 15$, $-16\leq k\leq 16$, $-20\leq l\leq 21$	
Reflections collected	19750	
Independent reflections	5184 [R(int) = 0.1557]	
Completeness to theta = 31.32°	91.9 %	
Refinement method	Full-matrix least-squares on F^2	
Data / restraints / parameters	5184 / 6 / 163	
Goodness-of-fit on F^2	0.907	
Final R indices [I>2sigma(I)]	R1 = 0.1000, wR2 = 0.2502	
R indices (all data)	R1 = 0.1527, wR2 = 0.2791	
Largest diff. peak and hole	1.659 and -1.009 $e.Å^{-3}$	

3.7.2 Further characterisation of **5**

A PXRD measurement was recorded on a freshly filtered sample of **5**. The obtained pattern correlates closely to the simulated powder pattern derived from the single crystal diffraction data, thus corroborating the accuracy of the refined model and confirming the phase-purity of the bulk sample (**Figure 3.40**). The IR spectrum of **5** reveals a series of overlapping stretching vibrations between *ca.* 1670 and 1590 cm^{-1}, resulting from the carbonyl stretch of the solvent DMF molecules, the C=N stretch of the tetrazole moieties and the coordinated carboxylate groups (ν_a(COO) (**Figure 3.41**). There are also overlapping bands present between 1438 and 1376 cm^{-1}, corresponding to symmetric C=O vibrations and DMF and tetrazole C-N bond stretches.

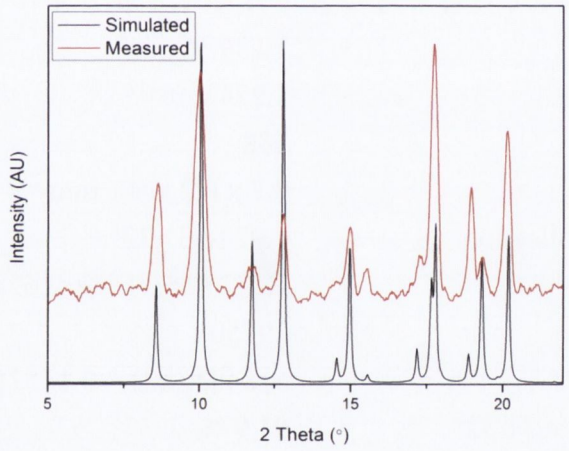


Figure 3.40: PXRD pattern of compound **5**, showing the simulated pattern as a black line and the measured pattern in red.

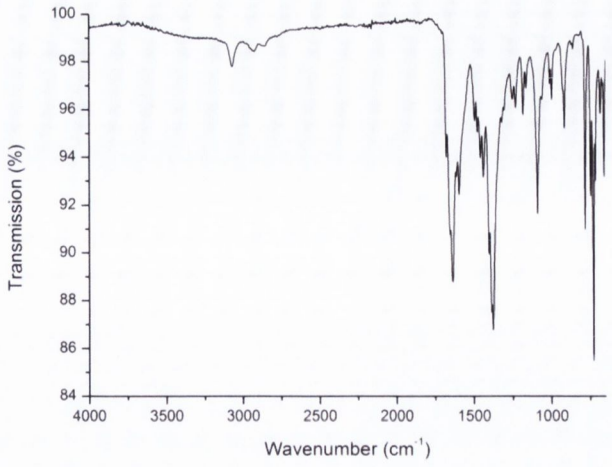


Figure 3.41: IR spectrum of **5**.

The thermolysis of **5** in an air atmosphere is characterised by a weight loss of 44% between *ca.* 30 and 260 °C attributable to the loss of the solvent DMF and MeOH molecules residing in the pores of the framework. The initial weight loss is followed by a further decrease of 45% as a result of the two step decomposition of the ligand between approximately 275 and 500 °C (theoretical 44%). The remaining material is most likely copper oxide.

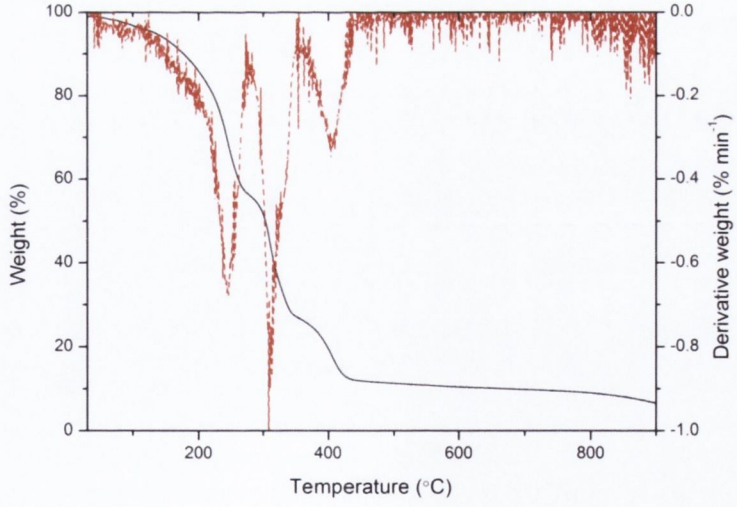


Figure 3.42: TGA of compound **5**, showing the percentage weight loss as a black line and the derivative of the percentage weight loss as the broken red line.

3.7.3 Surface area determination of compound **5**

The crystallographic model derived from the single crystal XRD data revealed that the open-framework structure of **5** contains channels of *ca.* 10 Å in diameter. In order to accurately determine the surface area of **5** it was necessary to remove the solvent molecules residing in the pores. This was achieved by exchanging the DMF molecules located in the pores with a lower boiling solvent, in this case dichloromethane (DCM). The solvent exchange process facilitates the application of lower temperatures to remove the solvent molecules within the structure. In addition, less polar solvents prevent hydrogen bonding interactions between solvent molecules and the framework and this may reduce capillary forces that can destroy the framework structure. This was achieved by submerging a sample of **5** in DCM and subsequently refreshing the DCM solution daily over the course of a week. The sample was then transferred to an Autosorb-IQ volumetric analyser and was subjected to surface area analysis after being heated under high vacuum at 85 °C for 12 hours in order to remove the DCM molecules.

The N_2 sorption properties of **5** revealed a reversible type I isotherm without reaching a saturation point at 1 atm, with a maximum uptake of 355 $cm^3 g^{-1}$ at 77 K (**Figure 3.43**). The BET surface area of compound **5** was determined to be *ca.* 935 $m^2 g^{-1}$ (**Figure 3.43**).

In addition to the surface area studies, the compound's capacity for storing H_2 and CO_2 gas was evaluated. The H_2 storage capability of **5** was calculated at 1 atm to be 213 $cm^3 g^{-1}$. This equates to a gas storage value of 1.9 wt% (**Figure 3.44**). Higher temperatures are necessary when performing CO_2 sorption studies, as CO_2 is a solid at 77 K, hence the measurements were undertaken at room temperature. In order to limit any sudden fluctuations in temperature the sorption cell was submerged in a large water bath. The CO_2 storage capacity of **5** at 290 K and 1 atm was found to be 212 $cm^3 g^{-1}$, corresponding to a storage capacity of 29 wt% (**Figure 3.44**). The CO_2 storage capacity of compound **5** is exceptionally high when compared to other comparable MOFs. For instance, its storage capacity is double that of HKUST-1 at 1 atm which matches at 9 atm the storage capability of **5**.[18] HKUST-1, $[Cu_3(BTC)_2(H_2O)_3]$, is a porous 3D MOF, composed of copper paddlewheel based SBUs linked *via* the ligand 1,3,5-benzenetricarboxylic acid (BTC) and contain 9x9 Å square shaped channels.[19] The high uptake of CO_2 may be attributable to the N-functionalities of the tetrazole moieties, as similar effects have been observed for other amine-based MOFs.[20]

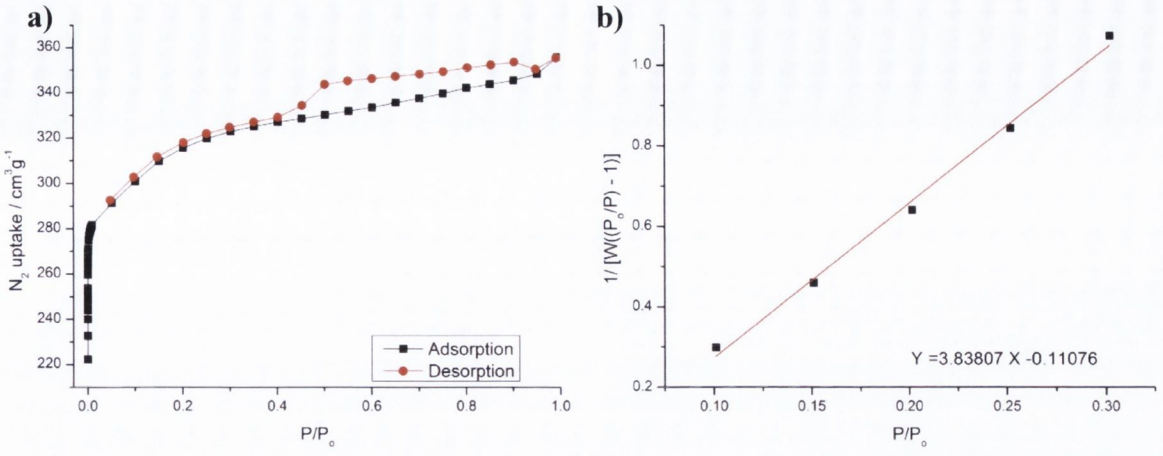


Figure 3.43: a) N_2 adsorption and desorption isotherm of **5** recorded at 77 K, **b)** plot of the linear region of the BET equation, derived from the N_2 adsorption isotherm of **5**.

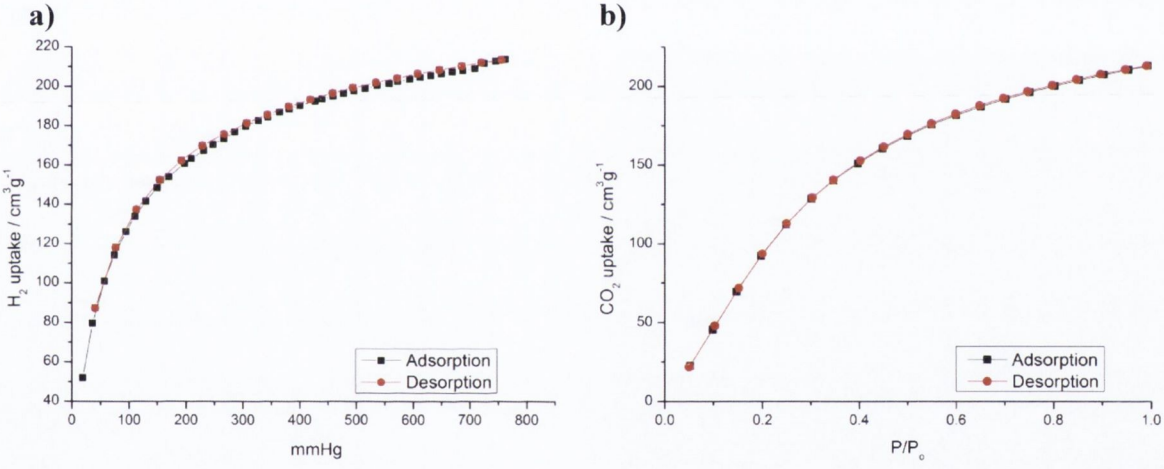


Figure 3.44: a) H_2 adsorption and desorption isotherm of **5** recorded at 77 K, **b)** CO_2 adsorption and desorption isotherm of **5** recorded at 290 K.

3.8 Conclusion

Two multi-dentate ligands, **L1** and **L2**, containing carboxylate and tetrazole groups, oxygen and nitrogen based donors respectively, were successfully synthesised. Their polydentate nature facilitated the formation of the network structures **1-5**. Furthermore, the inherent rigidity of **L2** resulted in the permanent porosity found in **5**.

In compounds **1** and **2** carboxylate groups bridge neighbouring metal centres to generate infinite 1D polymeric chains extending parallel to the *a*-axis. However, the different arrangement of **L1** in both compounds led to contrasting network structures. The polymeric chains in **1** are linked to neighbouring chains, *via* one of the ligand's tetrazole groups, along the *b*-axis to form 2D sheets that extend parallel to the *ab* plane. These sheets stack through dispersion forces, to generate a layered lamellar packing structure. The differing alignment of **L1** in **2** resulted in the 1D polymeric chains that cross link in approximately the *b*- and *c*-directions, to generate a densely packed 3D framework.

The densely packed structures formed using **L1**, prompted us to modify the ligand functionality and explore the formation of porous structures. Noting that only one tetrazole group on each ligand moiety is involved in binding to a metal centre in **1** and **2**, we decided to substitute one of the tetrazole groups with a carboxylate group, essentially adding a tetrazole group to isophthalic acid.

The initial structure formed with **L2** was compound **3**, which is composed of mononuclear Cd^{II} SBUs that are linked within the *ab*-plane to form 2D sheets. Ultimately a 3D supramolecular structure is formed as the separate layers assemble together through a combination of hydrogen bonding and π-π stacking interactions that prevail between adjacent layers.

Compound **4** justified our decision to alter the ligand, as each functional group on **L2** is coordinatively bonded to Zn^{II} ions with trigonal bipyramidal coordination geometries. The individual ligands in turn connect three neighbouring metal centres to form a 3D open-framework. However, as frequently observed for augmented frameworks, **4** is composed of two interdigitating networks, leading to a densely packed arrangement. Extensive experimental attempts to prepare a non-interpenetrated version of **4** were not successful

Finally, compound **5** is composed of dinuclear $\{Cu_2(COO)_4\}$ paddlewheel SBUs which are connected through the polydentate ligands to form a 3D porous MOF. The

structure was calculated as having an internal void volume of 52% of the unit cell volume that is accessible upon the removal of the DMF and MeOH solvent molecules that reside in the pores. The compound is characterised by permanent porosity revealing a type I adsorption isotherm and a BET surface area of *ca.* 935 $m^2 g^{-1}$. It shows a high CO_2 storage capacity of *ca.* 29 wt% at the ambient conditions of 1 atm and 290 K. The observed effect is consistent with other MOFs that contain N-functional moieties. Furthermore, the framework has a H_2 storage capacity of 1.9 wt% at 77 K and 1 atm, which is in-line with reported MOFs with comparable surface areas.

3.9 References

1. J. F. Eubank, R. D. Walsh and M. Eddaoudi, *Chemical Communications*, 2005, 2095-2097.
2. J. H. Liao, C. Y. Lai, C. D. Ho and C. T. Su, *Inorganic Chemistry Communications*, 2004, **7**, 402-404.
3. Y. B. Zhang, W. X. Zhang, F. Y. Feng, J. P. Zhang and X. M. Chen, *Angewandte Chemie-International Edition*, 2009, **48**, 5287-5290.
4. W. Ouellette, H. X. Liu, K. Whitenack, C. J. O'Connor and J. Zubieta, *Crystal Growth & Design*, 2009, **9**, 4258-4261.
5. W. C. Song, J. R. Li, P. C. Song, Y. Tao, Q. Yu, X. L. Tong and X. H. Bu, *Inorganic Chemistry*, 2009, **48**, 3792-3799.
6. M. Muttenthaler, M. Bartel, P. Weinberger, G. Hilscher and W. Linert, *Journal of Molecular Structure*, 2005, **741**, 159-169.
7. H. Y. He, J. Chen, X. H. Wang and L. G. Zhu, *Acta Crystallographica Section C-Crystal Structure Communications*, 2004, **60**, M540-M542.
8. Z. P. Yu, S. S. Xiong, G. P. Yong and Z. Y. Wang, *Journal of Coordination Chemistry*, 2009, **62**, 242-248.
9. CCDC, *Mercury CSD 3.0*, 2008.
10. K. Nakamoto, *Infrared and Raman Spectra of Inorganic and Coordination Compounds, Applications in Coordination, Organometallic, and Bioinorganic Chemistry* John Wiley & Sons, New Jersey, USA, 2009.
11. Z. P. Yu, Y. Xie, S. J. Wang, G. P. Yong and Z. Y. Wang, *Inorganic Chemistry Communications*, 2008, **11**, 372-376.
12. W. Fang, *Acta Crystallographica Section E-Structure Reports Online*, 2010, **66**, M1572-U1846.
13. L. L. Di, Y. Wang, G. W. Lin and T. Lu, *Acta Crystallographica Section E-Structure Reports Online*, 2010, **66**, M610-U193.
14. F. A. Yang, J. H. Chen, H. Y. Hsieh, S. Elango and L. P. Hwang, *Inorganic Chemistry*, 2003, **42**, 4603-4609.
15. M. Iqbal, I. Ahmad, S. Ali, N. Muhammad, S. Ahmed and M. Sohail, *Polyhedron*, 2013, **50**, 524-531.
16. U. Glasgow, *Platon*, 2006, **1.10**, A Multipurpose Crystallographic Tool.
17. S. M. Zhang, Z. Chang, T. L. Hu and X. H. Bu, *Inorganic Chemistry*, 2010, **49**, 11581-11586.

18. A. R. Millward and O. M. Yaghi, *Journal of the American Chemical Society*, 2005, **127**, 17998-17999.

19. S. S. Y. Chui, S. M. F. Lo, J. P. H. Charmant, A. G. Orpen and I. D. Williams, *Science*, 1999, **283**, 1148-1150.

20. X. J. Gu, Z. H. Lu and Q. Xu, *Chemical Communications*, 2010, **46**, 7400-7402.

Chapter 4

The exploitation of carboxylate stabilised SBUs for the generation of porous MOFs

4 The exploitation of carboxylate stabilised SBUs for the generation of porous MOFs

4.1 Introduction

Following on from the work discussed in Chapter 3, it was decided that we would next focus on an extended ligand that contains only one type of functional group. As was highlighted in Chapter 1, the bridging capabilities of carboxylate groups make them ideal functionalities for the generation of rigid polynuclear SBUs. Using this knowledge our aim was to exploit SBUs stabilised by carboxylate groups for the generation of novel open-frameworks. In order to achieve this it would be necessary to choose a rigid polycarboxylate ligand.

The ligand 1,3,5-benzene-trisethynyl benzoic acid, (**L3**), was chosen for its rigid and extended tritopic topology, that is characterised by a centroid-carboxylate and a carboxylate-carboxylate distance of 10 and 18 Å, respectively (**Scheme 4.1**). Until now only three **L3** based coordination complexes had been structurally characterised and reported in the literature. One being $[Ni(cyclam)]_3[\mathbf{L3}]_2$, which is composed of threefold interwoven 2D nets of Ni(cyclam) moieties linked *via* **L3**, (cyclam: 1,4,8,11-tetraazacyclotetradecane). The structure of the second reported MOF, MOF-180 was discussed in Chapter 1.[1,2] The previously discussed compound MOF-210 contains a combination of **L3** and the co-ligand biphenyl-4,4'-dicarboxylate.[2]

In this chapter the synthesis and structural characterisation of four novel 3D porous frameworks, synthesised using **L3** will be discussed. Two of which are zinc based compounds, one containing trinuclear SBUs and the second containing pentanuclear SBUs. A cobalt complex isostructural to the pentanuclear zinc compound and a **pto**-type framework containing dinuclear copper paddlewheel based SBUs will also be discussed.

4.2 Ligand Synthesis

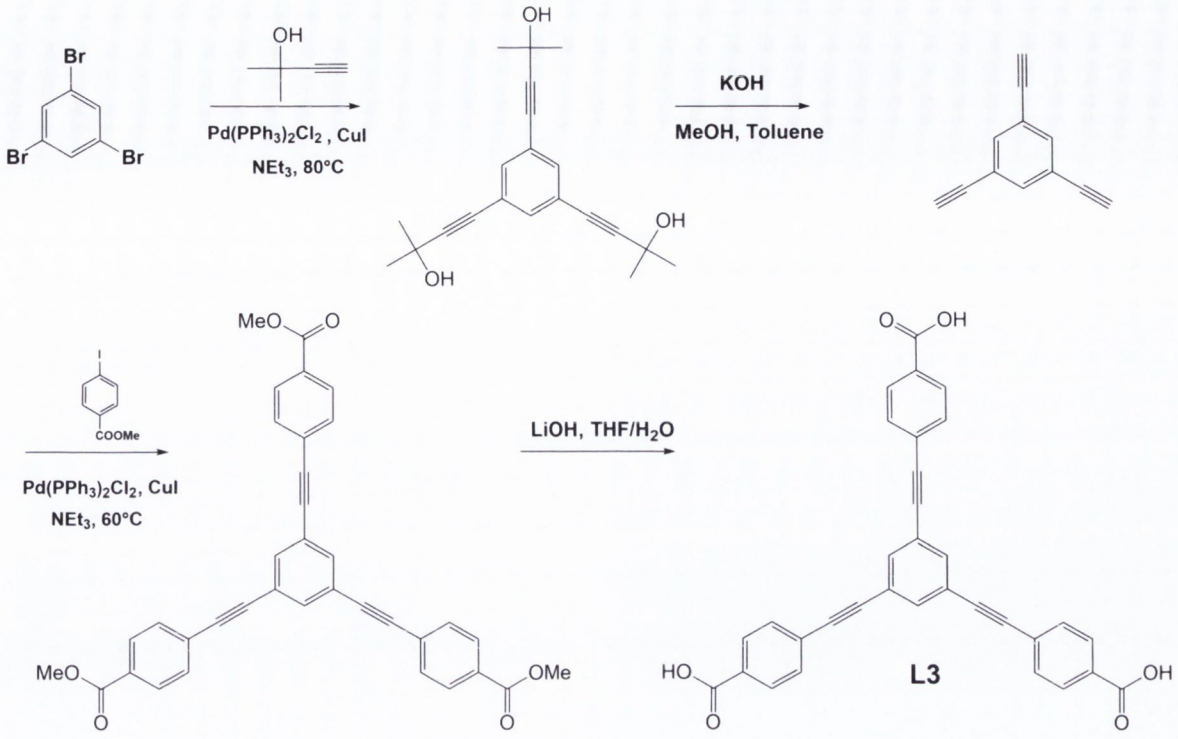
The ligand discussed in this chapter 1,3,5-benzene-trisethynyl benzoic acid, (**L3**), was synthesised using a modified literature procedure (**Scheme 4.1**).[3,4] The initial step involved a Sonogashira coupling reaction under inert gas conditions, between 1,3,5-tribromobenzene and 2-methyl-3-butyn-2-ol, with $Pd(PPh_3)Cl_2$ and CuI acting as catalysts and triethyl amine as both, a solvent and as a base. TLC was employed to monitor the progress of the reaction

and the insoluble salts were filtered off and the solvent removed when the reaction came to completion. The resulting solid material was recrystallised from ethyl acetate, to give 1,3,5-tris(2-methyl-2-hydroxy-3-butnyl)-benzene.

Sonogashira coupling reactions employ a palladium(0) catalyst along with a copper(I) co-catalyst to form a carbon-carbon bond between an aryl or vinyl halide and a terminal alkyne group; the reaction was first reported by Sonogashira *et al.* in 1975.[5] The palladium compound, in this case $Pd^{II}(PPh_3)Cl_2$ undergoes an initial *in situ* reduction to the active Pd^0 catalyst. This is followed by an oxidative addition reaction with the aryl halide to generate a Pd^{II} complex. At the same time CuI reacts with the terminal alkyne, which is deprotonated to form a copper acetylide complex. The copper co-catalyst is then regenerated *via* a transmettalation reaction between the Cu^I and Pd^{II} complexes and reductive elimination of the newly formed Pd^{II} complex results in the coupling of the two organic ligands and the regeneration of the Pd^0 catalyst.

The second step required a *retro*-Favorski reaction, utilising KOH as a base to synthesise 1,3,5-triethynylbenzene.[6] Acetone is produced as a side product and was continuously removed using a Dean-Stark trap, to ensure a high yield. Column chromatography was used to purify the product. This was followed by a second Sonogashira coupling reaction in step three, between the terminal alkynes of 1,3,5-triethynylbenzene and the aryl halide methyl-4-iodobenzoate to produce 4,4',4"-(benzene-1,3,5–triyltris(ethyne-2,1-diyl))tribenzoate, which was purified by recrystallisation from a DCM/MeOH mixture. Ester hydrolysis of 4,4',4"-(benzene-1,3,5–triyltris(ethyne-2,1-diyl))tribenzoate, resulted in the formation of **L3**.

A combination of ^{1}H-NMR, elemental analysis, mass spectrometry and FT-IR spectroscopy confirmed the formation of **L3**. ^{1}H-NMR in deuterated dimethyl sulfoxide reveals a signal at 13.2 ppm, which is most likely due to the hydrogen atom of the carboxylic acid groups (**Figure 4.1**). Adjacent to this is a doublet at 8.01 ppm attributable to the six hydrogen atoms in the *ortho*-positions relative to the carboxylic acid groups. There is a singlet present at 7.87 ppm, assigned to the three protons of the central phenyl unit and an additional doublet at 7.72 ppm corresponding to the six hydrogen atoms in the *meta*-position relative to that of the carboxylic acid moieties. FT-IR analysis revealed a spectrum with strong bands at 1684, 1605 and 1419 cm^{-1}, which is consistent with that reported by Kobayashi *et al.* (**Figure 4.2**).[3]



Scheme 4.1: Synthetic procedure used in the synthesis of **L3**.

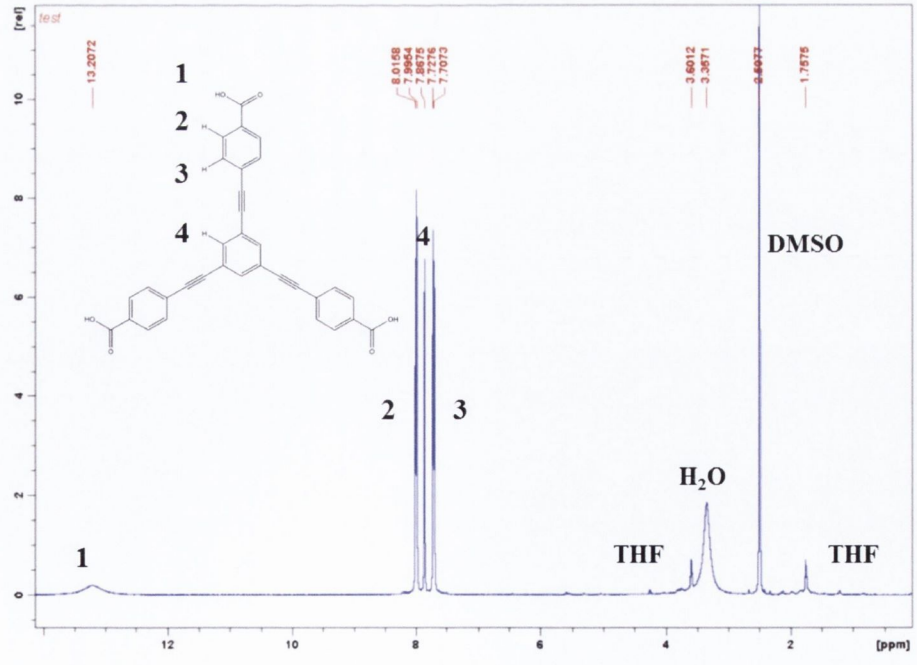


Figure 4.1: ^{1}H-NMR spectrum of **L3**.

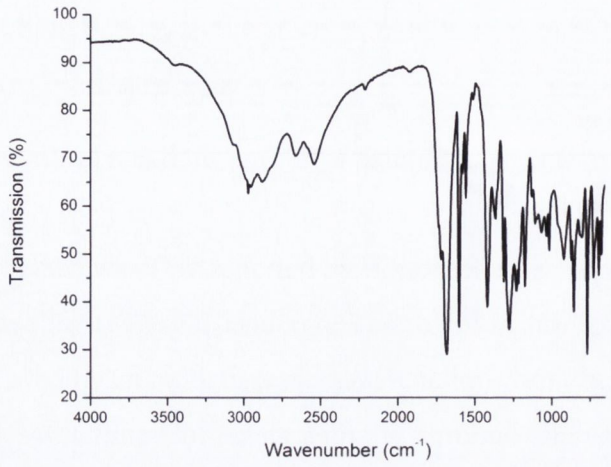


Figure 4.2: FT-IR spectrum of **L3**.

4.3 $[Zn_3(\mathbf{L3})_2(DMF)_2]$, (**6**)

As was stated in the introduction to this chapter, there were only three **L3** based coordination compounds that had thus far been reported in the literature, one of which being MOF-180 which contains $\{Zn_4O(O_2C)_6\}$ octahedral SBUs. This was synthesised by reacting zinc nitrate and **L3** in a very high metal to ligand ratio of 16:1.[2] We felt that through variation of the reaction conditions and by employing lower metal to ligand ratios, it could be possible to synthesise a novel framework composed of different SBUs.

4.3.1 Synthesis and structural characterisation of compound **6**

The reaction in DMF of $Zn(NO_3)_2{\cdot}6H_2O$ and the ligand **L3** in a mole ratio of 3:1 at 85 °C, yields colourless needle like crystals of **6** suitable for single crystal XRD.[7] **6** crystallises in the chiral tetragonal space group $P4_322$ or $P4_122$ (enantiomeric), whereby the resulting SBUs generate optical isomers. The programme Platon Squeeze was employed to account for disordered DMF solvent molecules present in the refined structure.[8]

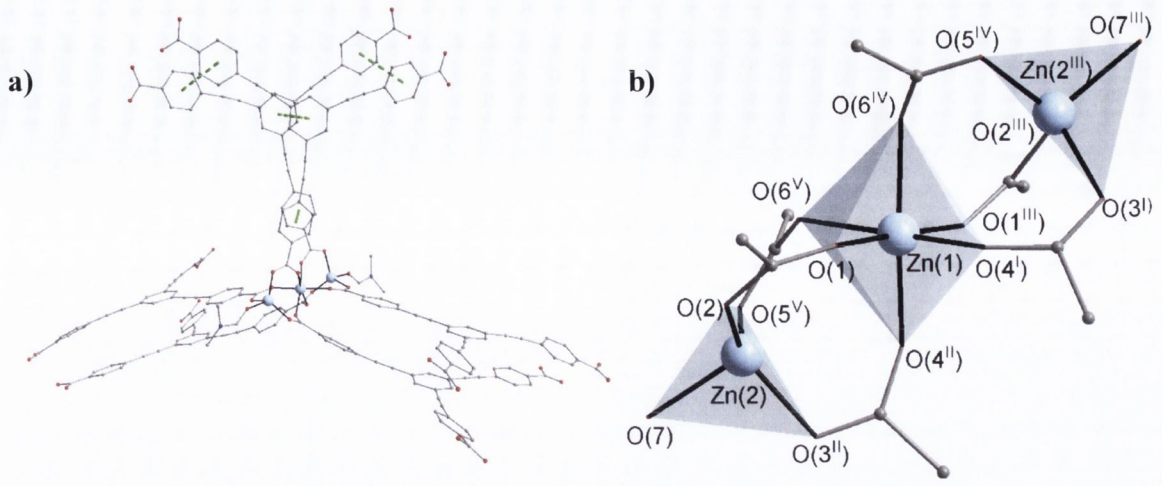


Figure 4.3: a), b) The $\{Zn_3(COO)_6\}$ SBU stabilised by six carboxylate groups. Symmetry codes: (I) x, 1-y, -0.25+z, (II) –x, 1-y, 0.75-z; (III) x, -y, 0.5-z; (IV) -x, y, 1-z; (v) -x, -y, -0.5+z. The dashed green lines represent the π-π stacking interactions between the pairs of ligands, the π-π interactions of the remaining two ligand pairs have been omitted for clarity. Colour code: Zn pale blue, C grey, N blue and O red. H atoms omitted for clarity.

The asymmetric unit of **6** contains two crystallographically independent zinc ions, one **L3** ligand and a DMF molecule. The two unique Zn^{II} ions (Zn(1) and Zn(2)) are linked *via* three bridging bidentate **L3** carboxylate groups and through symmetry operations a linear trinuclear $\{Zn_3(COO)_6\}$ hourglass like SBU is formed, with a Zn(2)-Zn(1)-Zn(2^{III}) angle of 179.98°. Each trinuclear node is stabilised by six bridging carboxylate functionalities originating from six separate fully deprotonated **L3** ligands and two coordinated DMF molecules, where there is a Zn(1)···Zn(2) interatomic distance of 3.53(4) Å.

The central atom of the trinuclear unit, Zn(1), adopts an octahedral coordination environment, whereby it is coordinated to six oxygen atoms originating from six separate bridging acid functionalities, with the Zn(1)-$O_{carboxylate}$ bond lengths varying between 2.046(3) and 2.085(2) Å (**Figure 4.3**). The terminal Zn(2) atom has a distorted tetrahedral coordination environment, generated by three carboxylate oxygen atoms (O(2), O(3^{II}) and O(2^{V})) and a DMF oxygen atom (O(7)) in the apical tip position. The Zn(2)-O bond lengths are shorter than found for the central Zn(1)-O bond length, with them ranging between 1.932(2) and 2.004(2) Å. A detailed list of bond lengths and angles can be found in **Table 4.1**. Comparable trinuclear $\{Zn_3(COO)_6\}$ SBUs, with similar Zn-O bond lengths, have been effectively used to generate a series of two and three-dimensional MOFs.[9,10,11]

Table 4.1: Selected bond distances and angles of the Zn^{II} coordination environments found in **6**. Symmetry codes: (I) 1-y, x, -0.25+z, (II) 1-y, -x, 0.75-z; (III) x, -y, 0.5-z; (IV) -x, y, 1-z; (v) -x, -y, -0.5+z.

Atoms	Distance (Å)/ Angle(°)	Atoms	Distance (Å)/ Angle(°)
Zn(1)-O(1)	**2.0731(2)**	O(1)-Zn(1)-O(6^{V})	**92.25(8)**
Zn(1)-O(4^{I})	**2.046(3)**	O(4^{I})-Zn(1)- O(4^{II})	**90.20(2)**
Zn(1)- O(6^{IV})	**2.085(2)**	O(4^{I})-Zn(1)- O(6^{IV})	**92.14(1)**
Zn(2)-O(2)	**1.932(2)**	O(4^{I})-Zn(1)- O(6^{V})	**171.88(9)**
Zn(2)-O(3^{II})	**1.970(2)**	O(6^{IV})-Zn(1)- O(6^{V})	**86.61(1)**
Zn(2)-O(5^{V})	**1.955(2)**	O(2)-Zn(2)- O(3^{II})	**110.16(1)**
Zn(2)-O(7)	**2.004(2)**	O(2)-Zn(2)- O(5^{V})	**125.75(9)**
		O(2)-Zn(2)- O(7)	**99.94(9)**
O(1)-Zn(1)-O(1^{III})	**178.25(1)**	O(3^{II})-Zn(2)- O(5^{V})	**115.73(1)**
O(1)-Zn(1)-O(4^{I})	**95.75(8)**	O(3^{II})-Zn(2)- O(7)	**98.72(1)**
O(1)-Zn(1)-O(4^{II})	**83.00(8)**	O(5^{V})-Zn(2)- O(7)	**100.14(1)**
O(1)-Zn(1)-O(6^{IV})	**89.02(7)**		

The 0D SBUs are linked to six additional trinuclear $\{Zn_3(COO)_6\}$ nodes *via* three pairs of weakly π-π interacting (centroid-centroid distance of 3.9-4.23 Å) **L3** ligands (**Figure 4.3**). Each ligand in turn is coordinated to three zinc SBUs, whereby two of their acid functionalities link nodes in the *c*-direction through a 4_3 screw axes and the remaining carboxylate group links the helical chains in accordance to a four-fold screw axes in the remaining directions of space, to generate a 3D framework. It is possible to simplify the network topology of **6** by envisaging each trinuclear zinc SBU and each ligand pairing as three connecting nodes, resulting in a (10^3) Schläfli symbol (**Figure 4.4** and **Figure 4.6**).

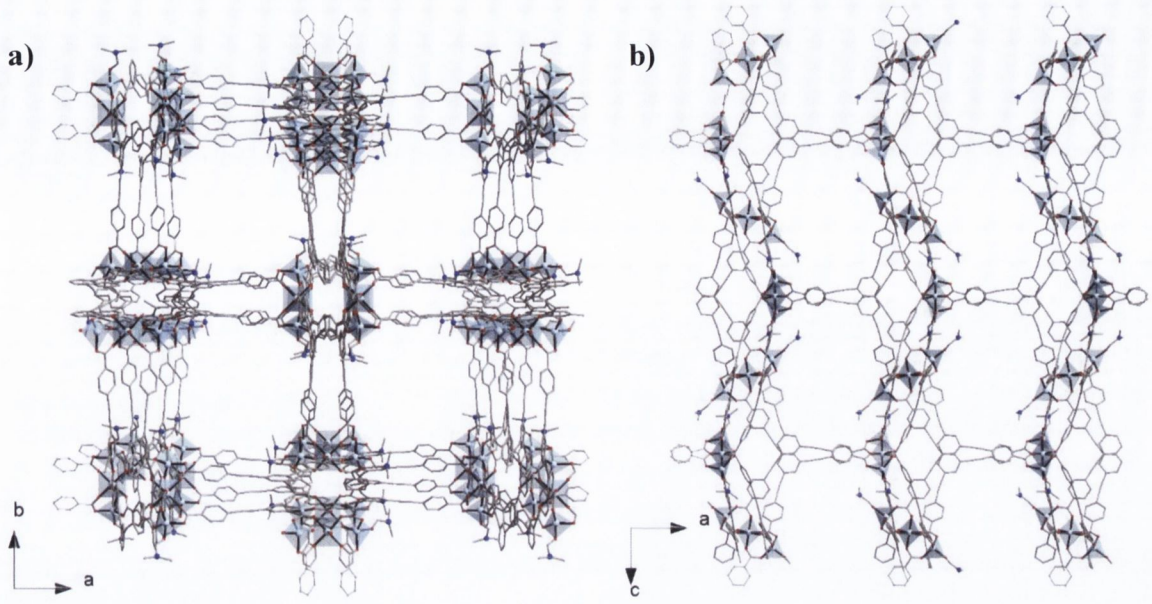


Figure 4.4: Network structure of **6** as seen along the crystallographic **a)** *c*-axis and **b)** *b*-axis. Colour code: Zn pale blue, C grey, N blue and O red. H atoms omitted for clarity.

6 contains two symmetry equivalent frameworks, which are two-fold interpenetrated (**Figure 4.5** and **Figure 4.7**). Dispersion forces between adjacent frameworks ensure that the ligand moieties are closely interwoven and consequently the interpenetration is not detrimental to pore size or the solvent accessible void volume, which was calculated to be 68% of the unit cell volume (11135 $Å^3$ out of 16287 $Å^3$).[8] This void volume is accessible from three directions of space; with the channels having a cross sectional diameter of *ca.* 12 Å and pore openings 16x11 Å in size. This compares favourably to a recently reported $[Zn_3(ChirBTB\text{-}2)_2]$ 3D framework, which is composed of similar trinuclear hourglass SBUs linked *via* the less extended tritopic ligand 1,3,5-tri{4-[2-(4-benzyl-2-oxooxazolidin-3-yl)]benzoate}benzene (ChirBTB-2), a derivative of BTB (4,4',4"-benzene-1,3,5-triyl-tribenzoic acid).[12] The 68% void volume calculated for **6** represents a significant increase over the 51% estimated for that of $[Zn_3(ChirBTB\text{-}2)_2]$. This high void volume results in a low calculated crystal density of 0.553 g cm^{-3}.

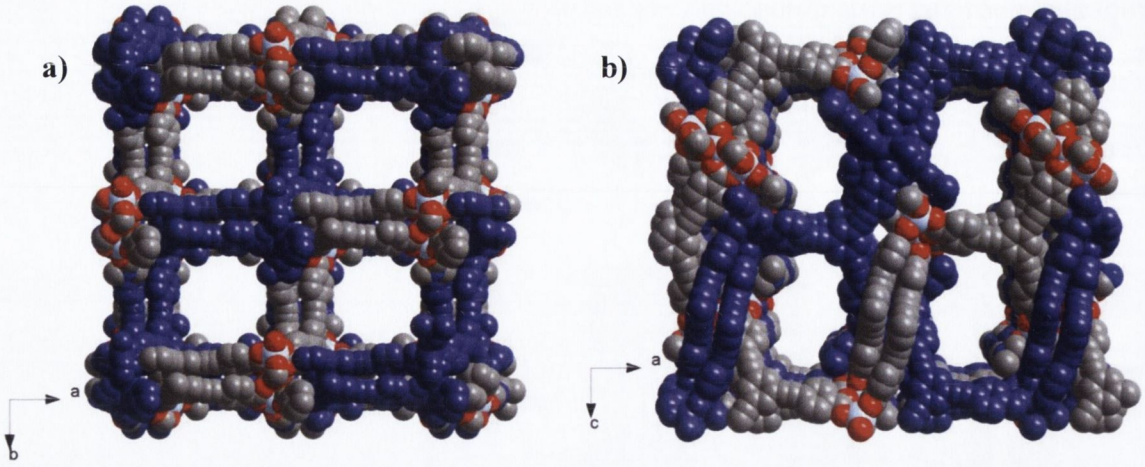


Figure 4.5: Space filling model of the dual interpenetrated networks present in **6**, viewed in the direction of the crystallographic **a)** *c*-axis **b)** *b*-axis. One network is coloured according to the colour scheme: Zn pale blue, C grey, N blue and O red. The second network is coloured indigo. H atoms omitted for clarity.

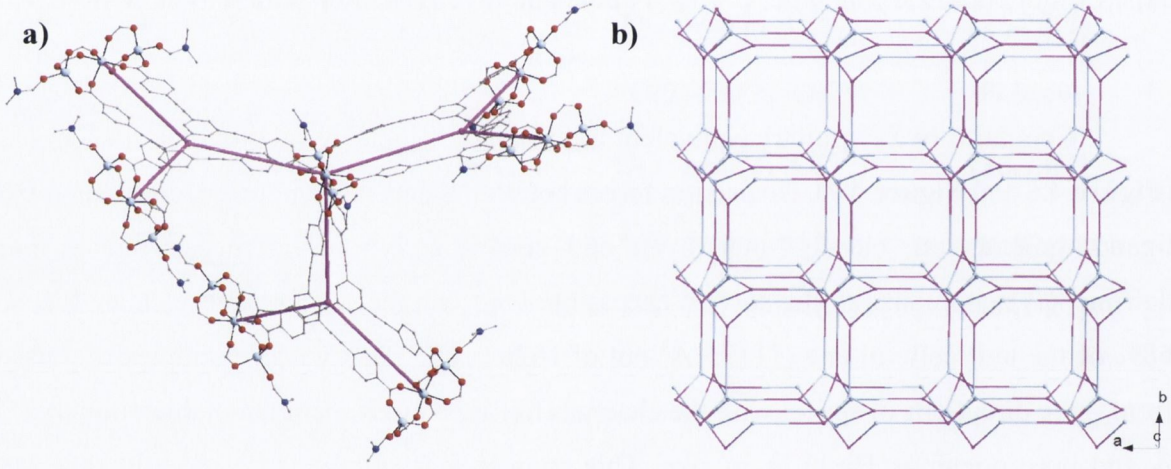


Figure 4.6: a) Simplification model used to generate the, **b)** (10^3) net topology found in **6**.

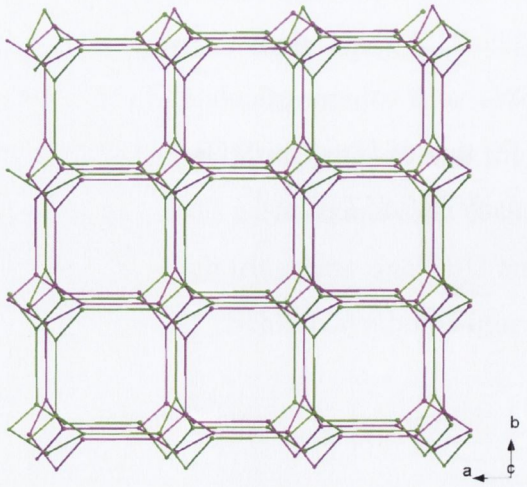


Figure 4.7: Two-fold interpenetrated networks found in **6**

Table 4.2: Crystal data and details of the structure determination for **6**.

Identification code	**6**	
Empirical formula	$C_{72}H_{44}N_2O_{14}Zn_3$	
Formula weight	1357.2 g mol^{-1}	
Temperature	250 K	
Wavelength	0.71073 Å	
Crystal system	Tetragonal	
Space group	$P4_322$	
Unit cell dimensions	a = 20.269 (2) Å	α= 90°.
	b = 20.269 (2) Å	β= 90°.
	c = 39.645 (4) Å	γ= 90°.
Volume	16287 (3) $Å^3$	
Z	4	
Density (calculated)	0.553 Mg/m^3	
Absorption coefficient	0.465 mm^{-1}	
F(000)	2768	
Crystal size	0.3 x 0.2 x 0.2 mm^3	
Theta range for data collection	1 to 25.71°	
Index ranges	$-24 \leq h \leq 22$, $-24 \leq k \leq 24$, $-48 \leq l \leq 40$	
Reflections collected	77843	
Independent reflections	15488 [R(int) = 0.1201]	
Completeness to theta = 25.71°	99.7 %	
Refinement method	Full-matrix least-squares on F^2	
Data / restraints / parameters	15488 / 6 / 391	
Goodness-of-fit on F^2	0.762	
Final R indices [I>2sigma(I)]	R_1 = 0.0430, wR_2 = 0.0674	
R indices (all data)	R_1 = 0.1259, wR_2 = 0.0794	
Largest diff. peak and hole	0.386 and -0.139 e.$Å^{-3}$	

4.3.2 Further characterisation of **6**

The large and highly accessible channels in **6** give rise to a rapid loss of solvent molecules when left exposed in an air atmosphere. Upon desolvation the compound loses its crystallinity and this unfortunately prevented the recording of a PXRD pattern.

The FT-IR spectrum of **6** reveals several overlapping bands located between 1653 and 1547 cm^{-1} assignable to aromatic C=C stretching vibrations and C=O stretching frequencies, arising from the coordinated DMF molecules and the bridging carboxylate groups of **L3**. Corresponding asymmetric stretching vibrations are present at 1405 and 1386 cm^{-1} (**Figure 4.8**). In addition the broad band centred at 3300 cm^{-1} indicates the presence of hydrogen bonding interactions between solvent molecules.

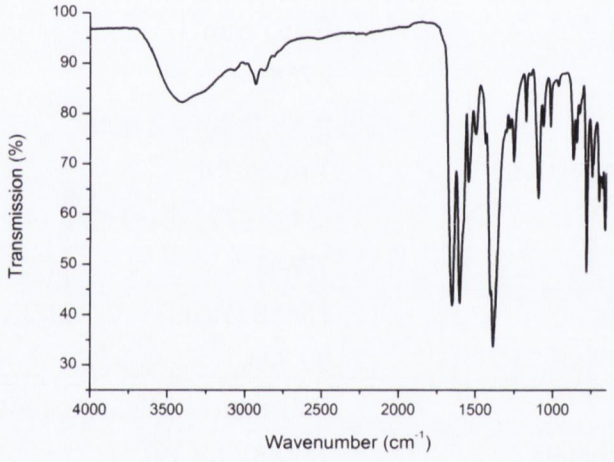


Figure 4.8: FT-IR spectrum of **6**.

The thermal treatment of compound **6** resulted in a reduction in mass of 32% between approximately 30 and 150 °C, accountable by the loss of solvent DMF molecules (**Figure 4.9**). This is followed by the loss of the coordinated DMF molecules between *ca.* 150 and 250 °C (theoretical 7%, experimental 8%). Finally, the thermolysis of the ligand occurs between 360 and 510 °C (theoretical 51%, experimental 49%).

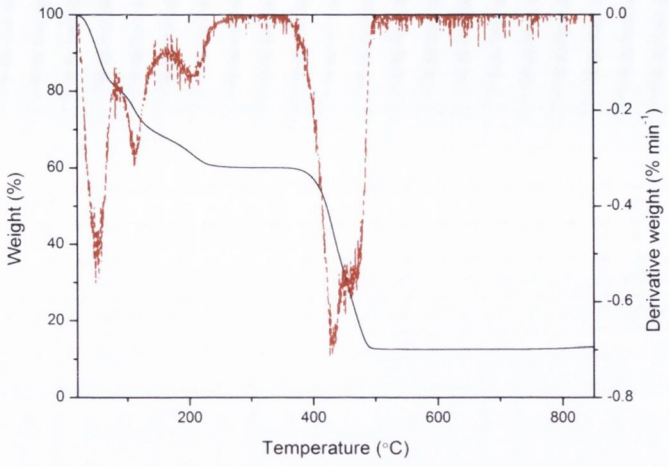


Figure 4.9: TGA of **6** performed in an air atmosphere, showing the percentage weight loss as a black line and the derivative of the percentage weight loss as the broken red line.

Surface area measurements have thus far proven to be unsuccessful. The solvent DMF molecules most likely contribute to the structural integrity of the framework and upon removal capillary forces lead to the collapse of the framework.

4.4 $(Me_2NH_2)[Zn_5(\mathbf{L3})_3(\mu_3\text{-}OH)_2(DMF)_2]$, (7)

4.4.1 Synthesis and structural characterisation of compound 7

It was evident during the initial attempts to synthesise larger crystals of **6** that increasing the mole ratio of Zn^{II}:**L3** beyond 4:1, produced large block shaped crystals, as opposed to the distinctive needles of compound **6**. By increasing this ratio further to 6:1, it was possible to synthesise phase pure batches of these new crystals. Single-crystal XRD revealed the larger crystals to be of the novel compound $(Me_2NH_2)[Zn_5(\mathbf{L3})_3(\mu_3\text{-}OH)_2(DMF)_2]$, (**7**), which crystallises in the monoclinic space group *C*2/c.[7] The previously reported compound MOF-180, which contains tetranuclear SBUs linked *via* the same ligand, is produced when the reaction ratio is increased to 9:1 and beyond.[2]

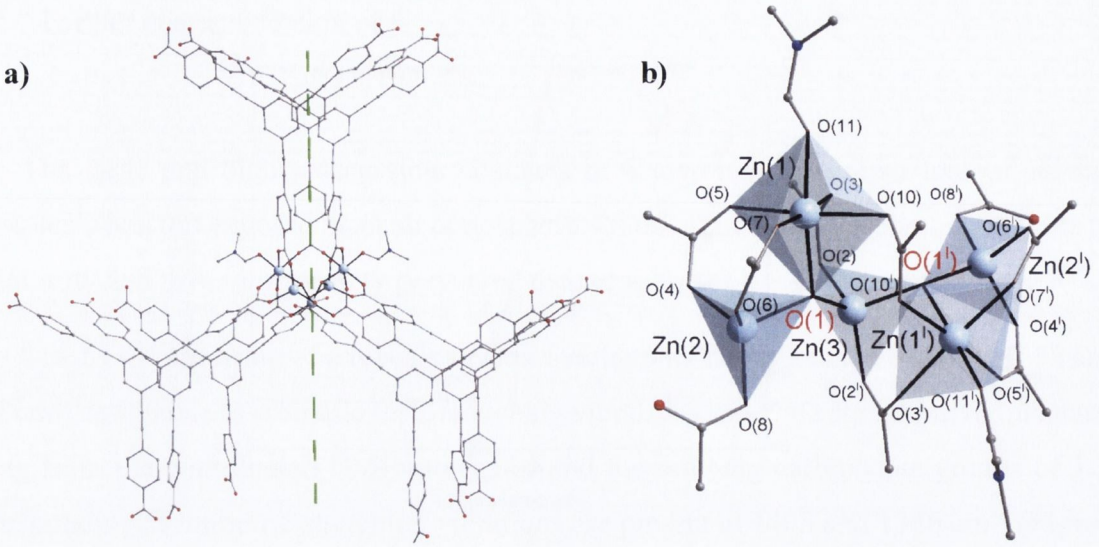


Figure 4.10: a), b) The $\{Zn_5(\mu_3\text{-}OH)_2(O_2C)_9\}$ SBU stabilised by nine carboxylate groups and two μ_3-OH ligands. The dashed green line represents a C_2 symmetry axis. Symmetry code: (I) 2-x, y, 0.5-z. Colour code: Zn pale blue, C grey, N blue and O red. H atoms omitted for clarity.

The asymmetric unit of **7** contains three crystallographically independent zinc ions, a triply bridging μ_3-OH group, a coordinated DMF molecule and one complete and one partially completed **L3** ligand, with the resulting framework being generated through symmetry operations. The novel pentanuclear $\{Zn_5(\mu_3\text{-}OH)_2(O_2C)_9\}$ SBU present in **7**, is composed of two triangular arrangements of zinc atoms (Zn(1), Zn(2), Zn(3), Zn(1^I) and Zn(2^I),) related through a C_2 symmetry operation (**Figure 4.10**). The SBU is stabilised by nine carboxylate groups, derived from nine fully deprotonated **L3** ligands. Seven of these acid functionalities act in a bridging bidentate mode, with the remaining two binding in a monodentate fashion. The pentanuclear node is completed by two triply bridging μ_3-OH groups (O(1) and O(1^I)) and two coordinated DMF molecules (O(11) and O(11^I)).

The central zinc ion Zn(3) adopts a distorted tetrahedral coordination environment, whereby it is coordinated to two oxygen atoms (O(1) and O(1^I)) from two μ_3-OH groups and to a further two oxygen atoms (O(2) and O(2^I)) from two bridging bidentate carboxylate groups. Adjacent to Zn(3) is Zn(2) which is also in a distorted tetrahedral coordination geometry. Zn(2) is coordinated to two oxygen atoms (O(4) and O(6)) from two bridging bidentate carboxylate groups, an oxygen atom (O(2)) from a single μ_3-OH group and finally to a monodentate carboxylate oxygen atom (O(8)). The distortion of the tetrahedral units is apparent by examining the O(1)-Zn(2)-O(6), O(1)-Zn(3)-O(1^I), and O(2)-Zn(3)-O(2^I) bond

angles of 100.87(8), 92.53(1) and 121.52(1)° respectively, which depart noticeably from the ideal angle of 109.5°.

The remaining crystallographically unique zinc ion, (Zn(1)), assumes a distorted octahedral coordination environment, where the equatorial positions are composed of four coordinated oxygen atoms (O(3), O(5), O(7) and O(10)) from four separate **L3** carboxylate groups. The apical positions are provided by two oxygen atoms derived from a μ_3-OH (O(2)) group and a coordinated DMF molecule (O(11)). The distortion of the octahedral geometry is highlighted by the bond angles O(3)-Zn(1)-O(5) (82.86(8)°) and O(1)-Zn(1)-O(11) (172.17(8)) which differ from the ideal angles of 90 and 180° respectively. **Table 4.3** contains a detailed list of bond lengths and angles, which are in the range of previously reported values for similar zinc compounds.[11,13] The individual pentanuclear units have an overall charge of -1 which is most likely balanced by dimethyl ammonium ($MeNH_2^+$) counterions, which are often produced when DMF is heated under solvothermal conditions.

Table 4.3: Selected bond distances and angles of the Zn^{II} coordination environment found in **7**. Symmetry codes: (I) 2-x, y, 0.5-z.

Atoms	Distance (Å)/ Angle(°)	Atoms	Distance (Å)/ Angle(°)
Zn(1)-O(1)	**2.0746(2)**	O(3)-Zn(1)-O(7)	**175.96(7)**
Zn(1)-O(3)	**2.161(2)**	O(3)-Zn(1)-O(10)	**92.85(7)**
Zn(1)-O(5)	**2.090(2)**	O(3)-Zn(1)-O(11)	**87.80(8)**
Zn(1)-O(7)	**2.0893(2)**	O(5)-Zn(1)-O(7)	**95.89(9)**
Zn(1)-O(10)	**2.1733(2)**	O(5)-Zn(1)-O(10)	**175.01(7)**
Zn(1)-O(11)	**2.0543(2)**	O(5)-Zn(1)-O(11)	**91.92(8)**
Zn(2)-O(1)	**1.974(2)**	O(7)-Zn(1)-O(10)	**88.22(8)**
Zn(2)-O(4)	**1.9448(2)**	O(7)-Zn(1)-O(11)	**88.40(8)**
Zn(2)-O(6)	**1.9689(2)**	O(10)-Zn(1)-O(11)	**85.35(7)**
Zn(2)-O(8)	**1.935(2)**	O(1)-Zn(2)-O(4)	**107.80(9)**
Zn(3)-O(1)	**2.028(2)**	O(1)-Zn(2)-O(6)	**100.87(8)**
Zn(3)-O(2)	**1.9062(2)**	O(1)-Zn(2)-O(8)	**108.30(1)**
		O(4)-Zn(2)-O(6)	**108.54(1)**
O(1)-Zn(1)-O(3)	**93.61(7)**	O(4)-Zn(2)-O(8)	**119.14(1)**

O(1)-Zn(1)-O(5)	**95.89(7)**	O(8)-Zn(2)-O(6)	**110.61(1)**
O(1)-Zn(1)-O(7)	**90.34(7)**	O(1)-Zn(3)-O(1^{I})	**92.53(1)**
O(1)-Zn(1)-O(10)	**86.89(7)**	O(1)-Zn(3)-O(2)	**104.51(8)**
O(1)-Zn(1)-O(11)	**172.17(8)**	O(1)-Zn(3)-O(2^{I})	**115.14(9)**
O(3)-Zn(1)-O(5)	**82.86(8)**	O(2)-Zn(3)-O(2^{I})	**121.52(1)**

The individual **L3** ligands are coordinated to five zinc atoms, *via* two bridging carboxylate groups, with the remaining acid moiety coordinating in a monodentate fashion to a fifth zinc atom. The nine **L3** molecules that stabilise each individual SBU can be subdivided into 3x3 groups of ligands that are separated by approximately 120° and point in the three directions of space, to link neighbouring pentanuclear clusters (**Figure 4.10** and **Figure 4.11**). The resulting 3D MOF has an observable honeycomb topology when viewed in the direction of the crystallographic *c*-axis and a Schläfli symbol of $(4^2.6)_2(4^6.6^{27}.8^3)$ (**Figure 4.11**). This Schläfli notion arises from envisaging each pentanuclear SBU as a nine-connected node and each ligand as a three-connecting node.

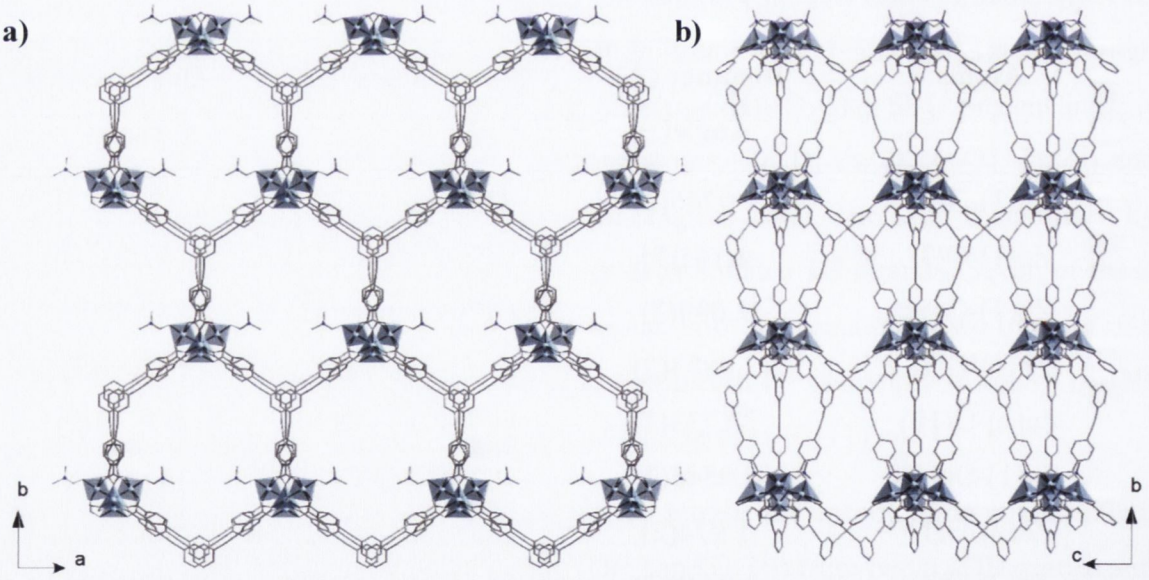


Figure 4.11: The network structure of **7** viewed in the direction of the crystallographic **a)** *c*-axis and **b)** *a*-axis. Colour code: Zn pale blue, C grey, N blue and O red. H atoms omitted for clarity.

Compound **7** is composed of dual interpenetrating symmetry equivalent frameworks (**Figure 4.12** and **Figure 4.14**). As was found in **6**, π-π stacking interactions, characterised

by a centroid-centroid distance of *ca.* 3.5 Å between aromatic groups of adjacent frameworks, ensures that the catenated networks are tightly interwoven. The solvent accessible void volume of **7** was calculated to be 49 % of the cell volume (7677 $Å^3$ of 15510 $Å^3$).[8] This void volume can be accessed *via* pore openings with cross sectional diameters of *ca.* 10.5 and 9 Å along the *c*-axis and in the [101] direction, respectively (**Figure 4.12**). The large void volume results in a low calculated crystal density of 0.868 g cm^{-3}.

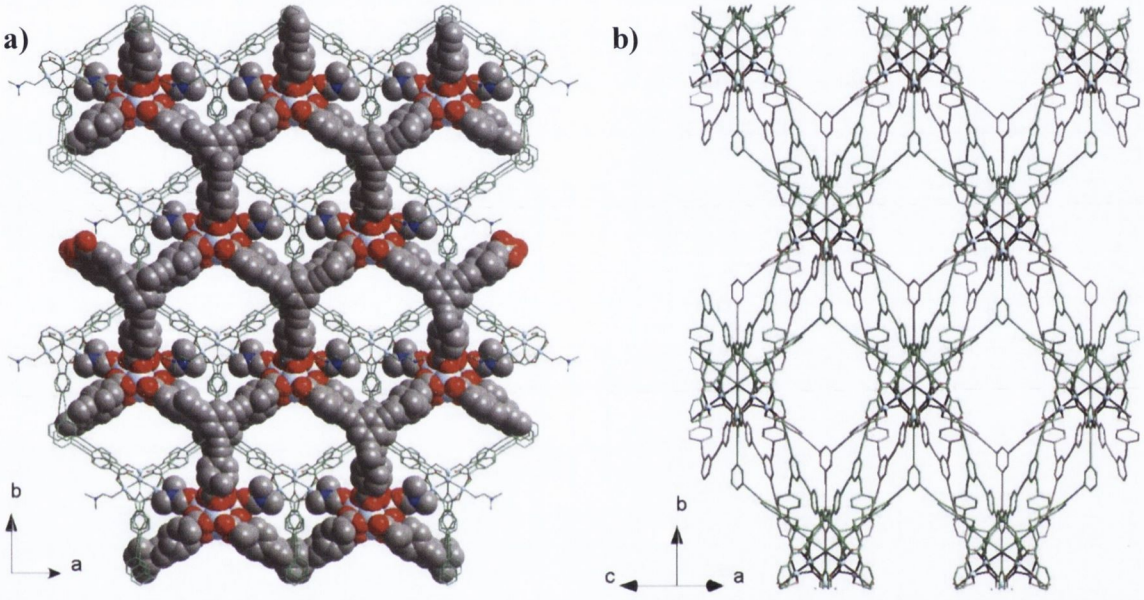


Figure 4.12: The dual interpenetrated frameworks present in **7** shown with **a)** one framework represented in a space filling model with the second as a green wireframe in the direction of the *c*-axis and **b)** one as a grey wireframe and the other as a green one with a view in the [101] direction. Colour code: Zn pale blue, C grey, N blue and O red. H atoms omitted for clarity.

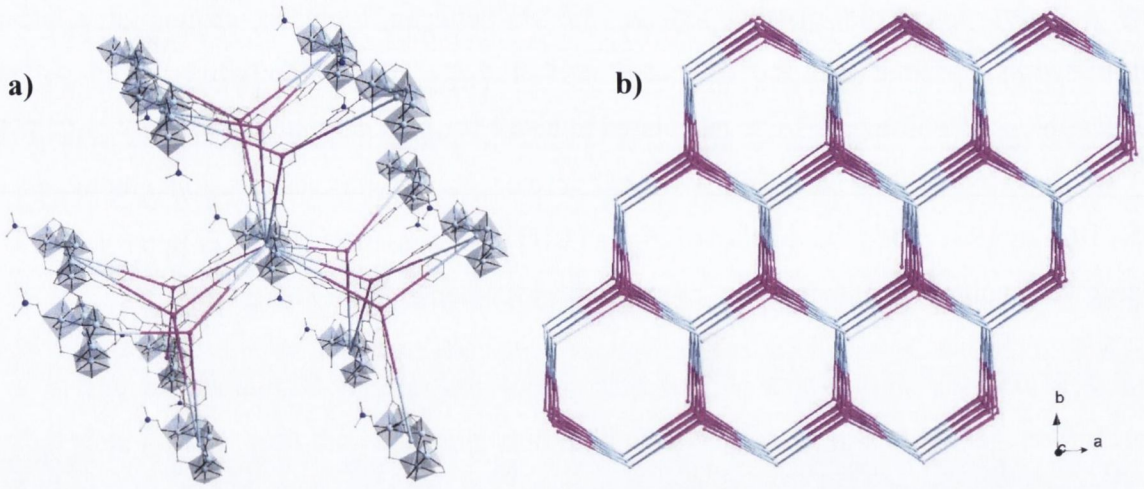


Figure 4.13: a) Simplification model used to generate the, **b)** $(4^2.6)_2(4^6.6^{27}.8^3)$ net topology found in **7**.

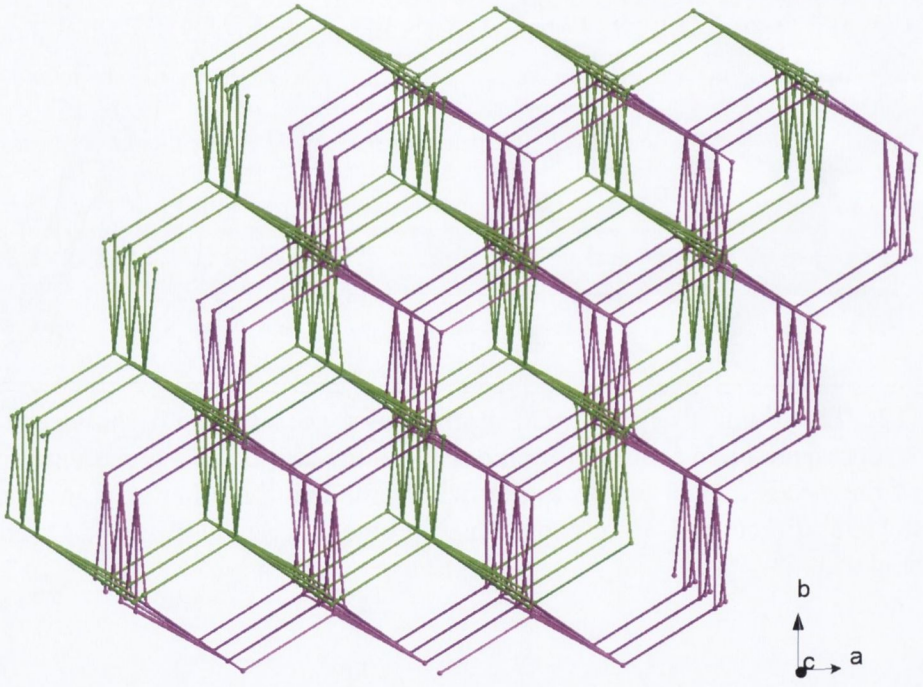


Figure 4.14: Simplified model of the two-fold interpenetrated frameworks found in **7**.

Table 4.4: Crystal data and details of the structure determination for **7**.

Identification code	**7**	
Empirical formula	$C_{105}H_{59}O_{22}N_2Zn_5$	
Formula weight	2027.39 g mol^{-1}	
Temperature	120 K	
Wavelength	0.71073 Å	
Crystal system	Monoclinic	
Space group	*C* 2/c	
Unit cell dimensions	a = 25.136 (2) Å	α= 90°.
	b = 37.055 (2) Å	β= 124.71 (2)°.
	c = 20.259 (4) Å	γ= 90°.
Volume	15510 (4) $Å^3$	
Z	4	
Density (calculated)	0.868 Mg/m^3	
Absorption coefficient	0.807 mm^{-1}	
F(000)	4116	
Crystal size	0.50 x 0.40 x 0.25 mm^3	
Theta range for data collection	1.10 to 25.68°	
Index ranges	$-29 \leq h \leq 30$, $-40 \leq k \leq 45$, $-24 \leq l \leq 21$	
Reflections collected	36437	
Independent reflections	14739 [R(int) = 0.0353]	
Completeness to theta = 25.68°	100 %	
Refinement method	Full-matrix least-squares on F^2	
Data / restraints / parameters	14739 / 0 / 597	
Goodness-of-fit on F^2	0.914	
Final R indices [I>2sigma(I)]	R_1 = 0.0472, wR_2 = 0.1303	
R indices (all data)	R_1 = 0.0672, wR_2 = 0.1385	
Largest diff. peak and hole	1.312 and -0.563 e.$Å^{-3}$	

4.4.2 Further characterisation of 7

A PXRD pattern of compound **7** was recorded and revealed the phase purity of the synthesised material and in addition provided further evidence for the accuracy of the refined single-crystal data (**Figure 4.15**). There was a gradual loss of crystallinity throughout the course of the measurement resulting from the evaporation of solvent DMF molecules and this may account for the broadening of signals.

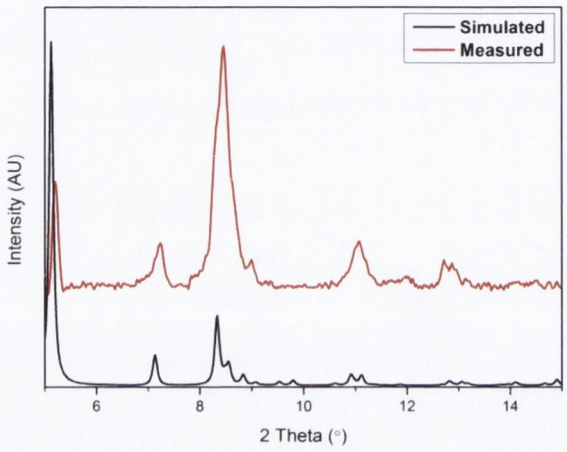


Figure 4.15: PXRD pattern of **7**, with the measured pattern in red and the simulated in black.

The FT-IR spectrum of **7** is characterised by several C=O stretching frequencies and an aromatic C=C stretching vibration between 1655 and 1547 cm^{-1}. This results from the overlapping of signals arising from the coordinated DMF molecules and the two separate carboxylate binding modes present in **7**. The strong band at 1386 cm^{-1} and an adjacent shoulder at 1402 cm^{-1} are from corresponding symmetric stretching vibrations (ν_sCOO) (**Figure 4.16**). As for **6**, the spectrum of 7 also reveals a broad signal centred at 3330 cm^{-1}, providing evidence for hydrogen bonding interactions between the solvent molecules.

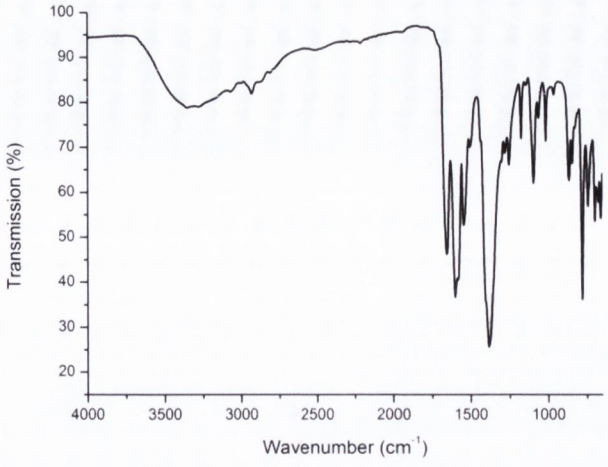


Figure 4.16: FT-IR spectrum of **7**.

The thermal stability of **7** was investigated by heating a freshly prepared sample between 25 and 900 °C and observing the subsequent weight loss (**Figure 4.17**). An initial weight loss of 29% can be ascribed to the loss of solvent and coordinated DMF molecules between *ca.* 25 and 240 °C. This desolvation was followed by the thermolysis of the proposed Me_2NH^+ counter ion between approximately 240 and 300 °C (calculated 1.6%, actual *ca.* 1.9%) and finally the thermal decomposition of the ligand results in a weight loss of 53% between 400 and 590 °C (calculated 55%). The end product is most likely an inorganic oxide.

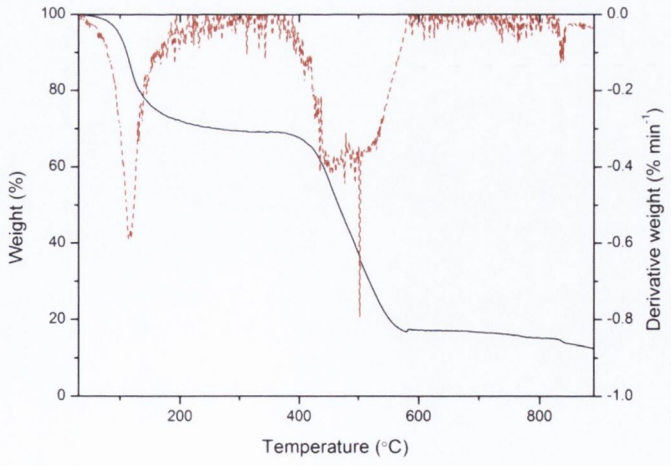


Figure 4.17: TGA of **7** performed in an air atmosphere, showing the percentage weight loss as a black line and the derivative of the percentage weight loss as the broken red line.

4.4.3 BET surface area determination of compound 7

In order to conduct surface area measurements on **7**, it was necessary to exchange the DMF molecules with a lower boiling point solvent. This was achieved by first soaking the crystals in acetone for three days, with the solution being refreshed daily. This was followed by the crystals being dispersed in DCM for a further three days and again the solvent was replenished daily. The crystals were then transferred into a quartz measuring cell and the sample heated under vacuum at 30 °C for one hour.

The N_2 isotherm displays a reversible isotherm and a BET surface area derived from this isotherm of 1338 $m^2 g^{-1}$ (**Figure 4.18**). In addition to this the H_2 sorption properties of **7** were studied at 77 K. The resulting isotherm revealed an uptake of 167 $cm^3 g^{-1}$ or 1.5 wt% at 77 K and 760 mmHg (**Figure 4.19**).

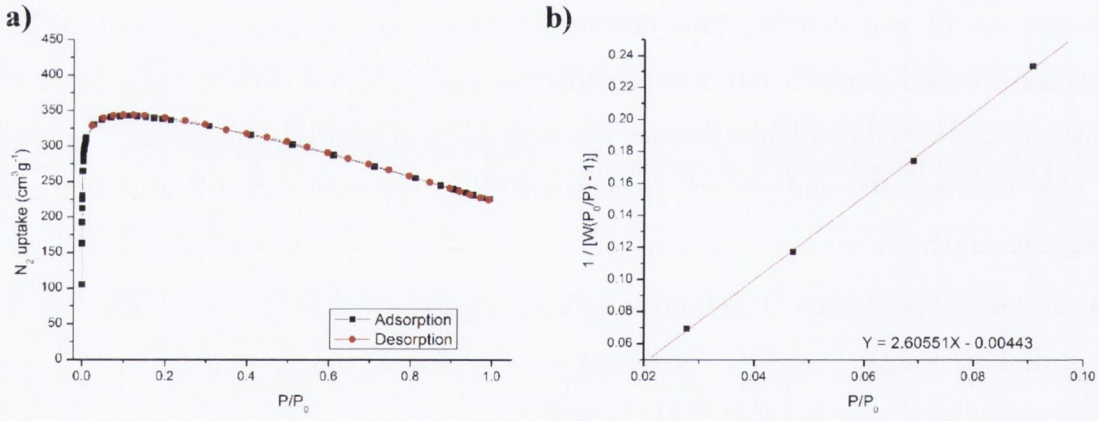


Figure 4.18: a) N_2 sorption isotherm of **7** measured at 77 K, **b)** plot of the linear region of the BET equation, derived from the N_2 adsorption isotherm of **7**.

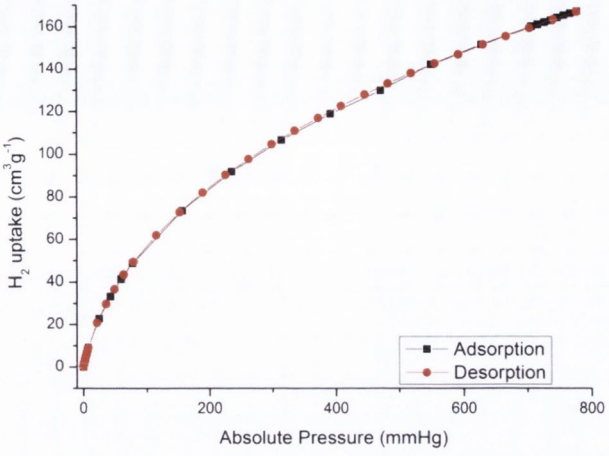


Figure 4.19: H_2 sorption isotherm of **7** measured at 77 K.

4.5 $(Me_2NH_2)[Co_5(\mathbf{L3})_3(\mu_3\text{-}OH)_2(DMF)_2]$, (**8**)

4.5.1 Synthesis and structural characterisation of compound **8**

The novel compound $(Me_2NH_2)[Co_5(\mathbf{L3})_3(\mu_3\text{-}OH)_2(DMF)_2]$, (**8**), was synthesised with a method analogous to that used for the synthesis of **7**, whereby $Co(NO_3)_2{\cdot}6H_2O$ and **L3** were reacted in a 6:1 mole ratio in DMF for four days at 85 °C. As was found for compound **7**, **8** crystallises in the monoclinic space group *C*2/c.

Refinement of the single crystal XRD data revealed that compound **8** is isostructural to **7**. The asymmetric unit of **8** contains one complete and one partially complete **L3** ligand, three distinct cobalt atoms (Co(1), Co(2) and Co(3)), a triply bridging OH group, a coordinated DMF molecule and two solvent DMF molecules. As observed for **7**, the resulting pentanuclear SBU is composed of two triangular arrangements of cobalt atoms (Co(1), Co(2), Co(3), $Co(1^{III})$ and $Co(3^{III})$) related through a C_2 symmetry operation (**Figure 4.20**). These metal clusters are again stabilised by seven bridging bidentate and two monodentate **L3** carboxylate groups (originating from nine separate ligands), two coordinated DMF molecules and two μ_3-OH groups.

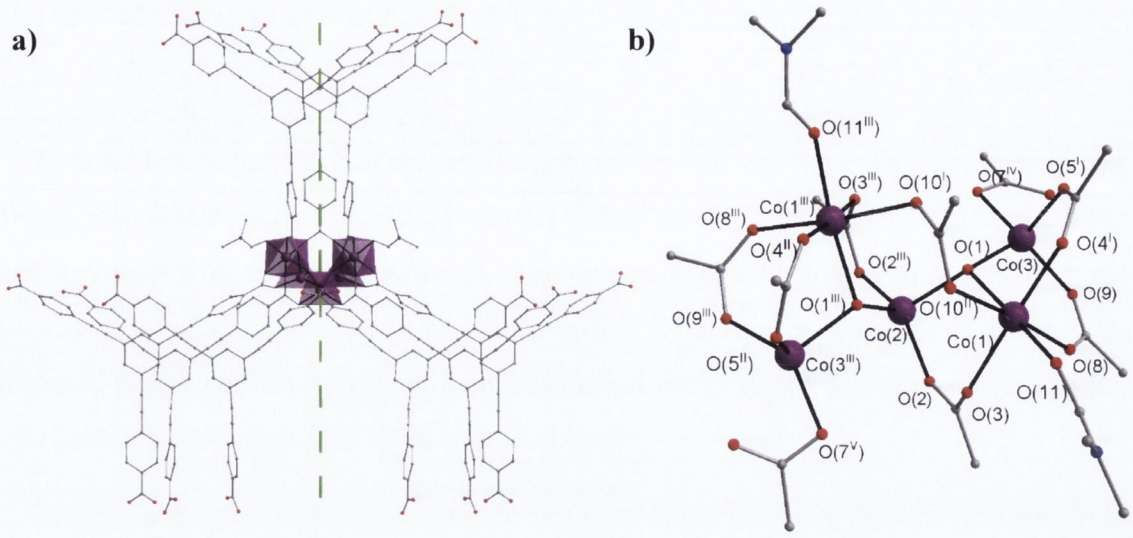


Figure 4.20: a), b) The $\{Co_5(\mu_3\text{-}OH)_2(O_2C)_9\}$ SBU stabilised by nine carboxylate groups and two μ_3-OH ligands. The dashed green line represents the C_2 symmetry axis. Symmetry codes: (I) 0.5-x, 0.5+y, 1.5-z; (II) 0.5+x, 0.5+y, z; (III) 1-x, y, 1.5-z; (IV) 1+x, y, 1+z; (V) -x, y, 0.5-z. Colour code: Co purple, C grey, N blue and O red. H atoms omitted for clarity.

The cobalt atoms Co(2) and Co(3) both adopt distorted tetrahedral coordination environments, where the Co-O bond distance vary between 1.940 (2) and 2.006(2) Å and are similar to the Zn-O bond lengths of Zn(2) and Zn(3) found in **7**. The distortion of the Co(3) coordination environment is most evident by observing the angle of $O(7^{IV})$-Co(3)-O(9) which at 132.26(2)° is significantly different from the ideal value of 109.5°. The cobalt atom Co(1) and its symmetry equivalents displays a slightly distorted octahedral coordination geometry with Co-O bond lengths ranging between 2.0791(2) and 2.160(2) Å. This distortion is most clearly demonstrated by observing the bond angle of 83.08(1)°generated by O(3)-Co(1)-O(8), and like the comparable bond angle of O(3)-Zn(1)-O(5) (82.86(8)°) in **7**, departs from the ideal angle of 90°.The relevant bond lengths are summarised in **Table 4.5** and are in accordance to previously reported values of related cobalt compounds that are stabilised by similar carboxylate functionalised ligands.[14]

The overall structure has the same two-fold interpenetrated topology found in **7** (**Figure 4.21** and **Figure 4.22**). Pore openings *ca.* 10.5 and 9.5 Å along the *c*-axis and [101] direction respectively give access to the void volume which was calculated to be 47% (7451 $Å^3$ out of a cell volume of 15957 $Å^3$). Consequently, as for **7**, this results in a low calculated crystal density of 0.892 g cm^{-3}.

Table 4.5: Selected bond distances and angles of the Co^{II} coordination environments found in **8**. Symmetry codes: Symmetry codes: (I) 0.5-x, 0.5+y, 1.5-z; (II) 0.5+x, 0.5+y, z; (III) 1-x, y, 1.5-z; (IV) 1+x, y, 1+z; (V) -x, y, 0.5-z.

Atoms	Distance (Å)/ Angle(°)	Atoms	Distance (Å)/ Angle(°)
Co(1)-O(1)	**2.0791(2)**	O(3)-Co(1)-O(8)	**83.08(1)**
Co(1)-O(3)	**2.136(2)**	O(3)-Co(1)-O(10^{II})	**92.87(8)**
Co(1)-O(4^{I})	**2.074(2)**	O(3)-Co(1)-O(11)	**87.83(9)**
Co(1)-O(8)	**2.088(2)**	O(4^{I})-Co(1)-O(8)	**96.28(1)**
Co(1)-O(10^{II})	**2.160(2)**	O(4^{I})-Co(1)-O(10^{II})	**87.60(9)**
Co(1)-O(11)	**2.073(2)**	O(4^{I})-Co(1)-O(11)	**89.72(9)**
Co(2)-O(1)	**2.002(2)**	O(8)-Co(1)-O(10^{II})	**174.47(8)**
Co(2)-O(2)	**1.940(2)**	O(8)-Co(1)-O(11)	**90.28(9)**
Co(3)-O(1)	**1.993(2)**	O(10^{II})-Co(1)-O(11)	**85.79(8)**
Co(3)-O(5^{I})	**2.006(2)**	O(1)-Co(2)-O(1^{III})	**95.28(1)**
Co(3)-O(7^{IV})	**1.992(3)**	O(1)-Co(2)-O(2)	**103.74(1)**
Co(3)-O(9)	**1.960(2)**	O(1)-Co(2)-O(2^{III})	**115.51(1)**
		O(2)-Co(2)-O(2^{III})	**120.54(2)**
O(1)-Co(1)-O(3)	**93.27(9)**	O(1)-Co(3)-O(5^{I})	**98.23(9)**
O(1)-Co(1)-O(4^{I})	**89.24(9)**	O(1)-Co(3)-O(7^{IV})	**103.53(2)**
O(1)-Co(1)-O(8)	**96.83(8)**	O(1)-Co(3)-O(9)	**107.00(1)**
O(1)-Co(1)-O(10^{II})	**87.13(8)**	O(5^{I})-Co(3)-O(7^{IV})	**106.86(2)**
O(1)-Co(1)-O(11)	**172.88(8)**	O(5^{I})-Co(3)-O(9)	**104.07(1)**
O(3)-Co(1)-O(4^{I})	**177.47(9)**	O(7^{IV})-Co(3)-O(9)	**132.26(2)**

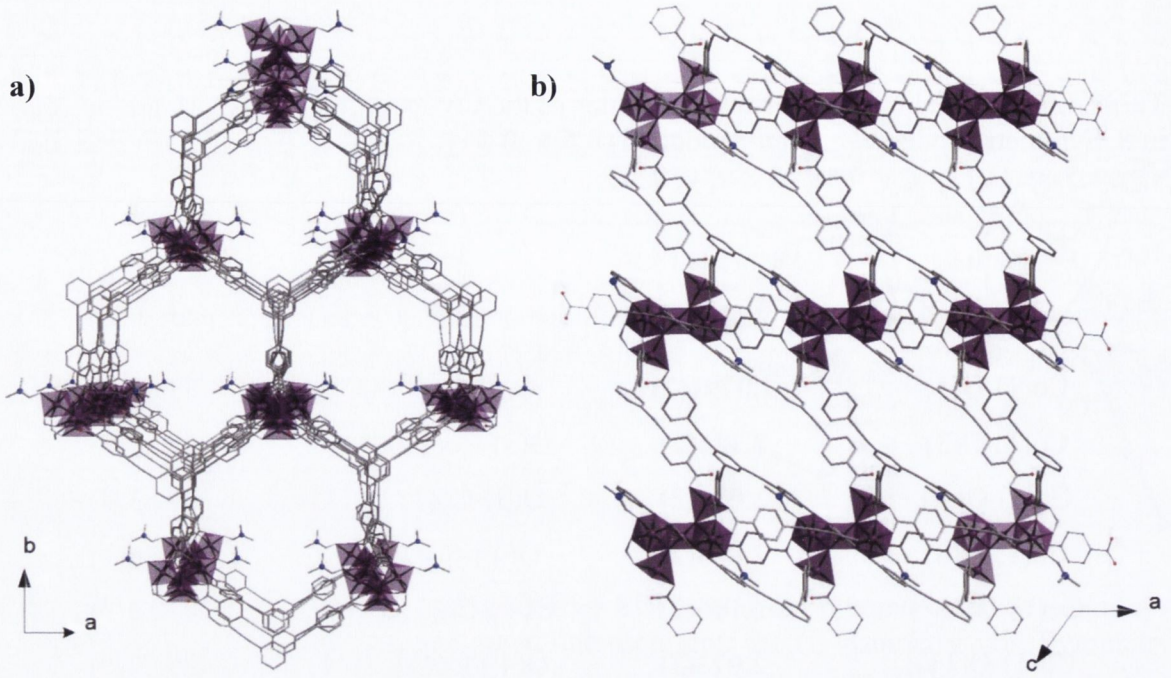


Figure 4.21: The network structure of **8** viewed in the direction of the crystallographic **a)** *c*-axis and **b)** *b*-axis. Colour code: Co purple, C grey, N blue and O red. H atoms omitted for clarity.

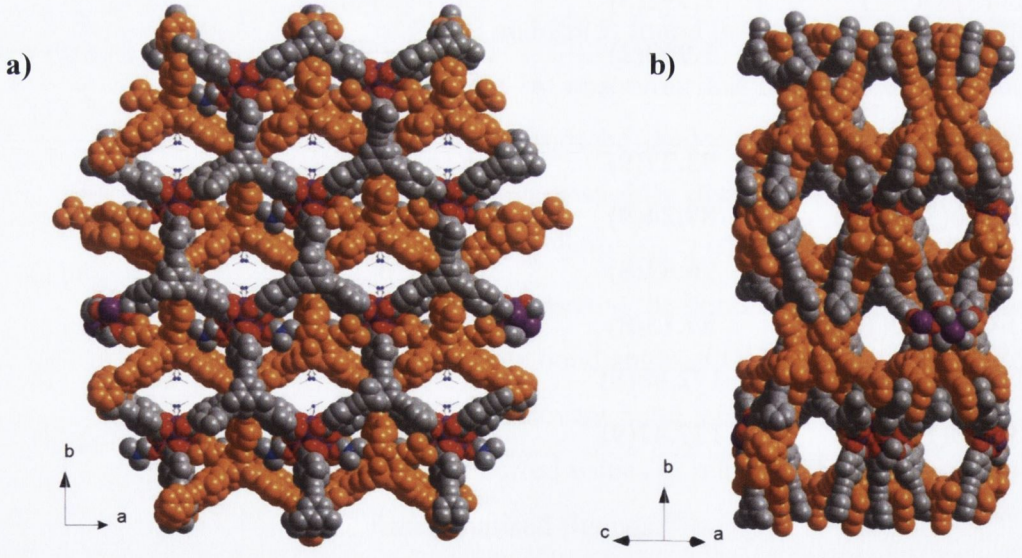


Figure 4.22: Space filling model of the two-fold interpenetrated frameworks in **8**, as viewed in the direction of the crystallographic **a)** *c*-axis and **b)** in the [101] direction. One framework has been highlighted orange with the remaining framework coloured according to the following colour scheme: Co purple, C grey, N blue and O red. H atoms have been omitted for clarity.

Table 4.6: Crystal data and details of the structure determination for **8**.

Identification code	**8**	
Empirical formula	$C_{111}H_{66}O_{24}N_4Co_5$	
Formula weight	2131.29 g mol^{-1}	
Temperature	230(2) K	
Wavelength	0.71073 Å	
Crystal system	Monoclinic	
Space group	*C* 2/c	
Unit cell dimensions	a = 25.582 (3) Å	α= 90°.
	b = 36.504 (4) Å	β= 125.82 (2)°.
	c = 21.075 (2) Å	γ= 90°.
Volume	15957 (3) $Å^3$	
Z	4	
Density (calculated)	0.892 Mg/m^3	
Absorption coefficient	0.557 mm^{-1}	
F(000)	4384	
Crystal size	0.50 x 0.40 x 0.3 mm^3	
Theta range for data collection	1.10 to 25.68°	
Index ranges	$-30 \leq h \leq 31$, $-44 \leq k \leq 22$, $-25 \leq l \leq 24$	
Reflections collected	37414	
Independent reflections	15154 [R(int) = 0.0516]	
Completeness to theta = 25.68°	100 %	
Refinement method	Full-matrix least-squares on F^2	
Data / restraints / parameters	15154 / 11 / 625	
Goodness-of-fit on F^2	0.942	
Final R indices [I>2sigma(I)]	R_1 = 0.0543, wR_2 = 0.1433	
R indices (all data)	R_1 = 0.0851, wR_2 = 0.1514	
Largest diff. peak and hole	0.665 and -0.659 e.$Å^{-3}$	

4.5.2 Further characterisation of **8**

PXRD analysis was conducted on a sample of **8** and confirmed the phase purity of the sample, as it closely matches that of a simulated PXRD pattern derived from the single-crystal XRD data (**Figure 4.23**). The gradual loss of crystallinity owing to the evaporation of solvent DMF molecules resulted in the broadening of signals in the measured pattern. Comparison of the respective PXRD patterns of **7** and **8** added additional evidence for their isostructural topologies. Furthermore, the recorded FT-IR spectrum of **8** fits very well with that of **7,** displaying the same overlapping stretching vibrations characteristic of **7** (**Figure 4.24**). TGA of **8** reveals a similar thermal decomposition pathway as found for **7**, with a weight loss of 28% between 25 and 260 °C which can be assigned to the removal of DMF molecules (both solvent and coordinated) and the thermolysis of the $MeNH_2^+$ counterion (**Figure 4.24**). This is followed by the oxidative degradation of the ligand between approximately 390 and 470 °C.

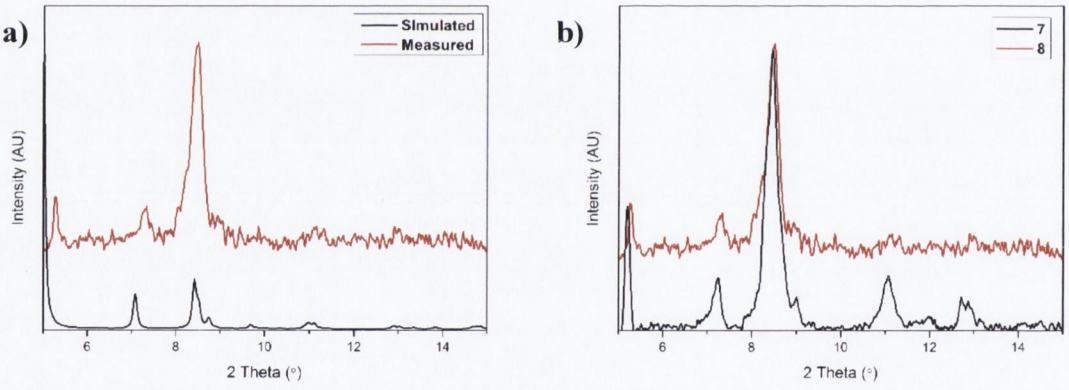


Figure 4.23: a) PXRD analysis of compound **8**, with the simulated pattern in black and the measured pattern in red, **b)** the PXRD pattern of **7** (black) plotted against **8** (red).

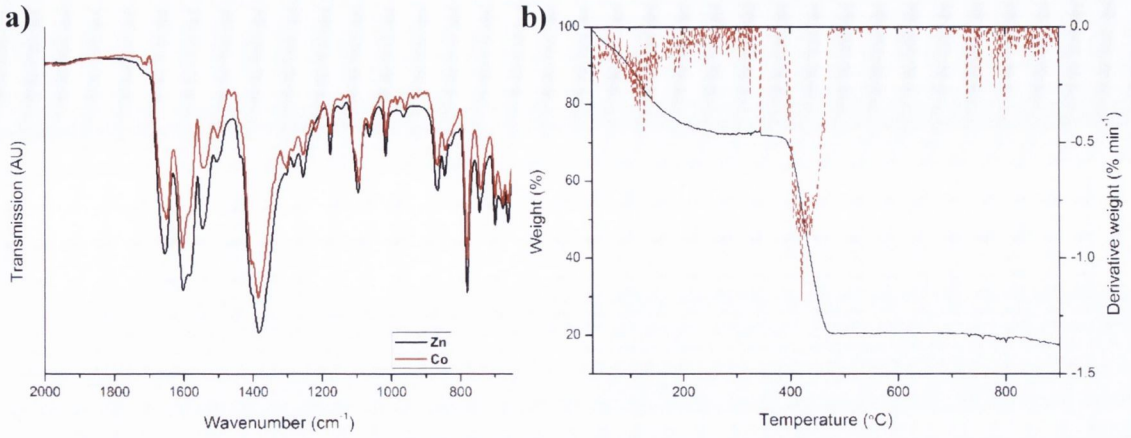


Figure 4.24: a) Comparison of the FT-IR spectra of the isostructural compounds **7** (black line) and **8** (red line), **b)** TGA of **8** performed in an air atmosphere, showing the percentage weight loss as a black line and the derivative of the percentage weight loss as the broken red line.

4.5.3 Surface area determination of compound **8**

A sample of **8** was activated prior to surface area measurements, using an analogous method to that used to remove solvent molecules from **7**. The resulting type 1 N_2 isotherm gave a BET surface area of *ca.* 1280 m^2g^{-1} (**Figure 4.25**). The H_2 sorption properties were investigated at 77 K and revealed an uptake of 110 cm^3 g^{-1} or *ca.* 1.2 wt% (**Figure 4.26**). The lower experimental surface of **8** compared to **7** may be due to the partial collapse of some of the pore openings upon removal of the solvent molecules under the applied activation conditions.

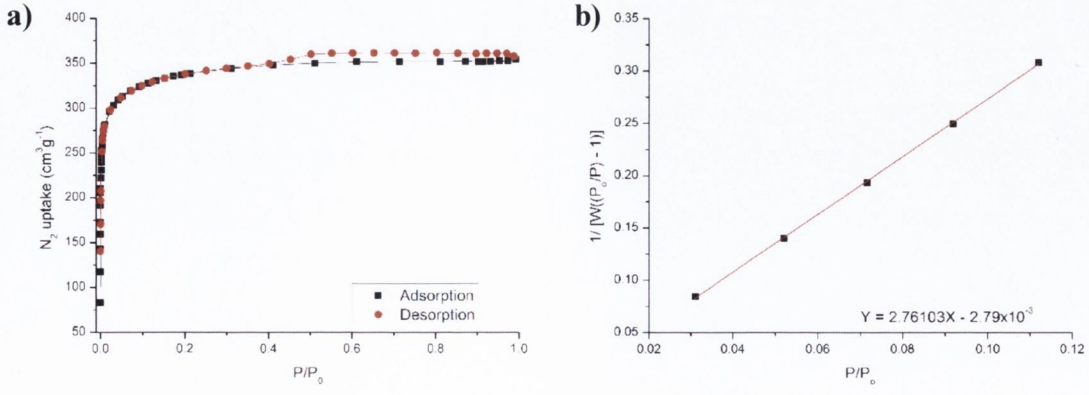


Figure 4.25: a) N_2 sorption isotherm of **8** measured at 77 K, **b)** plot of the linear region of the BET equation, derived from the N_2 adsorption isotherm of **8**.

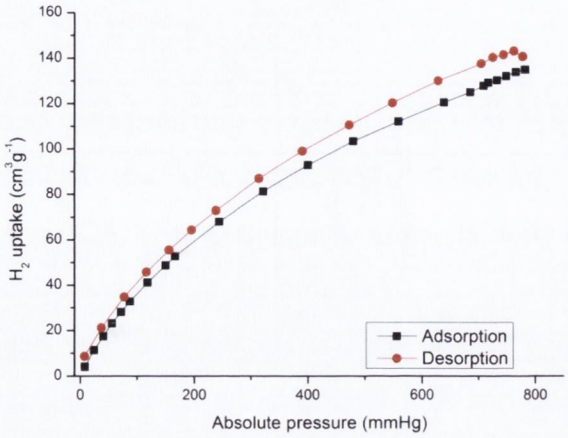


Figure 4.26: H_2 sorption isotherm of compound **8**, measured at 77 K.

4.6 $[Cu_3(\mathbf{L3})_2(H_2O)_3]$, (9)

MOF-14, $[Cu_3(BTB)_2(H_2O)_3]\cdot(DMF)_9(H_2O)_2$ is a dual-interpenetrated network, composed of interwoven **pto**-type frameworks of dinuclear copper paddlewheel SBUs, linked *via* 4,4',4"-benzene-1,3,5-triyl-tribenzoate (BTB).[15] After admiring the impressive structural features of MOF-14 and those of the recently published non-interpenetrated analogue DUT-34 reported by Kaskel *et al.*, we decided to investigate whether it would be possible to utilise an extended version of BTB to generate a new, even further augmented **pto**-type framework.[16] Our synthetic efforts resulted in the successful synthesis of the coordination compound $[Cu_3(\mathbf{L3})_2(H_2O)_3]$, (**9**).

4.6.1 Synthesis and structural characterisation of compound **9**

The treatment of $Cu(NO_3)_2\cdot 3H_2O$ and **L3** in DMF in a mole ratio of 1.5:1, at 85 °C yielded turquoise rhombic crystals of **9**. It was found that **9** crystallises in the cubic space group $Im\bar{3}$. The asymmetric unit of **9** is composed of two distinct copper ions, one third of a **L3** ligand and two coordinated water molecules, with the resulting structure being generated through symmetry operations.

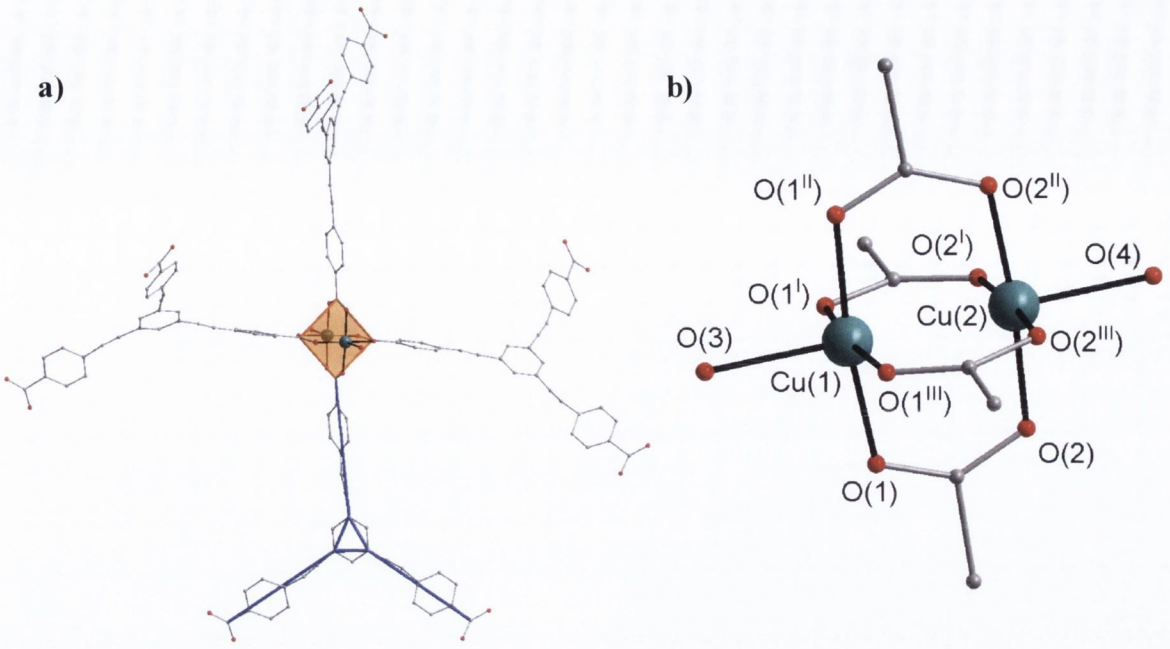


Figure 4.27: a), b) The $\{Cu_2(COO)_4(H_2O)_2\}$ SBU present in **9** stabilised by four **L3** bridging bidentate carboxylate groups. The blue bonds are used to represent the triangular SBU of **L3** and the orange square is utilised to depict the copper paddlewheel complex as a square planar SBU. Symmetry codes: (I) x, -y, z, (II) 1-x, -y, z, (III) 1-x, y, z. Colour code: Cu teal, C grey and O red. H atoms omitted for clarity.

The SBUs present in **9** are dinuclear copper paddlewheel complexes $\{Cu(COO)_4\}$, whereby the two copper ions are linked *via* four O,O'-*syn*, *syn* bridging bidentate carboxylate groups, derived from four separate fully deprotonated **L3** ligands (**Figure 4.27**). The carboxylate groups of the complex are arranged at *ca.* 90° angles relevant to each other. The apical positions of the paddlewheel are provided by coordinated water molecules, with the individual copper ions each adopting a distorted square pyramidal geometry, whereby there is an interatomic Cu···Cu distance of 2.611(3) Å. The Cu-$O_{carboxylate}$ bond lengths range between 1.922(5) and 1.963 (4) Å and the Cu-O_{water} bond lengths are 2.185(1) and 2.227(1) Å and are in accordance to previously reported values for copper paddlewheel complexes.[17] A more detailed list of bond lengths and angles can be found in **Table 4.7**.

Table 4.7: Selected bond distances and angles of the Cu^{II} coordination environments found in **9**. Symmetry codes: (I) x, -y, z, (II) 1-x, -y, z, (III) 1-x, y, z.

Atoms	Distance (Å)/ Angle(°)	Atoms	Distance (Å)/ Angle(°)
Cu(1)-O(1)	**1.963(4)**	O(1)-Cu(1)-O(1^{III})	**87.9(3)**
Cu(1)-O(3)	**2.227(1)**	O(1)-Cu(1)-O(3)	**93.89(1)**
Cu(2)-O(2)	**1.922(5)**	O(2)-Cu(2)-O(2^{I})	**88.7(3)**
Cu(2)-O(4)	**2.185(1)**	O(2)-Cu(2)-O(2^{II})	**174.0(3)**
		O(2)-Cu(2)-O(2^{III})	**91.0(3)**
O(1)-Cu(1)-O(1^{I})	**91.6(3)**	O(2)-Cu(2)-O(4)	**93.0(1)**
O(1)-Cu(1)-O(1^{II})	**172.2(3)**		

Each **L3** ligand is coordinated to six copper ions, *i.e.* three separate paddlewheel units, *via* their three carboxylate groups, with each individual SBU being coordinated to four **L3** ligands. This has the effect of generating a 3D MOF (**Figure 4.28**). By envisaging the copper paddlewheel units as a four connected node and the central benzene units of the **L3** ligands as a triangular node, it is possible to compare the resulting structure to that of the well-known **pto**-type topology with a Schläfli symbol of $(8^3)_4(8^6)_3$ (**Figure 4.29**).

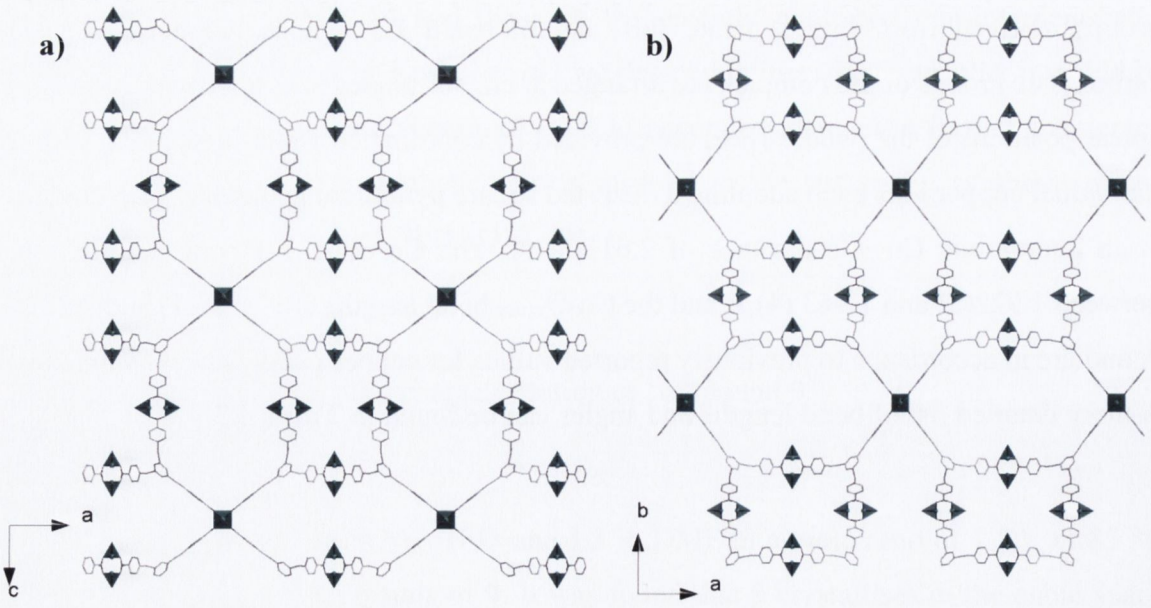


Figure 4.28: The network structure of **9** as seen in the crystallographic **a)** *b*-axis **b)** *c*-axis. Colour code: Cu teal, C grey and O red. H atoms omitted for clarity.

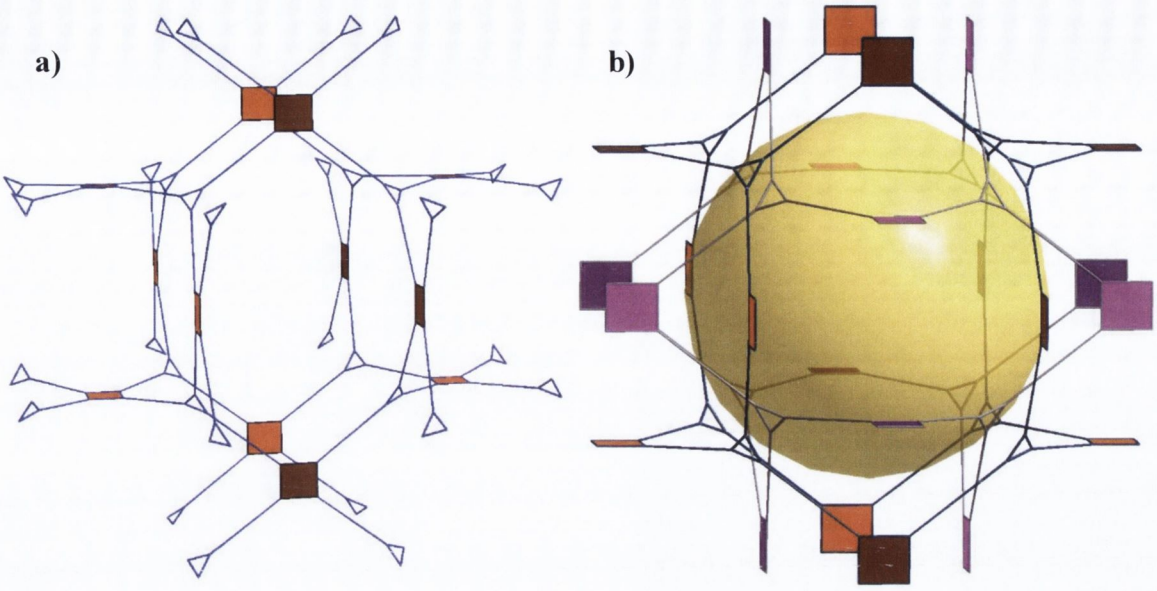


Figure 4.29: Schematic of **a)** the **pto** topology and, **b) pto-c** topology of the two-fold interpenetrated networks found in **9**. The triangular units represent the central phenyl moieties of the **L3** ligands, with the squares representing the plane of the rectangular copper paddlewheel SBUs, (see Figure 4.27). The yellow sphere, with a cross sectional diameter of 25 Å, depicts the cavity generated by the interpenetrated frameworks.

As was found in the other compounds discussed in this chapter, the structure of **9** is composed of two interwoven frameworks and so it can be classified as a **pto-c** framework, where the **c** indicates that it is a catenated framework (**Figure 4.30** and **Figure 4.32**). Supramolecular interactions promote the close packing of the ligand moieties, with an average distance of 3.30 Å between the centres of adjacent aromatic units of neighbouring frameworks. The structure contains internal cavities that are *ca.* 25 Å in diameter, that are accessible through hydrophilic windows 13 x 6 Å in width, resulting in a large solvent accessible void volume of 77% of the cell volume (30588 $Å^3$ out of a total volume of 39725 $Å^3$).[8] The very high the void volume present in **9** is responsible for the remarkably low calculated crystal density of 0.421 g cm^{-3}.

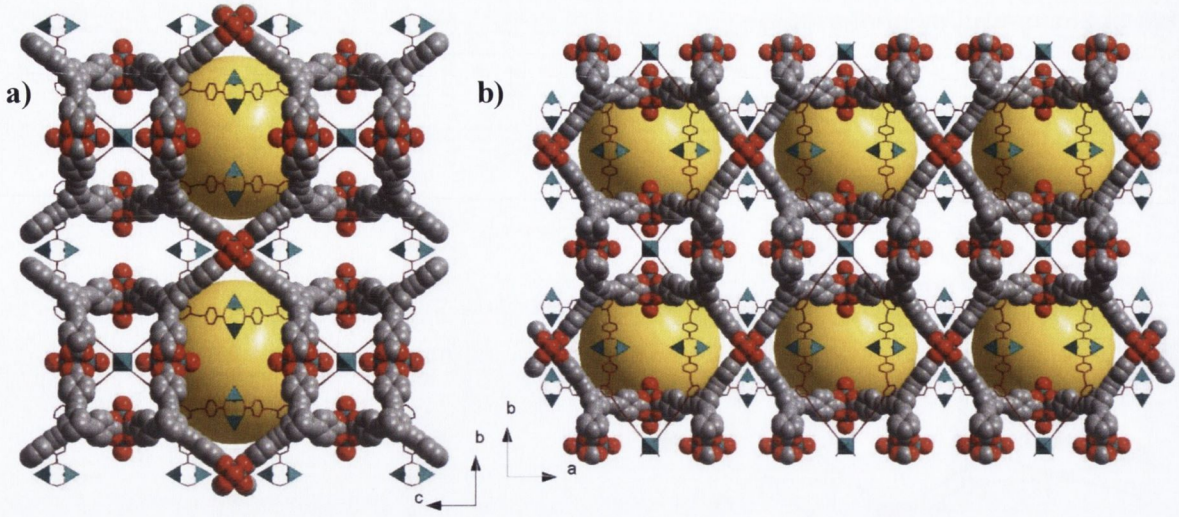


Figure 4.30: The interpenetrated networks found in **9**, as viewed in the directions of the crystallographic **a)** *a*-axis and **b)** *c*-axis. One framework is represented as a space filling model, with the second as a ball and stick model, with the individual bonds coloured red. The yellow spheres, with a cross sectional diameter of *ca.* 25 Å, depict the cavities generated by the interpenetrated frameworks. Colour code: Cu teal, C grey and O red. H atoms omitted for clarity.

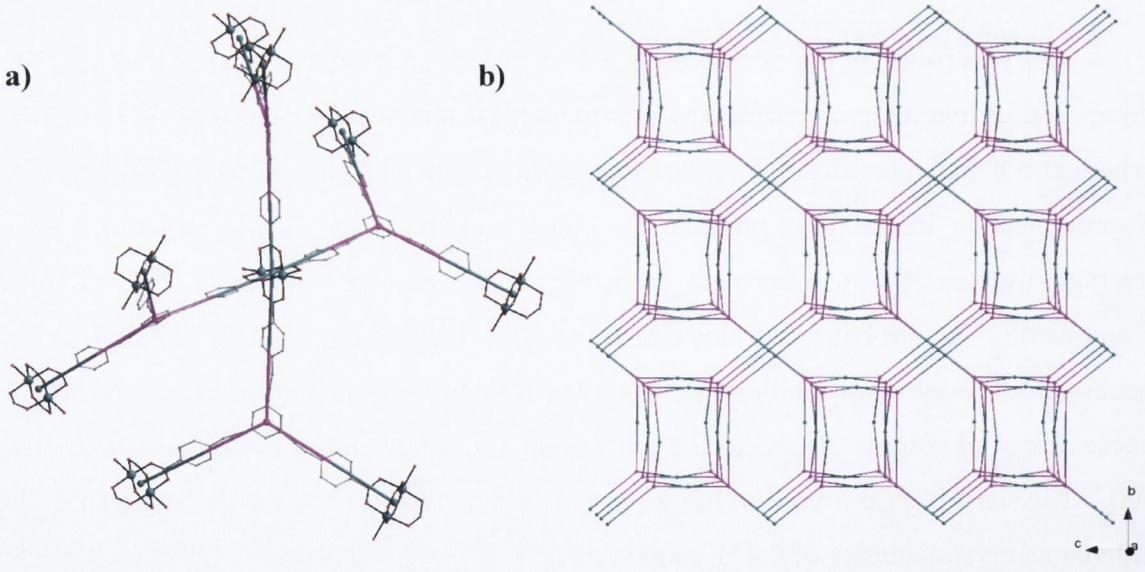


Figure 4.31: a) Simplification model used to generate the, **b)** $(8^3)_4(8^6)_3$ net topology found in **9**.

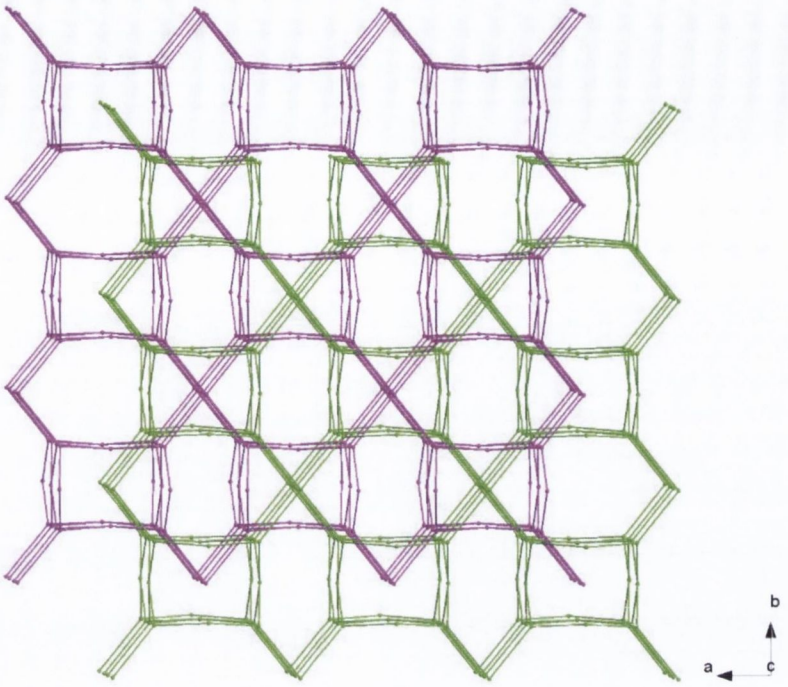


Figure 4.32: Simplified model of the two-fold interpenetrated networks found in **9**.

Table 4.8: Crystal data and details of the structure determination for **9**.

Identification code	**9**	
Empirical formula	$C_{22}H_{12}O_5Cu$	
Formula weight	419.87	
Temperature	223(2) K	
Wavelength	0.71073 Å	
Crystal system	Cubic	
Space group	$Im\bar{3}$	
Unit cell dimensions	a = 34.121(1) Å	α= 90°.
	b = 34.121(1) Å	β= 90°.
	c = 34.121(1) Å	γ= 90°.
Volume	39725(5) $Å^3$	
Z	24	
Density (calculated)	0.421 Mg/m^3	
Absorption coefficient	0.339 mm^{-1}	
F(000)	5112	
Crystal size	0.50 x 0.40 x 0.4 mm^3	
Theta range for data collection	1.688 to 20.944°	
Index ranges	$-33\leq h\leq 33$, $-32\leq k\leq 31$, $-34\leq l\leq 22$	
Reflections collected	34767	
Independent reflections	3744 [R(int) = 0.2032]	
Completeness to theta = 20.944°	99.1%	
Refinement method	Full-matrix least-squares on F^2	
Data / restraints / parameters	3744 / 19 / 122	
Goodness-of-fit on F^2	0.938	
Final R indices [I>2sigma(I)]	R_1 = 0.1169, wR_2 = 0.2594	
R indices (all data)	R_1 = 0.1964, wR_2 = 0.2972	
Largest diff. peak and hole	1.14 and -0.33 $e.Å^{-3}$	

4.6.2 Further characterisation of **9**

The rapid evaporation of the DMF molecules residing in the pores of **9** when left in an open atmosphere, led to a loss of crystallinity and thus prevented the recording of a PXRD pattern for **9**. In a comparable manner to the FT-IR spectra of the other compounds described in this chapter, the spectrum of **9** contains several signals between 1658 and 1540 cm^{-1} arising from the overlapping C=O stretches of DMF and bridging carboxylate groups and aromatic C=C stretching vibrations (**Figure 4.33**). Corresponding asymmetric C=O bands are present at 1404 and 1383 cm^{-1}. The broad band centred at 3200 cm^{-1}, indicates the presence of hydrogen bonding interactions between solvent molecules.

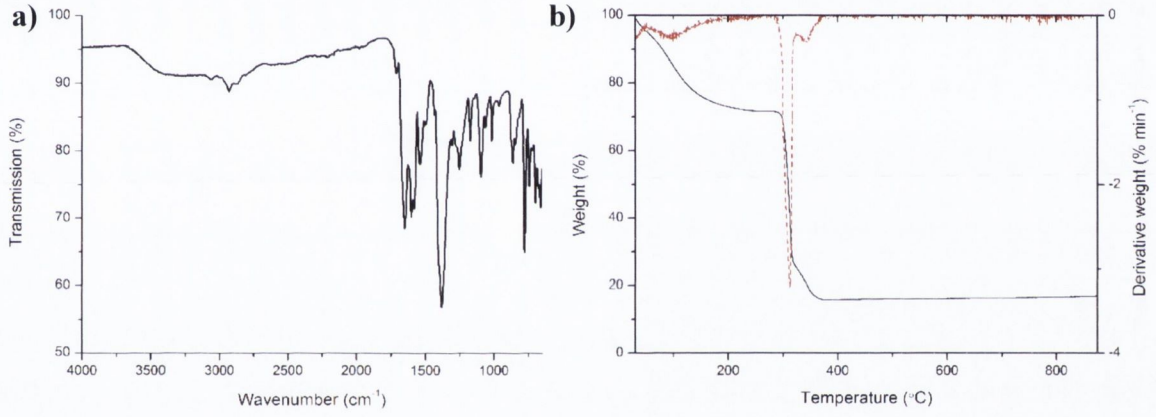


Figure 4.33: a) FT-IR spectrum and **b)** TGA of compound **9**.

Upon heating a sample of **9** in an air atmosphere, there is an initial weight loss of 28% between 25 and 230 °C, resulting from the loss of solvent DMF molecules and the coordinated water molecules (**Figure 4.33**). This is followed by the thermal decomposition of the ligand between *ca.* 280 and 380 °C (actual 57%, theoretical 60%). The TGA data indicates that the formula is $[Cu_3(\mathbf{L3})_2(H_2O)_3]\cdot 6DMF$, however, there was almost certainly a loss of solvent prior to initiating the experiment, as a result the formula is most likely different when it is stored in its mother liquor.

As for compound **6**, the solvent molecules present in the cavities of **9** appear to stabilise the framework, with the structure of **9** seeming to collapse upon removal of the guest molecules that reside in the void space. Consequently, gas storage and BET analysis of the compound have thus far proven to be unsuccessful.

4.7 Conclusion

The ligand **L3** was chosen for its polydentate and extended nature, which renders it ideal for the preparation of highly augmented porous MOFs. It was synthesised according to a four step reaction scheme involving two Sonogashira coupling reactions, a *retro*-Favorski reaction and an ester hydrolysis. Our choice of ligand was vindicated as it facilitated the formation of four 3D MOFs with large void volumes, namely compounds **6**-**9**. The rigidity of the ligand gives rise to the permanent porosity of compounds **7** and **8**.

Compound **6** is composed of trinuclear zinc hourglass SBUs, where the central zinc ion is in an octahedral coordination environment and is triply bridged *via* **L3** carboxylate groups to two adjacent zinc ions, which both adopt tetrahedral coordination geometries. The zinc clusters are linked to neighbouring SBUs through **L3** ligands to generate a 3D MOF with an augmented topology. The structure of **6** is composed of two such networks to give a two-fold interpenetrated network, with a solvent accessible void volume of 68%.

During the synthesis of **6** it was noticed that large block shaped crystals formed as opposed to the needle like crystals characteristic of **6** when the molar ratio of Zn^{II}:**L3** was increased beyond 4:1. Single-crystal XRD revealed these to be of the novel compound. $(Me_2NH_2)[Zn_5(\mathbf{L3})_3(\mu_3\text{-}OH)_2(DMF)_2]$, (**7**), which contains pentanuclear zinc based SBUs, composed of two triangular arrangements of zinc ions, stabilised by nine **L3** carboxylate groups, two μ_3-OH groups and two coordinated DMF molecules. Through symmetry operations a 3D MOF is formed. As for **6**, the structure of **7** is two-fold interpenetrated, with a void volume of 49%. The phase purity of the bulk material was verified by PXRD analysis. The catenation appeared to stabilise the network structure which maintains its integrity in a solvent free form. BET surface area analysis revealed **7** to have a surface area of 1338 $m^2 g^{-1}$ and a hydrogen storage capacity of *ca.* 1.5 wt% at 77 K and 760 mmHg.

$(Me_2NH_2)[Co_5(\mathbf{L3})_3(\mu_3\text{-}OH)_2(DMF)_2]$, (**8**), was synthesised using a comparable method to that used for **7** and single-crystal XRD revealed it to be isostructural to **7**, with FT-IR and PXRD studies confirming this. The type 1 N_2 sorption isotherm of an activated sample of **8** equated to a BET surface area of 1280 $m^2 g^{-1}$ and a corresponding hydrogen storage capacity of 1.2 wt% at 77 K and 760 mmHg.

Finally, $[Cu_3(\mathbf{L3})_2(H_2O)_3]$, (**9**), is a two-fold interpenetrated network, composed of dinuclear copper paddlewheel SBUs, stabilised by four bridging **L3** carboxylate groups.

Through the organic linker a 3D MOF with a **pto**-type topology is formed. The closely packed 2-fold interwoven networks in **9** give rise to an augmented topology with a very large solvent accessible void volume of 77% of the unit cell volume.

4.8 References

1. M. P. Suh, H. J. Choi, S. M. So and B. M. Kim, *Inorganic Chemistry*, 2003, **42**, 676-678.
2. H. Furukawa, N. Ko, Y. B. Go, N. Aratani, S. B. Choi, E. Choi, A. O. Yazaydin, R. Q. Snurr, M. O'Keeffe, J. Kim and O. M. Yaghi, *Science*, 2010, **329**, 424-428.
3. N. Kobayashi and M. Kijima, *Journal of Materials Chemistry*, 2008, **18**, 1037-1045.
4. D. L. Trumbo and C. S. Marvel, *Journal of Polymer Science Part a-Polymer Chemistry*, 1986, **24**, 2311-2326.
5. K. Sonogashira, Y. Tohda and N. Hagihara, *Tetrahedron Letters*, 1975, 4467-4470.
6. H. Kukula, S. Veit and A. Godt, *European Journal of Organic Chemistry*, 1999, 277-286.
7. N. Y. Zhu, G. Tobin and W. Schmitt, *Chemical Communications*, 2012, **48**, 3638-3640.
8. U. Glasgow, *Platon*, 2006, **1.10**, A Multipurpose Crystallographic Tool.
9. C. A. Williams, A. J. Blake, P. Hubberstey and M. Schröder, *Chemical Communications*, 2005, 5435-5437.
10. C. A. Bauer, T. V. Timofeeva, T. B. Settersten, B. D. Patterson, V. H. Liu, B. A. Simmons and M. D. Allendorf, *Journal of the American Chemical Society*, 2007, **129**, 7136-7144.
11. X. F. Wang, Y. B. Zhang, X. N. Cheng and X. M. Chen, *Crystengcomm*, 2008, **10**, 753-758.
12. K. Gedrich, M. Heitbaum, A. Notzon, I. Senkovska, R. Fröhlich, J. Getzschmann, U. Mueller, F. Glorius and S. Kaskel, *Chemistry-a European Journal*, 2011, **17**, 2099-2106.
13. S. Geranmayeh, A. Abbasi, A. H. Zarnani and M. Y. Skripkin, *Polyhedron*, 2013, **61**, 6-14.
14. F. Luo, Y. X. Che and J. M. Zheng, *Crystal Growth & Design*, 2009, **9**, 1066-1071.
15. B. L. Chen, M. Eddaoudi, S. T. Hyde, M. O'Keeffe and O. M. Yaghi, *Science*, 2001, **291**, 1021-1023.

16. N. Klein, I. Senkovska, I. A. Baburin, R. Grunker, U. Stoeck, M. Schlichtenmayer, B. Streppel, U. Mueller, S. Leoni, M. Hirscher and S. Kaskel, *Chemistry-a European Journal*, 2011, **17**, 13007-13016.

17. X. Lin, I. Telepeni, A. J. Blake, A. Dailly, C. M. Brown, J. M. Simmons, M. Zoppi, G. S. Walker, K. M. Thomas, T. J. Mays, P. Hubberstey, N. R. Champness and M. Schröder, *Journal of the American Chemical Society*, 2009, **131**, 2159-2171.

Chapter 5

Lanthanide-organic frameworks

5 Lanthanide-organic frameworks

5.1 Introduction

As was highlighted in section 1.4, research into LnMOFs is very much in its infancy, yet porous compounds of this type have shown to be highly adept materials for the sensing of ions and molecular species.[1,2,3] Utilising the knowledge accrued through the preparation of the high surface area Zn^{II} and Co^{II} based MOFs discussed in chapter 4, we set out to generate a new series of porous LnMOFs and to characterise their structural topologies and photoluminescent properties.

The extended nature and proven ability to form porous 3D MOFs, owing to its rigid structure and polydentate nature, makes **L3** an ideal candidate for the formation of permanently porous MOFs. In addition to this, we decided to exploit the less-extended ligand **L2** that contains N- and O- donor functionalities, as the structures outlined in Chapter 3 identified it as a versatile ligand that readily forms coordination networks.

5.2 [Ho(**L3**)$(H_2O)_2$], (**10**)

5.2.1 Synthesis and structural characterisation of compound **10**

Pale pink needle like crystals of [Ho(**L3**)$(H_2O)_2$], **10**, form *via* the reaction of $Ho(NO_3)\bullet 5H_2O$ and two mole equivalents of **L3** in DMF at 100 °C. The compound crystallises in the orthorhombic space group *I*ma/2 and the phase purity of the bulk material was confirmed *via* PXRD. During the data processing of the single-crystal X-ray data the program Platon SQUEEZE was employed to account for diffuse diffraction data that results from a large number of disordered solvent molecules which reside in the channels of **10**.[4] However, despite this analysis approach, the rather small size of the crystals made characterisation by single-crystal XRD difficult, resulting in a relatively high R1 value of 0.1388.

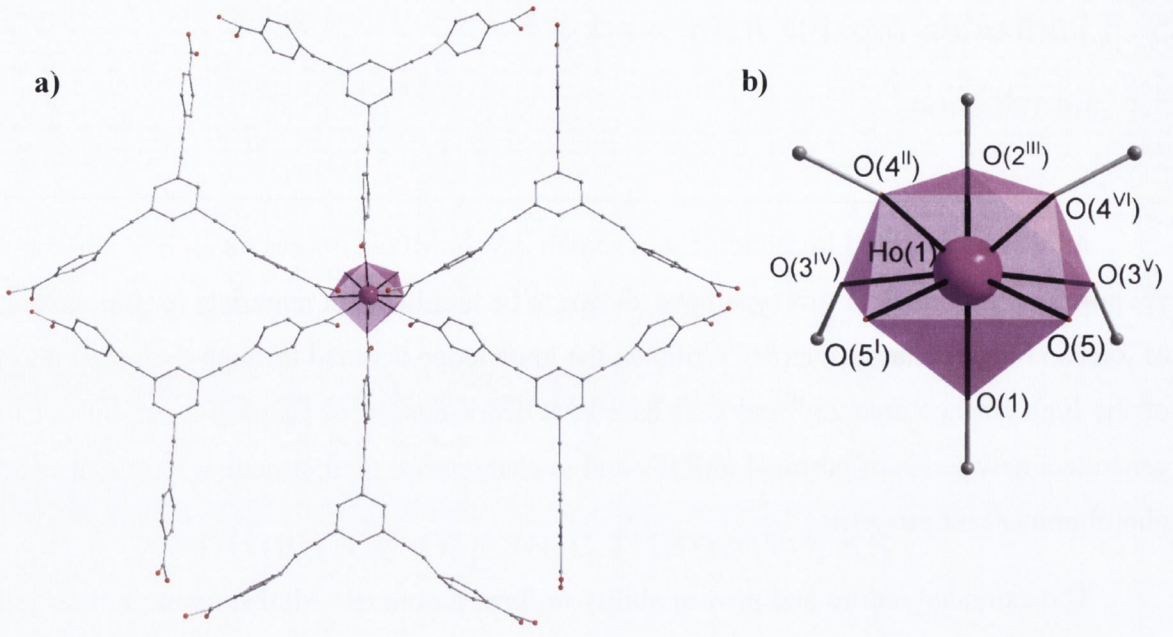


Figure 5.1: a) Ho^{III} coordination environment in **10**, **b)** Ho^{III} centre coordinated to six separate fully deprotonated **L3** ligands. Symmetry codes: (I) 1.5-x, y, z; (II) -0.5+x, 0.5+y, 0.5+z; (III) 1.5-x, 0.5-y, 0.5+z; (IV) -0.5+x, -y, z; (V) 2-x, -y, z; (VI) 2-x, 0.5+y, 0.5+z. Colour code: Ho pink, C grey, O red. H atoms omitted for clarity.

The asymmetric unit of **10** is composed of one symmetry independent Ho^{III} ion, one water molecule and half of a deprotonated **L3** ligand. The individual Ho^{III} ions are eight-fold coordinated, resulting in a highly distorted octa-coordinated geometry. The absence of significant ligand field stabilisation for lanthanide systems may explain the distorted nature of the coordination environment. The individual metal centres are coordinated to six oxygen atoms that arise from six separate deprotonated **L3** carboxylate groups, (O(1), $O(2^{III})$, $O(3^{IV})$, $O(3^{V})$, $O(4^{II})$, $O(4^{VI})$) and to a further two oxygen atoms (O(5), $O(5^{I})$) from two *cis*-coordinating water molecules (**Figure 5.1**).

The distortion is effectively demonstrated by observing the significantly different Ho-$O_{carboxylate}$ bond lengths, which vary in length from 2.12(3) to 2.367(2) Å. The bond lengths of 2.12(3) and 2.22(2) Å for Ho(1)–$O(4^{II})$ and Ho(1)–O(1) are lower than expected and most likely result from the difficult refinement of the diffraction data. However, the remaining bond lengths are in the range of previously report Ho^{III} complexes, as are the coordinated water molecules which have slightly longer Ho-O bond lengths of 2.462(2) Å.[5,6] A detailed list of bond lengths and angles can be found in **Table 5.1**.

Table 5.1: Selected bond distances and angles of the Ho^{III} coordination environment found in **10**. Symmetry codes: (I) 1.5-x, y, z; (II) -0.5+x, 0.5+y, 0.5+z; (III) 1.5-x, 0.5-y, 0.5+z; (IV) -0.5+x, -y, z; (V) 2-x, -y, z; (VI) 2-x, 0.5+y, 0.5+z.

Atoms	**Distance (Å)/ Angle (°)**	**Atoms**	**Angle(°)**
Ho(1)–O(1)	**2.22(2)**	$O(2^{III})$–Ho(1)–$O(3^{IV})$	**78.4(6)**
Ho(1)–$O(2^{III})$	**2.367(2)**	$O(2^{III})$–Ho(1)–$O(4^{II})$	**80.6(2)**
Ho(1)–$O(3^{IV})$	**2.347(2)**	$O(2^{III})$–Ho(1)–O(5)	**134.4(7)**
Ho(1)–$O(4^{II})$	**2.12(3)**	$O(3^{IV})$–Ho(1)–$O(4^{II})$	**61.2(1)**
Ho(1)–O(5)	**2.462(2)**	$O(3^{IV})$–Ho(1)–$O(4^{VI})$	**152.2(2)**
		$O(3^{IV})$–Ho(1)–O(5)	**146.5(6)**
O(1)–Ho(1)–$O(2^{III})$	**125.1(1)**	$O(3^{IV})$–Ho(1)–$O(5^{I})$	**73.1(6)**
O(1)–Ho(1)–$O(3^{IV})$	**79.3(5)**	$O(4^{II})$–Ho(1)–O(5)	**110.7(2)**
O(1)–Ho(1)–$O(4^{II})$	**128.1(2)**	$O(4^{II})$–Ho(1)–$O(5^{I})$	**54.7(2)**
O(1)–Ho(1)–O(5)	**83.6(6)**		

As was evident in compound **1** and **2**, the carboxylate functionalities in **10** act in a bis-monodentate *syn-syn* μ_2-bridging mode, linking neighbouring Ho^{III} ions along the *c*-axis, with an interatomic Ho(1)···$Ho(1^{I})$ distance of 4.164 (4) Å. This binding mode results in the generation of 1D Ho-Ho "zig-zag" like chains which extend in the crystallographic *c*-axis (**Figure 5.2**). Furthermore, it is possible to envisage these chains as infinite 2-fold helical rod-like $[Ho(CO_2)_3]_n$ SBUs, with the individual Ho^{III} ions being linked to adjacent metal centres through three bridging carboxylate groups (**Figure 5.2**).

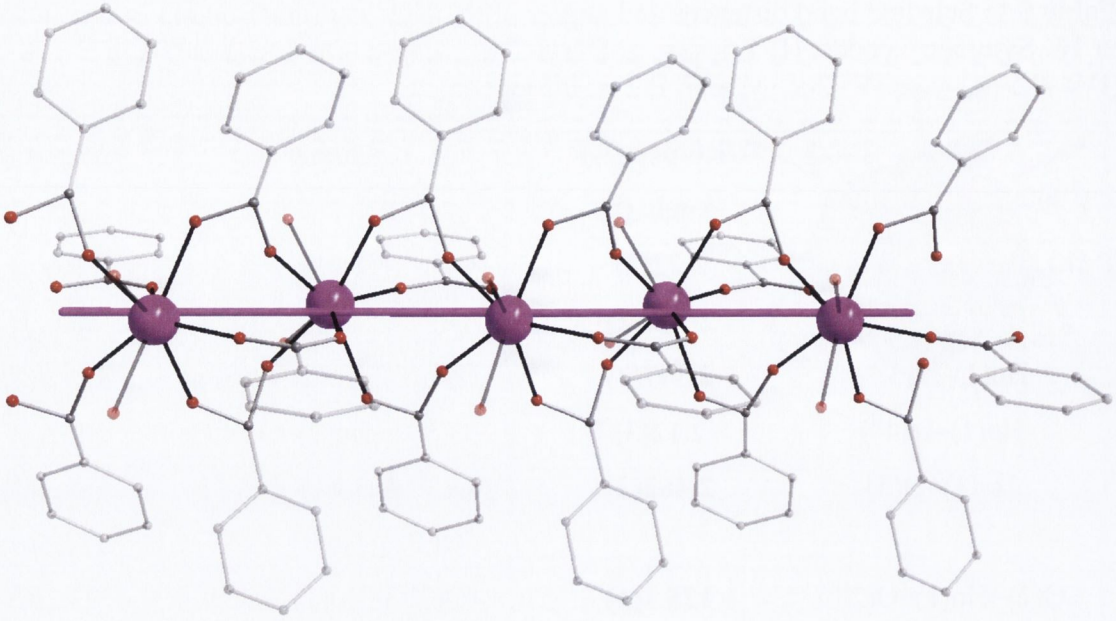


Figure 5.2: 1D polymeric Ho-Ho chain formed through bridging carboxylate groups. The 1D $[Ho(CO_2)_3]_n$ SBU is represented by the pink rod that aligns parallel to the crystallographic *c*-axis.

Each tritopic **L3** ligand in turn is coordinated to six separate Ho^{III} ions, connecting the individual Ho-Ho chains in the crystallographic *b*- and *c*- directions, to generate a neutral 3D non-interpenetrated framework, constructed through symmetry operations (**Figure 5.3** and **Figure 5.4**). The planes of the three outer phenyl rings of **L3** ligands adopt almost perpendicular orientations to the central phenyl ring (torsion angle of 84°). A shortest distance of *ca.* 8 Å between the phenyl ring moieties of neighbouring organic ligands in the structure of **10**, rules out any π-π interactions that may stabilise the 3D framework structure of **10**.

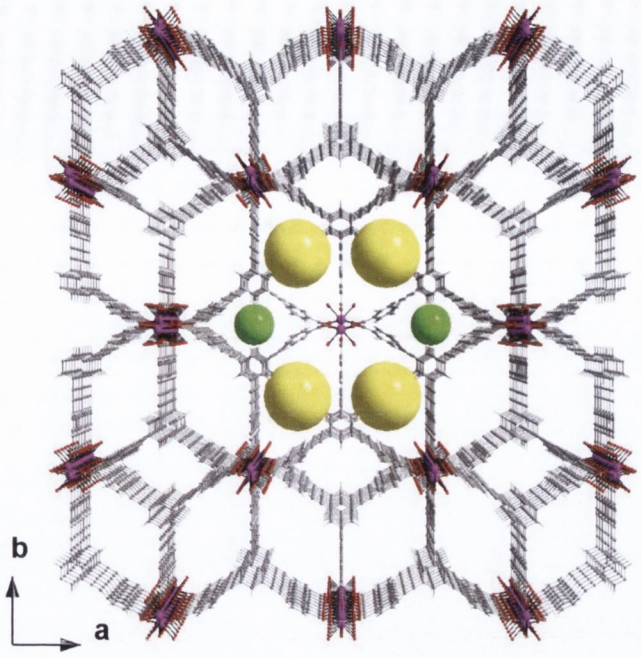


Figure 5.3: The network structure of **10** viewed in the direction of the crystallographic *c*-axis. The green and yellow spheres, 5 and 9 Å in diameter respectively, highlight the two unique channel types in **10**. Colour code: Ho pink, C grey, O red, H white.

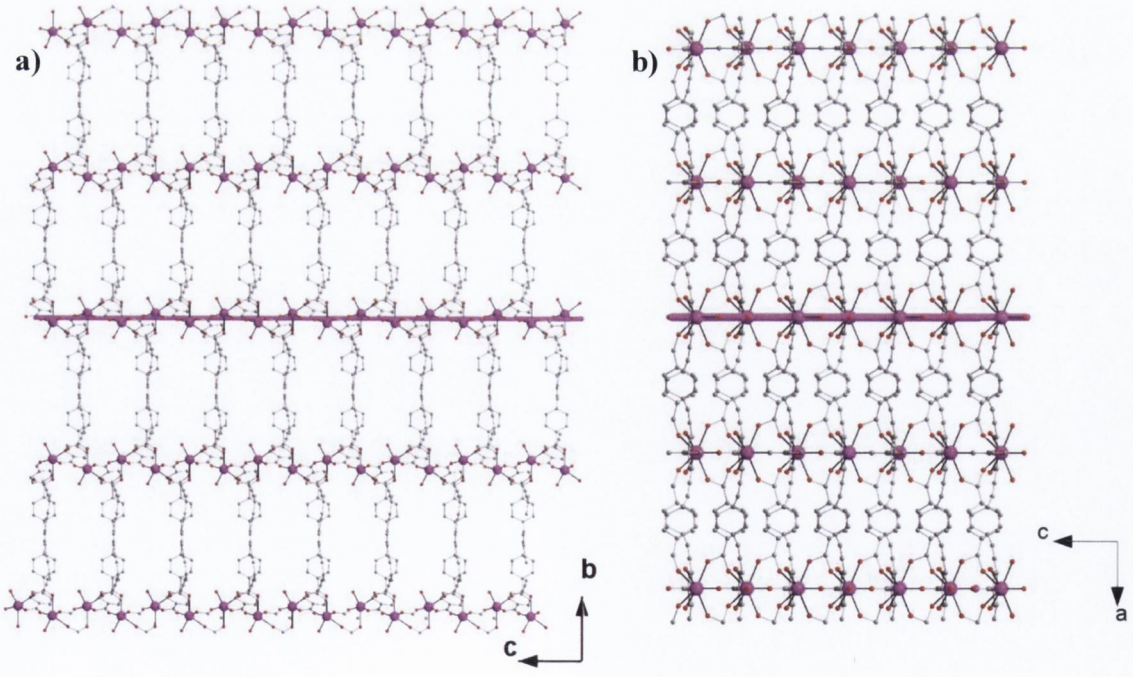


Figure 5.4: The network structure of **10** viewed in the direction of the crystallographic **a)** *a*-axis, **b)** *b*-axis. The pink rod represents the infinite $[Ho(CO_2)_3]_n$ SBUs. Colour code: Ho pink, C grey, O red. H atoms omitted for clarity.

In **10** there are two distinct channels with rhombic topology, containing solvent DMF molecules, which extend in the crystallographic *c*-axis (**Figure 5.3** and **Figure 5.5**). The larger channels are characterised by a cross sectional diameter of *ca.* 9 Å; the smaller channels by diameters of approximately 5 Å. Upon removal of the DMF molecules, the total solvent accessible void volume was calculated by PLATON to be 60% (3,547.3 $Å^3$ out of the total unit cell volume of 5,882.1 $Å^3$) and consequently this results in a low calculated crystal density of 0.906 g cm^{-3}.[4]

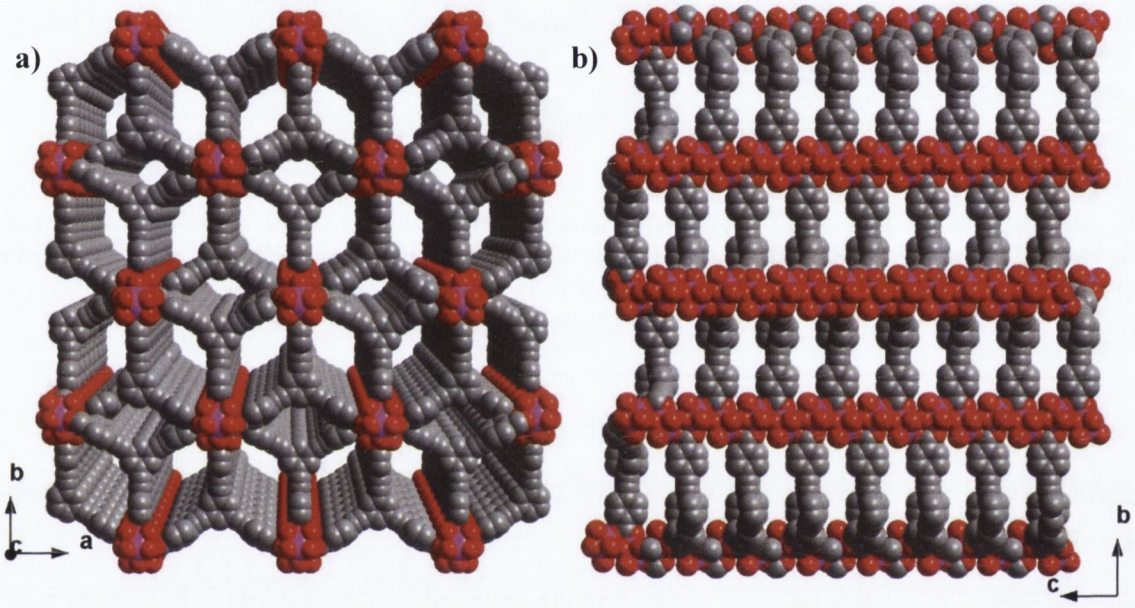


Figure 5.5: Space filling model of **10** as seen along the crystallographic **a)** *c*-axis, **b)** *a*-axis. Colour code: Ho pink, C grey, O red. H atoms omitted for clarity.

Table 5.2: Crystal data and details of the structure determination for **10.**

Identification code	**10**	
Empirical formula	$C_{33}H_{19}O_8Ho$	
Formula weight	708.44 g mol^{-1}	
Temperature	250(2) K	
Wavelength	0.71073 Å	
Crystal system	Orthorhombic	
Space group	*I*ma/2	
Unit cell dimensions	a = 21.403 (5) Å	α= 90°.
	b = 34.255 (5) Å	β= 90°.
	c = 8.023 (5) Å	γ= 90°.
Volume	5882.1 (4) $Å^3$	
Z	4	
Density (calculated)	0.906 Mg/m^3	
Absorption coefficient	1.380 mm^{-1}	
F(000)	1376	
Crystal size	0.15 x 0.1 x 0.05 mm^3	
Theta range for data collection	1.12 to 25.68°	
Index ranges	$-26\leq h\leq 26$, $-41\leq k\leq 41$, $-7\leq l\leq 9$	
Reflections collected	27706	
Independent reflections	5370[R(int) = 0.1263]	
Completeness to theta = 25.68°	98.9 %	
Refinement method	Full-matrix least-squares on F^2	
Data / restraints / parameters	5370 / 66 / 114	
Goodness-of-fit on F^2	1.437	
Final R indices [I>2sigma(I)]	R_1 = 0.1388, wR_2 = 0.3584	
R indices (all data)	R_1 = 0.2006, wR_2 = 0.4082	
Largest diff. peak and hole	2.791 and -3.974 e.$Å^{-3}$	

5.2.2 Further characterisation of **10**

A PXRD experiment was conducted on a crystalline sample of **10** and confirmed the phase purity of the bulk material; the experimentally obtained pattern correlates to the simulated powder pattern derived from the refined single crystal diffraction data (**Figure 5.6**). Slight deviations between the simulated and the measured powder patterns may be as a result of the gradual loss of crystallinity, due to loss of the solvent DMF molecules throughout the course of the X-ray diffraction measurement. Intensity differences are the result of orientation effects, as the compound was measured on a vertically aligned glass plate.

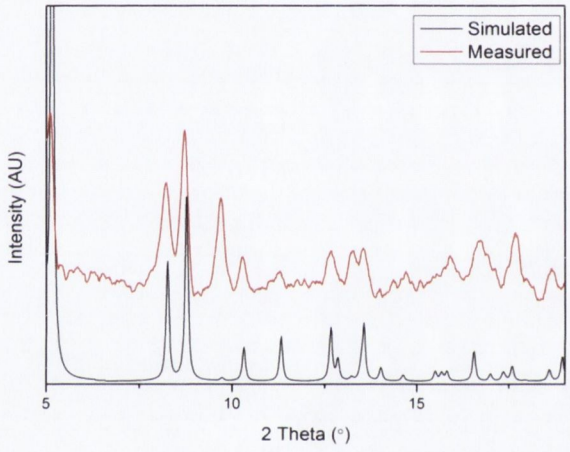


Figure 5.6: PXRD analysis of compound **10**, with the simulated spectrum in black and the measured pattern in red.

Analysis of the FT-IR spectrum of **10** reveals the broadening and almost disappearance of the –OH signal relative to that of the uncoordinated ligand (**Figure 5.7**). The close proximity of the aromatic C=C signal and the C=O stretching vibrations of the solvent DMF molecules and the bridging carboxylate groups results in overlapping signals between 1670 and 1535 cm^{-1}. Adjacent to these bands are related vibrations at 1408 and 1380 cm^{-1}.

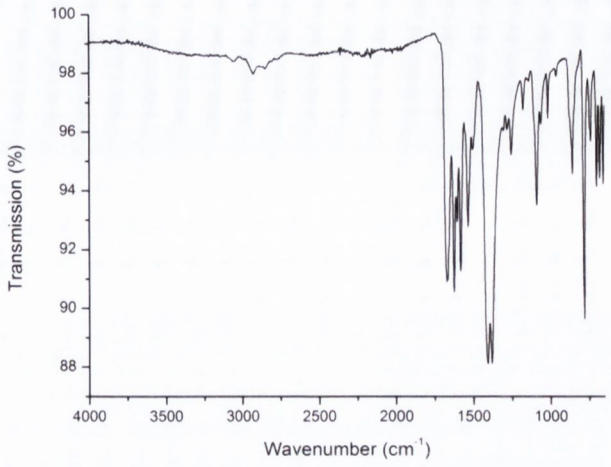


Figure 5.7: FT-IR spectrum of **10**.

TGA was performed on a freshly prepared sample of **10** in order to study its thermal stability (**Figure 5.8**). Crystals of **10** were heated in an air atmosphere from 24 to 900 °C at a rate of 10 °C min^{-1}. The initial weight loss of 33% between *ca.* 25 and 170 °C corresponds to the loss of DMF solvent molecules residing in the channels of the framework. A subsequent weight loss of approximately 3.5% is observed between approximately 170 and 300 °C and can be attributed to the loss of coordinated water molecules (theoretical 3.4%). This is followed by the collapse of the framework due to the oxidation of the organic ligand between 400 and 515 °C, (theoretical 47%, actual 45%), most likely resulting in holmium oxides.

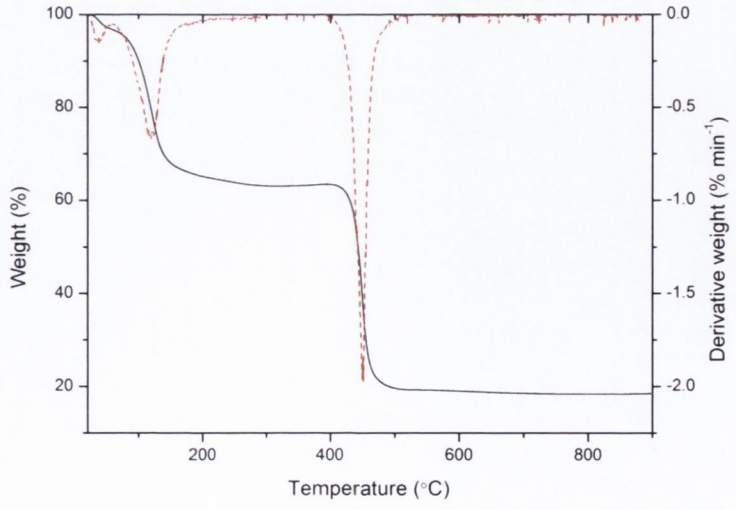


Figure 5.8: TGA of **10**, showing the percentage weight loss as a black line and the derivative of the percentage weight loss as the broken red line.

5.2.3 BET Surface area determination of **10**

The single crystal XRD analysis of **10** revealed the highly augmented open-framework structure of the compound (**section 5.2.1**). In order to determine the BET surface area of **10**, it was necessary to remove the DMF solvent molecules which reside in its pores. Two methods were implemented to achieve this: removal of the DMF using super critical CO_2 in a process known as critical point drying (CPD) or *via* solvent exchange in DCM.

After the solvent exchange process, the samples were transferred to an Autosorb-IQ volumetric analyser and subjected to surface area analysis after being heated under vacuum at 150 °C for 6 hours in order to remove the DCM molecules. Activation at lower temperatures does not produce an open-framework structure that gives rise to permanent porosity, with the desolvation process leading to a loss of crystallinity and the formation of an amorphous solid (**Figure 5.9**). Upon heating to 150 °C the structure seemed to 'reopen' and enabled the measurement of a stable surface area for the material. The resulting amorphous solid has a broadly similar IR spectrum to that of the untreated sample, indicating that it has a comparable coordination environment, the differences may arise due to slightly different carboxylate coordination modes in the dried sample (**Figure 5.9**). The thermally treated material reveals a thermal degradation that is closely related to that of **10**. As for the pristine crystals, thermolysis of the organic ligand commences at *ca.* 400 °C providing further evidence of their related structures (**Figure 5.10**).

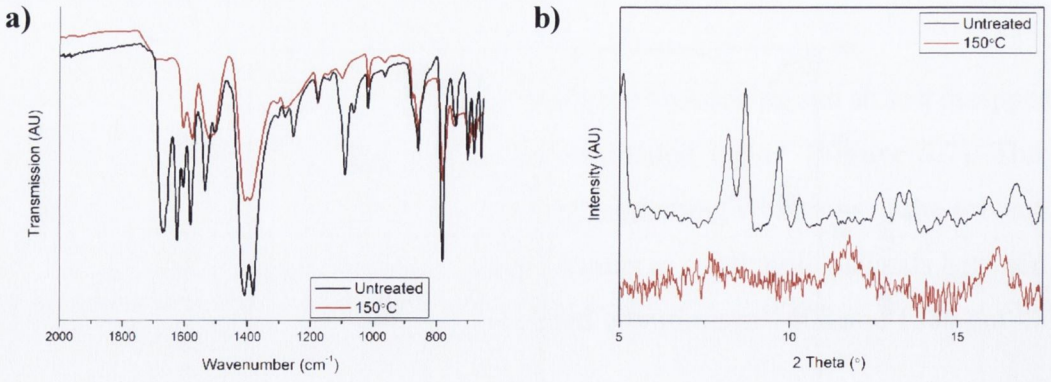


Figure 5.9: a) FT-IR and **b)** PXRD analysis, of an untreated sample of **10** and a sample heated under vacuum at 150 °C

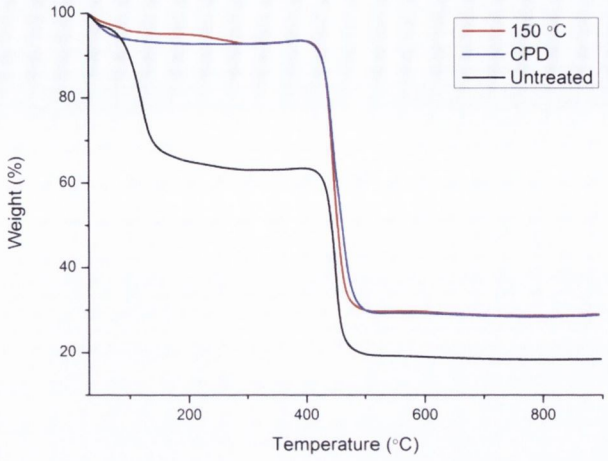


Figure 5.10: Comparison of the TGA curves of **10** and after desolvation at 150 °C and through CPD.

The gas sorption studies confirmed the permanent porosity of the thermally treated sample of **10**, with the two applied methods giving similar results. The conventional solvent-exchange and CPD methods produced comparable type I N_2 isotherms, which demonstrate an initial steep increase, followed by a gradual rise in the uptake of N_2 without reaching saturation (**Figure 5.11**). The solvent exchange and CPD activation methods resulted in BET surface areas of *ca.* 765 $m^2 g^{-1}$ and 720 $m^2 g^{-1}$, respectively (**Figure 5.12**). These values are comparable to the BET surface area of 730 $m^2 g^{-1}$ recorded for MIL-103, which contains the related, but less extend, ligand BTB (1,3,5-benznetrisbenzoic acid).[7] MIL-103, $Tb(BTB)(H_2O)\cdot 2(C_6H_{12}O)$, is a 3D porous framework composed of chains of corner sharing $[TbO_9]$ polyhedral, linked *via* BTB ligands, to generate a framework with hexagonal pores 10 Å in diameter, which are comparable to the pore size found in **10**.

The experimentally determined surface area is high in comparison to previously published LnMOFs, as lanthanide based framework structures often collapse upon removal of solvent molecules, due to structural rearrangement or instability of the lanthanide coordination environment that often contain coordinated solvent molecules. Thus, porous LnMOFs are comparatively rare when compared to transition metal based frameworks.[8,9]

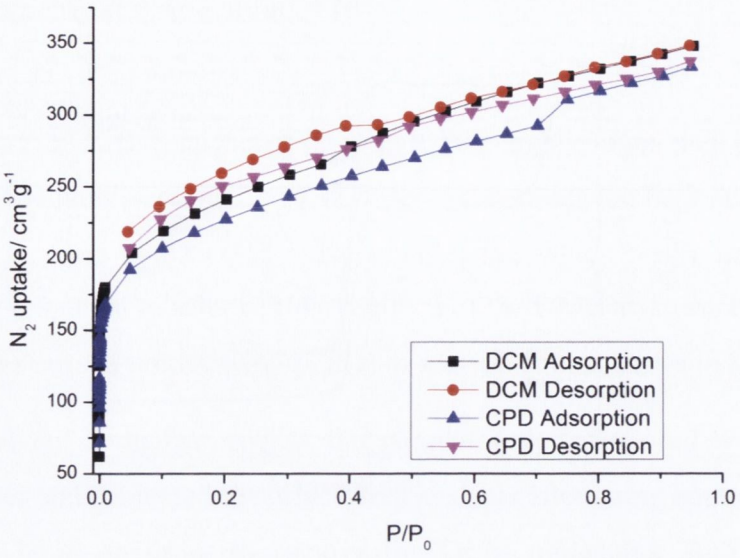


Figure 5.11: N_2 isotherms of **10**, after activation using DCM and heating to 150 °C and through the CPD method.

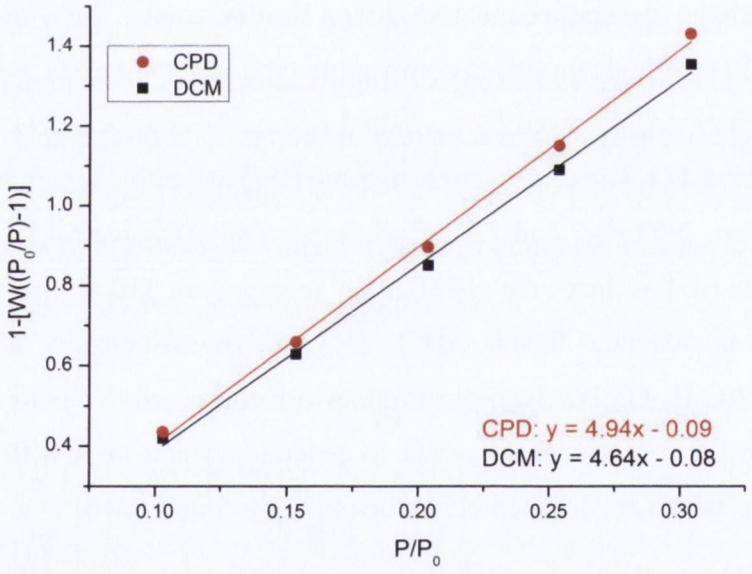


Figure 5.12: Plot of the linear region of the BET equation of **10** derived from the CPD (red) and DCM (black) activated N_2 adsorption isotherms.

The permanent porosity, achieved by the two activation approaches, may give rise to a functional material which may allow the selective uptake of small molecules, rendering this class of LnMOF as a potential candidate for sensing applications.

5.2.4 Magnetic properties of **10**

Molar susceptibility data was measured for **10** between 300 and 1.8 K. The χT product of 14.3 cm^3 K mol^{-1} at 300 K is in a close agreement with the expected value for one Ho^{III} ion of 14.1 cm^3 K mol^{-1}, where $S = 2$, $L = 6$, $g = 5/4$, $^5I_8$ (**Figure 5.13**). The thermal behaviour indicates the presence of antiferromagnetic interactions between the Ho^{III} ions, possibly mediated through the bridging carboxylate groups, as the value of χT continuously diminishes upon cooling to a minimum value of 2.5 cm^3 K mol^{-1} at 1.8 K. Measurements at 1000 and 10000 Oe revealed comparable behaviour.

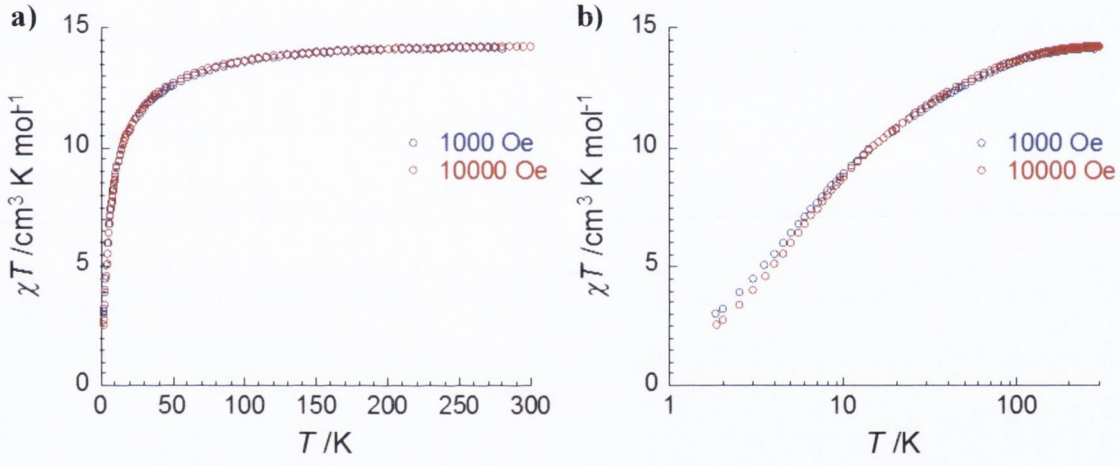


Figure 5.13: Plot of temperature dependence of the magnetic susceptibility at 1000 and 10000 Oe for **10**.

The field dependence of the magnetisation was measured between 1.8 and 8 K and displays a gradual increase in the magnetisation to a maximum value of 6.4 μ_B, without saturation at 1.8 K and 7 T, suggesting the presence of magnetic anisotropy (**Figure 5.14**). It is worth noting that no hysteresis effects have been observed upon measuring the field-dependence of the magnetisation above 1.8 K. The plot of *M vs H/T* also confirms the presence of magnetic anisotropy as the data cannot be superimposed on a single master-curve (**Figure 5.14**).[10] Also no ac susceptibility response in a zero dc field (at 1000 Hz) has been observed above 1.8 K.

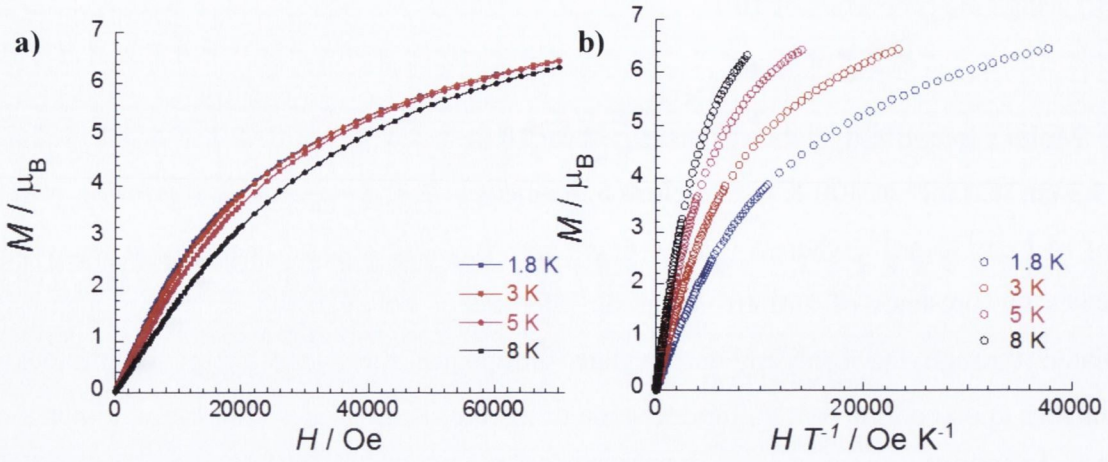


Figure 5.14: Plot of **a)** *M vs H* and **b)** *M vs H/T* between 1.8 and 8 K.

5.3 Lanthanide compounds structurally related to **10**

After investigating the structural properties of **10**, we set out to synthesise a series of isostructural lanthanide compounds related to **10** and to study their properties. The resulting structures were synthesised in an identical manner to **10**, albeit with $Ho(NO_3)_3 \cdot 5H_2O$ being replaced with the respective lanthanide nitrate salt. The resulting compounds were investigated by PXRD analysis, FT-IR spectroscopy and TGA. The small size of the resulting microcrystals prevented their examination *via* single crystal XRD analysis.

5.3.1 PXRD studies of the Ln^{III} compounds structurally related to **10**

PXRD patterns of the compounds **10(Dy)**, **10(Er)**, **10(Dy)**, **10(Eu)**, **10(Tb)** and **10(Yb)** correlate to a variable degree to the PXRD pattern of **10** (**Figure 5.15**, **Figure 5.16** and **Figure 5.17**). However the conducted PXRD studies were severely hampered by a rapid desolvation and the loss of crystallinity of the compounds under the applied conditions. Most compounds appear to lose their crystallinity within five minutes of being removed from the mother liquor. Discrepancies to the pattern of **10** are observed in particular for the Tb^{III} analogue, which may be attributed to the effects of desolvation (**Figure 5.16** and **Figure 5.17**). However, further evidence of their structurally related topologies arises from the

comparison of their closely matching FT-IR spectra and TGA curves, which will be discussed in sections 5.3.2 and 5.3.3

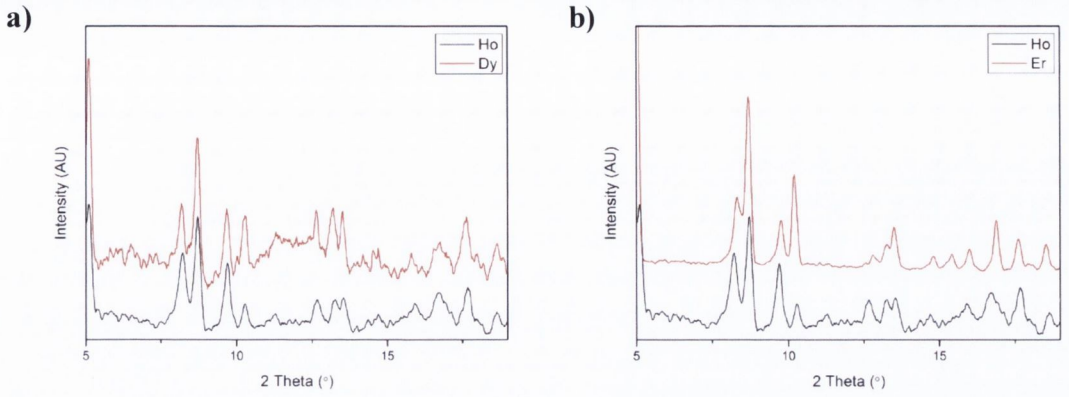


Figure 5.15: PXRD pattern of **a) 10(Dy)** and **b) 10(Er)** compared to **10**.

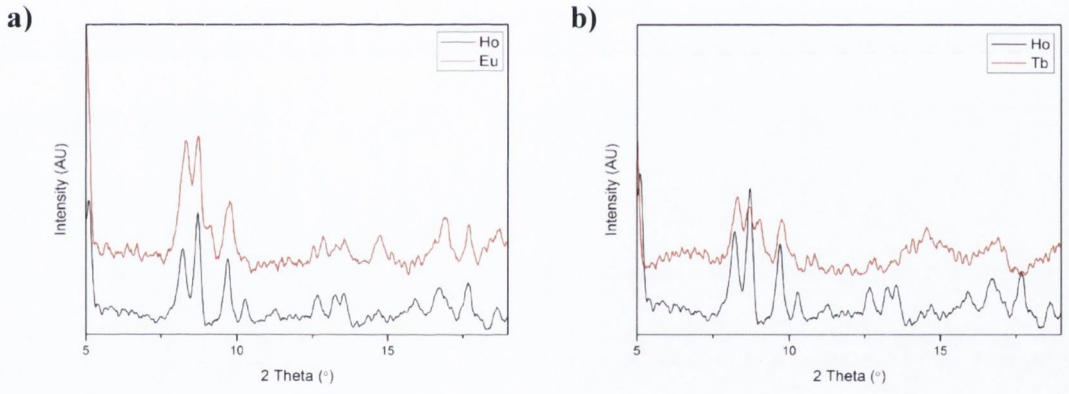


Figure 5.16: PXRD pattern of **a) 10(Eu)** and **b) 10(Tb)** compared to **10**.

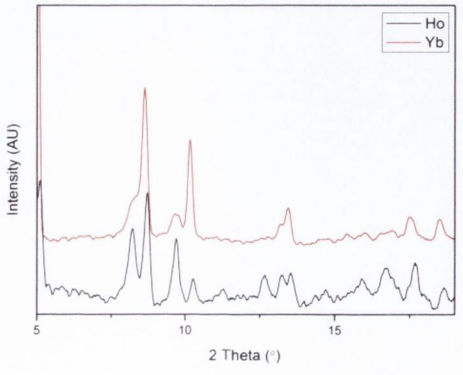


Figure 5.17: PXRD pattern of **10(Yb)** compared to **10**.

5.3.2 FT-IR spectra of Ln compounds structurally related to **10**

Additional evidence that the related Ln^{III} compounds are structurally closely related to **10** is provided by their respective FT-IR spectra which closely match that of **10** (**Figure 5.18**). The lanthanide compounds display the same overlapping stretching frequencies characteristic of **10** between *ca.* 1670 and 1535 cm^{-1} arising from the C=O stretch of the solvent DMF molecules, the bridging carboxylate groups (ν_aCOO) and the aromatic C=C stretch at 1603 cm^{-1}. Furthermore, the symmetric stretches (ν_sCOO) of the bridging carboxylate groups present between 1410-1406 cm^{-1} and *ca.* 1381 cm^{-1} correlate with the values of 1407 and 1380 cm^{-1} for **10**. Similar slight deviations between the positioning of comparable signals in an isostructural lanthanide series have previously been reported.[11]

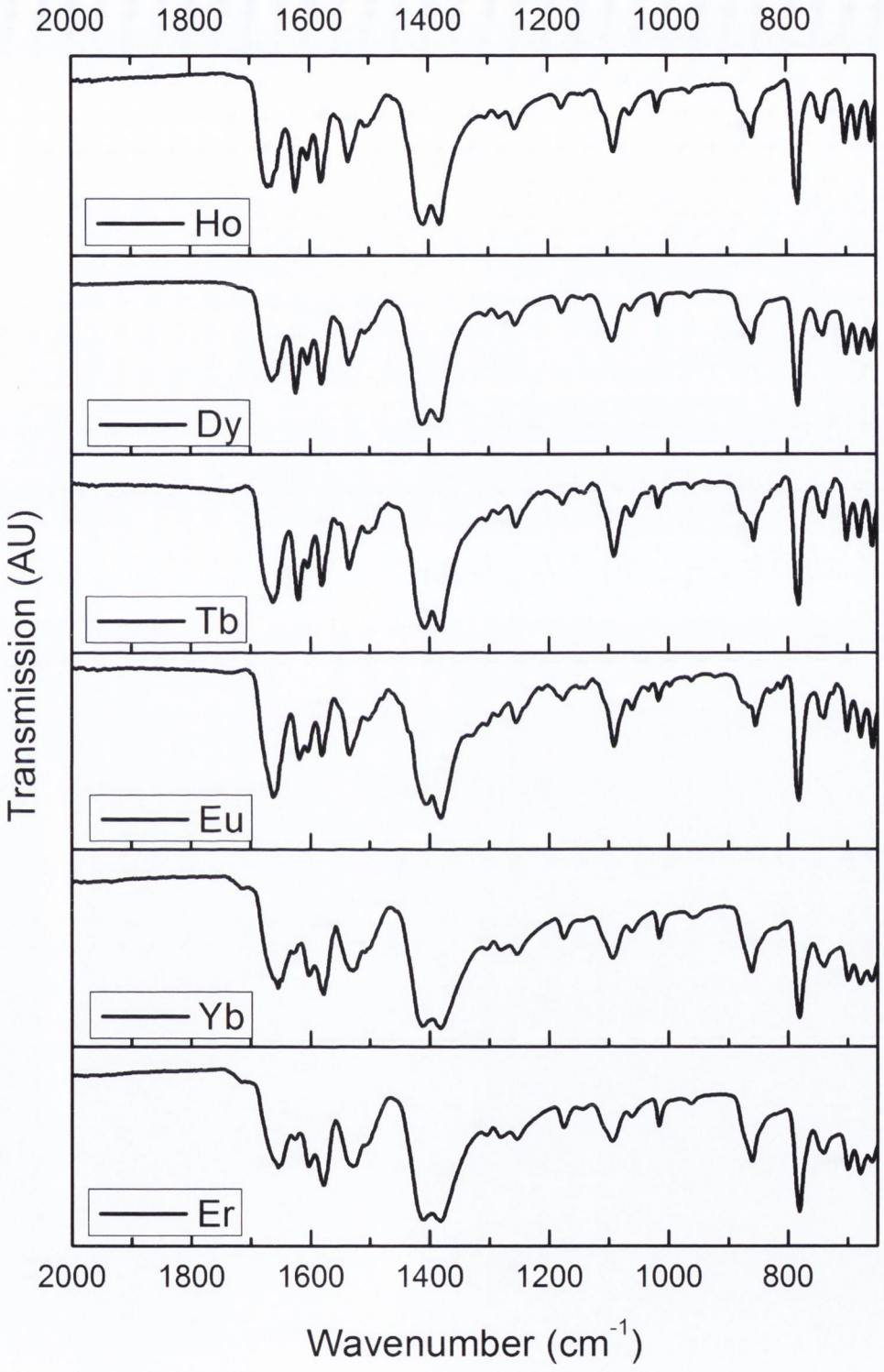


Figure 5.18: FT-IR spectra of the Dy^{III}, Tb^{III}, Eu^{III}, Yb^{III}, Er^{III} compounds structurally related to **10**.

5.3.3 TGA of Ln^{III} compounds structurally related to **10**

TGA of the series of prepared lanthanide compounds, were performed in an air atmosphere between room temperature and 900 °C (**Figure 5.19**). The investigated compounds reveal similar decomposition pathways, which closely match that of **10**.

The initial weight loss associated with the loss of solvent DMF molecules is observed below 150 °C (30-36% for **10**(Dy, Eu, Yb and Tb)). The lower weight loss recorded for the Er^{III} analogue (13%) suggests that there was a significant loss of solvent prior to conducting the measurement. The signal assigned to the constitutional DMF solvent molecules at 1670 cm^{-1} is significantly lower in intensity in **10(Er)**, than the corresponding signals in the other FT-IR spectra of the lanthanide compounds, providing further evidence of desolvation (**Figure 5.18**). The loss of solvent DMF molecules may also account for the varying weight losses demonstrated by the other samples.

The thermolysis of the organic ligand occurs between *ca.* 400 and 500 °C for **10**(Dy, Er, Yb and Tb) and between approximately 410 and 510 °C for **10(Er)**. The decomposition of the ligand in **10(Eu)**, occurs prior to this at 380 °C, however, the TGA curve of the europium structure is otherwise comparable to that of the related compounds, with similar weight losses observed in each step.

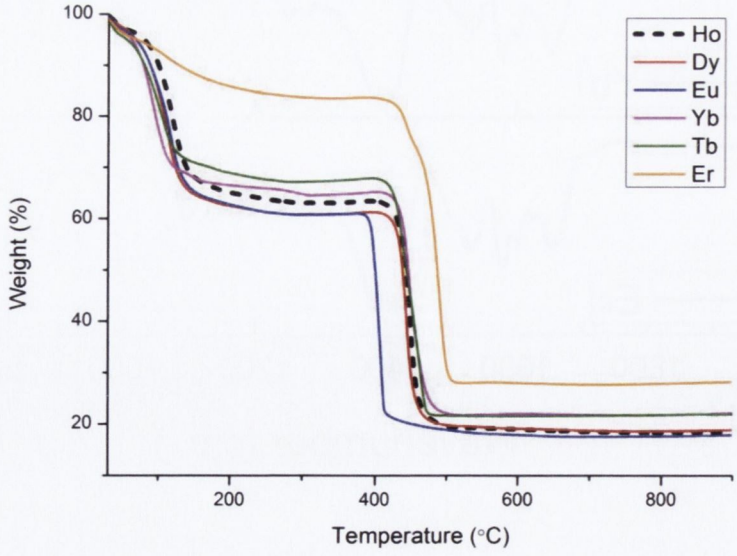


Figure 5.19: TGA of the lanthanide compounds structurally related to **10**.

5.3.4 Magnetic studies of **10(Dy)**

The temperature dependencies of the magnetic susceptibilities of **10(Dy)** were measured at 1000 and 10000 Oe between 1.8 and 300 K. The χT value of 13.6 $cm^3 K mol^{-1}$ is in a good agreement with the expected product of 14.2 for one Dy^{III} ion ($S = 5/2$, $L = 5$, $g = 4/3$, $^6H_{15/2}$) (**Figure 5.20**). **10(Dy)** demonstrates very similar magnetic behaviour to **10**, with a decrease in χT upon cooling indicating the presence of antiferromagnetic interactions between the Dy^{III} ions, reaching a minimum value of *ca.* 8 $cm^3 K mol^{-1}$ at 1.8 K and 1000 Oe. At low temperatures the field dependence of magnetisation reveals a steep increase below 1 T, followed by a gradual increase without saturation to 5.9 μ_B at 7 T and 1.8 K, indicating the presence of magnetic anisotropy and/ or the population of low-lying excited states (**Figure 5.21**).[12] As for **10** there were no hysteresis effects on measuring the field-dependence of the magnetisation above 1.8 K. The non-superimposable data found in a plot of *M vs H/T* confirms the presence of magnetic anisotropy (**Figure 5.21**). Finally no *ac* susceptibility was observed in a zero *dc* field above 1.8 K.

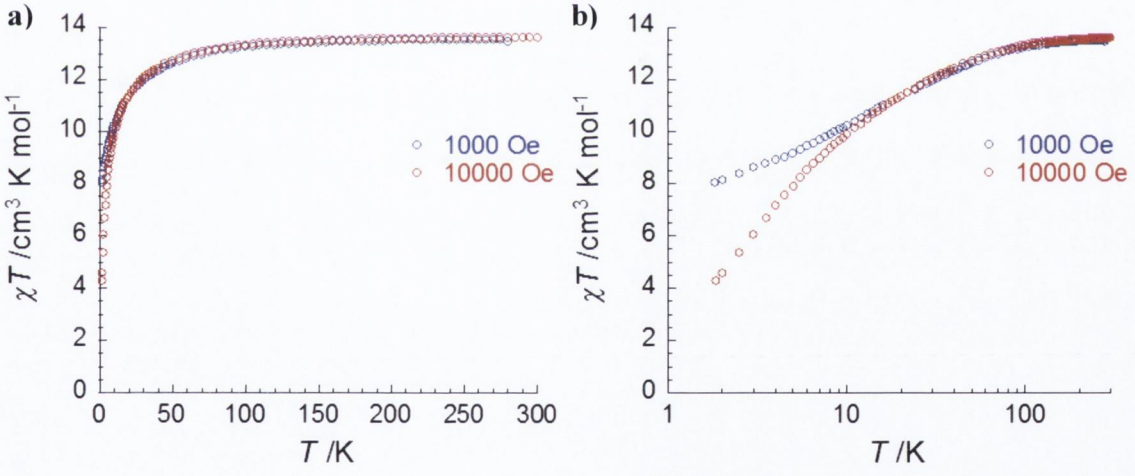


Figure 5.20: Plot of temperature dependence of the magnetic susceptibility at 1000 and 10000 Oe for **10(Dy)**.

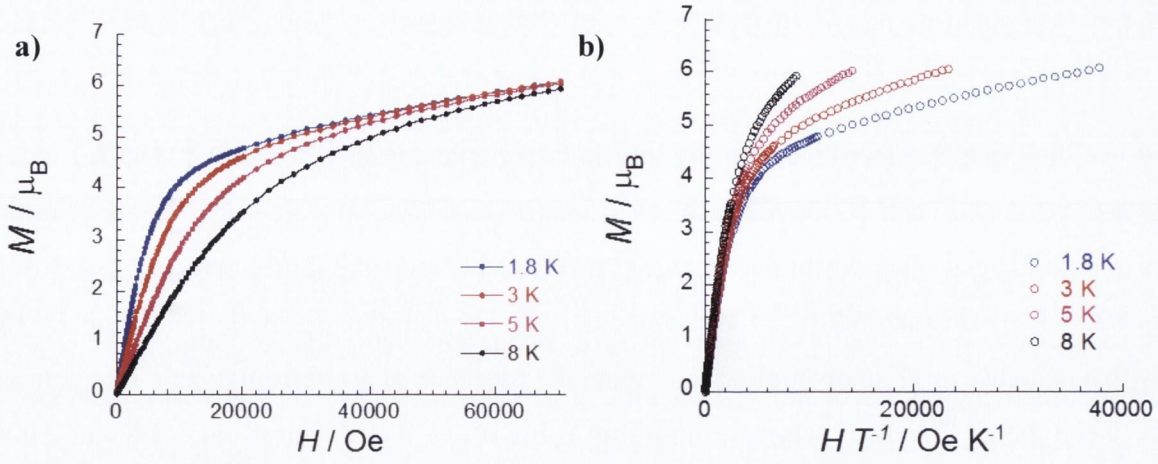


Figure 5.21: Plot of **a)** *M vs H* and **b)** *M vs H/T* for **10(Dy)** between 1.8 and 8 K.

5.4 Photoluminescent studies

5.4.1 **L3** emission and excitation spectra

The ligand **L3** displays a broad band emission between 375 and 640 nm, with the maximum emission occurring in the blue region at 440 nm (**Figure 5.22**). The excitation spectrum (λ_{an} = 440 nm) has a main band at 367 nm and a less intense band at 270 nm, with **L3** absorbing in the UV-visual spectrum between 220 and 600 nm (**Figure 5.22**).

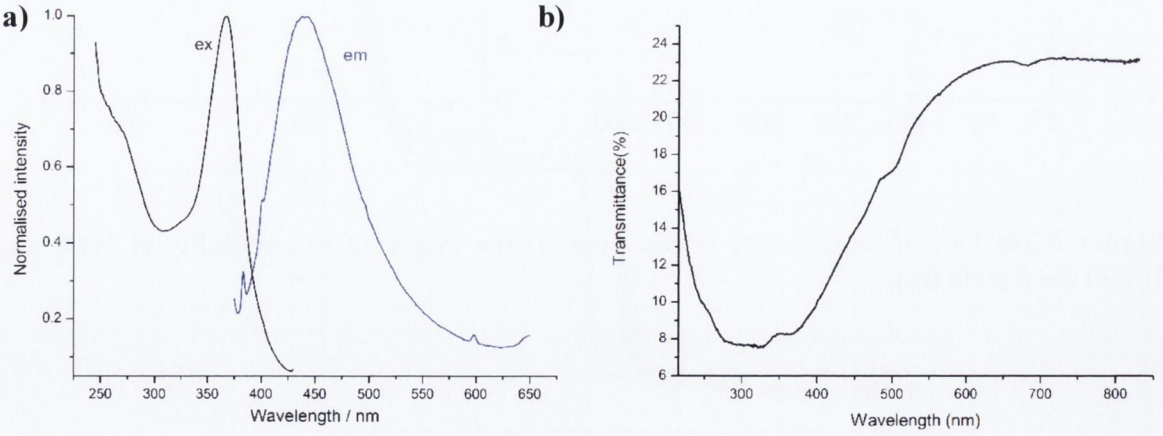


Figure 5.22: a) Normalised emission (λ_{ex} = 365 nm) and excitation (λ_{an} = 440 nm) spectra of **L3** in the solid state, **b)** absorption spectrum of **L3** in the solid state.

5.4.2 Photoluminescent studies of **10(Eu)**

10(Eu) exhibits the typical Eu^{III} $^5D_0 \rightarrow {}^7F_J$ (J=0-6) emission bands at 578, 592, 612, 650, 700, 745 and 815 nm respectively, the last two transitions being very weak (**Figure 5.23**). The excitation spectrum, recorded at 612 nm ($^5D_0 \rightarrow {}^7F_4$), displays a main band at 340 nm in addition to the Eu^{III} transitions $^5L_6 \leftarrow {}^7F_0$ and $^5D_2 \leftarrow {}^7F_0$ at 394 and 464 nm, respectively (**Figure 5.23**). The Eu^{III} transition $^5H_3 \leftarrow {}^7F_0$, which would be expected around 323 nm, is hidden by the broad band centred at 340 nm. **10(Eu)** absorbs strongly in the UV-visual spectrum between 220 and 550 nm, with the individual Eu^{III} transitions being obscured by the broad absorption band (**Figure 5.24**).

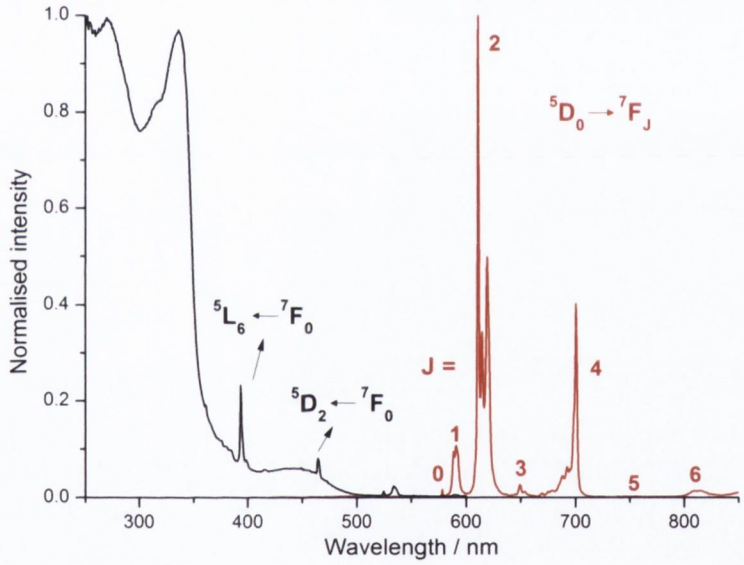


Figure 5.23: Normalised emission (red line) (λ_{ex} = 340 nm) and excitation (black line) (λ_{an} = 612 nm) spectra of **10(Eu)**.

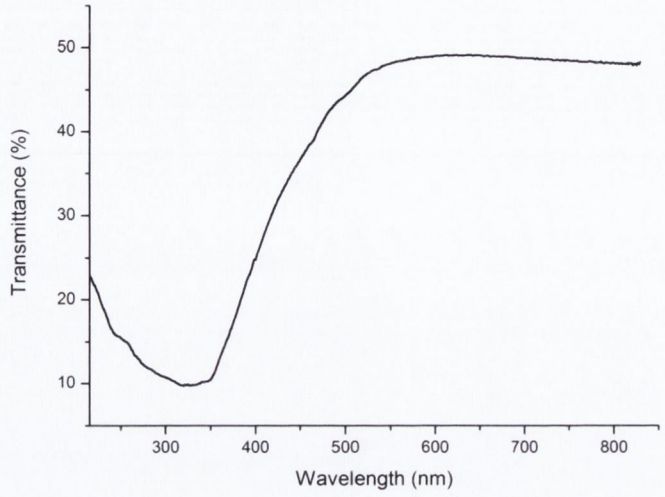


Figure 5.24: Absorption spectrum of **10(Eu)** in the solid state.

The ligand based emission band maximum is red-shifted upon complexation of **L3** to Eu^{III} by *ca.* 70 nm, from 440 nm (**Figure 5.22**) to 510 nm (**Figure 5.25**). Excitation at 340 nm revealed no ligand-based emission (**Figure 5.25**), thus indicating that the previously unidentified band centred at 340 nm in the excitation spectrum is metal based (**Figure 5.28**). Conversely, the ligand centred emission is larger when the Eu^{III} transition $^5L_6 \leftarrow {}^7F_0$ is directly excited at 394 nm. This is due to the broad LMCT band that expands between 370 and 500 nm, consequently excitation at 394 nm excites both the metal directly and the LMCT band, hence the presence of ligand based emission (**Figure 5.25**).

The Eu^{III}-centred emission proved to be insensitive to excitation at varying wavelengths, however, the ligand-centred emission showed a much greater sensitivity to excitation at differing wavelengths (**Figure 5.25**). The intensity of the ligand-based emission increases upon excitation directly into the ligand excited state at 365 nm, or when the Eu^{III}-centres are directly excited at 394 nm and 464 nm, both of which lie on LMCT bands. The later band was confirmed as a LMCT band by recording an excitation spectrum at 503 nm, which revealed a band (λ_{max} = 450 nm) attributable to a **L3** – Eu^{III} interaction, also visible was the **L3** absorption band (λ_{max} = 365 nm) (**Figure 5.25**).

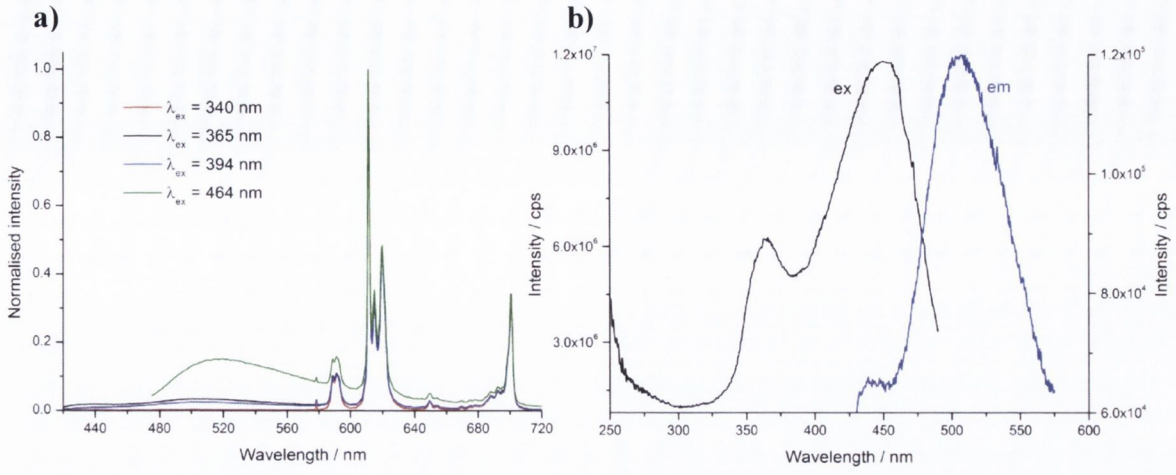


Figure 5.25: a) Emission spectrum of **10(Eu)** ($^5D_0 \rightarrow {}^7F_J$ (J = 0-4)) upon excitation at several wavelengths; the y-scale has been normalized to 1, relative to the maximum intensity observed at 612 nm, **b)** Emission (λ_{ex} = 365 nm) and excitation (λ_{an} = 503 nm) spectra of **10(Eu).**

For **10(Eu)** to be suitable as a luminescent material it would need to demonstrate a high degree of photostability. To ascertain the photostability of **10(Eu)**, a sample was excited repeatedly every ten seconds for two hours and the intensity of the Eu^{III} transitions were monitored at 579, 592, 612 and 702 nm (**Figure 5.26**). After two hours there was no decrease in emission intensity, thus, demonstrating the excellent photostability of **10(Eu)**.

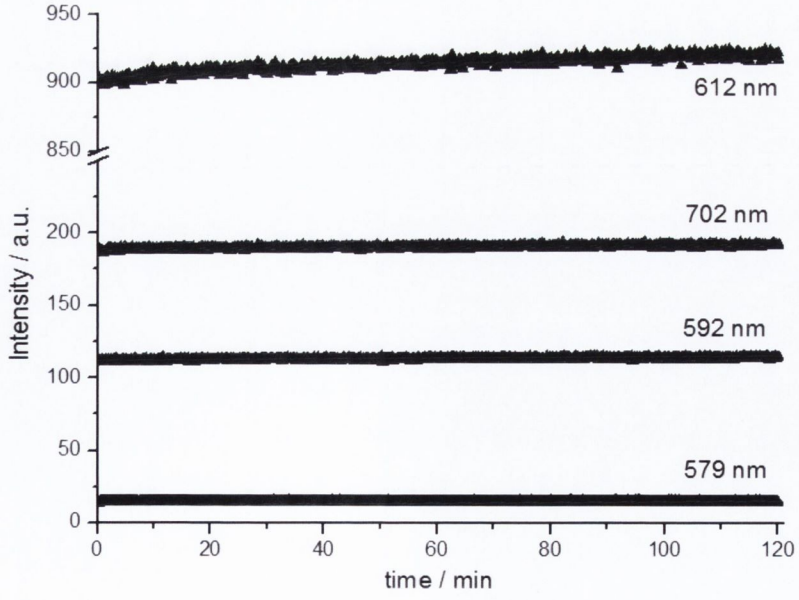


Figure 5.26: The Eu^{III} emission intensities of **10(Eu)** monitored at 579, 592, 612 and 702 nm, upon repetitive excitation at 340 nm for two hours.

5.4.3 Luminescent studies of **10(Eu)** doped with 2-naphthoyltrifluoroacetone (NTA)

The open-framework structure of **10** makes it an ideal candidate for the sensing of small molecules. Recognising this we decided to investigate the effect of doping a sample of the structurally related framework **10(Eu)** with 2-naphthoyltrifluoroacetone (NTA) (**Figure 5.27**). NTA was chosen for its proven ability to replace water molecules coordinated to lanthanide ions, with a resulting increase in emission intensity.[13,14] This was achieved by dispersing an untreated sample of the framework in a 10μM solution of NTA in DMF for three days, with the solution being refreshed daily.

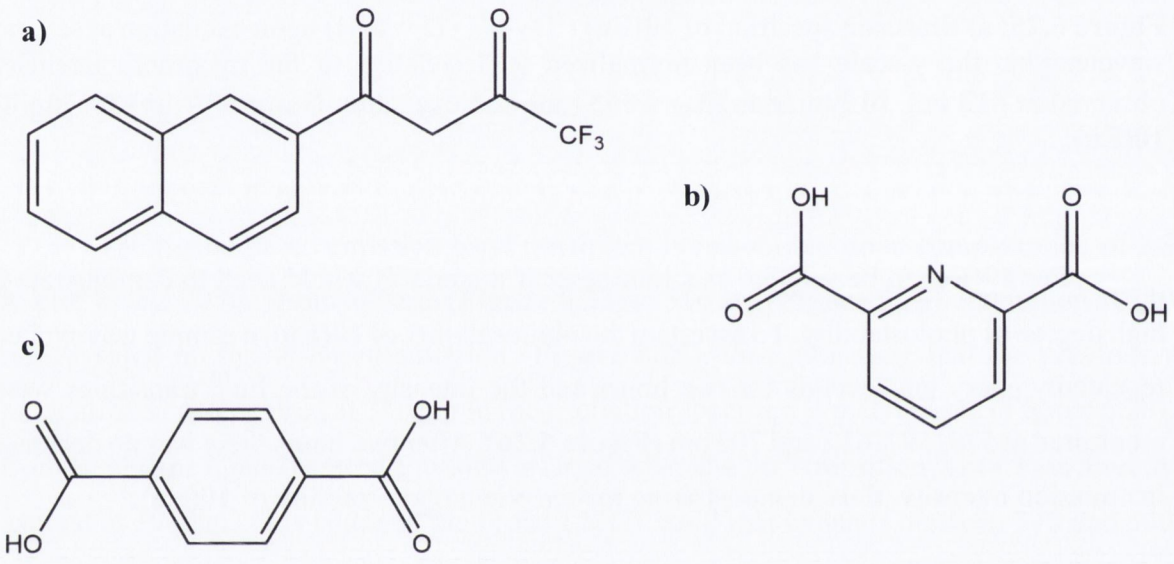


Figure 5.27: a) 2-naphthoyltrifluoroacetone (NTA), **b)** dipicolinic and **c)** terephthalic acid.

The emission and excitation spectra of the sample treated with NTA are very similar to that of the untreated sample of **10(Eu)**, (**Figure 5.28** and **Figure 5.29**). This is possibly due to the NTA molecules being unable to penetrate the pores of the structure, thus preventing the NTA molecules from replacing the coordinated water molecules. A sample of **10(Eu)** was heated under vacuum to remove the solvent DMF molecules present in the pores, in an effort to increase the probability that NTA molecules would penetrate the pores. However this resulted in a large decrease in photoluminescence. Due to a lack of structural information on the desolvated form we did not pursue this strategy any further.

Further evidence of NTA not interacting with **10(Eu)** arises through the investigation of the Eu($^5D_0$) excited state lifetimes. The untreated sample having lifetimes of $\tau_1 = 0.28 \pm$

0.01 (13%) and τ_2 = 0.933 ± 0.005 (87%). The sample doped with NTA exhibits almost identical lifetimes of τ_1 = 0.28 ± 0.02 (13%) and τ_2 = 0.94 ± 0.01 (87%). These values were calculated by monitoring the emission decay of the $^5D_0 \rightarrow {}^7F_2$ transition upon excitation at 340 nm and best-fitted to biexponential functions.

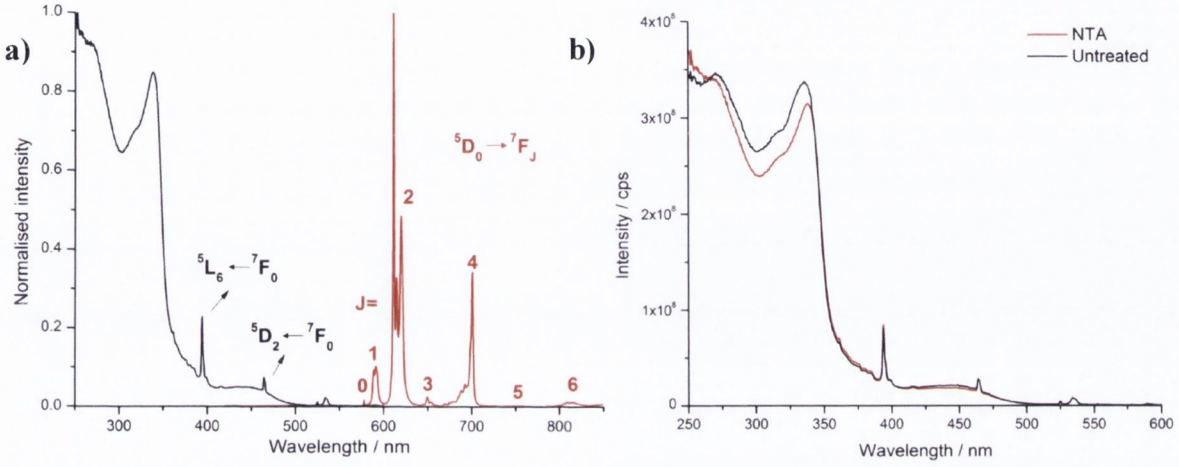


Figure 5.28: a) Normalised emission (λ_{ex} = 340 nm) and excitation (λ_{an} = 612 nm) spectra of **10(Eu)-NTA**, **b)** Comparison of the excitation spectra (λ_{an} = 612 nm) of **10(Eu)-NTA** (red line) and **10(Eu)** (black line).

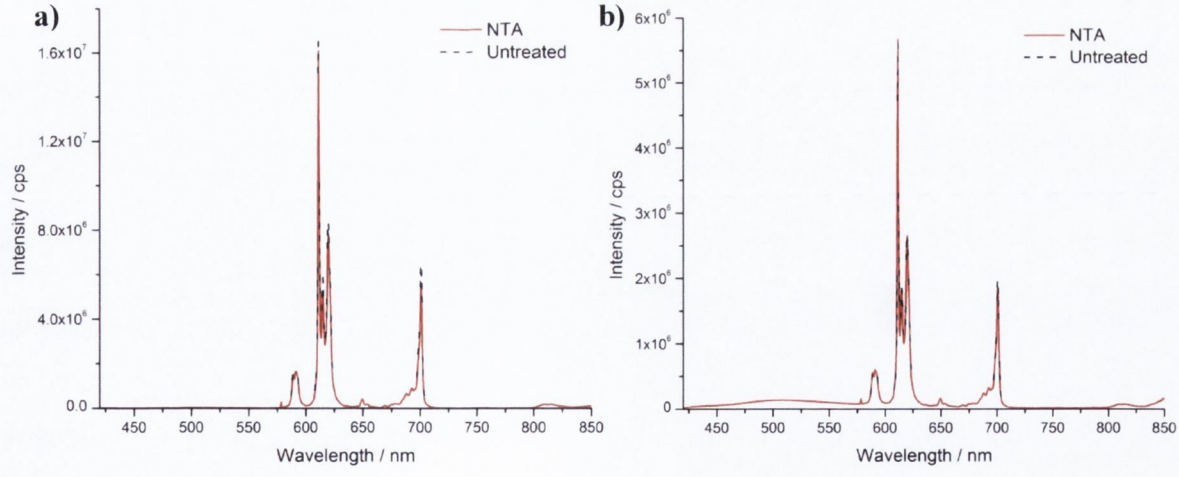


Figure 5.29: Emission spectra of **10(Eu)-NTA** (red line) and **10(Eu)** excitated at, **a)** 340 nm and, **b)** 394 nm.

To increase the likelihood of NTA interacting with the Eu^{III}-framework, the concentration of NTA was increased to 1mM. Unfortunately, this led to the degradation of

the framework, with the crystals of **10(Eu)** being visibly smaller after treatment with a 1mM DMF solution of NTA. This led us to conclude that the higher concentration of NTA initiated the leeching of the Eu^{III} ions present in the framework. This was confirmed by measuring the absorption and emission spectra of the supernatant liquid, which showed the presence of a Eu(NTA) complex.

In addition to NTA, dipicolinic acid and terephthalic acid were utilised at differing concentrations (1μM and 1mM) to replace the *cis*-coordinated water molecules (**Figure 5.27**). However, there were no observable differences in the emission and excitation spectra of the treated samples, except at the elevated concentrations, at which point the crystalline sample decomposed.

5.4.4 Luminescent studies of a **Nd(L3)** compound

Following on from the successful photoluminescent studies using **10(Eu)**, which focused on emissions in the visible spectrum, we decided to investigate whether **L3** would be an effective sensitiser for near-IR emission in a Nd^{III} complex.[15] The compound **Nd(L3)** was synthesised using an identical procedure to that used for the synthesis of **10**, whereby holmium nitrate was replaced with $Nd(NO_3)_3{\cdot}6H_2O$. The resulting colourless crystals were too small for single-crystal XRD. However, FT-IR spectroscopy indicated that it is structurally closely related to **10**, with the respective spectra being very similar (**Figure 5.30**). The minor differences in the FT-IR spectra may be as a result of slightly different carboxylate binding modes.

TGA provides further evidence of their related structures, with the two compounds having closely comparable thermal decomposition pathways, with the oxidative degradation of the ligand occurring at *ca.* 410 °C in both compounds. The large solvent loss revealed by the TGA curve (*ca.* 30%), indicates that the synthesised compound is an open-framework structure (**Figure 5.30**). There is a rapid loss of crystallinity upon removal of the compound from its mother liquor due to desolvation and consequently PXRD experiments were not effective, with the crystals of the compound degrading to give an amorphous material within a very short time period.

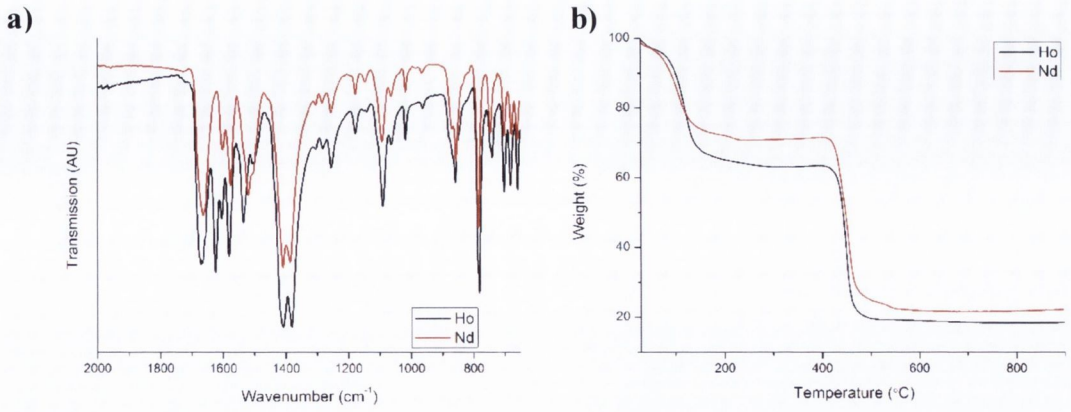


Figure 5.30: Comparison of the **a)** FT-IR spectra and **b)** TGA curves of ***10*** (black line) and **Nd(L3)** (red line).

The emission spectrum of **Nd(L3)** (λ_{ex} = 365 nm) displays bands characteristic of $^4F_{3/2} \longrightarrow {}^4I_J$ transitions (J = 9/2, 11/2 and 13/2), at 880, 1065 and 1330 nm respectively (**Figure 5.31**). The excitation spectrum (λ_{an} = 1065 nm) has a main band centred at 365 nm. The presence of this band identifies the ligand **L3** as an appropriate sensitiser for Nd^{III} near-IR emission. The remaining bands present in the excitation spectra are found at 525, 584, 627, 682 and 748 nm and are characteristic of the Nd^{III} transitions $^4G_{7/2} \leftarrow {}^4I_{9/2}$, $^4G_{5/2} \leftarrow {}^4I_{9/2}$, $^2H_{11/2} \leftarrow {}^4I_{9/2}$, $^4F_{9/2} \leftarrow {}^4I_{9/2}$ and $^4F_{7/2} \leftarrow {}^4I_{9/2}$ respectively and are also present in the corresponding absorption spectrum (**Figure 5.32**).[16]

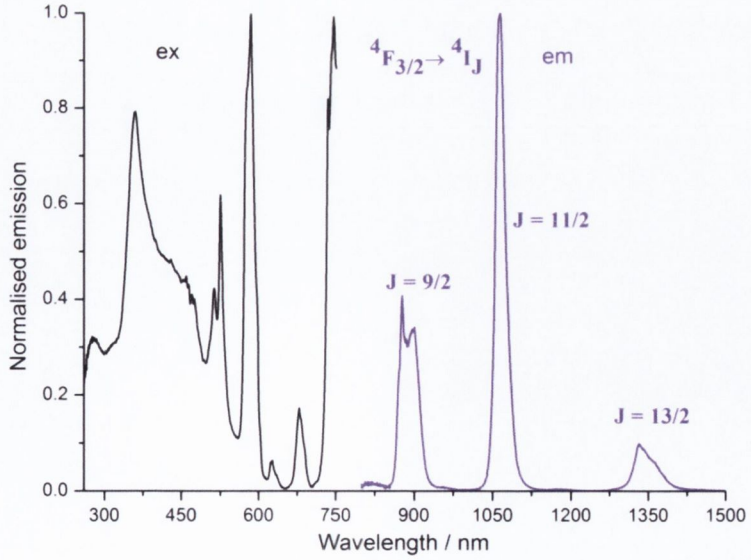


Figure 5.31: Normalised emission (λ_{ex} = 360 nm) and excitation (λ_{an} = 1065 nm) spectra of **Nd(L3)**.

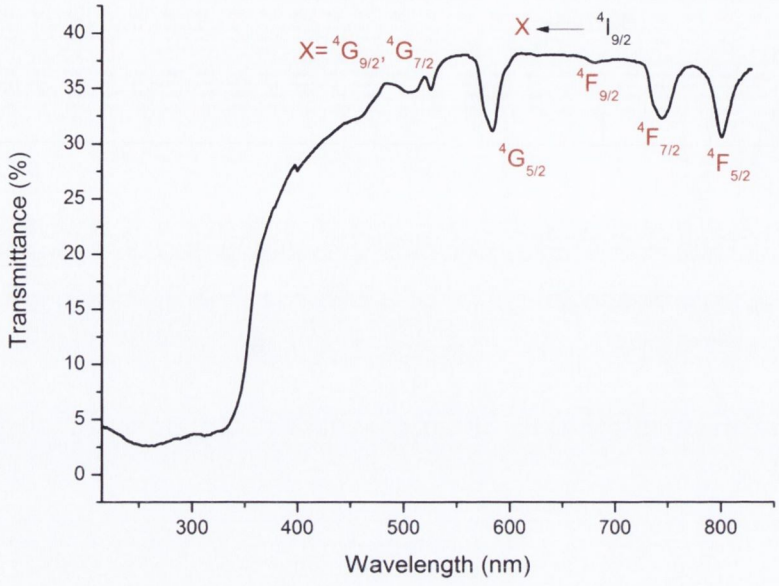


Figure 5.32: Absorption spectrum of **Nd(L3)** in the solid state.

The Nd^{III}-based emission proved to be more sensitive to excitation at varying wavelengths than the Eu^{III} in **10(Eu)** (**Figure 5.33**). The most intense emission was achieved when the sample was excited at 360 nm, thus corroborating the evidence from the excitation spectrum (**Figure 5.31**) that **L3** is an effective sensitiser for Nd^{III}.

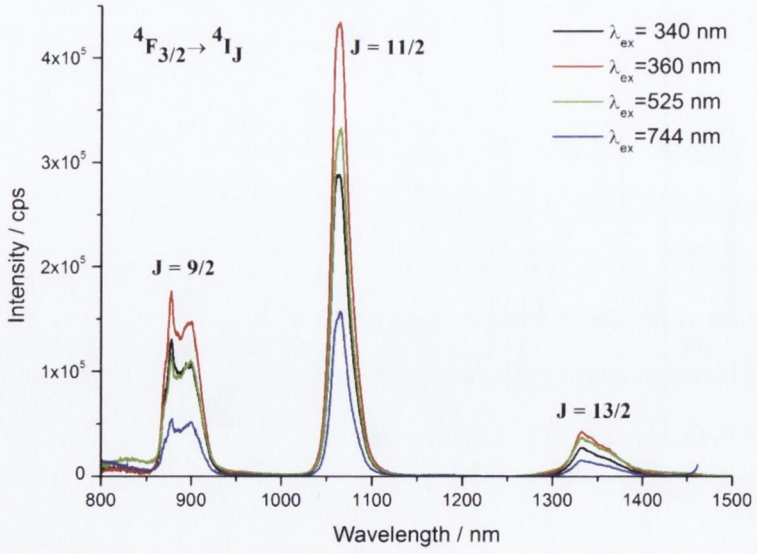


Figure 5.33: Emission spectrum of **Nd(L3)** ($^4F_{3/2} \rightarrow {}^4I_J$ (J = 9/2, 11/2, 13/2)) upon excitation at several wavelengths.

5.4.5 Luminescent studies of a **Sm(L3)** compound

The samarium complex (**Sm(L3)**) was synthesised using an equivalent methodology to that used in the synthesis of **10**. The resulting microcrystals of **Sm(L3)** proved to be too small for single-crystal XRD. Examination of the respective FT-IR data of **10** and **Sm(L3)** reveals largely comparable spectra, providing evidence that they are structurally closely related compounds. Further evidence of their topological similarities arises from the comparison of their TGA curves, with the thermolysis of the ligand occurring at *ca.* 410 °C in both compounds. The large solvent loss, *ca.* 23%, between 30 and 150 °C, demonstrated by **Sm(L3)** also indicates that it is an open-framework. As was reasoned for **Nd(L3)**, differences between the coordination modes of the carboxylate functionalities may account for the differing FT-IR spectra. As for the **Nd(L3)**, the **Sm(L3)** crystals desolvate rather quickly to produce an amorphous solid. This rapid loss of crystallinity hampered the powder XRD analysis using our instrumentation.

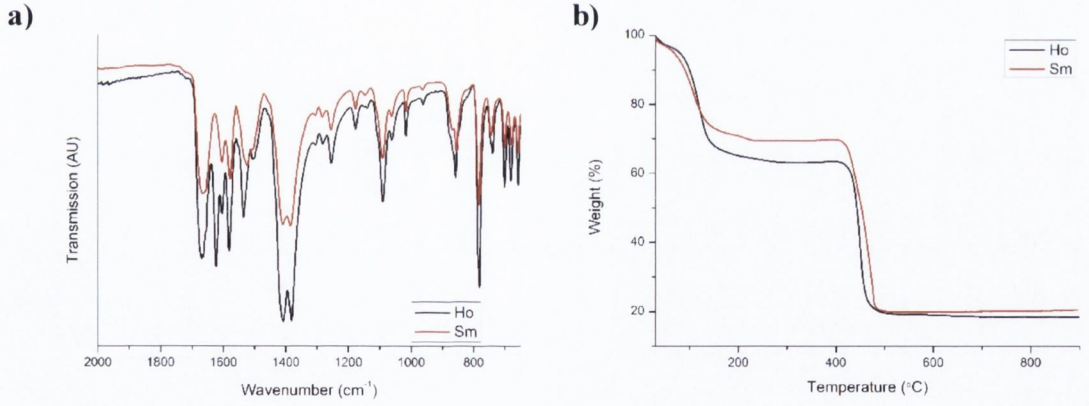


Figure 5.34: Comparison of the **a)** FT-IR spectra and **b)** TGA curves of **10** (black line) and **Sm(L3)** (red line).

After studying the photoluminescent properties of **10(Eu)** and **Nd(L3)**, that emit in the visible and near-infrared regions respectively, we decided to investigate the luminescent properties of the samarium complex, as it would possibly be capable of displaying metal-centred emission in both the visible and near-infrared ranges.

The Sm^{III} centred luminescence in the visible region upon excitation of **Sm(L3)** at 340 nm consists of four bands distributed between 550 and 750 nm that are assigned to the

$^4G_{5/2} \rightarrow {}^6H_J$ (J = 5/2, 7/2, 9/2, and 11/2) transitions (**Figure 5.35**). However, contrary to **10 (Eu)**, where the metal-centred emission was far more intense than the ligand-centred one, the majority of the emission spectra of **Sm(L3)** is composed of a large and intense fluorescence band centred at *ca.* 542 nm and several faint and sharp Sm^{III} emission bands. Excitation directly into the ligand excited state (λ_{ex} = 370 nm) results in intense ligand-centred emission, which obscures the faint Sm^{III} emission bands. **Sm(L3)** was found to absorb strongly in the UV-visual spectrum, with a broad absorption band occurring between *ca.* 220 and 550 nm (**Figure 5.36**).

Sm(L3) displays a relatively intense metal-centred emission in the range of 850-1500 nm upon excitation at 340 nm (**Figure 5.35**). The six characteristic emission bands are attributed to the $^4G_{5/2} \rightarrow {}^6F_J$, where J = 1/2 and 3/2 (850-915 nm), 5/2 (915-980 nm), 7/2 (980-1060 nm), 9/2 (1100-1250 nm) and 11/2 (1300-1450 nm).

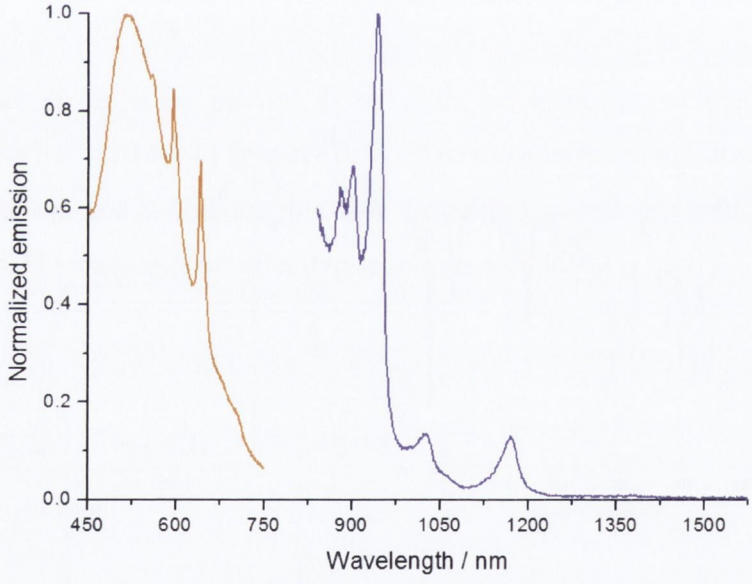


Figure 5.35: Visible (orange line) and near-infrared (purple line) emission spectrum of **Sm(L3)** upon excitation at 340 nm; the spectra are normalised for the sake of comparison.

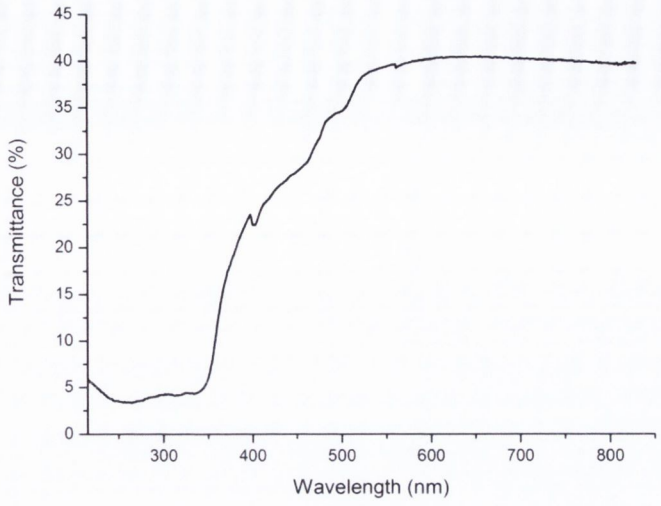


Figure 5.36: Absorption spectrum of **Sm(L3)** in the solid state.

5.5 $[Ho_2(\mathbf{L2})_4(H_2O)_4]$, (**11**)

After the successful synthesis of **10**, we set out to utilise **L2** to generate a new series of lanthanide frameworks.

5.5.1 Synthesis and structural characterisation of compound **11**

The compound $[Ho_2(\mathbf{L2})_4(H_2O)_4]$, **11**, forms reproducibly *via* the reaction of **L2** and $Ho(NO_3)_3{\cdot}5H_2O$ in a 4:1 mole ratio, in a H_2O/KOH solution, at 85 °C. Small pale pink rectangular crystals, suitable for single crystal XRD, separate from the reaction mixture. **11** crystallises in the monoclinic space group *C*2/c and the phase purity of the bulk material was verified by PXRD.

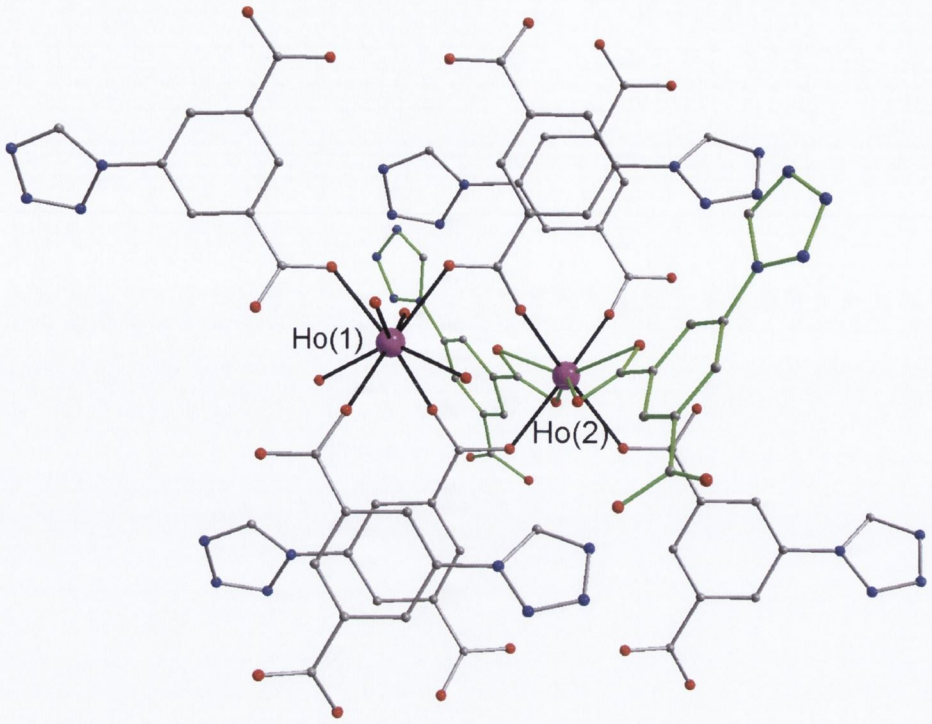


Figure 5.37: The two unique Ho^{III} metal centres found in **11**, coordinated to a total of eight separate **L2** ligands and to four coordination H_2O solvent molecules. The bonds of **L2(b)** have been highlighted green for clarity. Colour code: Ho pink, C grey, O red, N blue. H atoms omitted for clarity.

The asymmetric unit of **11** contains two crystallographically unique Ho^{III} centres, two distinct **L2** ligands and two coordinated water molecules. The two distinct Ho^{III} centres, Ho(1) and Ho(2), have distorted octa-coordinated binding geometries (**Figure 5.37** and **Figure 5.38**). Likewise for compound **10**, this distortion may be attributed to the lack of significant ligand field stabilisation energy. The two crystallographically unique **L2** ligands have differing coordination modes and henceforth will be referred to as **L2(a)** and **L2(b)**. The carboxylate groups of **L2(a)** are both deprotonated and act in a bis-monodentate *syn-syn* μ_2 mode, bridging neighbouring Ho^{III} ions. **L2(b)** has a single chelating carboxylate group, with the second acid group and its symmetry equivalents remaining protonated (**Figure 5.37**).

Ho(1) is coordinated to eight oxygen atoms, four of which derive from four **L2(a)** bridging carboxylate groups, (O(1), O(8), $O(1^{II})$, $O(8^{II})$), with the remaining oxygen atoms (O(9), O(10), $O(9^{II})$, $O(10^{II})$), arising from four coordinated water molecules (**Figure 5.38**). In a similar manner Ho(2) is also coordinated to four oxygen atoms from four deprotonated bridging **L2(a)** carboxylate groups, involving the atoms O(2), O(7), $O(2^{I})$ and $O(7^{I})$ (**Figure**

5.37 and **Figure 5.38**). However, Ho(2) is not coordinated to any water molecules, but is instead coordinated to four oxygen atoms, (O(5), O(6), O(5^{I}), O(6^{I})), arising from two chelating bidentate **L2(b)** carboxylate functionalities.

The bond lengths of bridging Ho-$O_{carboxylate}$ bonds vary between 2.259(6) - 2.327(5) Å; the Ho-$O_{carboxylate}$ bonds involving chelating functionalities are longer at 2.278(6) and 2.446(6) Å; the Ho-O_{water} bond lengths are 2.416(6) and 2.438(6) Å and are in the range of previously reported Ho^{III} complexes.[17] A detailed listing of selected bond lengths and angles can be found in **Table 5.3**.

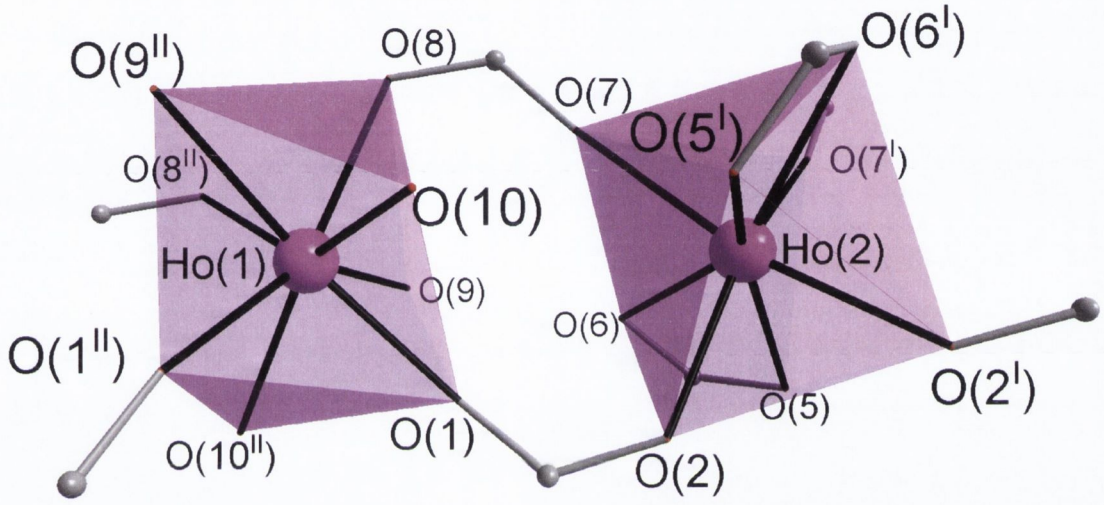


Figure 5.38: Coordination environment of the Ho^{III} metal centres in **11**. Colour code: Ho pink, C grey, O red. H atoms omitted for clarity.

Table 5.3: Selected bond distances and for **11**. Symmetry codes: (I) 1 - x, y, 0.5- z; (II) 2 - x, y, 0.5 - z.

Atoms	Distance (Å)/ Angle(°)	Atoms	Angle(°)
Ho(1)-O(1)	**2.259 (6)**	O(1)-Ho(1)-O(8)	**110.7 (2)**
Ho(1)-O(8)	**2.327 (5)**	O(1)-Ho(1)-O(9)	**71.4 (2)**
Ho(1)-O(9)	**2.416 (6)**	O(1)-Ho(1)-O(10)	**74.7 (2)**
Ho(1)-O(10)	**2.438 (6)**	O(8)-Ho(1)-O(9)	**76.1 (2)**
		O(8)-Ho(1)-O(10)	**76.9 (2)**
		O(9)-Ho(1)-O(10)	**70.9 (2)**

Ho(2)-O(2)	**2.320 (5)**	O(2)-Ho(2)-O(5)	**77.9(2)**
Ho(2)-O(5)	**2.422 (5)**	O(2)-Ho(2)-O(6)	**80.05(2)**
Ho(2)-O(6)	**2.446 (6)**	O(2)-Ho(2)-O(7)	**102.1(2)**
Ho(2)-O(7)	**2.278 (6)**	O(5)-Ho(2)-O(6)	**53.43(2)**
		O(5)-Ho(2)-O(7)	**129.46(2)**
		O(6)-Ho(2)-O(7)	**76.51(2)**

The polymeric structure of **11** is generated *via* the bridging carboxylate groups of **L2(a)** (**Figure 5.39**). In a comparable manner to **10**, the bridging functionalities generate infinite 1D holmium-carboxylate chains that align parallel to the crystallographic *a*-axis (**Figure 5.39**). These chains can be considered as infinite rod-like $[Ho(CO_2)_2]_n$ SBUs. The Ho^{III} centres in **11** are connected to neighbouring metal ions through two bridging carboxylates, as opposed to three bridging carboxylate groups in **10** and the unique holmium ions are separated by an interatomic Ho···Ho distance of 4.77(3) Å.

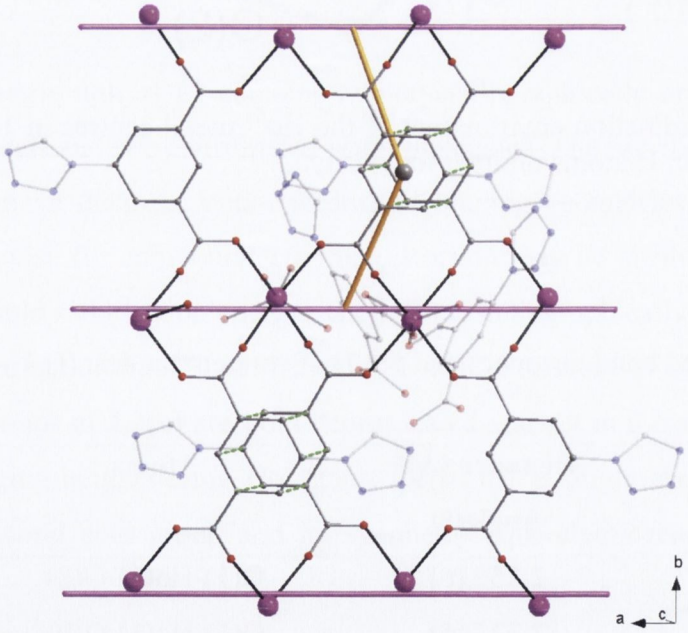


Figure 5.39: 1D polymeric Ho-Ho chain formed through the bridging carboxylate groups of **L2(a)**. The ligand **L2(b)** and the functionalities not involved in the generation of the 2D sheets are faded. The pink coloured rods represent the infinite $[Ho(CO_2)_2]_n$ SBUs in **11**. The dark grey spheres represent the centre of the central phenyl unit of the ligand, with the remaining ligand atoms represented as yellow lines. Dashed green lines depict π- π stacking interactions. Colour code: Ho pink, C grey, O red, N blue. H atoms omitted for clarity.

The 1D Ho-Ho chains are linked to neighbouring chains *via* the remaining carboxylate functionalities of the **L2(a)** ligands, resulting in neutral 2D sheets generated through symmetry operations, which extend in the *a*-direction. The tetrazole moieties are not involved in any coordinative bonding.

The phenyl moieties of adjacent **L2(a)** ligands show evidence of π-π stacking interactions, with a distance of *ca.* 3.5 Å between the centres of adjacent aromatic rings (**Figure 5.39**). The presence of these supramolecular interactions possibly aided the formation of the 2D sheets, and may be responsible for their densely packed nature.

A layered lamellar 3D supramolecular structure is formed through the packing of the neutral layers in the in the direction of the crystallographic *c*-direction. The packing structure is further facilitated through H-bonding interactions that are directed approximately along the *c*-axis. The H-bonds involve the protonated carboxylic acid groups of the **L2(b)** ligands and a coordinated water molecule on a Ho^{III} centre from an adjacent sheet (**Figure 5.40**, **Figure 5.41** and **Figure 5.42**). These H-bonding interactions are characterised by a distance of 2.84 Å between O(3) and a symmetry generated O(10) atom and results in a densely packed structure.

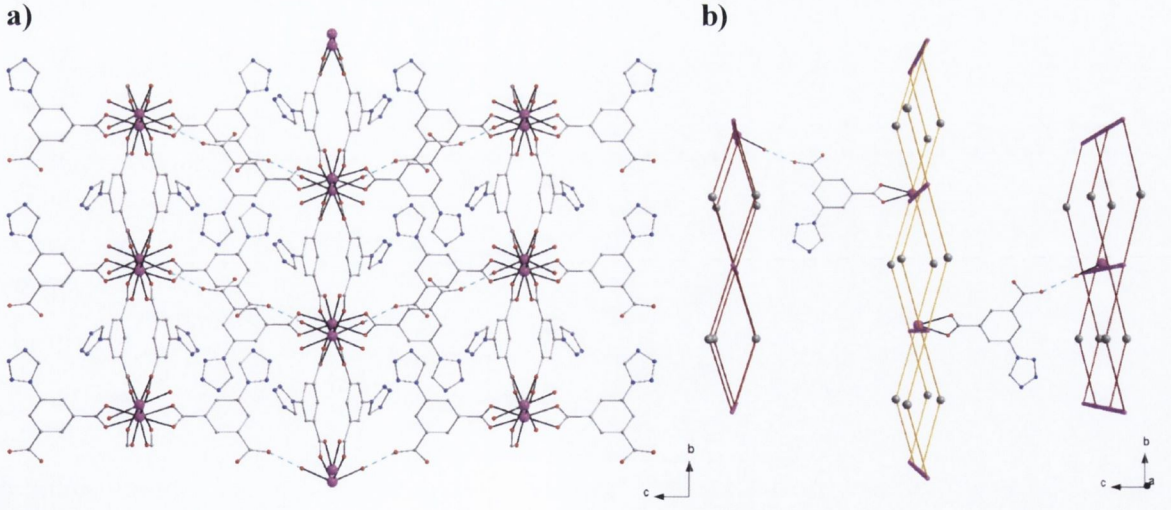


Figure 5.40: The packing structure of **11** viewed along the *a*-axis, **a)** ball and stick model, **b)** schematic representation of the packing structure. The dark grey spheres represent the centre of the phenyl unit of the ligand, with the remaining ligand atoms represented as either yellow or dark red lines. Dashed cyan lines represent H-bonding interactions. Colour code: Ho pink, C grey, O red, N blue. H atoms omitted for clarity.

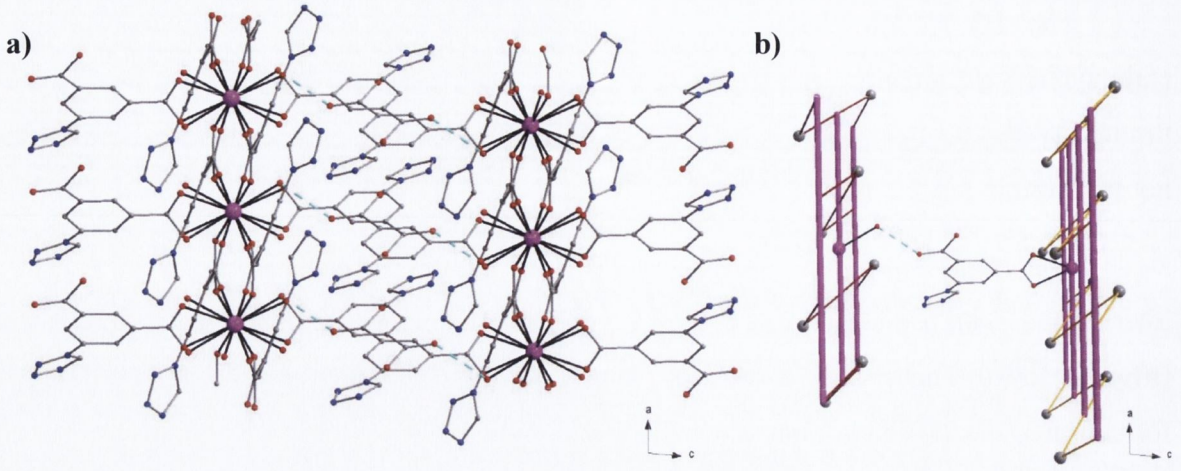


Figure 5.41: The packing structure of **11** viewed in the direction of the crystallographic *b*-axis, **a)** ball and stick model, **b)** schematic representation of the packing structure. The dark grey spheres represent the centre of the phenyl unit of the ligand, with the remaining ligand atoms represented as either yellow or dark red lines. Dashed cyan lines represent H-bonding interactions. Colour code: Ho pink, C grey, O red, N blue. H atoms omitted for clarity

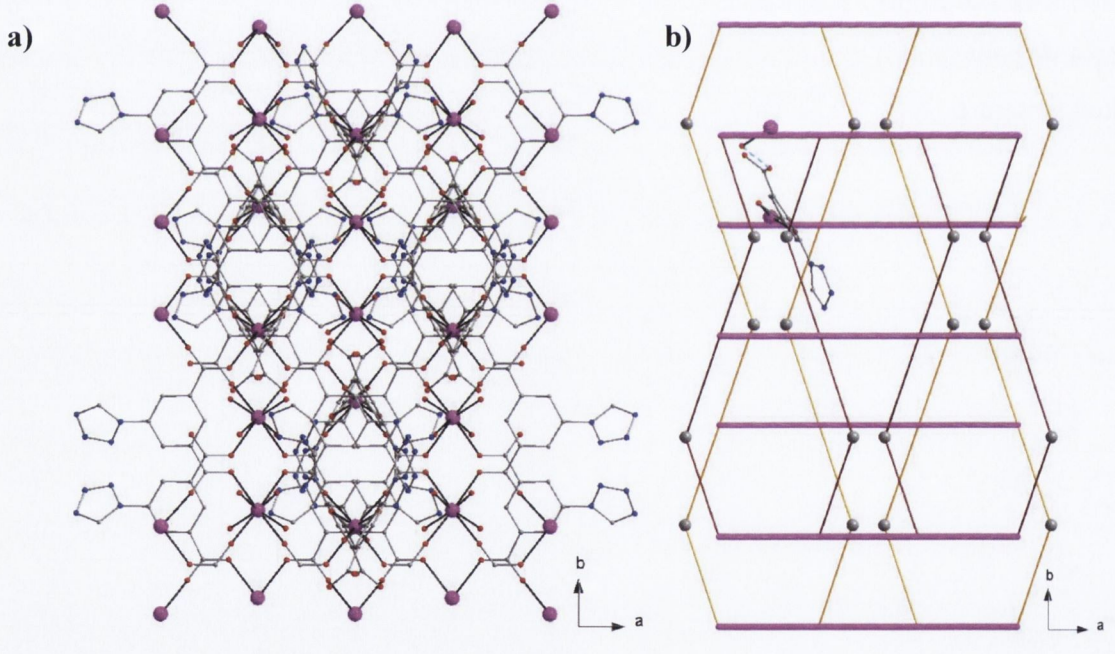


Figure 5.42: The packing structure of **11** viewed in the direction of the crystallographic *c*-axis, **a)** ball and stick model, **b)** schematic representation of the packing structure. The dark grey spheres represent the centre of the phenyl unit of the ligand, with the remaining ligand atoms represented as either yellow or dark red lines. Dashed cyan lines represent H-bonding interactions. Colour code: Ho pink, C grey, O red, N blue. H atoms omitted for clarity

Table 5.4: Crystal data and details of the structure determination for **11**.

Identification code	**11**	
Empirical formula	$C_{18}H_{13}N_8O_{10}Ho$	
Formula weight	666.29 g mol^{-1}	
Temperature	153(2) K	
Wavelength	1.54178 Å	
Crystal system	Monoclinic	
Space group	*C*2/c	
Unit cell dimensions	a = 9.406(5) Å	α= 90°.
	b = 18.881(5) Å	β= 96.150(5) °.
	c = 25.111(5) Å	γ= 90°.
Volume	4434(3) $Å^3$	
Z	8	
Density (calculated)	1.781 Mg/m^3	
Absorption coefficient	6.800 mm^{-1}	
F(000)	2384	
Crystal size	0.2 x 0.1 x 0.1 mm^3	
Theta range for data collection	3.54 to 61.182°	
Index ranges	$-10 \leq h \leq 6$, $-21 \leq k \leq 20$, $-27 \leq l \leq 28$	
Reflections collected	7467	
Independent reflections	3114 [R(int) = 0.0197]	
Completeness to theta = 61.182°	91.5 %	
Refinement method	Full-matrix least-squares on F^2	
Data / restraints / parameters	3114 / 24 / 313	
Goodness-of-fit on F^2	1.060	
Final R indices [I>2sigma(I)]	R_1 = 0.0693, wR_2 = 0.1807	
R indices (all data)	R_1 = 0.0703, wR_2 = 0.1821	
Largest diff. peak and hole	2.44 and -1.04 e.$Å^{-3}$	

5.5.2 Further characterisation of **11**

A PXRD experiment was conducted on a crystalline sample of **11**. The experimental powder pattern correlates to the simulated powder pattern derived from the refined single crystal diffraction data (**Figure 5.43**). Thus, the data confirms the phase purity of the bulk crystalline material and furthermore it supports the accuracy the refined structural model derived from the single crystal X-ray data.

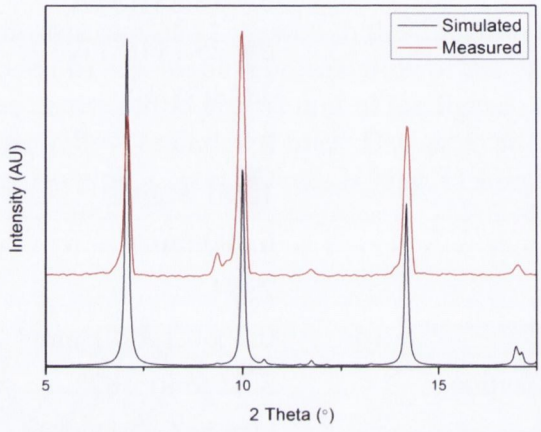


Figure 5.43: PXRD analysis of compound **11**, with the simulated pattern in black and the measured pattern in black.

The broad band centred at 3390 cm^{-1} in the FT-IR spectra of **11**, provides further evidence for the hydrogen bonding interactions present in **11** (**Figure 5.44**). The sharp signal present at 1709 cm^{-1} is attributable to the protonated carboxylic acid groups found in **11**. The distinctive band of the tetrazole C=N stretch is present at 1615 cm^{-1}. Adjacent to this, one can identify a band characteristic of the asymmetric C=O vibrations of the bridging and chelating carboxylate groups at 1567 and 1546 cm^{-1}. Additionally there is a broad signal at 1400 cm^{-1} and an adjacent shoulder at 1386 cm^{-1} resulting from the overlapping signals of symmetric carboxylate and C-N stretching vibrations.

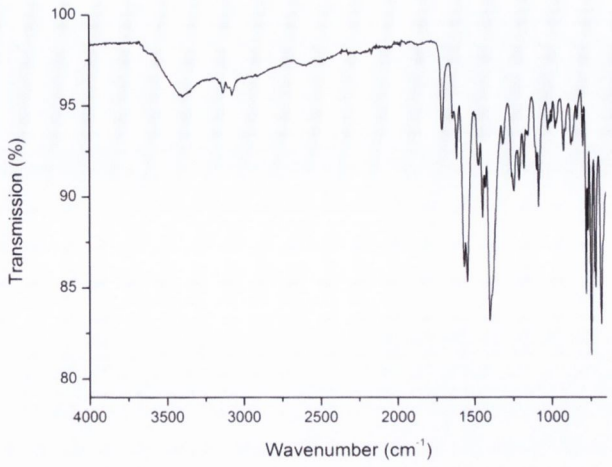


Figure 5.44: FT-IR spectrum of **11**.

The thermal stability of **11** was investigated by heating a sample of a freshly prepared sample from 25 °C to 900 °C, at a rate of 10 °C min^{-1} and recording the subsequent weight loss (**Figure 5.45**). A weight loss occurs between 140 and 230 °C, which is assignable to the loss of the coordinated water molecules (actual 4.6%, theoretical 5.4%). This is followed by the two-step thermal degradation of the organic ligand between *ca.* 230 and 510 °C.

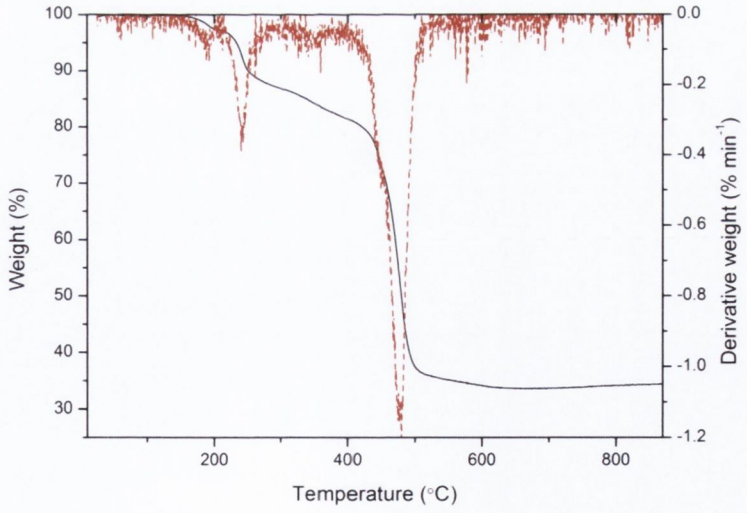


Figure 5.45: TGA of **11**, showing the percentage weight loss as a black line and the derivative of the percentage weight loss as the broken red line.

5.6 Lanthanide compounds structurally related to **11**

Dysprosium ($[Dy(\mathbf{L2})_4(H_2O)_4$) and ytterbium ($[Yb(\mathbf{L2})_4(H_2O)_4$) compounds isostructural to **11** were synthesised using an analogous synthetic procedure to that of **11**, with the respective lanthanide nitrate replacing holmium nitrate. The resulting crystals proved too small for single crystal XRD and hence their isostructural topologies were confirmed *via* a combination of PXRD analysis, FT-IR spectroscopy and TGA.

5.6.1 PXRD studies of the Ln^{III} compounds structurally related to **11**

PXRD analysis of the synthesised dysprosium and ytterbium compounds indicate that they are isostructural to **11**, (**Figure 5.46**). There are some slight deviations in the pattern of **11(Yb)** compared to that of **11**. The smaller ionic radii of Yb^{III} ions may result in a slightly smaller unit cell parameters and in agreement with the inverse relationship of Bragg's law, the larger 2Θ values for the Yb^{III} analogue may account for the slight deviations between the respective patterns.

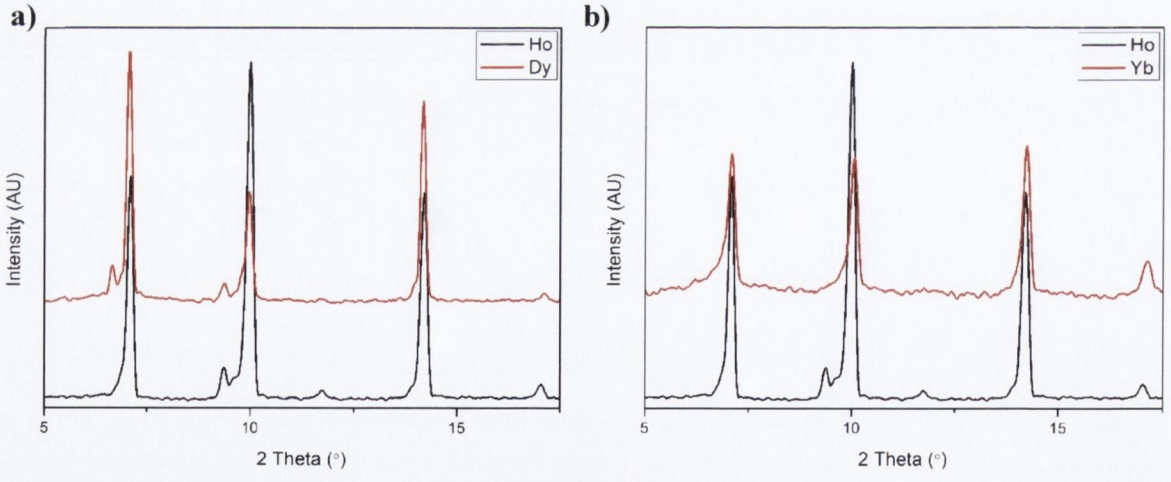


Figure 5.46: PXRD patterns of **a) 11(Dy)** and **b) 11(Yb)** compared to that of **11**.

5.6.2 FT-IR of Ln(**L2**) compounds isostructural to **11**

The FT-IR spectra of **11(Dy)** and **11(Yb)** provide additional evidence of their isostructural topologies, as they are almost identical to that of **11** (**Figure 5.47**). They both display a sharp signal characteristic of a protonated carboxylic acid group at 1710 cm^{-1}. The appearance of bands typical of asymmetric bridging and chelating carboxylate groups at *ca.* 1567 and 1546 cm^{-1} indicate that the carboxylate groups in **11(Dy)** and **11(Yb)** have identical coordination modes as found in **11**. Furthermore, **11(Dy)** and **11(Yb)** display the same overlapping bands as **11** at 1400 cm^{-1} and 1386 cm^{-1} resulting from carboxylate and C-N stretching vibrations.

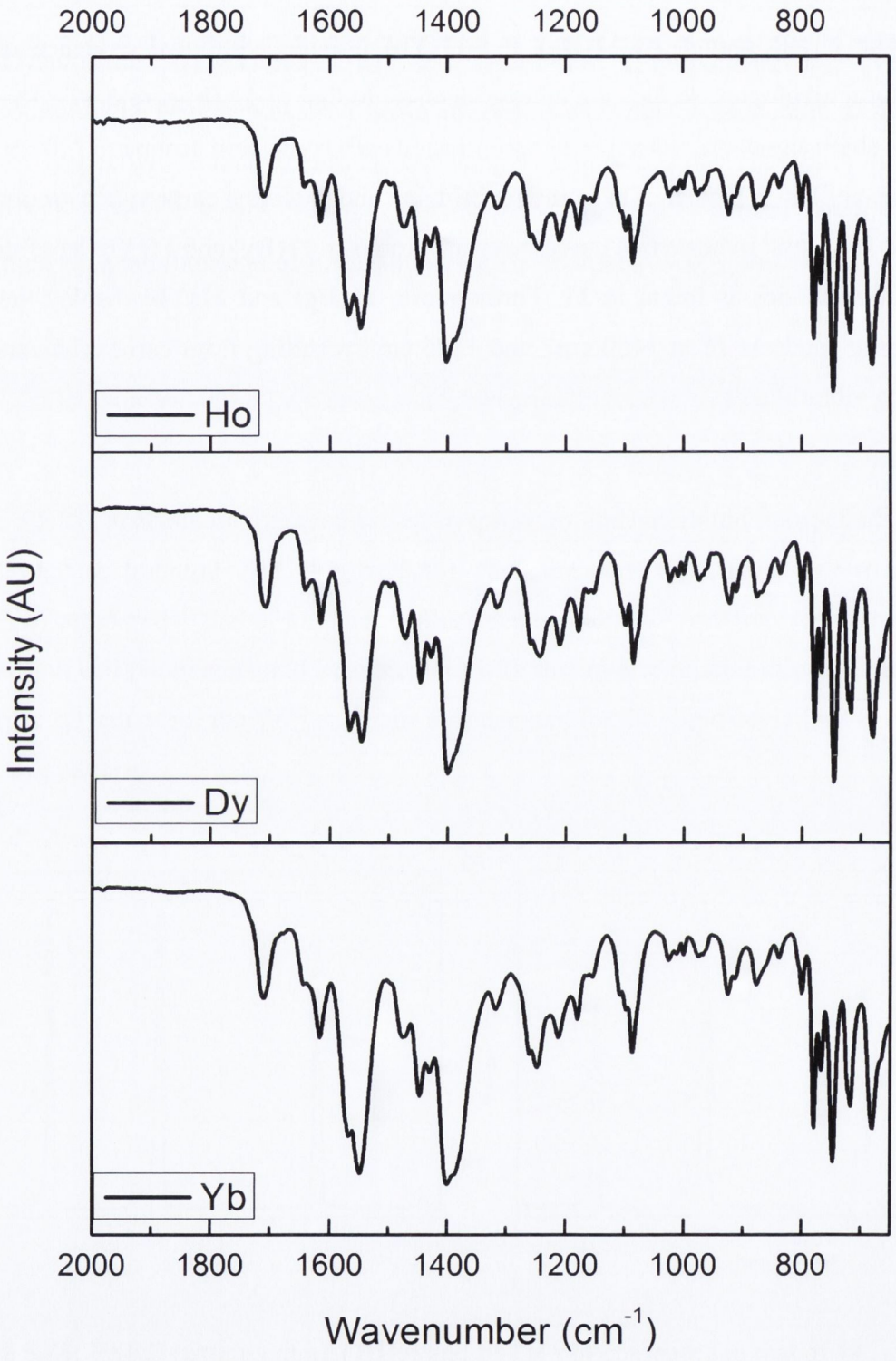


Figure 5.47: FT-IR spectra of **11**, **11(Dy)** and **11(Yb)**.

5.6.3 TGA of Ln^{III} compounds isostructural to **11**

The thermal decomposition pathway of **11(Dy)** and **11(Yb)** in an air atmosphere closely matches that of **11** (**Figure 5.48**). There is an initial weight loss of *ca.* 5 % between 30 and 220°C, attributable to the loss of coordinated water molecules. The degradation of the ligand for the isostructural compounds occurs between approximately 230 and 510 °C.

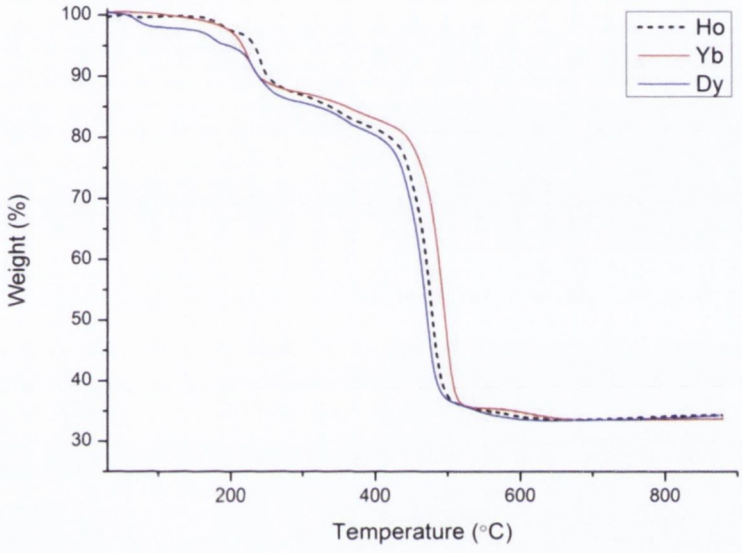


Figure 5.48: TGA of **11** and the related compounds **11(Yb)** and **11(Dy)**.

5.7 Conclusion

Following on from the successful synthesis of the porous transition metal based MOFs outlined in Chapter 4, we decided to utilise **L3** to explore the synthesis of lanthanide based MOFs.

Compound **10** contains infinite 1D holmium-carboxylate chains extending along the crystallographic *c*-axis. Through the extended tritopic ligand **L3**, these infinite $[Ho(CO_2)_3]_n$ SBUs are linked to generate a porous, non-interpenetrated 3D MOF, with an experimental BET surface area that varies between 720 and 765 $m^2 g^{-1}$ depending on the applied activation method. The measured value of χT, 14.3 cm^3 k mol^{-1}, is in a close agreement with the expected value of 14.0625 k mol^{-1} for one Ho^{III} ion (S = 2, L = 6, $^5I_8$), furthermore, the field dependence of the magnetisation suggested the presence of magnetic anisotropy.

Using the synthetic strategy employed to produce **10**, a series of structurally closely related lanthanide (Dy^{III}, Er^{III}, Eu^{III}, Tb^{III} and Yb^{III}) compounds was synthesised. The close structural relationship of the resulting complexes was confirmed using a combination of analytical techniques including PXRD, FT-IR, thermogravimetric and elemental analyses. The small size of the resulting crystals precluded us from studying them *via* single crystal XRD. Further evidence for the isostructural nature of **10(Dy)** and **10** arises from their closely matching magnetic properties. **10(Dy)** has a χT value of 13.6 cm^3 k mol^{-1} which is close to the expected value of 14.1667 for one Dy^{III} ion (S = 5/2, L = 5, $^6H_{15/2}$), the field dependence of magnetisation also indicates the presence of magnetic anisotropy.

The photoluminescent properties of the structurally related compounds **10(Eu)**, **Nd(L3)** and **Sm(L3)** were studied and showed **L3** to be an effective sensitiser for lanthanide ions. **L3** displays a broad band emission between 375 and 650 nm and upon complexation to Eu^{III} the emission maximum is red-shifted by 70 nm to 510 nm. **10(Eu)** displays typical Eu^{III} $^5D_0 \rightarrow {}^7F_0$ (J = 0-6) emission bands and displays excellent photostability. **L3** proved to be capable of sensitising Nd^{III} near-IR emission in **Nd(L3)** and the synthesised compound **Sm(L3)** displayed emission bands in both the visible and near-IR regions.

Finally, utilising the ligand **L2** that was first discussed in Chapter 3, we were able to synthesise compound **11**. This novel framework contains two crystallographically unique octa-coordinated Ho^{III} metal centres linked *via* bridging carboxylate groups to form infinite 1D Ho-Ho chains. The remaining carboxylate groups of the bridging organic ligands link

the individual chains to form 2D sheets. The packing of these sheets involve H-bonding interactions, to form a supramolecular layered lamellar structure.

The isostructural compounds **11(Dy)** and **11(Yb)** were synthesised in a similar manner to **11**. PXRD, FT-IR and TGA experiments confirmed that they are isostructural to **11**.

5.8 References

1. W. G. Lu, L. Jiang, X. L. Feng and T. B. Lu, *Inorganic Chemistry*, 2009, **48**, 6997-6999.
2. B. V. Harbuzaru, A. Corma, F. Rey, P. Atienzar, J. L. Jorda, H. Garcia, D. Ananias, L. D. Carlos and J. Rocha, *Angewandte Chemie-International Edition*, 2008, **47**, 1080-1083.
3. Y. W. Lin, B. R. Jian, S. C. Huang, C. H. Huang and K. F. Hsu, *Inorganic Chemistry*, 2010, **49**, 2316-2324.
4. U. Glasgow, *Platon*, 2006, **1.10**, A Multipurpose Crystallographic Tool.
5. X. Y. Tang, S. T. Yue, P. Li, N. Wang and Y. L. Liu, *Journal of Rare Earths*, 2008, **26**, 800-803.
6. X. Li and Z. Y. Zhang, *Journal of Chemical Crystallography*, 2005, **35**, 871-874.
7. T. Devic, C. Serre, N. Audebrand, J. Marrot and G. Férey, *Journal of the American Chemical Society*, 2005, **127**, 12788-12789.
8. C. Daiguebonne, N. Kerbellec, K. Bernot, Y. Gerault, A. Deluzet and O. Guillou, *Inorganic Chemistry*, 2006, **45**, 5399-5406.
9. T. Devic, V. Wagner, N. Guillou, A. Vimont, M. Haouas, M. Pascolini, C. Serre, J. Marrot, M. Daturi, F. Taulelle and G. Férey, *Microporous and Mesoporous Materials*, 2011, **140**, 25-33.
10. Z. Majeed, K. C. Mondal, G. E. Kostakis, Y. H. Lan, C. E. Anson and A. K. Powell, *Chemical Communications*, 2010, **46**, 2551-2553.
11. I. Rusinek, J. Sienkiewicz-Gromiuk, L. Mazur and Z. Rzaczynska, *Journal of Inorganic and Organometallic Polymers and Materials*, 2013, **23**, 1068-1077.
12. Z. Majeed, G. E. Kostakis, Y. H. Lan and A. K. Powell, *Dalton Transactions*, 2011, **40**, 12210-12216.
13. J. A. Fernandes, R. A. S. Ferreira, M. Pillinger, L. D. Carlos, J. Jepsen, A. Hazell, P. Ribeiro-Claro and I. S. Goncalves, *Journal of Luminescence*, 2005, **113**, 50-63.
14. J. P. Leonard, C. M. G. dos Santos, S. E. Plush, T. McCabe and T. Gunnlaugsson, *Chemical Communications*, 2007, 129-131.
15. S. Comby, J.-C. G. Bünzli, K. A. Gschneidner, Jr., , J.-C. G. Bünzli and V. K. Pecharsky, Eds., *Lanthanide Near-Infrared Luminescence in Molecular Probes and Devices. In Handbook on the Physics and Chemistry of Rare Earths*, Elsevier Science B.V., Amsterdam, 2007.

16. W. T. Carnall, P. R. Fields and K. Rajnak, *Journal of Chemical Physics*, 1968, **49**, 4412-4424.

17. Z. H. Li, D. F. Hong, L. P. Xue, W. J. Fu and B. T. Zhao, *Inorganica Chimica Acta*, 2013, **400**, 239-243.

Chapter 6

Conclusions

6 Conclusions

The aim of this research project was to synthesise and characterise novel MOFs, composed of both mononuclear and polynuclear SBUs, linked *via* tritopic organic linkers.

L1 was shown to be capable of producing network structures, however, it was found to be synthetically difficult to involve both of its tetrazole moieties in coordination bonding and this resulted in densely packed frameworks. Noting this it was decided to alter the ligand through the substitution of a tetrazole group for a carboxylic acid functionality. The resulting ligand **L2** proved to be highly versatile and capable of producing MOFs with both transition and lanthanide metal cations. Furthermore, the rigid nature of **L2** enabled the permanent porosity and large solvent accessible void volume of 52% found in [Cu(**L2**)], **5**. The high CO_2 storage capability of **5** may in part be attributed to the tetrazole moiety of **L2**, identifying it as a suitable functional group for future MOFs designed for CO_2 storage or separation.

The ligand **L3** proved to be highly adept at producing open-frameworks, owing to its rigid, extended and polycarboxylate topology. Additionally, the large number of aromatic moieties ensured that the interpenetrated frameworks found in compounds **6-9** were tightly interwoven and consequently catenation was not detrimental to their respective void volumes. Through the successful modification of the synthetic conditions it was possible to generate a series of SBUs, varying from copper paddlewheels and pentanuclear zinc complexes to infinite 1D $[Ho(CO_2)_3]_n$ SBUs. The pentanuclear clusters present in $(Me_2NH_2)[Zn_5(\mathbf{L3})_3(\mu_3\text{-}OH)_2(DMF)_2]$, **7**, and $(Me_2NH_2)[Co_5(\mathbf{L3})_3(\mu_3\text{-}OH)_2(DMF)_2]$, **8**, proved to be exceptionally rigid and together with the inflexible structure of **L3** facilitated the permanent porosity of the respective compounds after the removal of the solvent molecules residing in their channels. It is recommended that future studies involving compounds $[Zn_3(\mathbf{L3})_2(DMF)_2]$, **6**, and the **pto**-type framework $[Cu_3(\mathbf{L3})_2(H_2O)_3]$, **9**, are conducted in solution. This would prevent the destructive capillary forces that lead to the collapse of their open-frameworks, whilst facilitating the exploitation of their large internal cavities for possible applications such as heterogeneous catalysis.

Finally, the extended nature of **L3** successfully counteracted the high coordination number of the Ho^{III} cations present in $[Ho(\mathbf{L3})(H_2O)_2]$, **10**, to produce an open-framework with a large void space of 60% of the unit cell volume. It was found that the thermal treatment of **10** produces a rare example of a porous LnMOF. Photoluminescent studies

identified **L3** to be an effective sensitiser for both visible and near-infrared emission in compounds structurally closely related to **10**. As such, possible future work may be directed towards the introduction of additional lanthanide metal cations during the synthesis of **10(Eu)**, with the aim of fine-tuning its photoluminescent properties. By varying the concentration of the doped lanthanide ions it may be possible to generate an efficient solid state white light emitting material or a series of fluorescent labels.

Chapter 7

Experimental

7 Experimental

7.1 Materials and methods

7.1.1 Reagents

All chemicals and solvents were of reagent grade and purchased from Sigma-Aldrich Chem. Co. Ltd. or local solvent suppliers and were used as received, unless otherwise stated. Water was deionised before use.

7.1.2 Nuclear magnetic resonance spectroscopy

^{1}H-NMR, spectra were recorded on a Bruker DPX 400 spectrometer operating at 400.13 MHz by either Dr. John O'Brien or Dr. Manuel Rüther. Samples were analysed in deuterated solvents and are listed for each spectrum. Abbreviations for spectra: s, singlet; d, doublet; t, triplet; qt quartet; q, quaternary; m, multiplet; br broad and J, coupling constant.

7.1.3 Infrared spectroscopy

Infrared spectroscopy was recorded using a PerkinElmer Spectrum One FT-IR spectrometer using either a universal ATR sampling accessory or a diffuse reflectance sampling accessory. The scan rate was 16 scans per minute with a resolution of 4 scans in the range 4000-600 cm^{-1}. The following abbreviations were used to describe the intensities: vs, very strong; s, strong; m, medium; w, weak; vw, very weak; sh, shoulder; br, broad and vbr, very broad.

7.1.4 Mass spectrometry

Electrospray mass spectroscopy was carried out on a Micromass LCT Electrospray mass spectrometer by Dr. Martin Feeney. Samples were dissolved in HPLC grade solvents which are listed for each spectrum.

7.1.5 Elemental analysis

Elemental analysis was undertaken by the analytical lab in UCD Belfield, using an Exeter Analytical CE440 analyser.

7.1.6 Single crystal X-ray diffraction

Single crystal X-ray analyses for crystals described in this report were performed by either Dr. Thomas McCabe, Dr. Lei Zhang or Dr. Nian-Yong Zhu on either a Bruker SMART APEX CCD diffractometer, a Bruker Apex Duo diffractometer or a Rigaku Saturn-724 diffractometer.

The diffractometers utilise a graphite-monochromated Mo-Kα radiation ($\lambda = 0.71073$ Å) source. The omega scan method was used to collect either a full sphere or hemisphere of data for each crystal with a detector to crystal distance of either 5 or 6 cm at a temperature of 150 K unless otherwise stated. Data were collected, processed, and corrected for Lorentz and polarisation effects using SMART, SAINT-PLUS and Apex2 software packages.[1] The structures were solved using direct methods with the SHELXTL program package.[1] All non-hydrogen atoms were refined anisotropically. Hydrogen atoms (excluding water and carboxylic acid groups) were assigned to calculated positions using a riding model with appropriately fixed isotropic thermal parameters.

The data sets from the Rigaku Saturn-724 diffractometer were collected using the Crystal Clear-SM 1.4.0 software package and in each case 1680 diffraction images, of 0.5° per image, were recorded. Data integration, reduction and correction for absorption and polarisation effects were all performed using the Crystalclear-SM 1.4.0 software. Space group determination, structure solution and refinement were obtained using Crystalstructure ver. 3.8 and SHELXTL software.

Images based on refined data sets were produced with the software package Diamond 3.[2]

7.1.7 X-ray powder diffraction

X-ray powder diffraction measurements were performed using a Siemens D500 diffractometer with a Cu-K α_1 radiation with a wavelength of $\lambda = 1.54056$ Å.

7.1.8 Solvothermal synthesis

Solvothermal synthesis was carried out using a Parr Instrument Company Series 4760/4765 general-purpose digestion bomb employing a 20 ml Teflon insert. Maximum loading of the insert was dependent on reagents but a typical volume of 8-10 ml was used.

The heating cycles are specified for each reaction and were performed in a conventional convection oven.

7.1.9 Thermogravimetric Analysis

Thermogravimetric analysis (TGA) was carried out using a Perkin Elmer Pyris 1 TGA in air using a ceramic crucible (*ca.* 5 mg sample; heating rate of 10 °C min^{-1}; range 25-900 °C). The instrument was calibrated in air atmosphere to indium and nickel standards.

7.1.10 Magnetic measurements

All measurements were performed by Prof. Rodolphe Clérac at the Centre de Recherche Paul Pascal, Université de Bordeaux, France. The magnetic susceptibility measurements were obtained with the use of a MPMS-XL Quantum Design SQUID magnetometer. This magnemometer operates between 1.8 and 300 K for *dc* applied fields ranging between -7 to 7 T. Measurements were performed on polycrystalline samples, which were taken from the mother liquor and immediately placed inside a polyethylene bag to prevent solvent loss. The magnetic data were corrected for the sample holder and diamagnetic contributions.

7.1.11 Photoluminescence spectroscopy

Solid state photoluminescence spectroscopy were recorded on a Fluorolog-3 (Horiba Jobin Yvon) spectrophotometer. Spectra measured in the UV/visible range used a room temperature R9281x photomultiplier tube as the detector. Near-Infrared (NIR) spectra were measured using a liquid nitrogen cooled R5509 photomultiplier tube as the detector. Emission and excitation spectra were corrected for the wavelength response of the system and the intensity of the lamp profile over the excitation range, respectively, using correction factors supplied by the manufacturer. Photostability and lifetime measurements were conducted using a Varian-Cary-Eclipse luminescence spectrometer.

7.1.12 Gas sorption measurements

N_2, H_2 and CO_2 pressure measurements were performed on an Autosorb-IQ (Quantachrome) volumetric analyser. Samples were outgassed at 10^{-6} torr and at a

temperature specified for each sample. The dead volume was estimated using helium, under the assumption that it is not absorbed at any of the studied temperatures. Measurements undertaken at 77 K were performed in a liquid N_2 bath. Room temperature measurements were conducted in a water bath in order to maintain a constant temperature. To provide high accuracy and precision in determining p/p_0, the saturation pressure was measured throughout the gas sorption measurements by means of a dedicated saturation pressure transducer. Ultra-high grade N_2, H_2 and CO_2 (99.999% purity) were used throughout the experiments. The non-ideality of gases were obtained from the second viral coefficient at experimental temperatures.[3] The surface area of the relevant samples were determined from the N_2 isotherms.

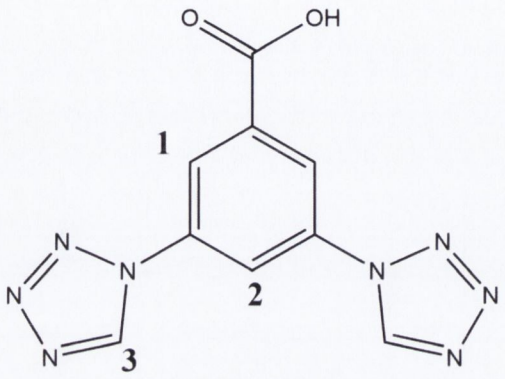
Super critical CO_2 was used in a process known as critical point drying (CPD). In this process the constitutional solvent molecules in a MOF are replaced with an 'intermediate' solvent with a lower surface tension and which homogenously mixes with liquid CO_2. To fully replace the solvent molecules, the compound is dispersed in the intermediate solvent and over a course of a few days the solvent is replenished several times with fresh solvent.

After the solvent exchange process is complete the material to be de-solvated is placed in a high-pressure vessel, contained within a Quorum Technologies K850 Critical Point Drier and liquid CO_2 is pumped into the chamber which has been pre-cooled to 5 °C. The higher density of the intermediate solvent causes it to sink to the bottom of the chamber, at which point the solvent can be removed through an opening at the base of the vessel. This process is repeated several times to guarantee that the intermediate solvent has been completely removed. At all times the sample is completely submerged in liquid CO_2 to ensure that no intermediate solvent evaporates which could potentially damage the delicate pores of the structure.

Once the intermediate solvent has been removed the chamber is slowly heated to 35-40 °C, resulting in an increase in pressure and the passing of the critical temperature and pressure points of CO_2. At this stage the meniscus of the liquid CO_2, which up until this point was visible through a glass window, disappears, due to the loss of surface tension and the CO_2 can be safely removed. An exhaust valve is opened and the CO_2 is very slowly released from the chamber. The sample can then be transferred to the Autosorb-IQ volumetric analyser for surface area measurements.

7.2 Ligand Synthesis

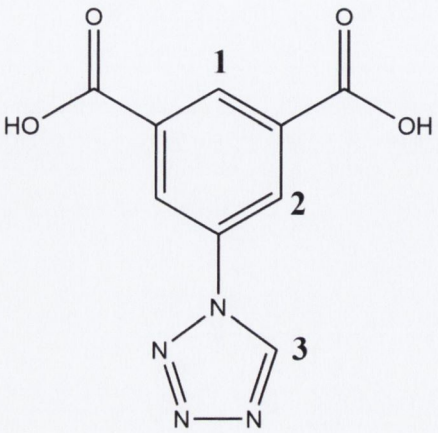
7.2.1 Synthesis of 3,5-di(1H-tetrazol-1-yl)benzoic acid, (**L1**)



3,5-Diaminobenzoic acid (10 g, 0.066 mol) and sodium azide (9.44 g, 0.145 mol) were added to glacial acetic acid (150 ml) in a 500 ml round bottom flask and stirred for 20 minutes. To this triethyl orthoformate (58.6 g, 65.8 ml, 0.396 mol) was added slowly with stirring. The mixture was then heated at 100 °C for 1 day. After cooling to room temperature a solution of HCl (20 ml, 37 w/w%) in deionised H_2O (200 ml) was added and stirred for one hour. The precipitate was filtered and washed with deionised H_2O and diethyl ether and dried in an oven at 50 °C for 12 hours, to give a dark grey powder.

Yield: 8.884 g (34.4 mmol, 53%); ^{1}H-NMR (DMSO-D_6, 400MHz): δ_H (ppm)= 10.3595 (s, 2H, H^3), 8.8258 (s, 2H, H^1), 8.6132 (s, 1H, H^2); ES-MS (DMSO) m/z = 257 $(C_9H_5N_8O_2)^-$; FT-IR (diffuse reflectance) ν_{max} cm^{-1}: 3,070 (w), 1,713 (s), 1,599 (m), 1,474 (m), 1,357 (m), 1,262 (s), 1,202 (s), 1,086 (s), 1,005 (m), 893 (m), 768 (vs), 674 (vs); Elemental analysis (%) for $C_9H_6N_8O_2$: Expected: C, 41.87%; H, 2.34%; N, 43.4%. Found: C, 42.59%; H, 2.89%; N, 41.4.

7.2.2 Synthesis of 5-(1H-tetrazol-1-yl)isophthalic acid, (**L2**)

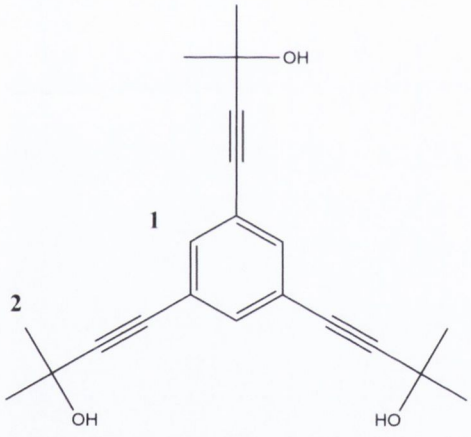


5-Aminoisophthalic acid (10 g, 0.0552 mol) and sodium azide (3.9 g, 0.060 mol) were added to glacial acetic acid (150 ml) in a 500 ml round bottom flask and stirred for 20 minutes. To this triethyl orthoformate (24.5 g, 27.5 ml, 0.165 mol) was added slowly with stirring. The mixture was heated to 100 °C for 6 hours. After cooling to room temperature a solution of HCl (40 ml, 37 w/w %) in deionised H_2O (200 ml) was added and stirred for

one hour. The precipitate was filtered and washed with deionised H_2O and diethyl ether and dried in an oven at 50 °C for 12 hours, to give a pale yellow powder.

Yield: 6.45 g (0.027.5 mol, 50%); ^{1}H-NMR (DMSO-D_6, 400MHz): δ_H (ppm)= 10.3522 (s, 1H, H^3), 8.6631 (s, 2H, H^2), 8.5684 (s, 1H, H^1); ES-MS (DMSO) m/z= 257 $[C_9H_6N_4O_4Na]^+$; FT-IR (diffuse reflectance) ν_{max} cm^{-1}: 3,129 (w), 2,522 (w), 1,888 (w), 1,714 (s), 1,661 (s), 1,606 (m), 1,429 (m), 1,479 (m), 1,438 (s), 1,319 (m), 1,291 (s), 1,231 (s). 1,205 (s), 1,176 (s), 1,143 (s), 1,084 (m), 1,071 (s), 1,006 m), 988 (s), 919 (s), 888 (m), 862 (m), 820 (m), 758 (vs), 711 (vs), 680 (vs); Elemental analysis (%) for $C_9H_6N_4O_4$: Expected: C, 46.16; H, 2.58; N, 23.96. Found: C, 46.94; H, 2.94; N, 22.77.

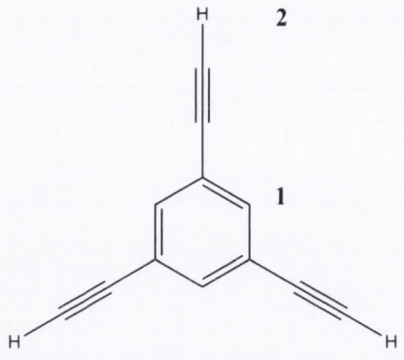
7.2.3 Synthesis of 1,3,5-tris(2-methyl-2-hydroxy-3-butnyl)-benzene



2-Methyl-3-butyn-2-ol (52.08 g, 0.619 mol) was added to a mixture of 1,3,5-tribromobenzene (31.5 g, 0.100 mol), $Pd(PPh_3)_2Cl_3$ (0.90 g, 1.28 mmol) and copper iodide (0.9 g, 4.73 mmol) in dried triethyl amine (200 ml). The resulting mixture was stirred under an inert nitrogen atmosphere for 24 hours at 100 °C. The resulting insoluble inorganic salt was removed by filtration and washed with triethyl amine. The solvent and unreacted 2-methyl-3-butyn-2-ol were removed and the dry, solid product was recrystallised from ethyl acetate. The crystals were filtered off and washed with a mixture of petroleum ether and ethyl acetate to give yellow crystals which were then dried under vacuum.

Yield: 19.98 g, (0.061 mol, 62%); ^{1}H-NMR ($CDCl_3$, 400MHz) δ_H (ppm): 7.41 (s, 3H, H^1), 1.61 (s, 18H, H^2).

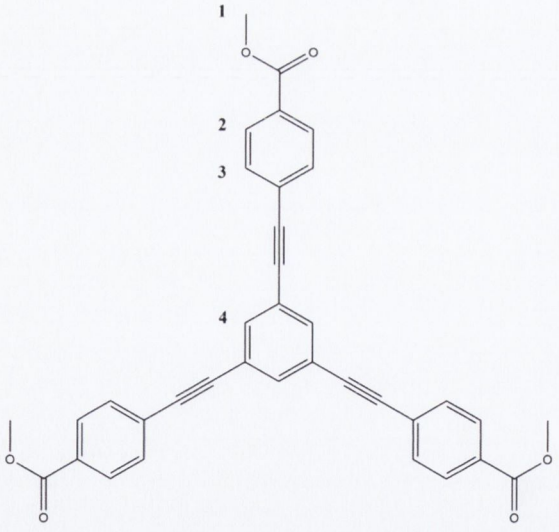
7.2.4 Synthesis of 1,3,5-triethynylbenzene



1,3,5-Tris(2-methyl-2-hydroxy-3-butnyl)-benzene (19.98 g, 0.06 mol) was dissolved in toluene (200 ml) and to this a solution of potassium hydroxide (5 g, 0.125 mol) in methanol (20 ml) was added. The resulting mixture was heated to 110 °C for 4 hours, when the reaction was deemed to be complete by TLC analysis. The acetone by-product was collected during the course of the reaction using a Dean-Stark apparatus. The cooled solution was acidified with HCl (3 M) and the resulting precipitate was filtered off and washed with toluene and dried overnight with $NaSO_4$. The toluene was removed and the resulting solid subjected to column chromatography, (petroleum ether: dichloromethane = 4:1 v:v), to give a pale yellow solid.

Yield: 3.884 g, (0.026 mol, 43%); ^{1}H-NMR ($CDCl_3$, 400MHz) δ_H (ppm): 7.60 (s, 3H, H^1), 3.14 (s, 3H,H^2).

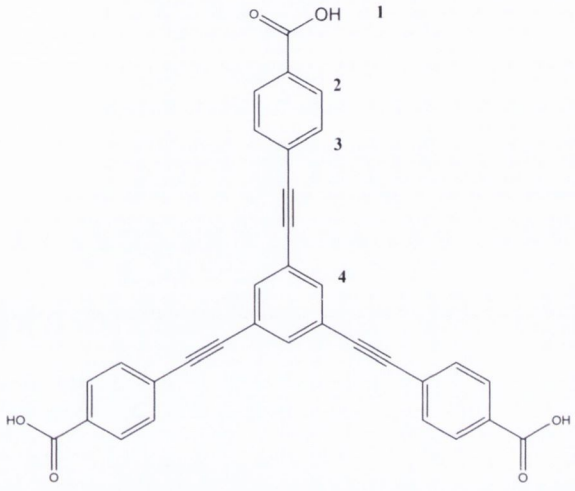
7.2.5 Synthesis of trimethyl-4,4',4"-(benzene-1,3,5–triyltris(ethyne-2,1-diyl))tribenzoate



Methyl-4-iodobenzoate (19.93 g, 79.96 mmol), copper iodide (0.40 g, 0.21 mmol) and $Pd(PPh3)_2Cl_2$ (0.6 g, 0.8 mmol) were dissolved in NEt_3 (330 ml) under a nitrogen atmosphere and to this a solution of 1,3,5-triethynylbenzene (3.76 g, 25 mmol) in triethyl amine (20 ml) was added. The resulting solution was stirred under a nitrogen atmosphere for 24 hours at 30 °C, when the reaction was monitored by TLC analysis. The product was purified by column chromatography (dichloromethane: ethyl actetate = 3:1, v:v) and finally through recrystallisation from a dichloromethane/methanol mixture (2:1, v:v). The resulting crystals were washed with MeOH and air dried to give off white pale cream crystals.

Yield: 12.78 g (23 mmol, 92%); ^{1}H-NMR ($CDCl_3$, 400MHz) δ_H (ppm): 8.06 (d, 6H, J=7.8Hz, H^2), 7.71 (s, 3H, H^4), 7.61 (d, 6H, J=7.8Hz, H^3), 3.96 (s, 9H, H^1).

7.2.6 Synthesis of 1,3,5-Benzene-trisethynyl benzoic acid, (**L3**)



Trimethyl-4,4',4"-(benzene-1,3,5-triyltris(ethyne-2,1-diyl))tribenzoate (12.69 g, 23 mmol) was dissolved in THF (300 ml) and to this a solution of $LiOH.H_2O$ (13.97 g, 0.33 mol) in H_2O (65 ml). The mixture was left stirring overnight and the volume of THF was reduced by half and cold HCl (3 M) was added until no further precipitate was formed. The resulting solid was purified through flash chromatography (THF) and dried with $MgSO_4$ to give a pale yellow powder.

Yield: 10.02 g (19.6 mmol, 85%); ES-MS (DMSO) m/z = 509.10 $(C_{33}H_{17}O_6)^-$; ^{1}H-NMR (DMSO-D_6, 400MHz) δ_H (ppm): 13.21 (3H, s, H^1), 8.01 (6H, d, J=8Hz, H^2), 7.87 (3H, s, H^4), 7.72 (6H, d, J=8Hz, H^3); FT-IR (diffuse reflectance) ν_{max} cm^{-1}: 2980 (br), 2761 (br), 2558 (br) 1690 (s), 1605 (s), 1560 (m), 1420 (s), 1314 (s), 1284 (s), 1177 (m), 1111 (w), 857 (s), 769 (s). Elemental analysis (%) for $C_{33}H_{18}O_6$: Expected: C, 77.64; H, 3.55; N, 0. Found: C, 76.89; H, 3.41; N, 0.

7.3 Synthesis of Coordination Compounds

7.3.1 Synthesis of $[Co(\mathbf{L1})_2]$, (**1**)

L1 (0.07 g, 0.27 mmol), cobalt nitrate hexahydrate (0.036 g, 0.13 mmol), potassium hydroxide (0.02 g), methanol (7 ml) and water (1 ml) were mixed in a Teflon lined autoclave for 30 minutes and the tube sealed and heated to 120 °C for 14 hours and allowed to cool slowly to room temperature over six hours. The mixture consisted of a pale orange solution

and orange crystals of [Co(**L1**)$_2$] along with an unidentified black powder, possibly unreacted ligand. The crystals were separated manually under a microscope and analysed.

Yield: *ca.* 40 %; FT-IR (diffuse reflectance) ν_{max} cm^{-1}: 3115 (w), 1618 (m), 1579 (vs), 1486 (m), 1415 (s), 1390 (s), 1321 (m), 1230 (m), 1196 (s), 1119 (s), 1085 (s), 1072 (m), 1030 (m), 1009 (s), 962 (w), 913 (m), 886 (s), 795 (s), 770 (s), 726 (vs), 678 (s); Elemental analysis (%) for [Co(**L1**)$_2$] : Expected: C, 37.71; H, 1.76; N, 39.09. Found: C, 37.53; H, 1.83, N, 37.86.

7.3.2 Synthesis of [Mn(**L1**)$_2$], (**2**)

A mixture of **L1** (0.07 g, 0.27 mmol), manganese acetate tetrahydrate (0.0245 g, 0.1 mmol), methanol (9 ml) and deionised water (1 ml) were placed in a 20 ml Teflon lined autoclave. The mixture was stirred for 30 minutes to give a cloudy black solution. The autoclave was sealed and heated at 115 °C for 15 hours. The autoclave was then allowed to cool slowly to room temperature over 5 hours. The mixture consisted of a colourless liquid and colourless cubic crystals of [Mn(**L1**)$_2$]. The mixture also contained an unidentified black powder, possibly unreacted ligand. The crystals were separated manually under a microscope and analysed.

Yield: *ca.* 50 %; FT-IR (diffuse reflectance) ν_{max} cm^{-1}: 3125 (w), 1615 (m), 1581 (vs), 1485 (m), 1471(m), 1413 (s), 1380(vs), 1233(m), 1200(w), 1115 (m), 1088 (s), 1030 (w), 1010 (m), 912 (m), 884 (m), 794 (s), 771(s), 716 (vs), 682 (s); Elemental analysis (%) for [Mn(**L1**)$_2$]: Expected: C, 37.97; H, 1.76; N, 39.36. Found: C, 38.21; H, 1.96; N, 37.7.

7.3.3 Synthesis of [Cd(**L2**)$_2$MeOH], (**3**)

L2 (0.07 g, 0.3 mmol), cadmium nitrate tetrahydrate (0.093 g, 0.03 mmol), methanol (8 ml) and deionised water (3 ml) were stirred for 20 minutes in a Teflon lined autoclave. The autoclave was sealed and heated to 100 °C for 18 hours and then was allowed to cool slowly to room temperature over 5 hours, to give a pale yellow solution and pale yellow rectangular crystals of [Cd(**L2**)$_2$MeOH].

Yield: *ca.* 40%; FT-IR (diffuse reflectance) ν_{max} cm^{-1}: 3126 (m), 1704 (m), 1615 (m), 1548 (vs), 1480 (m), 1427 (s), 1377 (s), 1254 (m), 1212 (m), 1081 (m), 1014 (m), 915 (m), 764 (vs), 745 (vs), 712 (s), 677 (s); Elemental analysis (%) for [Cd(**L2**)$_2$MeOH] : Expected: C, 37.43; H, 2.15; N, 18.38. Found: C, 36.75; H, 2.08; N, 17.78.

7.3.4 Synthesis of [Zn(**L2**)(H_2O)$_2$], (**4**)

A solution of **L2** (0.01 g, 0.042 mmol), potassium hydroxide (0.1 ml, 1 M in H_2O) and zinc nitrate hexahydrate (0.125g, 0.42 mmol) in H_2O (7 ml) were stirred for 20 minutes, in a Teflon lined autoclave. The autoclave was then sealed and heated at 85 °C for 36 hours. The resulting pale yellow block shaped crystals co-crystallised with a colourless microcrystalline material that was manually removed.

Yield: *ca.* 30%; FT-IR (diffuse reflectance) ν_{max} cm^{-1}: 3605 (w), 3517 (w), 3437 (br), 3300 (br), 3123 (m), 1615 (m), 1567 (s), 1475 (m), 1435 (m), 1377 (sh), 1365 (s), 1314 (sh), 1226 (w), 1186 (w), 1102 (w), 1087 (m), 775 (m); Elemental analysis (%) for [Zn(**L2**)(H_2O)$_2$]: Expected: C,32.41; H, 2.42; N, 16.80. Found: C, 32.01; H, 2.34; N, 16.42.

7.3.5 Synthesis of [Cu(**L2**)], (**5**)

L2 (0.013 g, 0.056 mmol), copper nitrate trihydrate (0.0193 g, 0.08 mmol), DMF (1.5 ml) and methanol (0.5 ml) were stirred in a 5 ml glass vial for 30 minutes to give a dark green solution. The vial was sealed and heated to 85 °C for 18 hours and then allowed to cool slowly to room temperature over 5 hours. The mixture was composed of dark green cubic crystals and a dark green solution. The crystals were washed with DMF (x3) and stored in DMF.

Yield: *ca.* 50%; FT-IR (diffuse reflectance) ν_{max} cm^{-1}: 1635(s), 1437 (m), 1401 (sh), 1386 (sh), 1376 (vs), 1182 (w), 1089 (m), 915 (m), 782 (9), 746 (m), 728 (vs), 659 (m): Elemental analysis (%) for [Cu^{II}(**L2**)]·DMF·MeOH: Expected: C, 38.95; H, 3.77; N, 17.47. Found: C, 38.24; H, 3.21; N, 16.95.

7.3.6 Synthesis of $[Zn_3(\mathbf{L3})_2(DMF)_2]$, (**6**)

L3 (0.044 g, 0.087 mmol) was added to a solution of DMF (6 ml) containing zinc nitrate hexahydrate (0.085 g, 0.28 mmol). The mixture was stirred and sonicated for 10 minutes, transferred into a 10 mL sealed glass vial and heated for 3 days at 85 °C. After cooling to room temperature needle-shaped crystals of $[Zn_3(\mathbf{L3})_2(DMF)_2]$ were separated, washed with DMF (x3) and kept in DMF for storage.

Yield: *ca.* 40%; FT-IR (diffuse reflectance) ν_{max} cm^{-1}: 3399 (br), 2930 (w), 1655 (s), 1604 (s), 1547 (s), 1495 (w), 1405 (sh), 1386 (s), 1254 (m), 1175 (w), 1095 (m), 1015 (w), 782 (s); Elemental Analysis (%) for $[Zn_3(\mathbf{L3})_2(DMF)_2]\cdot DMF\cdot 3H_2O$: Expected: C, 60.69; H, 3.87; N, 2.83; Found: C, 60.47; H, 3.38; N, 2.51.

7.3.7 Synthesis of $(Me_2NH_2)[Zn_5(\mathbf{L3})_3(\mu_3\text{-}OH)_2(DMF)_2]$, (**7**)

L3 (0.01 g, 0.020 mmol) was added to a solution of DMF (6 ml) containing zinc nitrate hexahydrate (0.037 g, 0.13 mmol). The mixture was stirred and sonicated for 10 minutes, transferred into a 10 mL sealed glass vial and heated for 3 days at 85°C. After cooling to room temperature pale yellow block crystals of $(Me_2NH_2)[Zn_5(\mathbf{L3})_3(\mu_3\text{-}OH)_2(DMF)_2]$ were obtained and washed with DMF (x3) and kept in DMF for storage.

Yield *ca.* 30%; FT-IR (diffuse reflectance) ν_{max} cm^{-1}: 3334 (br), 1655 (s), 1602 (s), 1580 (sh), 1547 (s), 1402 (sh), 1386 (s), 1254 (w), 1175 (w), 1095 (m), 1016 (w), 781 (s); Elemental Analysis (%) for $(Me_2NH_2)[Zn_5(OH)_2(\mathbf{L3})_3(DMF)_2]\cdot 6DMF\cdot 9H_2O$: Expected: C, 56.10; H, 4.86; N, 4.71; Found: C, 55.68; H, 4.31; N, 5.00.

7.3.8 Synthesis of $(Me_2NH_2)[Co_5(\mathbf{L3})_3(\mu_3\text{-}OH)_2(DMF)_2]$, (**8**)

Compound **8** was synthesised using an identical synthetic procedure to that used in the synthesis of **7**, with cobalt nitrate hexahydrate (0.038 g, 0.13 mmol) replacing zinc nitrate hexahydrate, to give orange block shaped crystals.

Yield *ca.* 30%; FT-IR (diffuse reflectance) ν_{max} cm^{-1}: 3332 (br), 2926 (w), 1650 (s), 1602 (s), 1582 (sh), 1544 (s), 1383 (s), 1301 (m), 1251 (m), 1175 (w), 1092 (m), 1015 (w), 780 (s); Elemental Analysis (%) for $(Me_2NH_2)[Co_5(OH)_2(\mathbf{L3})_3(DMF)_2]\cdot 6DMF\cdot 9H_2O$: Expected: C, 56.78; H, 4.92; N, 4.77; Found: C, 55.41; H, 4.41; N, 4.87.

7.3.9 $[Cu_3(\mathbf{L3})_2(H_2O)_3]$, (**9**)

L3 (0.0153 g, 0.03 mmol) was added to a glass vial (1.5 ml) containing copper nitrate trihydrate (0.0108 g, 0.045 mmol) in 1 ml DMF. The solution was sonicated for 10 minutes, the vial was sealed and placed in the oven at 85 °C for 36 hours. The resulting turquoise crystals were washed with DMF (x3) and stored in DMF.

Yield: *ca.* 40%; FT-IR (diffuse reflectance) ν_{max} cm^{-1}: 2952 (w), 1658 (s), 1603 (s), 1581 (s), 1404 (sh), 1383 (s), 1261 (w), 1101 (m), 867 (m), 781 (s); Elemental Analysis (%) for $[Cu_3(\mathbf{L3})_2(H_2O)_3]\cdot 6DMF$: Expected: C, 59.41; H, 4.63; N, 4.95; Found: C, 58.58; H, 4.83; N, 4.80.

7.3.10 Synthesis of $[Ho(\mathbf{L3})(H_2O)_2]$, (**10**)

A solution of **L3** (0.04 g, 0.08 mmol) in DMF (5 ml) was added to a 10 ml glass vial containing holmium nitrate pentahydrate (0.009 g, 0.02 mmol). The mixture was sonicated for 10 minutes, the vial was sealed and heated for 72 hours at 100 °C. After cooling to room temperature, the resulting small, pale pink crystals of $[Ho(\mathbf{L3})(H_2O)_2]$ were washed with DMF (x3) and stored in DMF.

Yield: *ca.* 20%; FT-IR (diffuse reflectance) ν_{max} cm^{-1}: 2925(br), 1670(s), 1624(s), 1604 (s), 1582 (s), 1535 (s), 1501 (m), 1407 (s), 1380 (s). 1257 (m), 1177 (w), 1090 (s), 1017 (m), 858 (m), 781 (s); Elemental analysis (%) for $[Ho(\mathbf{L3})(H_2O)_2].5DMF$: Expected: C, 53.68; H, 5.07; N, 6.52. Found: C, 52.57; H, 4.71; N, 6.94.

7.3.11 Compounds structurally related to [Ho(**L3**)$(H_2O)_2$], (**10**)

The compounds described in this section were prepared using analogous synthetic procedures to that used to synthesise **10**, with the relevant lanthanide nitrate replacing holmium nitrate pentahydrate using the same mole ratios. The obtained yields varied between 25-40%.

- [Dy(**L3**)$(H_2O)_2$], (**10(Dy)**):

FT-IR (diffuse reflectance) ν_{max} cm^{-1}: 1666(s), 1624 (s), 1604 (s), 1581 (s), 1535 (s), 1413 (s), 1380 (s), 1092 (s), 1017 (m), 858(m), 781 (s); Elemental analysis (%) for [Dy(**L3**)$(H_2O)_2$].5DMF: Expected: C,53.81; H, 5.08; N, 6.54. Found: C, 52.31; H, 4.61; N, 6.81.

- [Tb(**L3**)$(H_2O)_2$], (**10(Tb)**):

FT-IR (diffuse reflectance) ν_{max} cm^{-1}: 1662(s), 1621 (s), 1603 (s), 1581 (s), 1534 (s), 1413 (s), 1384 (s), 1090 (s), 1017 (m), 857(m), 782 (s); Elemental analysis (%) for [Tb(**L3**)$(H_2O)_2$].5DMF: Expected: C, 53.99; H, 5.10; N, 6.56. Found: C, 52.69; H, 4.97; N, 6.75.

- [Eu(**L3**)$(H_2O)_2$], (**10(Eu)**):

FT-IR (diffuse reflectance) ν_{max} cm^{-1}: 1661(s), 1620 (m), 1603 (s), 1580 (s), 1534 (s), 1413 (s), 1382 (s), 1091 (s), 1017 (m), 855(m), 782 (s); Elemental analysis (%) for [Ho(**L3**)$(H_2O)_2$].5DMF: Expected: C, 54.34; H, 5.08; N, 6.54. Found: C, 53.19; H, 4.76; N, 7.02.

- [Yb(**L3**)$(H_2O)_2$], (**10(Yb)**):

FT-IR (diffuse reflectance) ν_{max} cm^{-1}: 1658(s), 1626 (m), 1602 (s), 1578 (s), 1531 (s), 1413 (s), 1382 (s), 1093 (s), 1017 (m), 860(m), 781 (s); Elemental analysis (%) for [Yb(**L3**)$(H_2O)_2$].5DMF: Expected: C, 53.28; H, 5.03; N, 6.47. Found: C, 52.18; H, 4.66; N, 7.19.

- [Er(**L3**)$(H_2O)_2$], (**10(Er)**):

FT-IR (diffuse reflectance) ν_{max} cm^{-1}: 1654 (s), 1625 (m), 1602 (s), 1578 (s), 1528 (m), 1411

(s), 1382 (s), 1094 (s), 1017 (m), 860 (m), 781 (s); Elemental analysis (%) for [Yb(**L3**)$(H_2O)_2$].5DMF: Expected: C, 53.57; H, 5.06; N, 6.51. Found: C, 52.01; H, 4.62; N, 6.90.

- **[Nd(L3)]**:

FT-IR (diffuse reflectance) ν_{max} cm^{-1}: 1665 (s), 1605 (s), 1577 (s), 1517 (s), 1505 (sh), 1409 (s), 1387 (s), 1255 (w), 1174 (w), 1090 (s), 855 (m), 784 (s); Elemental analysis (%) for proposed formula of [Nd(**L3**)$(H_2O)_2$].5DMF: Expected: C, 54.74; H, 5.17; N, 6.65. Found: C, 54.64; H, 3.40; N, 3.90.

- **[Sm(L3)]**:

FT-IR (diffuse reflectance) ν_{max} cm^{-1}: 1665 (s), 1604 (s), 1577 (s), 1522 (s), 1503 (sh), 1411 (s), 1384 (s), 1253 (w), 1177 (w), 1090 (s), 855 (m), 783 (s); Elemental analysis (%) for proposed formula of [Sm(**L3**)$(H_2O)_2$].5DMF: Expected: C, 54.42; H, 5.14; N, 6.61. Found: C, 53.89; H, 3.38; N, 3.75.

7.3.12 Synthesis of $[Ho_2(\mathbf{L2})_4(H_2O)_4]$, (**11**)

L2 (0.02 g, 0.09 mmol) was added to a deionised water solution containing potassium hydroxide (0.17 ml, 1M) in a teflon lined autoclave and stirred until **L2** had fully dissolved. Holmium nitrate pentahydrate (0.009 g, 0.02 mmol) was then added to this and the resulting solution was stirred for 10 minutes, the autoclave sealed and heated at 85 °C for 24 hours.

Yield: *ca.* 40%. FT-IR (diffuse reflectance) ν_{max} cm^{-1}: 3396 (br), 3135 (w), 1709 (m), 1615 (m), 1567 (s), 1546 (s), 1471 (m), 1447 (m), 1400 (s) 1386 (sh), 1244 (m), 1210 (m), 1178 (m), 1086 (m), 922 (m), 779 (s), 746 (s); Elemental analysis (%) for $[Ho_2(\mathbf{L2})_4(H_2O)_4]$: Expected: C, 32.45; H, 1.97; N, 16.82. Found: C, 31.51; H, 1.89; N, 16.19.

7.3.13 Compounds structurally related to **11**

The compounds described in this section were prepared using analogous synthetic procedures to that used to synthesise **11**, with the relevant lanthanide nitrate salt replacing holmium nitrate pentahydrate. The obtained yields varied between 30 and 45%.

- $[Dy_2(\mathbf{L2})_4(H_2O)_4]$, **11(Dy)**:

FT-IR (diffuse reflectance) ν_{max} cm^{-1}: 1707 (m), 1641 (m), 1615 (m), 1567 (s), 1546 (s), 1471 (m), 1447 (m), 1430 (m), 1386 (sh), 1244 (m), 1210 (m), 1086 (m), 922 (m), 779 (s); Elemental analysis (%) for $[Dy_2(\mathbf{L2})_4(H_2O)_4]$: Expected: C, 32.57; H, 1.97; N, 16.88. Found: C, 31.7; H, 1.92; N, 16.42.

- $[Yb_2(\mathbf{L2})_4(H_2O)_4]$, **11(Yb)**:

FT-IR (diffuse reflectance) ν_{max} cm^{-1}: 1710 (m), 1644 (sh), 1615 (m), 1567 (s), 1549 (s), 1475 (m), 1447 (m), 14.1 (m), 1385 (sh), 1244 (m), 1212 (m), 1086 (m), 925 (m), 779 (s); Elemental analysis (%) for $[Yb_2(\mathbf{L2})_4(H_2O)_4]$: Expected: C, 32.06; H, 1.94; N, 16.62. Found: C, 31.17; H, 1.87; N, 16.19.

7.4 References:

1. Bruker-Axs Inc., Madison, Wisconsin, USA, Editon edn., 1997-2012.
2. K. Brandenburg, Putz. H. and M. Berndt, *Crystal Impact*, Kreuzherrenstr. 102, D-53227 Bonn, Germany, Editon edn., 2011., vol. 3.
3. E. B. S. J.H. Dymond, *The Viral Coefficients of Pure Gases and Mixtures*, Claredon Press, Oxford, 1980.

View Article Online / Journal Homepage / Table of Contents for this issue
Dynamic Article Links

ChemComm

Cite this: *Chem. Commun.*, 2012, **48**, 3638–3640

www.rsc.org/chemcomm

COMMUNICATION

Extending the family of Zn-based MOFs: synthetic approaches to chiral framework structures and MOFs with large pores and channels†

Nianyong Zhu, Gerard Tobin and Wolfgang Schmitt*

Received 24th November 2011, Accepted 9th February 2012
DOI: 10.1039/c2cc17357c

Tri- and pentanuclear, kinetically stable SBUs were exploited for the preparation of the novel MOFs $[Zn_3(BTEB)_2(DMF)_2]$ and $(Me_2NH_2)[Zn_5(BTEB)_3(\mu_3\text{-}OH)_2(DMF)_2]$. The applied synthetic approach results in topologies that are stabilised by tritopic benzene-trisethynylbenzoic acid (BTEB) linkers giving rise to chiral frameworks with large pores or channels.

Metal–organic frameworks (MOFs) are classified as crystalline materials consisting of clusters or metal ions linked coordinatively through organic ligands and resulting in microporous networks.[1] The interest in MOFs is a result of their advantageous characteristics which include facile synthesis, high porosity, and amenability to chemical modification for targeting purposes.[2] MOFs are regarded as key materials related to energy storage[3] and efficient usage of resources, as their unprecedented surface areas make them promising alternative materials for gas storage,[4] gas separation[5] and catalysis purposes.[6] Current activities focus on the development of synthetic concepts to novel MOFs whereby increased hydrogen and CO_2 storage capabilities may provide scientific concepts to initiate a shift towards more sustainable energy concepts. Most employed synthetic approaches to MOFs rely on self-assembly using simple inorganic metal ions as starting materials that may aggregate into oligonuclear complexes in the presence of suitable, cross-linking multi-dentate ligands. Careful selection of the metal ions, the nature of the assembled coordination clusters and ligands and consideration of their preferred coordination modes and geometries provide control over the resulting network topologies. Rigid, aromatic polycarboxylate ligands whose backbone structures can be extended modularly for instance through insertion of phenylene or ethynyl moieties are attractive ligands that give rise to ultra-high surface area materials with amenable pore structures and interpenetration patterns.

To explore the formation of new open-framework materials that give rise to high surface areas and interesting interpenetration patterns, the tri-functional ligand, 1,3,5-benzene-trisethynylbenzoic acid (BTEB), was chosen.[7] Its tritopic, triangular topology is characterized by a carboxylate–carboxylate and centroid–carboxlayte separation distance of *ca.* 18 Å and 10 Å. The only BTEB coordination compounds previously synthesized and structurally characterized comprise of a {Ni/cylam} 2D-network polymer[8] and a highly porous MOF containing octahedral $\{Zn_4O(O_2C)_6\}$ SBUs.[9] Here we report two new BTEB-based MOFs, $[Zn_3(BTEB)_2(DMF)_2]$ (**TCM-1**) and $(Me_2NH_2)[Zn_5(BTEB)_3(\mu_3\text{-}OH)_2(DMF)_2]$ (**TCM-2**), whose topologies and interpenetration patterns are determined by the nuclearity of kinetically stable, tri- and pentanuclear Zn(II) SBUs. In the former case the observed helical interpenetration patterns results in supramolecular chirality.

TCM-1 and **-2** form under solvothermal reaction conditions at 80 °C in DMF (ESI†). Phase-pure, colourless, needle-like crystals of **[TCM-1].solv** are obtained at a molar Zn^{2+}/BTEB ratio of 2 : 1. The MOF can be also obtained at a Zn^{2+}/BTEB ratio of 3.3 : 1. Above a molar reactant ratio of 3.8/1, **[TCM-2].solv** starts to co-crystallise as yellowish block crystals. Phase-pure samples of **[TCM-2].solv** can be obtained when the molar ratio is raised to 6 : 1. Further increased Zn^{2+} concentrations, *e.g.* Zn^{2+}/BTEB ratios of 9 : 1, result in the formation of MOF-180 that contains tetranuclear SBUs and whose structure was previously reported.[9]

TCM-1 contains trinuclear $\{Zn_3(O_2C)_6\}$ SBUs (Fig. 1a and b) in which the Zn-atoms are linearly arranged and triply bridged by bidentate carboxylate moieties that originate from six different fully deprotonated BTEB ligands. The central zinc atom is in an almost ideal octahedral coordination environment. The outer two Zn atoms adopt distorted tetrahedral coordination geometries whose remaining terminal sites are provided by O-donors from coordinating DMF molecules. Similar complexes have previously been isolated as 0D systems and used to prepare 3D-network structures.[10] **[TCM-1].solv** crystallizes either in the space group $P4_322$ or $P4_122$ (enantiomeric) representing a chiral supramolecular system in which the shape and topology of SBUs promote the formation of optical isomers. Each trinuclear Zn moiety is linked *via* π–π interacting BTEB pairs to three neighbouring Zn SBUs. Two carboxylate functionalities of each organic ligand link the complexes along 4_3 (or 4_1)-screw axes that coincide with the crystallographic *c*-axes (as seen in Fig. 2); the third deprotonated acid functionality connects the helical chains according to the 4-fold screw symmetry in the other directions of space to form a 3D network structure. **TCM-1** is 2-fold interpenetrated consisting of two symmetry equivalent nets that are not connected through covalent or coordination bonds (Fig. 2c and d). The symmetry of **TCM-1** and of the observed interpenetration pattern results in double

School of Chemistry & CRANN, University of Dublin, Trinity College Dublin, Dublin 2, Ireland. E-mail: schmittw@tcd.ie
† Electronic supplementary information (ESI) available. CCDC 810330 and 843699. For ESI and crystallographic data in CIF or other electronic format see DOI: 10.1039/c2cc17357c

This journal is © The Royal Society of Chemistry 2012

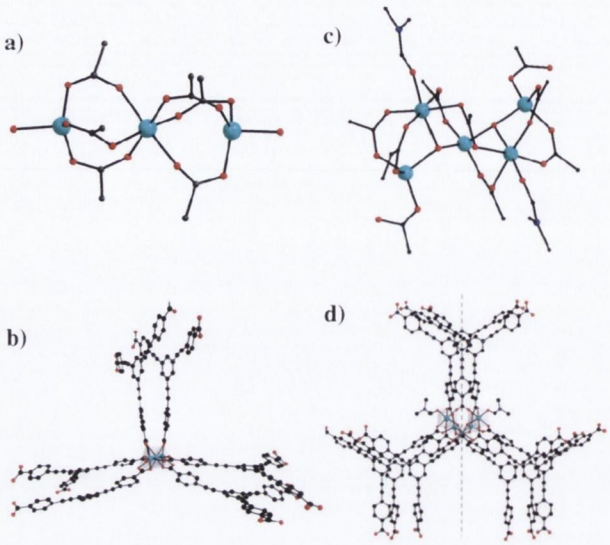


Fig. 1 (a, b) Trinuclear Zn(II) building unit in **TCM-1** that is stabilised by six carboxylate moieties (only O-donor atoms of the coordinating DMF molecules are represented); (c, d) pentanuclear Zn(II) SBU in **TCM-2** that is stabilised by nine carboxylate moieties (*C*2 symmetry axis indicated as intersected line). Colour code: Zn cyan, O red, C grey.

helical arrangements in which dispersion forces between the aromatic ligand moieties promote close inter-ligand contacts. Thus, the observed interpenetration mode stabilises the observed topology and does not significantly affect pore and channel diameters of the supramolecular assembly. **TCM-1** forms an open-framework structure whose void spaces are accessible from all directions of space. This feature distinguishes **TCM-1** from previously reported related structures that are stabilised by the less extended ligands, *e.g.* 4,4′,4″-*s*-triazine-2,4,6-triyltri-benzoate (TATB) or chiral derivatives.[11] In comparison to $[Zn_3(TATB)_2(HCOO)]$, the use of extended BTEB ligands results in a significant increase of the solvent-accessible void space from *ca.* 4535 Å^3 (54% of the unit cell volume) to *ca.* 11 135 Å^3 (72%). The cross-sectional diameter of the chiral channels in **TCM-1** when viewed in the direction of the crystallographic *c*-axis doubles to *ca.* 12 Å. **TCM-1** has channel openings that are characterised by 16 × 11 Å and that are absent in the related $[Zn_3(TATB)_2(HCOO)]$–MOF.

TCM-2 contains novel pentanuclear $\{Zn_5(\mu_3\text{-}OH)_2(O_2C)_9DMF_2\}$-SBUs in which two μ_3-OH ligands stabilise two triangular Zn^{II} arrangements (Fig. 1c and d). The atom positions of these triangular units are related by C_2 rotational symmetry. The complex is stabilized by 9 deprotonated BTEB ligands: 7 carboxylate functions act in a bridging bidentate mode and two as monodentate ligands. The hydroxo and carboxylate O-donor atoms facilitate distorted tetrahedral coordination geometries for four Zn^{II} atoms, including the central Zn atom. Two coordinating DMF molecules complete the octahedral coordination environments of the remaining two Zn^{II} sites. Each complex unit in **TCM-2** carries an overall −1 charge which is most likely compensated by disordered dimethyl ammonium counterions $Me_2NH_2^+$ which commonly form under solvothermal reaction conditions using DMF as solvent.

The new non-planar pentanuclear SBU in **TCM-2** acts as a 9-connecting node (Fig. 3). However, the 3-pointed, equilateral star symmetry of the organic ligand is further translated to the structure of the inorganic SBU. The ligands can be divided into 3 × 3 groups whose struts enclose *ca.* 120° angles and point in three distinct directions of space. This binding motif results in a 3D honeycomb topology when viewed in the [001] direction. As for **TCM-1**, **TCM-2** also contains two interpenetrated symmetry-equivalent frameworks, which are effectively interwoven with each other (Fig. 3). The observed interpenetration mode is highlighted in Fig. 3 and is stabilized by pairwise π–π-interactions between central aromatic phenyl ring moieties of the tritopic organic BTEB ligands (centroid–centroid distance of 3.36 Å between the aromatic rings). Despite this interpenetration effect, **TCM-2** contains large void spaces accounting for 49% of the cell volume. Pore openings of the network structure when viewed in the [001] and [101] directions have cross-sectional diameters of 10.5 Å and 9.0 Å, respectively.

Freshly prepared crystals of **[TCM-1].solv** desolvate readily and elemental analyses suggest that samples that were stored for several

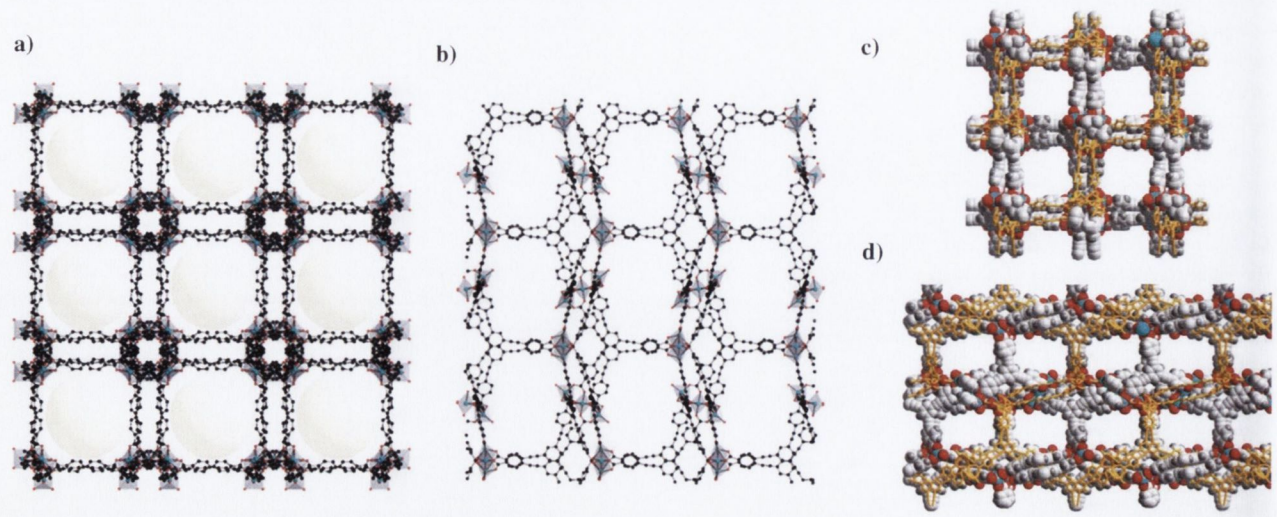


Fig. 2 Crystal structure of **TCM-1**. (a) View in the direction of the crystallographic *c*-axis; (b) view in the direction of the crystallographic *b*-axis; (c and d) 2-fold interpenetration in **TCM-1** when viewed in the direction of the crystallographic *c*-axis and *a*-axis. One network shows in space filling representation whilst the second is shown as orange wireframe; constitutional solvent molecules neglected for clarity. Colour code: Zn cyan, O red, C grey.

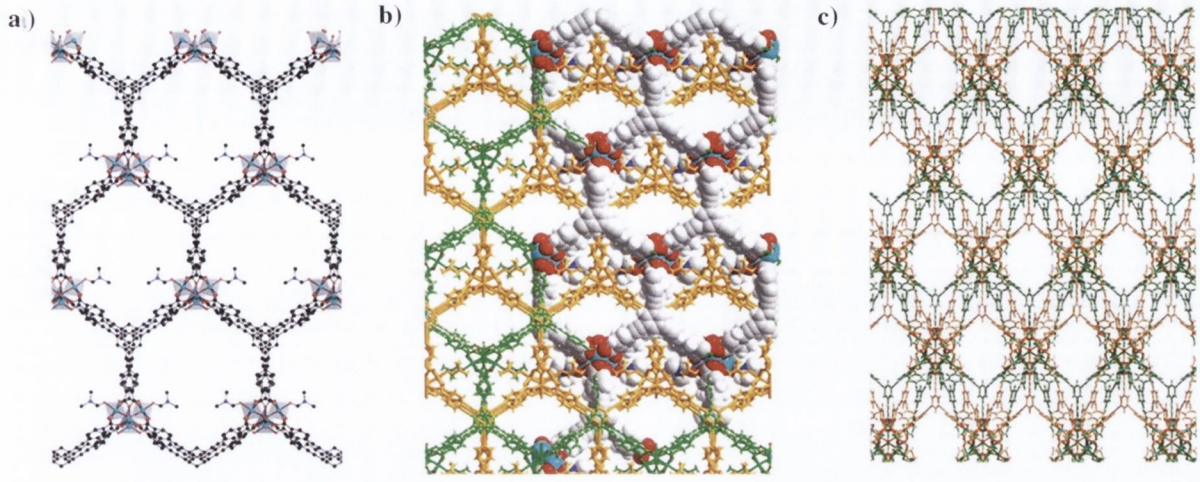


Fig. 3 View of the framework structure of **TCM-2** viewed in the direction of the crystallographic *c*-axis (Zn cyan, O red, C grey). (b) Interpenetration pattern in **TCM-2** with the view in the direction of the crystallographic *c*-axis (independent frameworks highlighted in different colours). (c) Interpenetrated networks (green and brown) with the view in the [101]-axis.

weeks at room temperature only retain one constitutional DMF and two water molecules per formula unit. Thermogravimetric analyses of freshly prepared samples in an air atmosphere confirm a weight loss of *ca.* 50% between 20 and 120 °C attributable to the loss of constitutional solvent molecules from the network structure. A thermogravimetric step of 7 wt% most likely originates from the removal of the two coordinated DMF molecules. Above 370 °C the oxidative degradation of the organic ligand is observed. **TCM-2** reveals a very similar decomposition behaviour. A weight loss of 37% between 20 and 120 °C is the result of the desolvation of the compound. A weight loss of 9% between 120 and 200 °C stems from the removal of the coordinated DMF molecules before the oxidative degradation of the $Me_2NH_2^+$ cations (4% between 200 °C and 350 °C) and the organic ligands above 350 °C destroy the framework structure. Elemental analyses suggest that bulk samples of **TCM-2** that were stored for several weeks at room temperature retain five DMF and nine constitutional water molecules per formula unit.

The most important attributes of these MOFs which relate to energy applications stem from their surface areas available for gas sorption applications. The structural analysis of **TCM-1** and its calculated void volume give rise to a relatively high surface area (2000–4000 $m^2\ g^{-1}$) whilst the chiral framework structure can be maintained. However, our preliminary activation and BET experiments using **[TCM-1].solv** show that the structure tends to collapse due to the capillary forces that prevail upon solvent removal or due to the loss of the coordinating terminal DMF molecules and associated phase transitions. Preliminary drying attempts using supercritical CO_2 suggest that the framework structure may be maintained upon desolvation. Activation of **[TCM-2].solv** involved the exchange of constitutional solvent molecules by acetone and by dichloromethane. Outgassing was achieved under vacuum conditions at 30 °C. N_2 sorption studies gave a BET surface area of 1338 $m^2\ g^{-1}$ and a corresponding Langmuir surface area of 1393 $m^2\ g^{-1}$. Outgassing attempts at 60 °C or 100 °C did not improve the surface areas and may be associated with the removal of the coordinating DMF molecules or the decomposition of the counterions and an accompanying phase change resulting in closure of the pores. H_2 adsorption studies on **TCM-2** were carried out at 77 K at $p/p_o \approx 1$ (p_o near 1 atm). The absorbed H_2 quantity correlates to 150 cc g^{-1}, corresponding to 13 mg g^{-1} or *ca.* 1.3 wt%.

In summary, we report the syntheses, structures and properties of two unprecedented Zn-based MOFs. The applied synthetic approach takes advantage of kinetically stable SBUs that form selectively and phase-pure depending on the molar ratios of the reactants. We are currently devising approaches to exploit their chiral framework structures and large pores and channels for gas storage and catalysis purposes.

Notes and references

1 *Metal–organic framework-design and applications*, ed. L. R. McGillivray, John Wiley & Sons, Inc., 2010.
2 See special issue edited by J. R. Long and O. M. Yaghi, *Chem. Soc. Rev.*, 2009, **38**, 1201.
3 J. Yang, A. Sudik, C. Wolverton and D. J. Siegel, *Chem. Soc. Rev.*, 2010, **39**, 656.
4 (*a*) J. L. C. Rowsell and O. M. Yaghi, *Angew. Chem., Int. Ed.*, 2005, **44**, 4670; (*b*) X. Lin, J. Jia, P. Hubberstey, M. Schröder and N. R. Champness, *CrystEngComm*, 2007, **9**, 438; (*c*) M. Dinca and J. R. Long, *Angew. Chem., Int. Ed.*, 2008, **47**, 6766; (*d*) R. E. Morris and P. S. Wheatley, *Angew. Chem., Int. Ed.*, 2008, **47**, 4966.
5 (*a*) J.-R. Li, R. J. Kuppler and H.-C. Zhou, *Chem. Soc. Rev.*, 2009, **38**, 1477; (*b*) O. M. Yaghi, G. Li and H. Li, *Nature*, 1995, **378**, 703.
6 (*a*) W. Lin, *J. Solid State Chem.*, 2005, **178**, 2486; (*b*) R.-Q. Zou, H. Sakurai, S. Han, R.-Q. Zhong and Q. Xu, *J. Am. Chem. Soc.*, 2007, **129**, 8402; (*c*) S. Horike, M. Dinca, K. Tamaki and J. R. Long, *J. Am. Chem. Soc.*, 2008, **130**, 5854; (*d*) Y. Liu, W. Xuan and Y. Cui, *Adv. Mater.*, 2010, **22**, 4112.
7 R. K. Castellano and J. Rebek, Jr., *J. Am. Chem. Soc.*, 1998, **120**, 3657.
8 M. P. Suh, H. J. Choi, S. M. So and B. M. Kim, *Inorg. Chem.*, 2003, **42**, 676.
9 H. Furukawa, N. Ko, Y. B. Go, N. Aratani, S. B. Choi, E. Choi, A. O. Yazaydin, R. Q. Snurr, M. O'Keeffe, J. Kim and O. M. Yaghi, *Science*, 2010, **329**, 424.
10 see *e.g.* (*a*) C. A. Williams, A. J. Blake, P. Hubberstey and M. Schröder, *Chem. Commun.*, 2005, 5435; (*b*) W. Clegg, I. R. Little and B. P. Straughan, *Chem. Commun.*, 1985, 73; (*c*) X. F. Wang, Y. B. Zhang, X. N. Cheng and X. M. Chen, *CrystEngComm*, 2008, **10**, 753; (*d*) J. Y. Lee, L. Pan, S. P. Kelly, J. Jagiello, T. J. Emge and J. Li, *Adv. Mater.*, 2005, **17**, 2703.
11 (*a*) Y. Ke, D. J. Collins, D. Sun and H. C. Zhou, *Inorg. Chem.*, 2006, **45**, 1897; (*b*) D. Sun, Y. Ke, D. J. Collins, G. A. Lorigan and H. C. Zhou, *Inorg. Chem.*, 2007, **46**, 2725; (*c*) K. Gedrich, M. Heitbaum, A. Notzon, I. Senkovska, R. Fröhlich, J. Getzschmann, U. Mueller, F. Glorius and S. Kaskel, *Chem.–Eur. J.*, 2011, **17**, 2099.

This journal is © The Royal Society of Chemistry 2012